

# **Unravelling the Anomalous Nature of the Aqueous Nanochannels in Lyotropic Liquid Crystals**

A Thesis

Submitted in Partial Fulfillment of the Requirements for  
the Degree of

**Doctor of Philosophy**

by

**Konoya Das**

Reg. ID: 20142011



**Indian Institute of Science Education and Research (IISER), Pune**

**2021**

**Dedicated to my family**



Indian Institute of Science Education and Research (IISER), Pune

---

## Certificate

---

It is hereby certified that the work described in this thesis entitled “*Unravelling the Anomalous Nature of the Aqueous Nanochannels in Lyotropic Liquid Crystals*” submitted by *Ms. Konoya Das* was carried out by the candidate, under my supervision. The work presented here or any part of it has not been included in any other thesis submitted previously for the award of any degree or diploma from any other university or institution.

Date: 21.01.2021

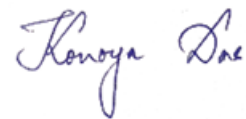
A handwritten signature in blue ink that reads "Partha Hazra".

**Dr. Partha Hazra**  
Research Supervisor  
Email: [p.hazra@iiserpune.ac.in](mailto:p.hazra@iiserpune.ac.in)  
Contact No.: +91(20)25908077

## Declaration

I declare that this written submission represents my ideas in my own words and I have adequately cited and referenced the original sources wherever other's ideas have been included. I also declare that I have adhered to all principles of academic honesty and integrity and have not misrepresented or fabricated or falsified any idea/ data/ fact/ source in my submission. I understand that violation of the above will cause disciplinary action by the Institute and can also evoke penal action from the sources which have thus not been properly cited or from whom proper permission has not been taken where needed.

Date: 21.01.2021



**Konoya Das**

Reg. Id: 20142011

## Acknowledgment

I would like to express my gratitude to Dr. Partha Hazra, my thesis supervisor, for his guidance and counsel throughout my PhD journey. His able supervision and encouragement have helped me develop a set of skills that will remain with me for the rest of my research career. He has inculcated in me the skill to design and execute different projects, the art of writing research papers and the patience to deal with difficulties in research. I am deeply indebted for all the support that he has provided me during the last few months, including his ceaseless efforts in helping me work from home in this pandemic.

I am thankful to my research advisory committee (RAC) members, Dr. Angshuman Nag and Dr. Guruswamy Kumaraswamy, for their valuable suggestions, advice, heartening encouragement and insightful discussions. I would like to thank my collaborators, Dr. Subrahmanyam Sappati and Dr. Girish Singh Bisht. Dr. Sappati has been an important part of the theoretical calculations presented in this thesis. His never-ending patience and eagerness to try new studies have added to the quality of my research. I am thankful to Girish for his help with the syntheses of a few compounds, despite his research commitments. I am grateful to Mr. Roshan Dsouza and Mr. Prasad Gosavi of Anton Paar India Pvt. Ltd. for their help in carrying out the small angle X-ray spectroscopic (SAXS) measurements I would like to thank Dr. P. A. Hassan of Bhabha Atomic Research Centre and Dr. T.U. Patro of Defence Institute of Advanced Technology, Pune for letting us carry out the SAXS measurements at their respective institutes. I sincerely acknowledge the former director, Dr. K. N. Ganesh, and the present director, Dr. J. B. Udgaonkar, of the Indian Institute of Science Education and Research (IISER), Pune for providing world-class research facilities. I am thankful to the Chair Chemistry, Dr. H. N. Gopi for the financial support from the Chemistry Department to attend the 15th DAE-BRNS Biennial Trombay Symposium on Radiation & Photochemistry, 2020. I am grateful to all the faculties of IISER Pune for their ever-readiness to extend help and guidance. My PhD journey would not have been comfortable and hassle-free without the efforts of the administrative staff of IISER Pune and the Chemistry Office, especially Mr. Mayuresh, Mr. Tushar and Mr. Yathish. I would also like to thank Ms. Nisha Kurkure and Mr. Suresh Kumar for IT support. The support and the resources provided by 'PARAM Brahma Facility' under the National Supercomputing Mission, at IISER, Pune are gratefully acknowledged. I would like to thank the Infosys Travel Foundation for the financial support to attend National Workshop on Fluorescence and Raman Spectroscopy (FCS), 2018. I am deeply indebted to

IISER Pune for my PhD research fellowship.

My PhD journey would have been incomplete without my lab members, Dr. Rajkumar Koninti, Dr. Sagar Satpathi, Dr. Bibhisan Roy, Aslam Uddin, Joy Chatterjee, Abhijit Chatterjee, Goutham Sukumaran and Dr. Imtiyaz Bhatt. My lab members created a dynamic, friendly and uplifting environment both in and outside the lab. I have spent many happy moments with them in the last few years. Special thanks are due to Dr. Rajkumar and Dr. Sagar who have been the greatest hands-on teachers in the form of seniors. It would have been difficult to sustain my PhD journey without their innumerable valuable lessons, research advice, the critical assessment of my work and unceasing support. I am thankful to my friends in IISER, Girish, Sajid, Partho Da, Rajkumar Da, Prashant, Chethan, Writakshi, Om and many others who have been a huge source of comfort and happiness in this not-so-easy journey. They have stood together with me through many ups and downs. I am grateful to Sri Vidya, Tumpa, Sagar, Rahul and Asif for being the best friends that anyone could ask for. I have always found them by my side in the toughest of circumstances and I am thankful for the assurance that I can always count on them. I sincerely thank all my batchmates (Integrated MS-PhD 2014), seniors and juniors for their help and support in my PhD tenure. I also thank all my teachers, who have taught me important lessons at various steps of my life. A special thanks is due to my uncle, Dr. Satinath Banerjee, for his help, encouragement and guidance during my admission related interview in IISER.

Mere words can never express the depth of my gratitude towards my family, who have been my strongest and most faithful support in these few years. My father, Dr. Kanchan Das, has been the voice of calm reason in all my difficult moments these last few years. His encouragement to always look at the 'big picture' and not get bogged down by day-to-day problems has helped me grow into a resilient person. My mother, Mrs. Sushmita Das's, humour and strength have been a stress-reliever even in the trickiest situations and never failed to bring a smile to my face. My sister, Koninika, has always tried to make sure that I never feel lonely away from home and miss out on any of the celebrations. I would not have been able to reach this day without the unconditional love, infinite patience, deep trust and freedom that my family has always given me.

Konoya Das

## Contents

List of Abbreviations.....	i
Synopsis.....	iii
Rights and Permissions.....	vii
Publications.....	viii

### **1. Introduction: Lyotropic Liquid Crystals – Self-Assembled Nanostructured Mesophases**

1.1 Liquid Crystal.....	1.1
1.2 Categories of Liquid Crystal	
1.2.1 Thermotropic Liquid Crystal.....	1.5
1.2.1.a Nematic Mesophase.....	1.5
1.2.1.b Cholesteric Mesophase.....	1.6
1.2.1.c Smectic Mesophase.....	1.7
1.2.1.d Discotic Mesophase.....	1.7
1.2.2 Lyotropic Liquid Crystal.....	1.8
1.3 Polymorphism in Lyotropic Liquid Crystal	
1.3.1 Lamellar Mesophase.....	1.9
1.3.2 Inverse Hexagonal Mesophase.....	1.10
1.3.3 Inverse Bicontinuous Mesophases.....	1.10
1.3.4 Inverse Discrete Micellar/ Discontinuous Cubic Mesophases.....	1.11
1.4 Topological Characteristics of the Inverse LLC Phases	
1.4.1 Critical Packing Parameter and Interfacial Curvature.....	1.12
1.4.2 Energetics of the Membrane Interface.....	1.15
1.4.2.a Interfacial Curvature Elastic Energy.....	1.15
1.4.2.b Hydrophobic Packing Stress.....	1.16
1.5 Relevance of Inverse Lyotropic Liquid Crystals.....	1.16
1.6 Motivation of the Thesis.....	1.18
1.7 References.....	1.20

### **2. Experimental: Materials and Techniques**

2.1 Materials.....	2.1
--------------------	-----

2.2 Synthesis and Sample Preparation	
2.2.1 Synthesis of Fluorescent Dyes.....	2.1
2.2.2 Preparation of the LLC Phases.....	2.3
2.3 Experimental Techniques	
2.3.1 Polarised Optical Microscopy (POM).....	2.4
2.3.2 Small Angle X-ray Scattering (SAXS).....	2.6
2.3.3 Steady State Absorption.....	2.9
2.3.4 Steady State Fluorescence Emission.....	2.9
2.3.5 Fluorescence Lifetime Measurements.....	2.9
2.3.5.a Time-Correlated Single Photon Counting (TCSPC).....	2.10
2.3.5.b Femtosecond Time-Resolved Fluorescence Upconversion.....	2.12
2.3.6 Time-Resolved Fluorescence Anisotropy.....	2.13
2.4 Excited State Processes	
2.4.1 Excited State Solvent Relaxation.....	2.16
2.4.2 Excited State Intramolecular Proton Transfer (ESIPT).....	2.18
2.4.3 Excited State Proton Coupled Electron Transfer (PCET).....	2.20
2.5 References.....	2.21
<b>3. Impact of Topology on the Characteristics of Water inside Cubic Lyotropic Liquid Crystalline Systems</b>	
3.1 Introduction.....	3.1
3.2 Results and Discussion	
3.2.1 Steady State Emission Study.....	3.4
3.2.2 Hydration Dynamics of the Cubic LLC Phases.....	3.6
3.2.3 Time-Resolved Fluorescence Anisotropy Study.....	3.14
3.3 Conclusion.....	3.16
3.4 References.....	3.17
3.5 Appendix.....	3.21
3.5.1 Calculation of missing solvation components.....	3.24
3.5.2 Appendix Reference.....	3.24
<b>4. Peculiar Hydrogen Bonding Behaviour of Water Molecules inside the Aqueous Nanochannels of Lyotropic Liquid Crystals</b>	
4.1 Introduction.....	4.1



4.2 Results and Discussion	
4.2.1 Characterization of LLC Phases.....	4.4
4.2.2 Steady State Emission Study.....	4.5
4.2.3 Time-Resolved Fluorescence Study.....	4.10
4.3 Conclusion.....	4.19
4.4 References.....	4.20
4.5 Appendix.....	4.24
4.5.1 Details of Quantum Chemical Calculations.....	4.29
4.5.2 Appendix References.....	4.32
<b>5. Proton Coupled Electron Transfer in the Aqueous Nanochannels of Lyotropic Liquid Crystals: Interplay of H-Bonding and Polarity Effects</b>	
5.1 Introduction.....	5.1
5.2 Results and Discussion	
5.2.1 Characterization of LLC Phases.....	5.5
5.2.2 Steady State Emission Studies.....	5.5
5.2.3 Time-Resolved Fluorescence Study.....	5.9
5.3 Conclusion.....	5.16
5.4 References.....	5.17
5.5 Appendix.....	5.20
5.5.1 Details of Computational Studies.....	5.27
5.5.2 Appendix References.....	5.32
<b>6. Future Prospects.....</b>	<b>6.1</b>

## List of Abbreviations

3HF	3-Hydroxyflavone
ADC	Analog-to-Digital Converter
CPP	Critical Packing Parameter
cP	Centipoise
CFD	Constant Fraction Discriminator
C-480	Coumarin 480
C-343	Coumarin 343
DFT	Density Functional Theory
DMA3HF	4'-N,N-dimethylamino-3-hydroxyflavone
DMA3MeF	4'-N,N-dimethylamino-3-methoxyflavone
ESIPT	Excited State Intramolecular Proton Transfer
ESICT	Excited Intramolecular Charge Transfer
EDDM	Electron Density Difference Maps
FWHM	Full width at Half Maximum
FIS	Fisetin
fs	Femtosecond
GML	Monolinolein
GMO	Monoolein
HOMO	Highest Occupied Molecular Orbital
IEFPCM	Integral Equation Formalism of Polarizable Continuum Model
IRC	Intrinsic Reaction Coordinate
LLC	Lyotropic Liquid Crystal
LC	Liquid Crystal
LUMO	Lowest Occupied Molecular Orbital
MD	Molecular Dynamics
$\mu\text{M}$	Micromolar
ns	Nanosecond

POM	Polarised Optical Microscopy
ps	Picosecond
PCET	Proton Coupled Electron Transfer
PTC	Proton Transfer Coordinate
PES	Potential Energy Surface
PMT	Photomultiplier Tube
REES	Red Edge Excitation Shift
RDF	Radial Distribution Function
SAXS	Small Angle X-ray Scattering
TCSPC	Time-Correlated Single Photon Counting
TAC	Time-to-Amplitude Converter
TDSS	Time Dependent Stokes Shift
TD-DFT	Time Dependent Density Functional Theory
TRES	Time-Resolved Emission Spectrum
TRANES	Time-Resolved Area Normalised Spectrum
UV-Vis	Ultraviolet-Visible

## Synopsis

Lyotropic liquid crystals (LLCs), a class of self-assembled nanostructured soft materials that comprise lipids and water, have carved out a niche for themselves as potential materials in a wide array of applications. It is popularly perceived that the diverse functionalities of the LLCs are closely related to the properties of the nanoscopic arrangements, including the precise nature of the aqueous nanochannels, the hydration behaviour and the local heterogeneity. The objective of the studies, presented in this thesis, was to characterise the fundamental molecular-level description of the aqueous LLC nanochannels as well as bridge the gap between the topological features of the mesophases and the intrinsic physical properties of the channels.

### **Chapter 1. Introduction: Lyotropic Liquid Crystals – Self-Assembled Nanostructured Mesophases**

The chapter is a brief description of liquid crystals and their two major categories, out of which one is the lyotropic mesophases. The chapter focuses on the polymorphism exhibited by the lyotropic liquid crystals and the unique topological architecture of each LLC mesophase. The distinct structural features of the LLCs endow each mesophase with a particular set of macroscopic properties, which in turn is linked with specific functionalities. The main difference in the various LLC structures arise from the geometry of the lipid-water interface, which is dictated by the shape of the lipid, the extent of hydration, the temperature, the curvature of the interface and the hydrophobic chain frustrations. The effects of various external factors on the critical packing parameters have been described. Depending on the critical packing parameter, the lipid-water interface can have a zero or a finite curvature either towards or away from the aqueous domains. The studies presented in this thesis are based on the inverse LLCs wherein water domains are enclosed within a continuous lipid matrix.

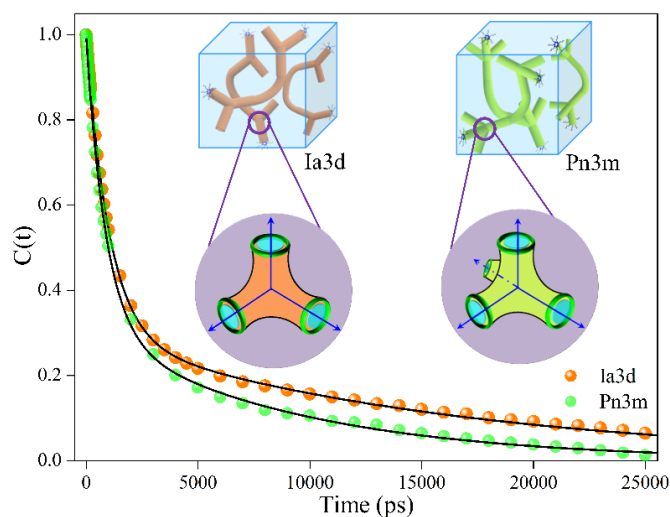
### **Chapter 2. Experimental: Materials and Techniques**

This chapter describes the preparation of the LLC phases as well as their characterisation using polarised optical microscopy and small angle X-ray scattering. The chapter also includes a brief explanation of the steady state and time-resolved fluorescence techniques that have been employed in the studies including TCPSC and femtosecond fluorescence upconversion. The various excited state phenomena, hydration dynamics, fluorescence lifetime anisotropy, excited state intramolecular proton transfer and excited state proton coupled charge transfer, that have been employed to characterise the various physical aspects of the LLC nanochannels have been described in brief.

### Chapter 3. Impact of Topology on the Characteristics of Water inside Cubic Lyotropic Liquid Crystalline Systems

Water molecules inside the lipid-based cubic liquid crystalline phases are found to dictate their various functionalities, such as protein crystallization, virus detection, delivery of drug and biomolecules, etc. This chapter focuses on the differences in the aqueous nanochannels of the two cubic mesophases in terms of their microviscosity and hydration dynamics. For this, two probes, coumarin-343 (C-343) and coumarin-480 (C-480), have been incorporated in the symmetrically different cubic phases, gyroid (Ia3d) and diamond (Pn3m). Steady state results indicate that the polarity at the lipid-water interface to be similar to that of ethanol whereas, the polarity near the more hydrophilic parts of the nanochannel resembles that of ethylene glycol. Time-resolved fluorescence anisotropy studies suggest a gradient in the microviscosity inside the LLC nanochannels. The hydration dynamics have been probed by the time-dependent Stokes shift method of the two probes. The results indicate the existence of three distinct kinds of dynamics. Ia3d exhibits a higher microviscosity and a slower hydration dynamic as compared to those in Pn3m. The reason for this disparity is associated with the differences in the topology of the two structures including the hydrophobic packing stress, the negative interfacial curvature, and the curvature elastic energy of the lipid-water interface.

*J. Phys. Chem. B* 2019, 123, 4118–4128

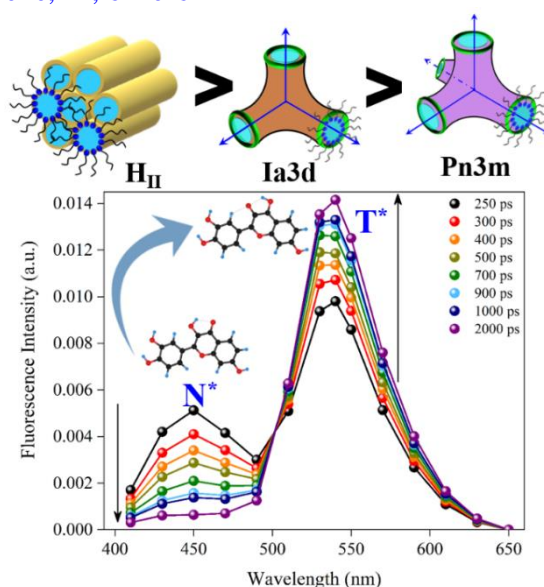


### Chapter 4. Peculiar Hydrogen Bonding Behaviour of Water Molecules inside the Aqueous Nanochannels of Lyotropic Liquid Crystals

The unique hydrogen-bonded structure of water sets it apart from other solvents and drives the properties of water to a large extent. In this context, elucidation of the hydrogen bonding properties of the water molecules inside the nanochannels is essential for obtaining a complete

picture of the LLC materials. Two excited state intramolecular proton transfer (ESIPT) exhibiting molecules, fisetin and 3-hydroxyflavone, were used to determine the hydrogen bond donating and accepting parameters of the LLC water molecules. The steady state results imply a heterogeneity in the hydrogen bonding properties inside the LLC nanochannels. Upon photoexcitation of the normal form of the ESIPT molecules, despite a reported general alcohol like polarity of the LLC nanochannels, the hydrogen bonding behaviour of the LLC water molecules is similar to that of moderately polar aprotic solvents such as acetonitrile. In contrast, on excitation of the anionic species, the spectral pattern in LLCs is similar to that in bulk alcohols. Additionally, the effect of the LLC water molecules on the rate of the intramolecular hydrogen transfer process has been explored. The ESIPT rates of both the probes, which are ultrafast ( $< 20$  ps) in bulk solvents, get slowed down dramatically by almost 15 times inside the LLC phases. This signals towards the unique behaviour of the water molecules inside the LLC nanochannels. The structural topology of the LLC phases influences the ESIPT rate with the timescale of the process increasing from the cubic to the hexagonal phase.

[Phys. Chem. Chem. Phys., 2020, 22, 6210-6221](#)

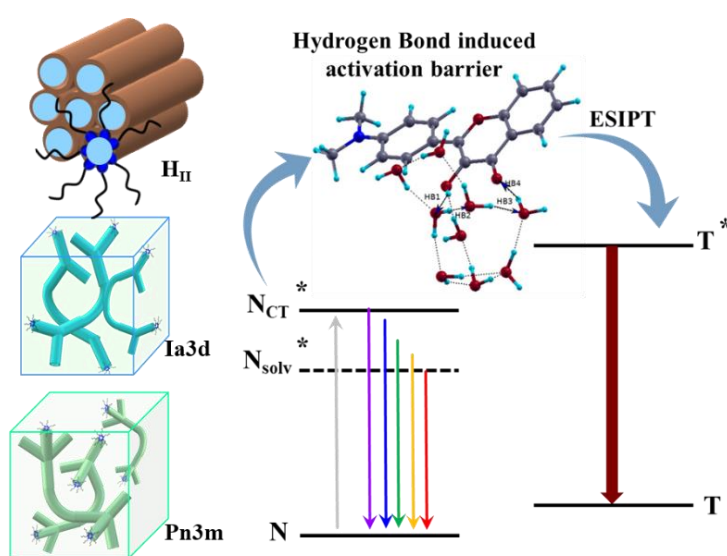


## Chapter 5. Proton Coupled Electron Transfer in the Aqueous Nanochannels of Lyotropic Liquid Crystals: Interplay of H-Bonding and Polarity Effects

The previous chapters were focussed on characterising a particular aspect of the LLC channels. In this chapter, the effects of polarity and hydrogen bonding parameters of the LLC water molecules have been simultaneously characterized and distinguished using a single fluorescent probe, 4'-N,N-Dimethylamino-3-hydroxyflavone (DMA3HF). The combination of excited state intramolecular charge and proton transfer phenomena in the molecule renders it sensitive

to polarity, hydration dynamics as well as hydrogen bonding capabilities of the surrounding medium. The multi-parametric sensitivity of DMA3HF eliminates the disadvantage of location-dependent sensing. The steady state spectral features of the DMA3HF-loaded LLC phases imply that the molecule experiences an acetonitrile-like polarity, however the efficiency and the dynamics of the proton transfer process deviates substantially from bulk acetonitrile. The observations indicate that rather than the polarity effect, the hydrogen bonding effects of the LLC water molecules play the leading role in determining the proton transfer efficiency. The formation of strong hydrogen-bonded solute-solvent complexes in the LLCs, due to the high hydrogen bond accepting ability of the interfacial water molecules, leads to a high activation barrier for ESIPT and slows down its dynamics by >20 times. The hydrogen bonding effects on the energetics of two distinct ESIPT pathways have been modelled theoretically and the results indicate that the proton transfer via an extended hydrogen-bonded water wire leads to a significantly high ESIPT activation barrier.

[J. Phys. Chem. Lett. 2021, 12, 2651–2659](#)



## Chapter 6. Future Prospects

The implications of the observations from the various studies have been discussed as well as the future scope of studies in LLC materials.

## Rights and Permissions

### Chapter 1:

Figure 1.1 – (a) Reproduced with permission from *Int. J. Polym. Sci.*, 2012, **2012**, 767581; and (b) Reproduced with permission from B. A. Averill, *Principles of General Chemistry*, 2012.

Figure 1.2 – (a) Reproduced with permission from *Nature*, 1988, **331**, 457. Copyright: Springer Nature; (b) Reproduced with permission from *Science*, 2009, **325**, 449. Copyright: The American Association for the Advancement of Science; and (c) Reproduced with permission from *Proc. Natl. Acad. Sci.*, 2012, **109**, 15712.

Figure 1.6 - Reproduced with permission from *J. Chem. Phys.*, 2018, **148**, 054902. Copyright: AIP Publishing.

Figure 1.8 - Reproduced with permission from *Chem. Soc. Rev.*, 2012, **41**, 1297. Copyright: Royal Society of Chemistry.

### Chapter 2:

Figure 2.1 – (a) Reproduced with permission from *Biomaterials*, 2000, **21**, 223. Copyright: Elsevier; (b) Reproduced with permission from *Langmuir*, 2005, **21**, 3322. Copyright: American Chemical Society.

### Chapter 3:

Reprinted (adapted) with permission from *J. Phys. Chem. B*, 2019, **123**, 4118. Copyright: American Chemical Society.

### Chapter 4:

Reprinted (adapted) with permission from *Phys. Chem. Chem. Phys.*, 2020, **22**, 6210. Copyright: Royal Society of Chemistry.

### Chapter 5:

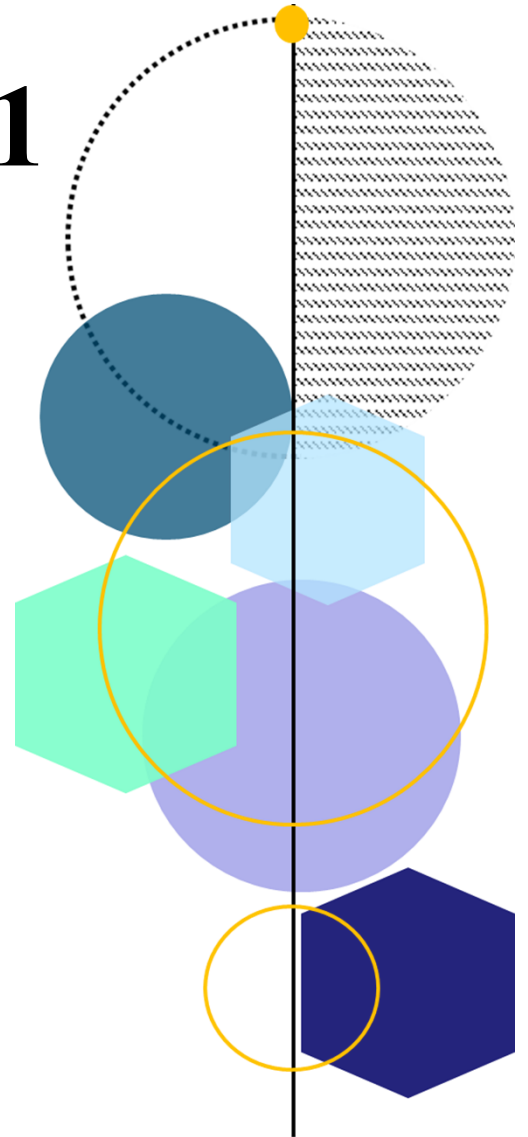
Reprinted (adapted) with permission from *J. Phys. Chem. Lett.*, 2021, **12**, 2651. Copyright: American Chemical Society.



## Publications

1. **Konoya Das**, Bibhisan Roy, Sagar Satpathi, Partha Hazra, Impact of Topology on the Characteristics of Water inside Cubic Lyotropic Liquid Crystalline Systems. *J. Phys. Chem. B*, 123, 4118–4128, 2019
2. **Konoya Das**, Subrahmanyam Sappati, Partha Hazra, Peculiar Hydrogen Bonding Behaviour of Water Molecules inside the Aqueous Nanochannels of Lyotropic Liquid Crystals. *Phys. Chem. Chem. Phys.*, 22, 6210-6221, 2020.
3. **Konoya Das**, Subrahmanyam Sappati, Girish Singh Bisht, Partha Hazra, Proton Coupled Electron Transfer in the Aqueous Nanochannels of Lyotropic Liquid Crystals: Interplay of H-Bonding and Polarity Effects. *J. Phys. Chem. Lett.*, 12, 2651–2659, 2021.
4. **Konoya Das**, Sagar Satpathi, Partha Hazra, Effect of Bile Salt Aggregates on the Prototropic Equilibria of Harmine, a Fluorescent  $\beta$ -Carboline Alkaloid. *ChemistrySelect*, 3, 1697-1707, 2018.
5. Sagar Satpathi, Subrahmanyam Sappati, **Konoya Das**, Partha Hazra, Structural Characteristics Requisite for the Ligand-based Selective Detection of i-motif DNA, *Org. Biomol. Chem.*, 17, 5392-5399, 2019.
6. Sagar Satpathi, **Konoya Das**, Partha Hazra, Silica Nano-channel Induced i-motif Formation and Stabilization at Neutral and Alkaline pH. *Chem. Commun.*, 54, 7054-7057, 2018.

# Chapter 1



**Introduction: Lyotropic  
Liquid Crystals – Self-  
Assembled Nanostructured  
Mesophases**

## 1.1 Liquid Crystal

In 1888, Austrian chemist and botanist Friedrich Reinitzer discovered a new state of matter while studying the chemical function of cholesterol in plants.<sup>1-3</sup> He observed that cholesteryl benzoate, a derivative of cholesterol, seemingly exhibited two distinct melting points<sup>1</sup> - one at 145.5 °C, where the crystalline cholesteryl benzoate melted into a cloudy liquid and another at 178.5 °C wherein the cloudy liquid changed sharply to a clear liquid (Figure 1.1).<sup>1,4</sup> Reinitzer noted that the reverse order of phases was detected on cooling the clear liquid. He found that on cooling, violet and blue colours appear, but quickly disappear leaving the sample turbid but fluid.<sup>2,5</sup> On further cooling, the colours reappear and ultimately give rise to a white crystalline mass. This observation was in stark contrast to the then knowledge of traditional crystalline materials, where a crystal was believed to lose both colour and solidity at a single unique temperature.<sup>6</sup> Reinitzer conveyed his results to the German scientist Otto Lehmann, who at that time was known for his work on the microscopic crystal analysis and the phenomenon of phase transitions.<sup>1,7</sup> Otto Lehmann was the first to suggest the term “Flüssige Krystalle”, that is, ‘Liquid Crystal’ to describe this new state of matter, which was liquid in terms of mobility and crystalline in its optical properties.<sup>4</sup> Interestingly, many reports were published prior to 1888 on anisotropic compounds such as myelin and magnesium stearate, which were later realised to be liquid crystals.<sup>8,9</sup> The liquid crystalline phase is an intermediate between the isotropic liquid phase and the crystalline solid phase and is thus defined as a mesophase (from the ancient Greek word “mesos” meaning “intermediate”).<sup>10</sup> Liquid crystals (LC) are also popularly coined as the ‘fourth state of matter’.<sup>11</sup> In a recent review, Tschierske has provided a succinct definition for LC phases. He describes the LC phase as a condensed state having orientational or positional long-range order in at least one direction with no fixed position for the individual molecules.<sup>12</sup> In LC materials, the standard highly ordered nature of crystalline solids are partially reduced, making the materials fluidic or plastic.<sup>10</sup> Thus, LCs are ‘soft materials’ that form mobile and ordered states.<sup>13</sup> Despite the discovery of LCs in 1888, till 1900, only a few materials exhibiting LC behaviour were known. Daniel Vorländer was the first chemist to explore the behaviour of LC materials from the standpoint of chemical properties by the systematic synthesis of compounds with specific predetermined shapes.<sup>8</sup> In fact, Vorländer may be called as the ‘father of liquid crystal chemistry’. Today, more than a century after the discovery of LCs, they are now an important class of advanced materials.

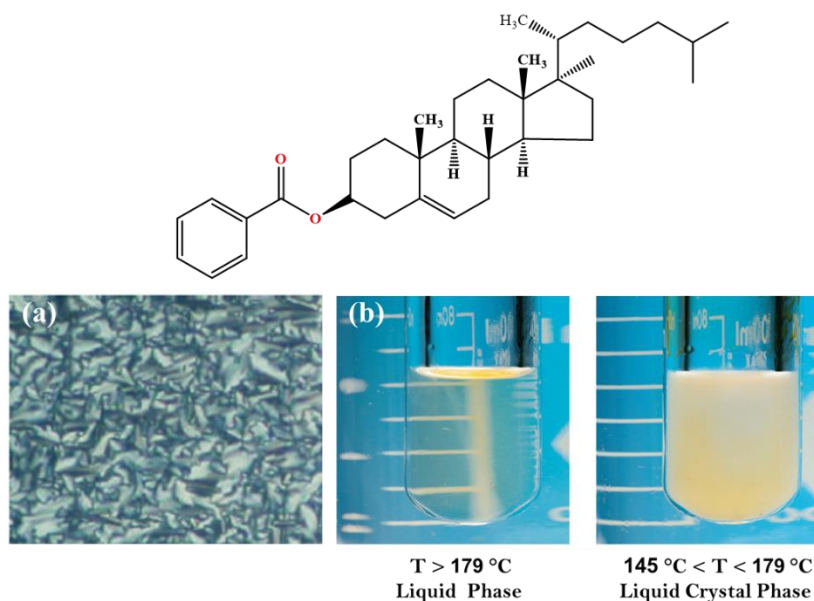


**Figure 1.1.** Chemical structure of cholesteryl benzoate and (a) polarised optical microscopy image of the cholesteryl benzoate LC (*Int. J. Polym. Sci.*, 2012, **2012**, 767581) and (b) the corresponding physical transformation of liquid phase into the turbid LC phase (B. A. Averill, *Principles of General Chemistry*, 2012).

In 1968, the first models of numerous devices based on LCs were displayed at a press conference in New York City.<sup>6, 14</sup> The devices, including a numeric indicator, a fully functional digital clock, and a television test pattern, revolutionised LC materials and paved the path for a new industry. In 1968, inventors George Heilmeier and Bernard Lechner demonstrated the world's first matrix liquid crystal display (LCD).<sup>15</sup> The inception of LCD, an indispensable part of the modern technological world, led to the creation of a whole generation of new technological devices.<sup>14</sup> Today, LCs are existent everywhere, in the display screens of various gadgets like televisions, laptops, tablets and phones. Besides this, LCs also have extensive utilisation in non-display applications, particularly in optoelectronics and photonics.<sup>16, 17</sup> LCs have an inherent tendency to reorient themselves in the presence of an external field such as electric or optical fields, as a response to the applied field.<sup>18, 19</sup> As a result of this, LCs modulate the light that passes through them. Based on this principle, LCs are widely used as optical filters and switches,<sup>19-21</sup> beam-steering devices,<sup>22</sup> spatial light modulators,<sup>23</sup> lasers<sup>24, 25</sup> and optical non-linear components<sup>26</sup>. Additionally, LCs also have attractive utilizations in energy-based applications and organic electronics like organic photovoltaics and semiconductors, owing to their properties of both 'long-range order' and 'dynamics'.<sup>27-30</sup> In fact, the efficiency of LCs in energy conversion processes can sometimes dominate over that of their crystalline counterparts.<sup>31</sup> In recent times, nanocomposites of LCs have also gained recognition as

functional materials. For instance, electrospun micro/nano-textile fibres that have been functionalised by LCs in the core are deemed to have significant potential.<sup>32</sup> Furthermore, the combination of polymers and LCs gives rise to a plethora of attractive applications owing to the rapid and efficient shape change in these materials. Thus, LC elastomers have been employed in a variety of actuators like light-driven motors<sup>33</sup> and artificial muscles<sup>34</sup>.

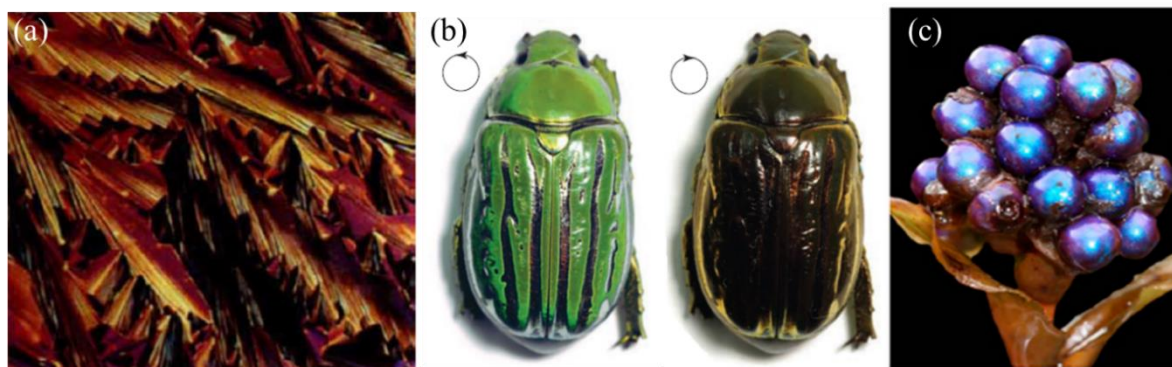


**Figure 1.2.** LCs in various biological systems. (a) Polarised optical image of smectic-like phase of DNA. (b) Bright green colour of the beetle *C. gloriosa*, which almost disappears when seen with a right circular polariser (B). (c) Bright iridescence of preserved *Pollia* fruits. Figure (a) has been reproduced with permission from reference 37 (*Nature*, 1988, **331**, 457-460). Figure (b) has been reproduced with permission from reference 57 (*Science*, 2009, **325**, 449). Figure (c) has been reproduced with permission from reference 59 (*Proc. Natl. Acad. Sci.*, 2012, **109**, 15712).

Besides, the myriad technological applications of LCs, the materials are abundant in both plants and animals, playing a crucial role in biology. The notion that LCs were an important part of life processes was put forth by J. D. Bernal in 1933.<sup>35</sup> Bernal proposed that the anisotropic nature of LCs in terms of their internal structure and directional properties have far-reaching implications rendering them important for biological processes. Since then, a multitude of studies have attempted to establish the role of LCs in living organisms. It has been found that LCs exist in various nooks and crannies of nature. Living systems are generally dynamic in their properties; that is, the cellular and sub-cellular domains constantly change their structure in response to external triggers. LCs influence the self-assembly of biological systems and help to build structural aspects like fluidity, strength and elasticity, thus dictating the inherent nature of the biological systems to a large extent (Book citation).<sup>36</sup> In 1962, Perutz first observed that the fundamental building block of life, i.e., DNA molecules form multiple LC phases (Figure 1.2).<sup>36</sup> Subsequently, numerous groups have studied the effect and significance of LCs in DNA.<sup>37-39</sup> A few other important examples of biological LCs are chromosomes<sup>40, 41</sup> and collagen<sup>42-44</sup>. Another important instance of LCs in nature is the

membrane of living cells.<sup>45-48</sup> The cell membrane provides structure and support to internal proteins while also retaining a certain degree of fluidity to enable the free movement of molecules across it.<sup>45</sup> The physical behaviour of membranes thus closely matches with that of LCs. The major portion of cell membranes comprises phospholipids in an aqueous medium and exhibits an LC phase. Saw and co-workers have recently observed that epithelial cells also behave like active LCs.<sup>49</sup> They report that this LC-like behaviour governs cell death and the mechanism for cell extrusion. Additionally, Saw and co-workers have also observed LC behaviour in biological tissues.<sup>50</sup> They have probed the importance of LC properties in tissue behaviour such as epithelial expansion, tissue homeostasis, the atherosclerosis disease state and tissue engineering. In short, LCs are an integral part of biological systems both in vitro (e.g., cellulose, peptides, and protein assemblies) and in vivo (e.g., cellular lipid membrane, packed DNA in bacteria, and aligned fibroblasts).<sup>51</sup> Interestingly, a recent report suggests that the importance of LCs in the biological world may be far greater, that is LCs may have been responsible for the origin of life itself.<sup>52</sup> Scientists widely believe that early life and the emergence of DNA as the building block of life may have occurred through an “RNA World”, wherein RNA plays the dual role of carrying and sustaining primordial metabolism.<sup>52-54</sup> In this context, Todisco *et al.* have reported a range of conditions where RNA oligomers self-assemble into concentrated, ordered, fluid LC domains.<sup>52</sup> They also observed that nucleic acids that are based on LC boosts the formation of longer RNA strands from short precursors. Their study indicates that if the origin of life is based on an “RNA World”, it could have been preceded by an “LC World”. However, the function of biological LCs does not end here. The unique optical properties of LCs also play a key role in the evolution of most species.<sup>6</sup> Most living creatures make use of bright colouration to communicate, escape from predators by camouflage and relay information about the species.<sup>55,56</sup> The bright metallic iridescence in quite a few living species results from the reflective properties of LC arrangements (Figure 1.2). For instance, the jewel scarabs of the beetle family have vivid hues from bright green to metallic silver and gold. Sharma and co-workers attribute the bright green metallic colour to the tendency of the underlying cellular structure to reflect left circularly polarized light selectively.<sup>57</sup> This feature arises due to the ordering of the cells in concentric nested arcs analogous to the ordering in chiral LCs. Similarly, the intense electric blue colour of the marble berries (*Pollicia condensata*), which is one of the most brightly coloured land-based organism to date, is not a result of selective absorption by any pigment or dye.<sup>58,59</sup> In fact, the bright colour arises due to the LC behaviour of the cellulose in the fruit. The structural colours in contrast to pigmental colours

ensures that the iridescence of the fruit remains even after it falls from the plant. The LC behaviour of cellulose also imparts vibrant blue-green colour to the tropical rainforest plant, *Mapania caudata*.<sup>60</sup>

The vitality of LCs in day-to-day life, both from a biological aspect and from the viewpoint of their numerous applications in different fields, has led to LCs as one of the most important and well-explored branches of research. Countless scientists all over the world are investing extensive efforts to unravel the mysteries of this ‘fourth state of matter’.

## 1.2 Categories of Liquid Crystal

LCs can be broadly differentiated into majorly two classes - thermotropic LCs and lyotropic LCs. Each class is further sub-categorised based on the LC structures. The various types of LCs have been described in this section.

### 1.2.1 Thermotropic Liquid Crystal

Thermotropic LC phases are usually composed of single compound systems wherein the LC phases are formed as a function of temperature, either by heating a solid or by cooling an isotropic liquid.<sup>61</sup> The long-range orientational order in thermotropic LCs arise from the different interactions in partially rigid anisotropic molecules.<sup>62</sup> At the melting point ( $T_m$ ), the motion of the molecules increases due to thermal fluctuations and the material transitions from the solid phase to the LC phase.<sup>10, 63</sup> Further heating beyond the melting point can lead to the formation of polymorphic LC structures or the isotropic liquid phase. Depending on the shape and structure of the molecular system, different types of thermotropic mesophases are possible. The French crystallographer, Georges Friedel reported the first classification and nomenclature of the different LC mesophases.<sup>64</sup> Typically, Thermotropic LCs are classified as nematic, cholesteric, smectic and discotic mesophases (Figure 1.3). Thermotropic LCs are most famous for their application in the display screens of the various device.

#### 1.2.1.a Nematic Mesophase

The nematic mesophase is the least ordered thermotropic LC, possessing only long-range orientational order.<sup>65</sup> The nematic phases are formed by rod-shaped, elongated molecules with a high aspect ratio. The long axis of the molecules are approximately parallel, that is, the molecules align themselves along a common direction, which is defined by a directing vector. However, the molecules are free to rotate in all the directions along the long axis and thus the nematic phase lack positional order. The complete absence of positional order implies that the centres of mass of the molecules have a translational symmetry similar to isotropic liquids.<sup>66</sup>

Some examples of nematic mesogens are p-quinquephenyl, 4,4'-diheptylazobenzene, p-p'-butylbenzylidenaminocinnamitrile, 4,4' -diheptylazobenzene etc.<sup>67</sup>

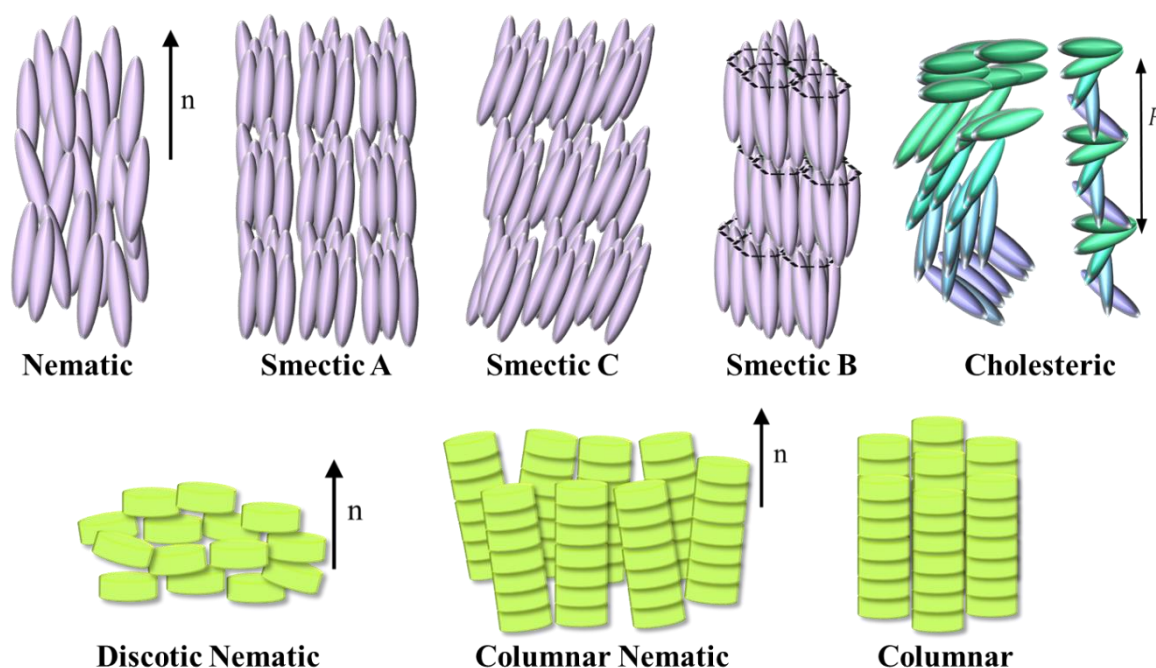


**Figure 1.3.** Schematic representation of the various thermotropic LC mesophases.

### 1.2.1.b Cholesteric Mesophase

The cholesteric mesophase is an extension of the nematic phase. It is essentially a chiral nematic phase, thus the mesophase is formed exclusively by optically active rod-like molecules. In this phase, the long axis direction of the molecules in each layer forms a certain angle with the direction of the molecular axis of the previous layer.<sup>10, 63</sup> This continuous rotation of the director vector ( $n$ ) leads to the formation of a helical superstructure.<sup>10</sup> The local ordering of the cholesteric phase is similar to that of the nematic phase. Many cholesterol derivatives belong to this class of thermotropic LCs, which explains the historical nomenclature of the mesophase as cholesteric rather than chiral nematic.<sup>67</sup> The structure of cholesteric LCs is primarily described by two structural parameters: the helical pitch and the twist sense.<sup>6, 64, 68</sup> The pitch is defined as the distance along the helix, corresponding to a rotation of  $360^\circ$ . The helicoid structure of cholesteric LCs induces unique optical properties resulting from the selective reflections of each twisted layer. Light is reflected when the wavelength matches with the helical pitch of the structure.<sup>69, 70</sup> If the pitch is tight, the reflections mainly occur in the ultraviolet-blue region. However, when the helical pitch is loose, longer wavelengths such as red or orange are favourably reflected. Cholesteric LCs make up a huge portion of the



biological LCs, especially in systems with colourful iridescence like scarab beetles and pollia berries.<sup>6</sup> Owing to their optical properties, cholesteric LCs have vast applications as coloured filters, reflectors and polarizers.<sup>69</sup>

### 1.2.1.c Smectic Mesophase

The smectic or lamellar mesophases comprise multiple layers of stacked molecules, and the mesophase possesses a certain degree of positional order.<sup>71,72</sup> Each layer of the smectic phase can be considered as a two-dimensional nematic phase. The root of the word “smectic” is the Greek word for soap and the nomenclature is justified as the thick, slippery substance found at the bottom of soaps is generally an LC.<sup>73</sup> The smectic phases can be further classified into different mesophases depending on the ordering of the phases.<sup>73,74</sup> The least ordered smectic mesophase is smectic A, which can be picturised as stacked layers of the nematic phase. The director vector of each layer is parallel to the direction of the stacking. Tilting the director vector away from the normal of the layer towards a certain direction represents the smectic C mesophase. The smectic B mesophase consists of positional order within each layer wherein the layers are stacked similar to the smectic A phase, but the molecules in each layer have an additional short-range hexagonal ordering. The molecules are free to rotate in the smectic B phase, enabling the layers to slide over each other.<sup>10</sup> Some representative examples of molecules that form the smectic mesophases are, p-n-octyloxybenzoic acid, ethyl p-azoxybenzoate, ethyl-p-ethoxybenzal-p'-aminocinnamate.<sup>73</sup>

### 1.2.1.d Discotic Mesophase

Discotic mesophases, as can be imagined from the nomenclature, are made up of disc-shaped molecules. Despite previous theoretical predictions, the first clear experimental evidence of LC behaviour by disc-like molecules was given by Chandrashekar *et al.*,<sup>75</sup> opening up new avenues of LC research. Discotic mesogens typically consist of a flat and rigid aromatic core, flanked by flexible side chains.<sup>10,27,76</sup> Derivatives of the triphenylene moiety are the most common discotic mesogens.<sup>77</sup> The discotic mesogens can aggregate into various mesophases like discotic nematic, columnar, columnar nematic, hexagonal columnar *etc.* due to the  $\pi$ - $\pi$  stacking of the aromatic cores.<sup>76,78,79</sup> An attractive attribute of the discotic mesophases are their unique structural and electronic properties, which renders them useful in the fabrication of electronic devices like organic semiconductors.<sup>27</sup> The discotic LCs are also reported to be ideal candidates for molecular wires in various optical and electronic devices such as photocopiers, laser printers, photovoltaic cells, light-emitting diodes, field-effect transistors, and holographic data storage.<sup>28</sup>

## 1.2.2 Lyotropic Liquid Crystal

Lyotropic LCs (LLCs), also known as *lyotropics* or *lyomesophases*, have been known almost from the very beginning of the discovery of LCs. LLCs are two-component mesophases, consisting of an amphiphile and a polar solvent, usually water.<sup>80-84</sup> The formation of LLCs is driven by the self-assembly of the amphiphiles in the solvent as a result of the hydrophobic effect.<sup>85, 86</sup> The hydrophilic headgroups of the amphiphiles have favourable interactions with the polar solvent, which hydrates the headgroup moieties via hydrogen bonding. In contrast, the hydrophobic aliphatic chains of the amphiphiles tend to cluster together to minimise the interactions with the polar solvent. These interactions lead to the formation of self-assembled structures. The most common and trivial example of an LLC is the formation of micellar structures of soap in water. The nature of the LLC structures is dictated to a large extent by the shape of the amphiphiles and can be broadly categorised into Type 0, Type I and Type II mesophases (Figure 1.4).<sup>87, 88</sup> Amphiphiles that have a relatively small polar headgroup as compared to the size of the aliphatic chain, which is wedge-shaped amphiphiles, tend to curve towards the solvent domain. This self-assembly, termed Type II or inverse LLC mesophase, is a ‘water-in-oil’ kind of a system wherein the solvated polar headgroups are arranged in a continuous non-polar matrix of the aliphatic chains of the amphiphiles. On the other hand, amphiphiles that are cone-shaped or in other words, have a larger headgroup compared to the amphiphilic tail give rise to self-assembled structures with a curvature away from the solvent domains. This system, known as the Type I or normal mesophase, is an ‘oil-in-water’ version with oil domains suspended in a continuous polar matrix. Amphiphiles, in which the relative cross-sections of the hydrophilic headgroup and the straight hydrophobic chain are similar, that is the molecules are roughly shaped like a cylinder, tend to have a zero curvature. These LLC structures are termed as the type 0 mesophase.

LCs are ubiquitous and lyotropic LCs are the most commonly found in nature.<sup>6</sup> LLCs have been an important field of scientific research in the last few years owing to their importance in myriad applications, including food technology, medicine and healthcare, nanotechnology, biotechnology, cosmetic industry, diagnostics etc.<sup>86, 87</sup> One appealing facet of LLCs is their non-toxicity and biocompatibility, which has popularised these soft materials over their toxic counterparts. The scientific research presented in this thesis is based on the inverse LLC mesophases, with water as a solvent. It should be noted that, although water is the most common polar solvent in the inverse LLC phases, recent studies have brought forth non-

aqueous based inverse LLC mesophases with amides<sup>89</sup> or protic ionic liquids<sup>90,91</sup> as the solvent medium.

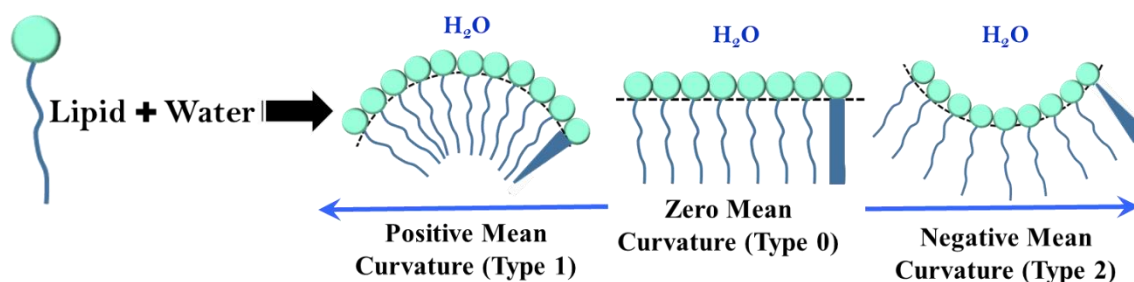


**Figure 1.4.** Self-assembly of lipids in water giving rise to different kinds of lipid-water interfacial curvature depending on the shape of the lipids.

### 1.3 Polymorphism in Lyotropic Liquid Crystal

The inverse LLC phases are typically formed by lipids such as unsaturated monoglycerides (monoolein and monolinolein),<sup>92, 93</sup> monoacylglycerols (monoelaidin),<sup>94</sup> glycolipids like  $\beta$ -Glc-OC<sub>6</sub>C<sub>10</sub><sup>95</sup> or aliphatic alcohols like phytantriol<sup>96, 97</sup>. Lipids demonstrate rich polymorphism in the aqueous medium, giving rise to several self-assembled nanostructures with either simple geometries like layers, spheres or tubes and/or complex topologies like mathematical minimal surfaces.<sup>98-100</sup> The lipids exhibit binary temperature-composition phase diagrams; in other words, different inverse LLC phases are obtained on varying the conditions of temperature and the volume fraction of water being.<sup>87, 98, 101</sup> The LLC polymorphism is a crucial aspect in industrial, technological and scientific applications.

#### 1.3.1 Lamellar Mesophase

The lamellar mesophase is one of the simplest LLC phases and is usually formed at low water contents. Structurally, the lamellar phase comprises lipid bilayers stacked one on top of another, with each bilayer separated by a layer of water molecules.<sup>81, 102, 103</sup> The hydrophilic headgroups of the lipid bilayer are oriented towards the aqueous domains while the hydrophobic lipid chains in the bilayer are stacked back-to-back, filling up the lipid layer. The lamellar mesophase does not possess any intrinsic curvature; that is, the mesophase is shaped like flat layers. The lamellar phases themselves can be of multiple kinds; for instance, the fluid lamellar phase ( $L_{\alpha}$ ) (Figure 1.5), the gel lamellar phase ( $L_{\beta}$ ) and the crystalline lamellar phase ( $L_c$ ). The fluid lamellar phase transforms into the gel phase on cooling below the Krafft point.<sup>104</sup> On the other hand, the  $L_c$  phase is completely crystalline with fixed positional order of the lipid molecules.<sup>98</sup> Thus, the disordered and fluid lamellar  $L_{\alpha}$  phase is the only true LC mesophase.

### 1.3.2 Inverse Hexagonal Mesophase

The inverse hexagonal mesophase ( $H_{II}$ ) has a cylindrical geometry with a  $P6mm$  space group symmetry. The one-dimensional  $H_{II}$  phase nanostructure comprises infinitely long lipid tubes filled with water and positioned in a hexagonal lattice (Figure 1.5).<sup>99</sup> The lipid molecules in the  $H_{II}$  phase have a negative curvature towards the aqueous domains. The  $H_{II}$  phase is characterised by fan-shaped textures in polarised optical microscopy, reflecting the presence of focal conic domains of the columns. At high temperatures, the  $H_{II}$  mesophase transforms into the fluid isotropic inverse micellar phase ( $L_2$ ).

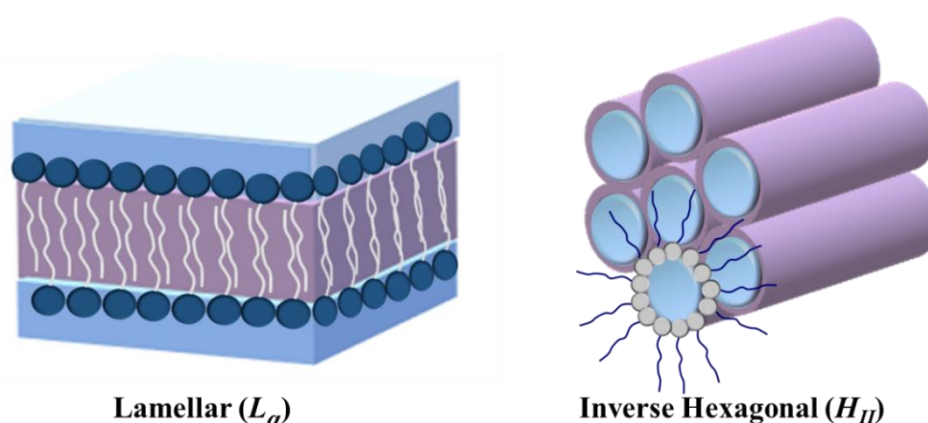


**Figure 1.5.** Schematic representation of the lamellar and the reverse hexagonal ( $H_{II}$ ) LLC phases.

### 1.3.3 Inverse Bicontinuous Cubic Mesophases

Unlike  $H_{II}$  and  $L_\alpha$  phases that have relatively simple structural features, the bicontinuous cubic phases are based on triply periodic infinite mathematical minimal surfaces.<sup>105</sup> Mathematically, the infinite triply periodic minimal surface (IPMS) is defined as a surface with zero mean curvature at every point on the surface.<sup>105, 106</sup> The most well-known and basic examples of the IPMS surfaces include the Schoen gyroid surface, the Schwarz diamond surface, and the Schwarz primitive surface.<sup>107, 108</sup> In the bicontinuous cubic phases, a single continuous lipid bilayer is draped on an IPMS surface, which separates two intertwined but non-intersecting water domains.<sup>109, 110</sup> The inverse cubic phases are distinguished by their space groups as  $Ia3d$ ,  $Pn3m$  and  $Im3m$  (Figure 1.6). In the  $Ia3d$  or gyroid mesophase, the two interpenetrating water networks have a tri-fold connectivity ( $120^\circ$ ). The two networks have opposite chirality and are related to each other by an inverse operation.<sup>98, 109</sup> Notably, the  $Ia3d$  structure is achiral overall. On the other hand, in the  $Pn3m$  or diamond mesophase, the two water channels meet at a tetrahedral angle ( $109.5^\circ$ ) in tetra-fold connectivity. The  $Im3m$  or the

primitive LLC phase is characterised by a six-fold connectivity of the water channels at a 90° angle. The  $Ia3d$  phase lacks the two-fold axis and the mirror plane symmetries, which are both present in the  $Pn3m$  and  $Im3m$  topologies.<sup>87</sup> The three bicontinuous cubic phases are mathematically linked by the Bonnet equation and can be inter-transformed by stretching deformations.<sup>111, 112</sup> The bicontinuous cubic phases do not exhibit any optical texture in polarised optical microscopy owing to their highly symmetrical cubic topology. However, all three mesophases give rise to unique scattering peaks in small angle X-ray scattering measurements. In most cases, the cubic phases transition from  $Ia3d$  to  $Pn3m$  and then to  $Im3m$  with increasing hydration.

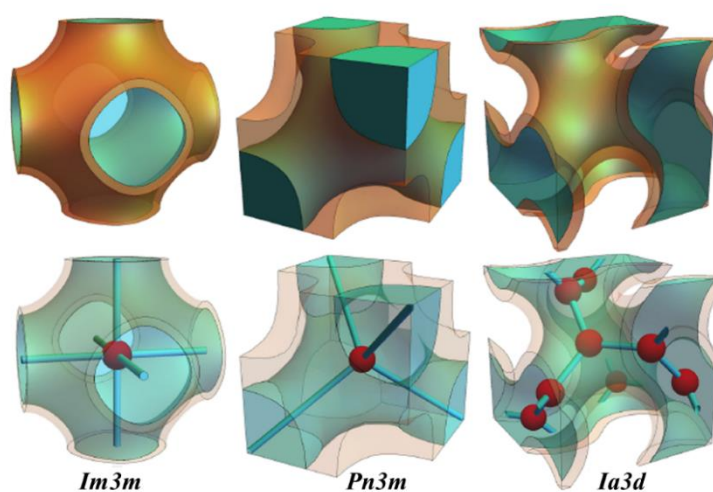


**Figure 1.6.** Representation of the bicontinuous cubic LLC mesophases and the corresponding lattices. The figure as been reproduced with permission from reference 164 (*J. Chem. Phys.*, 2018, **148**, 054902).

### 1.3.4 Inverse Discrete Micellar/ Discontinuous Cubic Mesophases

Some specific cubic phases are generally not observed in simple lipid-water binary systems, but they form in the presence of an additive like tetradecane. These nanostructures consist of discrete micelles arranged in a regular periodic cubic lattice. Like the bicontinuous cubic phases, the discontinuous cubic phases are differentiated by their space group, for instance, the  $Fd3m$ ,  $Pm3n$  and  $P4_332$ . Among these, the  $Fd3m$  phase is the most commonly studied structure. The  $Fd3m$  phase comprises two distinctly shaped and sized micellar structures in a double diamond cubic lattice.<sup>113</sup> The micellar structures are not the regular spherically shaped ones, but have dodecahedron and hexakaidecahedron shapes.<sup>87</sup> The unit cell of  $Fd3m$  comprises 16 small inverse micelles and 8 larger inverse micelles per lattice.<sup>114</sup> Importantly, the  $Fd3m$  mesophase has also been observed for some binary lipid-water systems

like diphytanylglucosylglycerol/water and dialkylxylopyranosylglycerol/water systems.<sup>114, 115</sup> Although the discrete micellar cubic phases are not as wide-spread and popular as the inverse bicontinuous cubic phases, they are an important and crucial part of the inverse LLCs.

## 1.4 Topological Characteristics of the Inverse LLC Phases

The overall topology of the LLC phases is governed by several parameters, of which the shape of the lipid molecule is of paramount importance. The shape of the molecule influences the packing of the lipid molecules in the nanostructure. The critical packing parameter in turn dictates the curvature of the lipid-water interface in the mesophases and hence the curvature elastic energy.<sup>88</sup>

### 1.4.1 Critical Packing Parameter and Interfacial Curvature

The rich structural polymorphism exhibited by a single lipid-water system, on simply varying the temperature and hydration content conditions, arises from the concept of critical packing parameter (CPP). Israelachvili and co-workers proposed the concept of CPP in the self-assembly of amphiphiles. The CPP is defined as follows.

$$CPP = \frac{v}{a_0 l_c} \quad (1.1)$$

Here,  $v$  is the volume of the hydrophobic core of the lipids,  $a_0$  is the effective area of the hydrophilic head group and  $l_c$  is the length of the aliphatic chain in the molten state. The self-assembly of amphiphiles in water is determined by the delicate balance between the attractive and repulsive forces of the solute-solute molecules and the solute-solvent molecules.<sup>88</sup> These interactions are, in turn, significantly dependent on the molecular shape of the amphiphiles. Thus, the critical packing parameter connects the shape of the amphiphile with the preferred geometry. Consequently, the CPP values of amphiphiles can predict whether the molecules tend to curve towards (inverse mesophases) or away from the aqueous domain (normal mesophases). The normal phases are formed by cone-shaped amphiphiles with a relatively larger cross-section of the hydrophilic headgroup as compared to the aliphatic chain. In such molecules, the lateral stress between the hydrophilic headgroups is high, and thus the molecules tend to curve towards the hydrophobic chains to relieve this repulsive frustration. The normal phases are characterised by a  $CPP < 1$  value. On the other hand, in the inverse phases that are formed by wedge-shaped amphiphiles, the cross-section of the hydrophilic headgroup is relatively lesser than that of the hydrophobic tail. As a result, the lateral stress between the hydrophobic tails is higher, and the molecules tend to curve away from the hydrophobic chains.

The inverse phases have an intrinsic  $CPP > 1$  value. Notably, the lateral stress can be a combination of electrostatic repulsive interactions, hydrogen bonding interactions and steric interactions.<sup>88</sup> Amphiphiles, which are cylindrical have similar cross-sections of the hydrophilic headgroup and the aliphatic chain, giving rise to a  $CPP=1$  value. In such cases, the amphiphiles have a zero curvature and self-assemble as flat lamellar mesophases.

Despite the importance of the molecular shape in influencing the LC self-assembly, it is not the only driving factor. The topology of the lipid-water interface determined by the  $CPP$  is driven by the extent of hydration, the temperature, the steric interactions and ionic strength.<sup>87</sup> <sup>88</sup> For example, the effective or net size of the hydrophilic headgroup is dictated by both the extent of hydration and the temperature. At higher water contents, the effective cross-section of the hydrophilic headgroup increases due to increased hydration, causing a decrease in the packing parameter. On the other hand, on increasing the temperature the effective size of the headgroup decreases due to dehydration. Thus, keeping the extent of water constant, but increasing the temperature leads to nanostructures with a higher packing parameter. For monoglyceride-based LLCs, it has been reported that the  $H_{II}$  has a  $CPP \sim 1.7$ . In contrast, the bicontinuous cubic phases have a  $CPP \sim 1.3$ .<sup>46</sup> It is important to note here that in a given set of conditions, the self-assembled LLC nanostructure tends to adopt a geometry that is the least frustrated.

Within each category of the LLC phases, either type I or type II, the order-order phase transition between the mesophases depends on the curvature geometry of the lipid-water interface. The intrinsic negative lipid-water interfacial curvature of each mesophase is distinct, and for the case of the inverse mesophases, it follows a trend of  $L_{\alpha} < Im3m < Pn3m < Ia3d < H_{II} < L_2$ . Mathematically, the relationship between the curvature of the lipid-water interface and the packing parameter is as follows.<sup>116</sup>

$$CPP = 1 + Hl_c + \frac{Kl^2}{3} \quad (1.2)$$

$$\langle K \rangle = \frac{3}{2l^2} (1 - CPP) \quad (1.3)$$

Here,  $H$  and  $K$  are the mean interfacial curvature and the Gaussian curvature, respectively. The local shape of any surface can be defined by two principal curvatures ( $c_1$  and  $c_2$ ) (Figure 1.7).<sup>117</sup>

<sup>118</sup> One of the curvatures represents the rate of maximum bending of the surface and the corresponding tangent direction and the other characterises the rate and extent of the minimum bending of the surface and the associated tangent direction. By definition, the gaussian

curvature is the product of the two principal curvatures while the mean curvature is the average of the two principal curvatures.

$$K = c_1 c_2 \quad (1.4)$$

$$H = \frac{c_1 + c_2}{2} \quad (1.5)$$

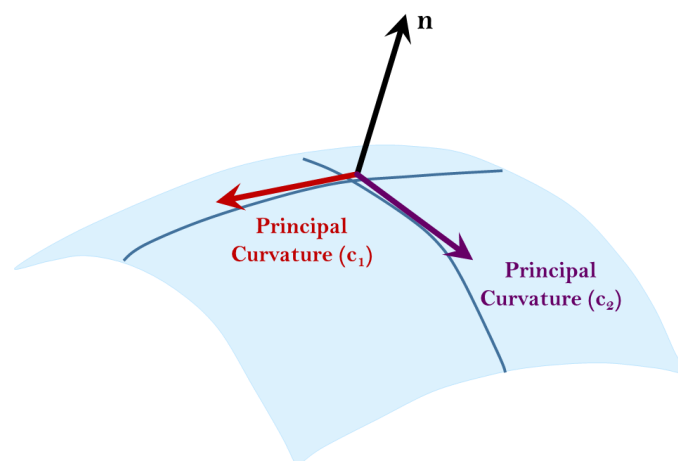


**Figure 1.7.** Schematic representation of the two principal curvatures for a mathematical surface.

To illustrate, a flat interface has both zero mean and Gaussian curvatures. On the other hand, a hyperboloid has a negative Gaussian curvature, a cylinder has zero Gaussian curvature and a sphere has positive Gaussian curvature. A minimal surface is one where the mean curvature is zero at all points of the surface. Minimal surfaces such as the bicontinuous cubic mesophases, have a Gaussian curvature,  $K \leq 0$ . The mean curvature in all the inverse LLC phases is negative, apart from the lamellar phase where  $H=0$ , corresponding to the curvature of the lipid interface towards the aqueous domains. The progressive decrease of CPP upon hydration causes changes in the Gaussian curvature, which leads to the order–order transitions sequence.<sup>119, 120</sup> For example, Mezzenga and co-workers found that the addition of a sugar ester with a highly polar sucrose headgroup increases the effective area of the lipid headgroups in the LLC phases.<sup>119</sup> This decreases the CPP value, and subsequently, the negative value of the Gaussian curvature increases (Equation 1.3). In other words, the radius of the curvature increases, implying that the spontaneous curvature of the lipid bilayer towards the aqueous domains decreases. Thus, a transformation is induced from the  $Pn3m$  to the  $Im3m$  mesophase, wherein the latter possesses a higher radius of curvature. All the lyotropic phase behaviour can be reasoned in terms of the mean and Gaussian interfacial curvatures that are dictated by the packing parameter.<sup>99</sup>



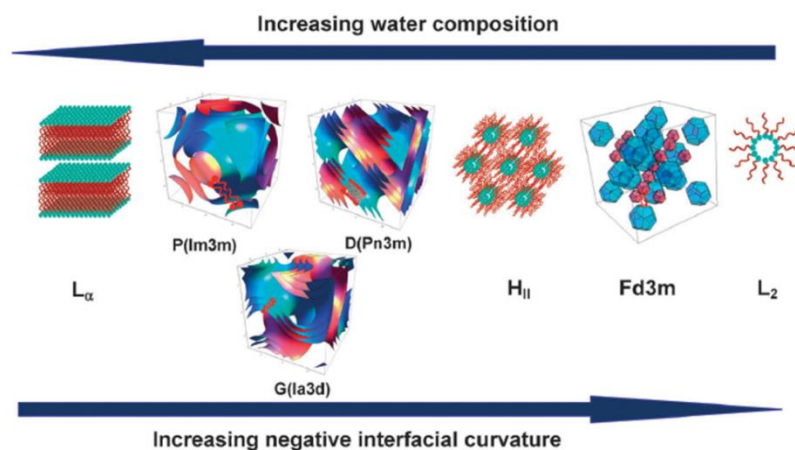


**Figure 1.8.** The relationship between the various LLC mesophases in terms of the lipid-water interfacial curvature and water composition. The figure has been reproduced with permission from reference 88 (*Chem. Soc. Rev.*, 2012, **41**, 1297-1322).

## 1.4.2 Energetics of the Membrane Interface

Gruner *et al.* proposed that the assembly of the lipid and water would be associated with three major energetics, the lipid-water interfacial curvature elasticity ( $g_c$ ), the packing of the hydrophobic chains ( $g_p$ ) and other additional interactions ( $g_{inter}$ ) including the electrostatic interactions and the hydration force.<sup>121, 122</sup> In most cases, the additional interaction forces ( $g_{inter}$ ) is considered as negligible, and thus the LLC nanostructures are mainly governed by the interfacial curvature elastic energy and the hydrophobic packing stress.<sup>88, 122</sup>

### 1.4.2.a Interfacial Curvature Elastic Energy

For mathematical simplicity, Helfrich considered the lipid bilayer as an infinitely thin elastic surface.<sup>123</sup> Deformations of this thin infinite surface with respect to the mean and Gaussian curvature, would thus require certain energy. The curvature elastic energy is defined as the energy cost associated with the deformation of the infinite thin surface from its spontaneous mean curvature at its relaxed state. The spontaneous mean curvature is determined by the distribution of lateral stresses across the actual lipid monolayer. Mathematically, the curvature elastic energy is defined as,<sup>122</sup>

$$g_c = 2\kappa(H - H_0)^2 + \kappa_G K \quad (1.6)$$

Here,  $H_0$  is the spontaneous mean curvature,  $\kappa$  is the bending modulus,  $\kappa_G$  is the Gaussian modulus,  $H$  is the mean curvature, and  $K$  is the Gaussian curvature. The curvature elastic parameters are sensitive to the effects of both temperature and pressure.<sup>124, 125</sup> The LLC mesophases will transition from the lamellar to bicontinuous cubic, to the hexagonal cylindrical and finally to the spherical geometry with an increase in the desire for interfacial curvature

(Figure 1.8).<sup>88</sup> Among the cubic phases, the  $Ia3d$  phase has a higher curvature elastic energy than the  $Pn3m$  phase.<sup>126</sup>

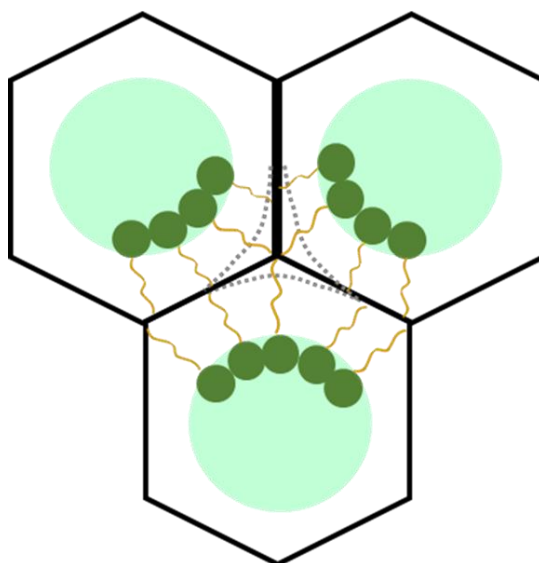


**Figure 1.9.** Schematic representation of hydrophobic packing stress in the  $H_{II}$  phase wherein the lipid chains elongate or compress to fill the voids in the framework.

#### 1.4.2.b Hydrophobic Packing Stress

In a binary lipid-water system, the lipid molecules cannot possess a uniform interfacial curvature and fill the hydrophobic core uniformly.<sup>88</sup> In other words, if the mesophases are treated as close packings of idealized inverse circular cylinders or inverse spheres, there exists void volumes in the structure. Such void volumes are energetically unfavourable. Thus, they have to be uniformly filled, either by some of the hydrocarbon chains of the lipids or by adding non-polar molecules such as alkanes into the void regions.<sup>122, 127, 128</sup> The filling up of the void volume by the lipid chains require the lipids to deviate from their preferred conformations through stretching or compression (Figure 1.9). This deformation has an energy penalty associated with it, which is termed as the hydrophobic packing frustration.<sup>129</sup> The  $H_{II}$  phase has a higher packing frustration than the bicontinuous cubic phases.<sup>122</sup> Among the cubic phases themselves, the hydrophobic packing stress follows an order of gyroid > diamond > primitive.

### 1.5 Relevance of Inverse Lyotropic Liquid Crystals

Despite being discovered more than a century ago, the immense potential of LLCs have been realised by scientists only in the last few decades. Today, LLCs have managed to gain a strong foothold in industries spanning across various fields and scientists across the world are investing extensive efforts to amplify the applications of LLCs. Firstly, LLCs are an

indispensable part of the food industry.<sup>92, 130, 131</sup> LLCs make up some of the most common foods like salad dressings, mayonnaise etc. The viscoelastic nature of LLC food materials enables them to be loaded with specific aromas and flavours while still preserving the rheological properties. Besides this, LLCs are popular candidates for the solubilisation of biologically active food additives that require protection against hydrolysis or oxidation and are insoluble in both pure aqueous and oil phase.<sup>132</sup> A unique structural advantage of LLCs is that these materials can compartmentalize amphiphilic, hydrophilic and lipophilic target molecules in specific domains.<sup>86</sup> LLCs can thus control chemical reactions and chain reactions by bringing certain molecules in close contact while isolating other ones, resulting in different reaction directions, based on whether the reactants and products are located in the water or oil domains.<sup>86</sup> Based on this hypothesis, LLCs have been employed as efficient nanoreactors and nanotemplates for the synthesis of microparticles and nanoparticles,<sup>133, 134</sup> quantum dots<sup>135</sup> and for fabricating other nanostructured materials.<sup>82, 136, 137</sup> The highly ordered internal structure of the LLCs imparts the material with superior opportunities in designing and templating of nanostructures as compared to their polymer counterparts.<sup>88</sup> In particular, the H<sub>II</sub> mesophase is deemed to be an efficient and smart nanoreactor for the fabrication of 1D, 2D and 3D nanomaterials and various energy-based applications.<sup>138, 139</sup> LLCs have also garnered considerable attention for the transport of drugs in the field of medicine and pharmacy.<sup>140-143</sup> The absolute biocompatibility and non-toxicity of LLCs and their thermodynamic stability are specifically attractive in this context. In addition, on the grounds of their varying topological features, different LLC mesophases give rise to different drug release rates. For instance, the cubic phases and H<sub>II</sub> phase are employed for a long and sustained release of drugs.<sup>144-146</sup> At the same time, a pH triggered transformation of the H<sub>II</sub> phase to the bicontinuous cubic phases gives rise to a spontaneous burst release.<sup>147, 148</sup> LLC phases have also been used for diagnostic applications. A recent study reports the use of LLCs for selective cancer imaging and therapy.<sup>149</sup> The bicontinuous cubic phases have been employed for the rapid detection of various pathogens and virus, including *Ebola* and HIV.<sup>150</sup> Another notable utilization of the bicontinuous cubic phases is for the crystallization of large membrane proteins, which do not crystallize in bulk.<sup>151-154</sup> As crystallization is the only method by which the complex three-dimensional structures of proteins and the mechanism of intercellular reactions can be discerned, this particular application of cubic phases has rendered these materials particularly important in recent years. The bicontinuous cubic phases also act as excellent hosting platforms for membrane-bound enzymes and help the enzymes to retain stability and activity for long

time durations.<sup>155</sup> Apart from these applications of the inverse LLCs, they also play important roles in biological systems. The polymorphism of LLCs is reflected in the intracellular membranes in various biological systems.<sup>47, 156</sup> The cubic phases, in particular, are important in biological systems. Larsson first put forth that the IPMS structure of cubic phases resembles closely with the lipidic membranes in nature.<sup>46</sup> The biological aspects of the cubic phases have thus been focussed upon by many researchers owing to their roles in membrane fusion, control of membrane protein functions and various intracellular structures of membranes.<sup>88, 157, 158</sup>

## 1.6 Motivation of the Thesis

The exceptional diverse functionalities of the inverse LLCs are closely related to the topological features of the mesophases and the arrangement of the nanoscopic domains.<sup>86</sup> To be specific, the precise nature of the aqueous nanochannel, interfacial hydration, hydration dynamics, water transport behaviour and other properties of the mesophases depend on the macroscopic functionalities of the LLCs.<sup>159</sup> Thus, it is crucial to bridge the gap between the macroscopic functionalities of the LLCs, which is central to the performance of the materials, and the topological characteristics of the nanostructures. In addition, the unique structural features of each mesophase are associated with a particular set of macroscopic properties, which in turn is linked with specific functionalities.<sup>86</sup> Consequently, it is essential to understand the effect of geometrical topology on the behaviour of the water molecules encased in the nanochannels. The importance of the molecular level description of the LLC mesophases and the parameters that dictate the LLC properties at the molecular level is reflected in the recent ongoing research of various groups. To cite a few examples, the dynamics of the water molecules in the nanochannels of a few mesophases have been determined by multiple techniques. Zhong et al. have probed the ultrafast dynamics of the water networks in the  $Pn3m$  mesophase using femtosecond time-resolved fluorescence techniques.<sup>160</sup> The hydration dynamics in the  $H_{II}$  aqueous nanochannels have also been elucidated by dielectric relaxation spectroscopy.<sup>161</sup> Both these studies point towards the presence of multiple discrete water layer inside the nanochannels of the LLC mesophases. Our group has also recently evidenced the distinct dynamics of the various water layers in the nanochannels of  $H_{II}$  and  $L_2$  phases by time-resolved fluorescence spectroscopic techniques.<sup>162</sup> The intrinsic dynamics of the LLC water molecules are also related to the nanochannels' diffusion properties. Mezzenga and co-workers have elucidated the relationship between the geometrical characteristics of the LLC mesophases and the diffusion-controlled transport of point-sized molecules in the aqueous

nanochannels using a combination of experimental and theoretical techniques.<sup>163-165</sup> The diffusion of the different kinds of water molecules have also been modelled for the H<sub>II</sub> mesophase by molecular dynamics simulation.<sup>166</sup> In addition, several studies have also focussed on the different molecular interactions that determine the structural aspects of the mesophases. For example, the cooperative behaviour of the lipid headgroups and the kinetic aspects of the H<sub>II</sub> interface have been probed by dielectric relaxation spectroscopy.<sup>167, 168</sup> Abou-Zied and co-workers have recently characterised the hydrophobicity and dynamics in the lipidic tail regions of the mesophases using fluorescence techniques.<sup>169</sup> They have also reported increased basicity near the lipid-water interface of the inverse bicontinuous cubic phases by employing the spectral sensitivity of tryptophan,<sup>159</sup> which was also observed in one of our previous studies.<sup>170</sup>

Although, there have been considerable efforts from the scientific community to elucidate the molecular-level picture of the mesophases, be it the hydrophobic regions or the aqueous domains of the LLCs, a complete understanding of all the facets of the heterogenous nanoscopic domains is far from being achieved. Based on the fact that in the last decade, LLCs have proved their indispensability in a wide number of fields spanning across multiple specialised domains, it becomes even more critical to understand all the aspects of the LLC nanodomains. The objective of this thesis was to gain an in-depth understanding of the fundamental physical parameters of the aqueous nanochannels of the LLC phases and to correlate the physical properties of the LLC water molecules with the structural features of the mesophases. In this regard, Chapter 3 deals with the influence of the different cubic structural features towards the physical properties of the water molecules in the nanochannels.<sup>171</sup> Despite the closeness in the structural features of the two bicontinuous cubic phases, *Ia3d* and *Pn3m*, the microviscosities and hydration dynamics of the various water layers differed considerably in the two phases. In addition, the slow components of the hydration dynamics corresponding to the trapped and ‘pseudo-bound’ water layers were probed, which had not been previously studied for any of the cubic phases. In Chapter 4, the hydrogen bond donating and accepting abilities of the LLC water molecules were determined by the phenomenon of excited state intramolecular proton transfer.<sup>172</sup> Considering that the hydrogen-bonded structure of water is the driving force behind the properties of the solvent, the explicit nature of the hydrogen bonding abilities of the LLC aqueous networks provides a fundamental knowledge of the aqueous domains. A distinct heterogeneity in the hydrogen bonding abilities was observed at the various depths of the LLC nanochannels. In addition, we also observed the effects of the

hydrogen bonding behaviour of the LLC water molecules on the dynamics of the proton transfer process. However, one disadvantage of using fluorescent probes that are specifically sensitive to one particular property of the surrounding medium, such as either polarity or hydrogen bonding parameters or hydration dynamics, is location-dependent behaviour. To overcome this, we employed a single multi-parametric environment sensitive fluorescent probe in the final chapter to simultaneously characterise and distinguish between the various physical properties of the LLC water molecules (Chapter 5).<sup>173</sup> This study helped us to evaluate the interplay between the effects of hydrogen-bonding and polarity of the aqueous nanochannels. The research findings presented in this thesis provide new physical insights into the molecular properties of the LLC aqueous domains and adds significantly to the existing knowledge about these materials.

## 1.7 References

1. H. Kelker, *Mol. Cryst. Liq. Cryst.*, 1973, **21**, 1-48.
2. F. Reinitzer, *Liq. Cryst.*, 1989, **5**, 7-18.
3. S. T. Lagerwall, *Liq. Cryst.*, 2013, **40**, 1698-1729.
4. G. H. Brown and W. G. Shaw, *Chem. Rev.*, 1957, **57**, 1049-1157.
5. H. Stegemeyer, *Liq. Cryst.*, 1989, **5**, 5-6.
6. M. Mitov, *Soft Matter*, 2017, **13**, 4176-4209.
7. H. Kelker, *Mol. Cryst. Liq. Cryst.*, 1988, **165**, 1-43.
8. D. Demus, *Mol. Cryst. Liq. Cryst. Sci. Technol., Sect. A*, 2001, **364**, 25-91.
9. V. Vill, *Mol. Cryst. Liq. Cryst. Sci. Technol., Sect. A*, 1992, **213**, 67-71.
10. K. Goossens, K. Lava, C. W. Bielawski and K. Binnemans, *Chem. Rev.*, 2016, **116**, 4643-4807.
11. F. D. Saeva, *Liquid Crystals: The Fourth State of Matter*, Marcel Dekker Inc.. New York, 1979.
12. C. Tschierske, *Angew. Chem., Int. Ed.*, 2013, **52**, 8828-8878.
13. T. Kato, N. Mizoshita and K. Kishimoto, *Angew. Chem., Int. Ed.*, 2006, **45**, 38-68.
14. J. A. Castellano, *Liquid Gold-The Story of Liquid Crystal Displays and the Creation of an Industry*, World Scientific, Singapore, 2005.
15. J. C. Jones, *Liq. Cryst. Today*, 2018, **27**, 44-70.
16. B. T. Hogan, E. Kovalska, M. F. Craciun and A. Baldycheva, *J. Mater. Chem. C*, 2017, **5**, 11185-11195.

17. J. Beeckman, K. Neyts and P. Vanbrabant, *Opt. Eng.*, 2011, **50**, 081202.
18. Y. Garbovskiy, A. V. Emelyanenko and A. Glushchenko, *Nanoscale*, 2020, **12**, 16438-16442.
19. A. D'Alessandro and R. Asquini, *Mol. Cryst. Liq. Cryst.*, 2003, **398**, 207-221.
20. C. Peralta, A. Pons and J. Campos, *J. Opt.*, 2010, **12**, 015707.
21. R. L. J. Michael Harris, JuneKoo Rhee, James A. Webb *Optical Switching : Liquid-Crystal Based Optical Switching*, Springer, Boston, MA, 2006.
22. C. J. Henderson, D. G. Leyva and T. D. Wilkinson, *J. Lightwave Technol.*, 2006, **24**, 1989-1997.
23. I. G. Manolis, T. D. Wilkinson, M. M. Redmond and W. A. Crossland, *IEEE Photonics Technol. Lett.*, 2002, **14**, 801-803.
24. L. Yu-Pin, C. Chao-Yuan, P. Ru-Pin and P. Ci-Ling, *Opt. Eng.*, 2004, **43**, 234-238.
25. K. Sato, K. Mizutani, S. Sudo, K. Tsuruoka, K. Naniwae and K. Kudo, *J. Lightwave Technol.*, 2007, **25**, 2226-2232.
26. I. C. Khoo, *Phys. Rep.*, 2009, **471**, 221-267.
27. S. Sergeev, W. Pisula and Y. H. Geerts, *Chem. Soc. Rev.*, 2007, **36**, 1902-1929.
28. S. Laschat, A. Baro, N. Steinke, F. Giesselmann, C. Hägele, G. Scalia, R. Judele, E. Kapatsina, S. Sauer, A. Schreivogel and M. Tosoni, *Angew. Chem., Int. Ed.*, 2007, **46**, 4832-4887.
29. M. O'Neill and S. M. Kelly, *Adv. Mater.*, 2011, **23**, 566-584.
30. M. O'Neill and S. M. Kelly, *Adv. Mater.*, 2003, **15**, 1135-1146.
31. J. Harden, M. Chambers, R. Verduzco, P. Luchette, J. T. Gleeson, S. Sprunt and A. Jákli, *Appl. Phys. Lett.*, 2010, **96**, 102907.
32. J. P. F. Lagerwall, J. T. McCann, E. Formo, G. Scalia and Y. Xia, *Chem. Commun.*, 2008, 5420-5422.
33. M. Yamada, M. Kondo, J.-i. Mamiya, Y. Yu, M. Kinoshita, C. J. Barrett and T. Ikeda, *Angew. Chem., Int. Ed.*, 2008, **47**, 4986-4988.
34. D. L. Thomsen, P. Keller, J. Naciri, R. Pink, H. Jeon, D. Shenoy and B. R. Ratna, *Macromolecules*, 2001, **34**, 5868-5875.
35. Bernal, Lawrence, Oseen, H. Zocher, Kast, Ornstein, Feachem, N. K. Adam, Desch, Lowry, Rawlins, Herrmann, Foëx, Malkin, Porter, Stewart, G. W. Stewart, A. M. Taylor, Ostwald, Carpenter and G. S. Hartley, *Trans. Faraday Soc.*, 1933, **29**, 1060-1085.

36. S. A. Jewell, *Liquid Crystals in Living Systems and Liquid Crystals in the Development of Life : Handbook of Liquid Crystals*, Wiley VCH Verlag GmbH & Co., 2nd edn., 2014.
37. T. E. Strzelecka, M. W. Davidson and R. L. Rill, *Nature*, 1988, **331**, 457-460.
38. J. Olesiak-Banska, H. Mojzisova, D. Chauvat, M. Zielinski, K. Matczyszyn, P. Tauc and J. Zyss, *Biopolymers*, 2011, **95**, 365-375.
39. T. P. Fraccia, G. P. Smith, G. Zanchetta, E. Paraboschi, Y. Yi, D. M. Walba, G. Dieci, N. A. Clark and T. Bellini, *Nat. Commun.*, 2015, **6**, 6424.
40. J. T. Y. Wong, *Microorganisms*, 2019, **7**.
41. M. H. Chow, K. T. H. Yan, M. J. Bennett and J. T. Y. Wong, *Eukaryotic Cell*, 2010, **9**, 1577.
42. J. C. Price, P. Roach and A. J. El Haj, *ACS Biomater. Sci. Eng.*, 2016, **2**, 625-633.
43. P. De Sa Peixoto, A. Deniset-Besseau, M.-C. Schanne-Klein and G. Mosser, *Soft Matter*, 2011, **7**, 11203-11210.
44. J. E. Kirkwood and G. G. Fuller, *Langmuir*, 2009, **25**, 3200-3206.
45. S. A. Jewell, *Liq. Cryst.*, 2011, **38**, 1699-1714.
46. K. Larsson, *J. Phys. Chem.*, 1989, **93**, 7304-7314.
47. G. Lindblom and L. Rilfors, *Biochim. Biophys. Acta, Rev. Biomembr.*, 1989, **988**, 221-256.
48. P. J. Wojtowicz, *Lytropic Liquid Crystals and Biological Membranes: The Crucial Role of Water. In: Introduction to Liquid Crystals*, Springer, Boston, MA, 1975.
49. T. B. Saw, A. Doostmohammadi, V. Nier, L. Kocgozlu, S. Thampi, Y. Toyama, P. Marcq, C. T. Lim, J. M. Yeomans and B. Ladoux, *Nature*, 2017, **544**, 212-216.
50. T. B. Saw, W. Xi, B. Ladoux and C. T. Lim, *Adv. Mater.*, 2018, **30**, 1802579.
51. J. Zhao, U. Gulan, T. Horie, N. Ohmura, J. Han, C. Yang, J. Kong, S. Wang and B. B. Xu, *Small*, 2019, **15**, 1900019.
52. M. Todisco, T. P. Fraccia, G. P. Smith, A. Corno, L. Bethge, S. Klussmann, E. M. Paraboschi, R. Asselta, D. Colombo, G. Zanchetta, N. A. Clark and T. Bellini, *ACS Nano*, 2018, **12**, 9750-9762.
53. W. Gilbert, *Nature*, 1986, **319**, 618-618.
54. G. F. Joyce, *Nature*, 2002, **418**, 214-221.
55. M. Théry and D. Gomez, in *Advances in Insect Physiology*, eds. J. Casas and S. J. Simpson, Academic Press, 2010, vol. 38, pp. 267-353.



56. R. E. Silberglied and O. R. Taylor, *Behav. Ecol. Sociobiol.*, 1978, **3**, 203-243.
57. V. Sharma, M. Crne, J. O. Park and M. Srinivasarao, *Science*, 2009, **325**, 449.
58. A. G. Dumanli, G. Kamita, J. Landman, H. van der Kooij, B. J. Glover, J. J. Baumberg, U. Steiner and S. Vignolini, *Adv. Opt. Mater.*, 2014, **2**, 646-650.
59. S. Vignolini, P. J. Rudall, A. V. Rowland, A. Reed, E. Moyroud, R. B. Faden, J. J. Baumberg, B. J. Glover and U. Steiner, *Proc. Natl. Acad. Sci.*, 2012, **109**, 15712.
60. G. Strout, S. D. Russell, D. P. Pulsifer, S. Erten, A. Lakhtakia and D. W. Lee, *Ann. Bot.*, 2013, **112**, 1141-1148.
61. J. G. D. Demus, G. W. Gray, H.-W. Spiess, V. Vill, *Handbook of liquid crystals: Fundamentals*, Wiley-VCH Verlag GmbH, 1st edn., 1998.
62. D. W. Bruce, D. A. Dunmur, E. Lalinde, P. M. Maitlis and P. Styring, *Nature*, 1986, **323**, 791-792.
63. E. I. Kovshev, L. M. Blinov and V. V. Titov, *Russ. Chem. Rev.*, 1977, **46**, 395-419.
64. P. P. Patrick Oswald, *Nematic and Cholesteric Liquid Crystals: Concepts and Physical Properties Illustrated by Experiments*, Taylor and Francis, 2005.
65. *Handbook of Liquid Crystals: Nematic and Chiral Nematic Liquid Crystals*, Wiley-VCH Weinheim, 2nd edn., 2014.
66. *Phase Transitions in Liquid Crystals* Springer US, New York 1992.
67. W. H. d. J. Ger Vertogen, *Thermotropic Liquid Crystals, Fundamentals*, Springer, Berlin, Heidelberg, , 1988.
68. V. A. Belyakov, V. E. Dmitrienko and V. P. Orlov, *Sov. Phys. Usp.*, 1979, **22**, 64-88.
69. M. Mitov and N. Dessaud, *Nat. Mater.*, 2006, **5**, 361-364.
70. G. Agez, C. Bayon and M. Mitov, *Acta Biomater.*, 2017, **48**, 357-367.
71. G. W. G. Gray, J. W. , *Smectic Liquid Crystals: Textures and Structures*, Glasgow: Leonard Hill, London, 1984.
72. *Handbook of Liquid Crystals: Smectic and Columnar Liquid Crystals*, Wiley-VCH: Weinheim, 2nd edn., 2014.
73. A. J. A. Saupe, *One- and Two-Dimensional Fluids Properties of Smectic, Lamellar and Columnar Liquid Crystals*, Taylor & Francis 2006
74. J. P. F. Lagerwall and F. Giesselmann, *ChemPhysChem*, 2006, **7**, 20-45.
75. S. Chandrasekhar, B. K. Sadashiva and K. A. Suresh, *Pramana*, 1977, **9**, 471-480.

76. T. Wöhrle, I. Wurzbach, J. Kirres, A. Kostidou, N. Kapernaum, J. Litterscheidt, J. C. Haenle, P. Staffeld, A. Baro, F. Giesselmann and S. Laschat, *Chem. Rev.*, 2016, **116**, 1139-1241.
77. S. Chandrasekhar, *Liq. Cryst.*, 1993, **14**, 3-14.
78. S. Kumar, *Chem. Soc. Rev.*, 2006, **35**, 83-109.
79. T. Kato, T. Yasuda, Y. Kamikawa and M. Yoshio, *Chem. Commun.*, 2009, 729-739.
80. I. Dierking and A. Martins Figueiredo Neto, *Crystals*, 2020, **10**.
81. G. J. T. Tiddy, *Phys. Rep.*, 1980, **57**, 1-46.
82. *Self-Assembled Supramolecular Architectures: Lyotropic Liquid Crystals*, John Wiley & Sons, Inc., 2012.
83. A. C. K. C. L. Khetrapal, A.S. Tracey, P. Diehl, *Nuclear Magnetic Resonance Studies in Lyotropic Liquid Crystals*, Springer-Verlag Berlin, Heidelberg, 1975.
84. I.-C. Khoo, *Liquid Crystals*, John Wiley & Sons, Inc., Hoboken, New Jersey, 2nd edn., 2007.
85. D. Chandler, *Nature*, 2005, **437**, 640-647.
86. R. Mezzenga, J. M. Seddon, C. J. Drummond, B. J. Boyd, G. E. Schröder-Turk and L. Sagalowicz, *Adv. Mater.*, 2019, **31**, 1900818.
87. N. Garti, D. Libster and A. Aserin, *Food Funct.*, 2012, **3**, 700-713.
88. C. Fong, T. Le and C. J. Drummond, *Chem. Soc. Rev.*, 2012, **41**, 1297-1322.
89. T. L. Greaves, A. Weerawardena and C. J. Drummond, *Phys. Chem. Chem. Phys.*, 2011, **13**, 9180-9186.
90. D. Yalcin, C. J. Drummond and T. L. Greaves, *Soft Matter*, 2020, **16**, 9456-9470.
91. X. Mulet, D. F. Kennedy, T. L. Greaves, L. J. Waddington, A. Hawley, N. Kirby and C. J. Drummond, *J. Phys. Chem. Lett.*, 2010, **1**, 2651-2654.
92. R. Mezzenga, P. Schurtenberger, A. Burbidge and M. Michel, *Nat. Mater.*, 2005, **4**, 729-740.
93. H. Qiu and M. Caffrey, *Biomaterials*, 2000, **21**, 223-234.
94. C. V. Kulkarni, *Langmuir*, 2011, **27**, 11790-11800.
95. M. Salim, N. I. Zahid, C. Y. Liew and R. Hashim, *Liq. Cryst.*, 2016, **43**, 168-174.
96. J. Barauskas and T. Landh, *Langmuir*, 2003, **19**, 9562-9565.
97. Y.-D. Dong, I. Larson, T. Hanley and B. J. Boyd, *Langmuir*, 2006, **22**, 9512-9518.
98. C. V. Kulkarni, W. Wachter, G. Iglesias-Salto, S. Engelskirchen and S. Ahualli, *Phys. Chem. Chem. Phys.*, 2011, **13**, 3004-3021.

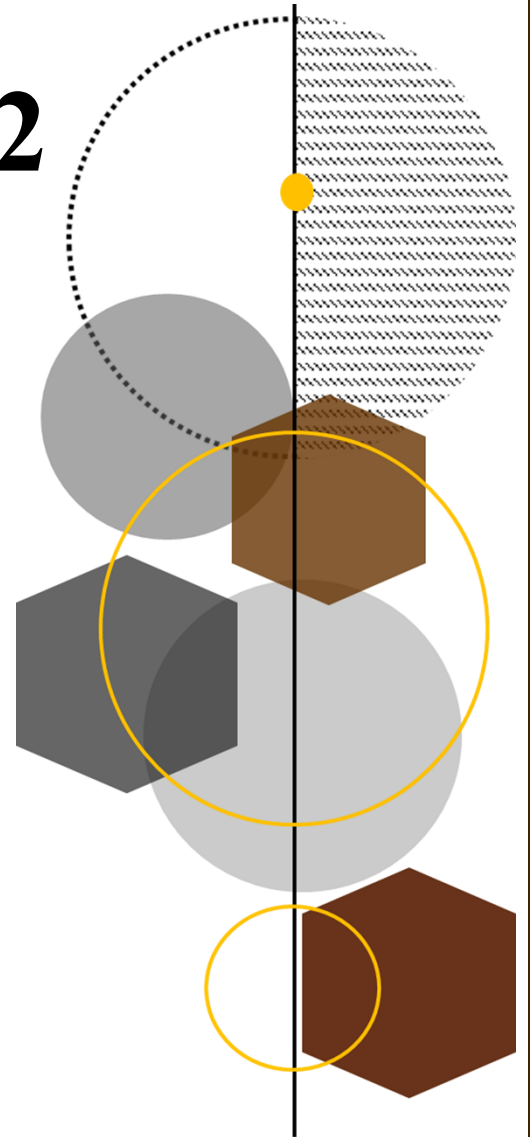
99. J. M. Seddon, *Biochim. Biophys. Acta, Rev. Biomembr.*, 1990, **1031**, 1-69.
100. S. T. Hyde, *Handbook of Applied Surface and Colloid Chemistry*, John Wiley & Sons, Ltd., 2001.
101. R. T. Koynova, B., *Phase Transitions and Phase Behavior of Lipids: Encyclopedia of Biophysics.*, Springer Berlin, Heidelberg, 2013.
102. C. V. Kulkarni, *Nanoscale*, 2012, **4**, 5779-5791.
103. J. M. S. a. R. H. Templer, *Handbook of Biological Physics*, Elsevier Science B.V., Amsterdam, 1995.
104. *Texture in Food: Semi-Solid Foods*, Woodhead Publishing, 2003.
105. S. T. Hyde and S. Andersson, *Z. Kristallogr. Cryst. Mater*, 1985, **170**, 225-240.
106. E. A. Lord and A. L. Mackay, *Curr. Sci.*, 2003, **85**, 346-362.
107. S. B. Hyde, Z.; Landh, T.; Lidin, S.; Ninham, B. W. , *The Language of Shape: The Role of Curvature in Condensed Matter: Physics, Chemistry and Biology*, Elsevier Science, Amsterdam, 1st edn., 1996.
108. S. Andersson, S. T. Hyde, K. Larsson and S. Lidin, *Chem. Rev.*, 1988, **88**, 221-242.
109. X. Cao, D. Xu, Y. Yao, L. Han, O. Terasaki and S. Che, *Chem. Mater.*, 2016, **28**, 3691-3702.
110. G. C. Shearman, O. Ces and R. H. Templer, *Soft Matter*, 2010, **6**, 256-262.
111. A. Fogden and S. T. Hyde, *Eur. Phys. J. B*, 1999, **7**, 91-104.
112. A. M. Squires, R. H. Templer, J. M. Seddon, J. Woenkhaus, R. Winter, T. Narayanan and S. Finet, *Physical review. E, Statistical, nonlinear, and soft matter physics*, 2005, **72**, 011502.
113. A. Yaghmur, L. de Campo, S. Salentinig, L. Sagalowicz, M. E. Leser and O. Glatter, *Langmuir*, 2006, **22**, 517-521.
114. J. M. Seddon, N. Zeb, R. H. Templer, R. N. McElhaney and D. A. Mannock, *Langmuir*, 1996, **12**, 5250-5253.
115. H. Minamikawa and M. Hato, *Langmuir*, 1998, **14**, 4503-4509.
116. S. T. Hyde and S. Andersson, *Z. Kristallogr. Cryst. Mater*, 1984, **168**, 213-220.
117. X. Ye, *Computer Aided Geometric Design*, 1996, **13**, 549-567.
118. A. N. Pressley, *Elementary Differential Geometry*, Springer-Verlag, 2001.
119. R. Negrini and R. Mezzenga, *Langmuir*, 2012, **28**, 16455-16462.
120. R. H. Templer, J. M. Seddon, N. A. Warrender, A. Syrykh, Z. Huang, R. Winter and J. Erbes, *J. Phys. Chem. B*, 1998, **102**, 7251-7261.

121. G. L. Kirk, S. M. Gruner and D. L. Stein, *Biochemistry*, 1984, **23**, 1093-1102.
122. G. C. Shearman, O. Ces, R. H. Templer and J. M. Seddon, *J. Phys.: Condens. Matter*, 2006, **18**, S1105-S1124.
123. W. Helfrich, *Z Naturforsch C*, 1973, **28**, 693-703.
124. R. M. Epand, R. F. Epand, A. Decicco and D. Schwarz, *Eur. J. Biochem.*, 2000, **267**, 2909-2915.
125. Y. Kawabata, M. Nagao, H. Seto, S. Komura, T. Takeda, D. Schwahn, N. L. Yamada and H. Nobutou, *Phys. Rev. Lett.*, 2004, **92**, 056103.
126. C. V. Kulkarni, T.-Y. Tang, A. M. Seddon, J. M. Seddon, O. Ces and R. H. Templer, *Soft Matter*, 2010, **6**, 3191-3194.
127. P. M. Duesing, R. H. Templer and J. M. Seddon, *Langmuir*, 1997, **13**, 351-359.
128. R. H. Templer, J. M. Seddon, P. M. Duesing, R. Winter and J. Erbes, *J. Phys. Chem. B*, 1998, **102**, 7262-7271.
129. G. C. Shearman, B. J. Khoo, M.-L. Motherwell, K. A. Brakke, O. Ces, C. E. Conn, J. M. Seddon and R. H. Templer, *Langmuir*, 2007, **23**, 7276-7285.
130. K. Larsson, *Curr. Opin. Colloid Interface Sci.*, 2009, **14**, 16-20.
131. F. C. Amin Sadeghpour, Richard Smith-Uchotski, Arwen, *Lyotropic Liquid Crystalline Phases for the Formulation of Future Functional Foods*, IOP Publishing, 2020.
132. I. Amar-Yuli, D. Libster, A. Aserin and N. Garti, *Curr. Opin. Colloid Interface Sci.*, 2009, **14**, 21-32.
133. T. M. Dellinger and P. V. Braun, *Chem. Mater.*, 2004, **16**, 2201-2207.
134. S. Umadevi, R. Umamaheswari and V. Ganesh, *Liq. Cryst.*, 2017, **44**, 1409-1420.
135. E. B. Olutaş, F. M. Balcı and Ö. Dag, *Langmuir*, 2015, **31**, 10265-10271.
136. X. Zhang, W. Lu, J. Dai, L. Bourgeois, J. Yao, H. Wang, J. R. Friend, D. Zhao and D. R. MacFarlane, *Sci. Rep.*, 2014, **4**, 7420.
137. S. Akbar, J. Boswell, C. Worsley, J. M. Elliott and A. M. Squires, *Langmuir*, 2018, **34**, 6991-6996.
138. S. Ghosh, L. Ramos and H. Remita, *Nanoscale*, 2018, **10**, 5793-5819.
139. S. Dutt, P. F. Siril and S. Remita, *RSC Adv.*, 2017, **7**, 5733-5750.
140. L. D. Garti N., Aserin A., *Solubilization and Delivery of Drugs from GMO-Based Lyotropic Liquid Crystals: Nanoscience with Liquid Crystals.*, Springer, Cham, 2014.
141. C. J. H. Porter, N. L. Trevaskis and W. N. Charman, *Nat. Rev. Drug Discovery*, 2007, **6**, 231-248.

142. X. Mulet, B. J. Boyd and C. J. Drummond, *J. Colloid Interface Sci.*, 2013, **393**, 1-20.
143. J. C. Shah, Y. Sadhale and D. M. Chilukuri, *Adv. Drug Delivery Rev.*, 2001, **47**, 229-250.
144. M. Wadsäter, J. Barauskas, T. Nylander and F. Tiberg, *ACS Appl. Mater. Interfaces*, 2014, **6**, 7063-7069.
145. B. J. Boyd, D. V. Whittaker, S.-M. Khoo and G. Davey, *International Journal of Pharmaceutics*, 2006, **309**, 218-226.
146. C. Guo, J. Wang, F. Cao, R. J. Lee and G. Zhai, *Drug Discovery Today*, 2010, **15**, 1032-1040.
147. R. Negrini, W.-K. Fong, B. J. Boyd and R. Mezzenga, *Chem. Commun.*, 2015, **51**, 6671-6674.
148. R. Negrini and R. Mezzenga, *Langmuir*, 2011, **27**, 5296-5303.
149. S. Urandur, V. T. Banala, R. P. Shukla, S. Gautam, D. Marwaha, N. Rai, M. Sharma, S. Sharma, P. Ramarao and P. R. Mishra, *Acta Biomater.*, 2020, **113**, 522-540.
150. J. J. Vallooran, S. Handschin, S. M. Pillai, B. N. Vetter, S. Rusch, H.-P. Beck and R. Mezzenga, *Adv. Funct. Mater.*, 2016, **26**, 181-190.
151. A. Bogorodskiy, F. Frolov, A. Mishin, E. Round, V. Polovinkin, V. Cherezov, V. Gordeliy, G. Büldt, T. Gensch and V. Borshchevskiy, *Cryst. Growth Des.*, 2015, **15**, 5656-5660.
152. A. Ishchenko, L. Peng, E. Zinovev, A. Vlasov, S. C. Lee, A. Kuklin, A. Mishin, V. Borshchevskiy, Q. Zhang and V. Cherezov, *Cryst. Growth Des.*, 2017, **17**, 3502-3511.
153. L. Salvati Manni, A. Zabara, Y. M. Osornio, J. Schöppe, A. Batyuk, A. Plückthun, J. S. Siegel, R. Mezzenga and E. M. Landau, *Angew. Chem., Int. Ed.*, 2015, **54**, 1027-1031.
154. A. Zabara, J. T. Y. Chong, I. Martiel, L. Stark, B. A. Cromer, C. Speziale, C. J. Drummond and R. Mezzenga, *Nat. Commun.*, 2018, **9**, 544.
155. W. Sun, J. J. Vallooran, W.-K. Fong and R. Mezzenga, *J. Phys. Chem. Lett.*, 2016, **7**, 1507-1512.
156. V. Luzzati, *Curr. Opin. Struct. Biol.*, 1997, **7**, 661-668.
157. L. van 't Hag, S. L. Gras, C. E. Conn and C. J. Drummond, *Chem. Soc. Rev.*, 2017, **46**, 2705-2731.

158. Q. Xiao, Z. Wang, D. Williams, P. Leowanawat, M. Peterca, S. E. Sherman, S. Zhang, D. A. Hammer, P. A. Heiney, S. R. King, D. M. Markovitz, S. André, H.-J. Gabius, M. L. Klein and V. Percec, *ACS Cent. Sci.*, 2016, **2**, 943-953.
159. N. I. Zahid, O. K. Abou-Zied and R. Hashim, *J. Phys. Chem. C*, 2013, **117**, 26636-26643.
160. J. Kim, W. Lu, W. Qiu, L. Wang, M. Caffrey and D. Zhong, *J. Phys. Chem. B*, 2006, **110**, 21994-22000.
161. W. Wachter, G. Trimmel, R. Buchner and O. Glatter, *Soft Matter*, 2011, **7**, 1409-1417.
162. B. Roy, S. Satpathi, K. Gavvala, R. K. Koninti and P. Hazra, *J. Phys. Chem. B*, 2015, **119**, 11721-11731.
163. R. Ghanbari, S. Assenza and R. Mezzenga, *J. Chem. Phys.*, 2019, **150**, 094901.
164. S. Assenza and R. Mezzenga, *J. Chem. Phys.*, 2018, **148**, 054902.
165. W. Sun, J. J. Vallooran and R. Mezzenga, *Langmuir*, 2015, **31**, 4558-4565.
166. H. Nguan, S. Ahmadi and R. Hashim, *Phys. Chem. Chem. Phys.*, 2014, **16**, 324-334.
167. P. B. Ishai, D. Libster, A. Aserin, N. Garti and Y. Feldman, *J. Phys. Chem. B*, 2009, **113**, 12639-12647.
168. T. Mishraki, P. Ben Ishai, D. Babukh, A. Aserin, Y. Feldman and N. Garti, *J. Colloid Interface Sci.*, 2013, **396**, 178-186.
169. N. I. Zahid, L. Ji, M. F. Khyasudeen, A. Friedrich, R. Hashim, T. B. Marder and O. K. Abou-Zied, *Langmuir*, 2019, **35**, 9584-9592.
170. B. Roy and P. Hazra, *J. Mol. Liq.*, 2019, **285**, 178-184.
171. K. Das, B. Roy, S. Satpathi and P. Hazra, *J. Phys. Chem. B*, 2019, **123**, 4118-4128.
172. K. Das, S. Sappati and P. Hazra, *Phys. Chem. Chem. Phys.*, 2020, **22**, 6210-6221.
173. K. Das, S. Sappati, G. S. Bisht and P. Hazra, *J. Phys. Chem. Lett.*, 2021, **12**, 2651-2659.

# Chapter 2



**Experimental: Materials  
and Techniques**

## 2.1 Materials

The various chemicals, including the fluorescent probes and monoglyceride lipids that have been used in the experimental studies in the thesis have been listed below along with the corresponding purity.

Chemical	Source	Purity	Chapter
1-Linoleoyl-rac-glycerol (Monolinolein)	Sigma-Aldrich	≥ 97%	3, 5
1-Oleoyl-rac-glycerol (Monoolein)	Sigma-Aldrich	≥ 99%	2
Coumarin 343	Sigma-Aldrich	97% dye content	3
Coumarin 480	Sigma-Aldrich	98% dye content	3
Fisetin	Sigma-Aldrich	≥ 98%	4
3-Hydroxyflavone	Sigma-Aldrich	≥ 98%	4
4-(dimethylamino)benzaldehyde	Sigma-Aldrich	99%	5
1-(2-hydroxyphenyl)ethanone	Sigma-Aldrich	99%	5
Hydrogen peroxide (30%)	Sigma-Aldrich	ISO	5
Sodium hydroxide	Sigma-Aldrich	≥ 97%	5
Methyl Iodide	Sigma-Aldrich	≥ 99%	5

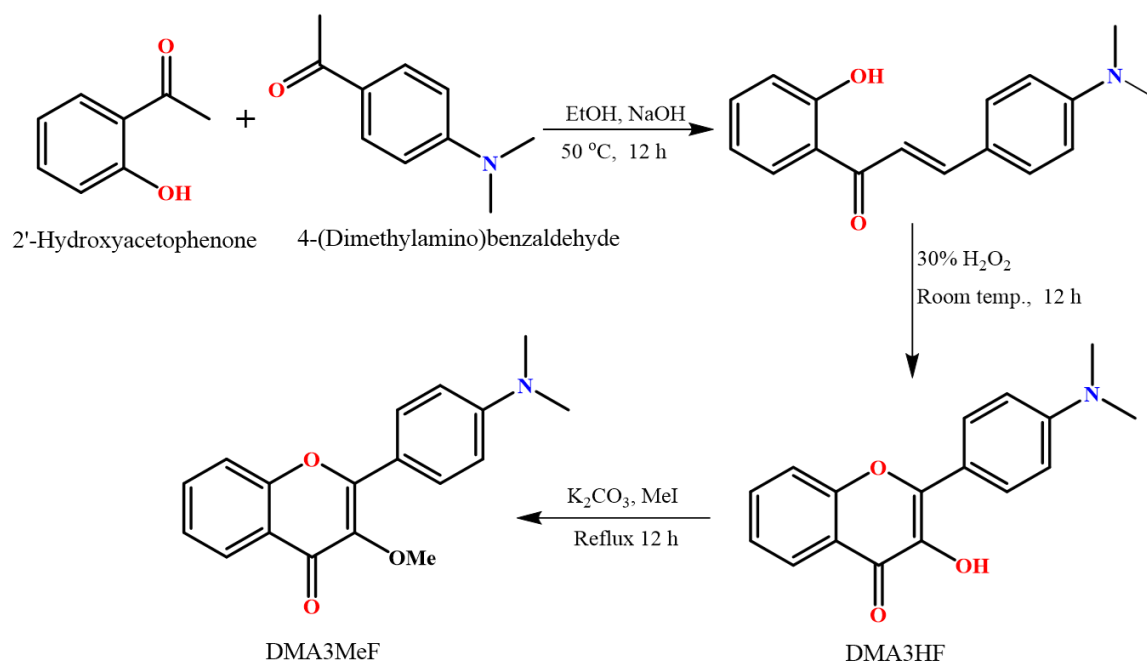
## 2.2 Synthesis and Sample Preparation

### 2.2.1 Synthesis of Fluorescent Dyes

4'-N,N-dimethylamino-3-hydroxyflavone (DMA3HF) and 4'-N,N-dimethylamino-3-methoxyflavone (DMA3MeF) were synthesized based on reported synthesis protocols.<sup>1,2</sup> The synthesised compounds were characterised by <sup>1</sup>H and <sup>13</sup>C NMR spectra and high-resolution mass spectra (HRMS). The <sup>1</sup>H and <sup>13</sup>C NMR spectra were recorded at 400 and 100 MHz respectively, using Bruker and JEOL spectrometers. Deuterated chloroform was used as the solvent medium. The NMR signals have been abbreviated as – b, broad; s, singlet; d, doublet; t, triplet; q, quartet; td, doublet of triplet; dd, double doublet; m, multiplet, tt, triplet of triplet



and ddd, doublet of doublet of doublets. The HRMS measurements were performed using Waters-synapt G2 with electrospray ionization (ESI).



**Scheme 2.1.** Synthesis route for the dyes DMA3HF and DMA3MeF.

#### 4'-N,N-dimethylamino-3-hydroxyflavone (DMA3HF).

5 mmol of both 4-(dimethylamino)benzaldehyde and 1-(2-hydroxyphenyl)ethanone were combined together in 20 ml of ethanol (Scheme 2.1). An aqueous solution of NaOH (1.5 g in 10 ml water) was added to the reaction mixture. Subsequently, the mixture was stirred for ~ 12 h at 50 °C. The reaction mixture was then cooled to room temperature, after which 1M HCl was added to it. The mixture was purified using column chromatography over 100-200 mesh size silica-gel. The obtained solid was then taken in a solution mixture of 20 mL ethanol and aqueous NaOH (1.5 g in 10 ml water). 5 mL of 30% H<sub>2</sub>O<sub>2</sub> was slowly added to the reaction mixture at 0 °C. The reaction mixture was stirred at room temperature for 12 h. After the completion of the reaction, the mixture was neutralized with 1M HCl. The resultant product was purified using column chromatography.

<sup>1</sup>H NMR (400 MHz, CDCl<sub>3</sub>) δ 8.21 (dd, J = 8.0, 1.4 Hz, 1H), 8.16 (d, J = 9.1 Hz, 2H), 7.64 – 7.58 (m, 1H), 7.51 (d, J = 8.4 Hz, 1H), 7.34 (t, J = 7.4 Hz, 1H), 6.74 (d, J = 9.1 Hz, 2H), 3.02 (s, 6H).

<sup>13</sup>C NMR (100 MHz, CDCl<sub>3</sub>) δ 172.56, 155.06, 151.30, 146.79, 137.07, 132.80, 129.25, 125.24, 124.14, 120.94, 118.19, 118.04, 111.46, 40.07.

**HRMS** (ESI)  $m/z$  calculated for  $C_{17}H_{15}NO_3$  ( $M+H$ )<sup>+</sup>: 282.1129, found: 282.1130.

#### **4'-N,N-dimethylamino-3-methoxyflavone (DMA3MeF).**

5 mmol of the previously synthesised DMA3HF (5 mmol) was taken together with 10 mmol of  $K_2CO_3$  in acetone (Scheme 2.1). To this reaction mixture, 5.5 mmol of methyl iodide was added, and the reaction was kept at reflux for 12 h. The mixture was then cooled down to room temperature, and the solvent was evaporated using reduced pressure. Following this, the crude reaction mixture was diluted with Milli-Q water. The resultant compound was extracted in dichloromethane, and the organic layer was evaporated using reduced pressure. The pure DMA3MeF was isolated by using column chromatography.

**$^1H$  NMR** (400 MHz,  $CDCl_3$ )  $\delta$  8.25 (dd,  $J = 8.0, 1.4$  Hz, 1H), 8.14 – 8.07 (m, 2H), 7.66 – 7.59 (m, 1H), 7.50 (d,  $J = 8.2$  Hz, 1H), 7.35 (t,  $J = 7.5$  Hz, 1H), 6.80 – 6.73 (m, 2H), 3.88 (s, 3H), 3.06 (s, 6H).

**$^{13}C$  NMR** (100 MHz,  $CDCl_3$ )  $\delta$  174.77, 156.67, 155.18, 151.82, 140.23, 132.97, 130.01, 125.77, 124.39, 124.37, 117.83, 111.44, 59.78, 40.12.

**HRMS** (ESI)  $m/z$  calculated for  $C_{18}H_{17}NO_3$  ( $M+H$ )<sup>+</sup>: 296.2286, found: 296.1296.

### **2.2.2 Preparation of the LLC Phases**

The LLC phases presented in this thesis are based on monoglyceride lipids (monoolein and monolinolein). The phase diagrams of both monoolein<sup>3</sup> and monolinolein<sup>4</sup> are well established (Figure 2.1). The studies in this thesis have been performed on the inverse hexagonal ( $H_{II}$ ) and the  $Ia3d$  and  $Pn3m$  bicontinuous cubic mesophases. As is evident from the phase diagrams, specific temperature-water composition regions correspond to the different morphologies of the mesophases. For each study, the requisite dye/fluorescent probe was loaded into the aqueous nanochannels of the LLC phases. The fluorescent dye loaded LLC mesophases were prepared according to the reported phase diagrams of monoolein<sup>3</sup> (GMO) and monolinolein<sup>4</sup> (GML). The GML based mesophases were prepared at 22% water content, while the GMO based mesophases were prepared at 23% water content. For all the samples, the dye content was maintained at 8-12  $\mu M$ . Following the phase diagrams, the lipid was first heated at the required temperature for each particular mesophase. The required temperatures for the GML based  $H_{II}$ ,  $Pn3m$  and  $Ia3d$  mesophases at 22% water content were 75 °C, 55 °C and 40 °C, respectively. The temperatures for the GMO based  $H_{II}$ ,  $Pn3m$  and  $Ia3d$  mesophases at 23%

water content were 95 °C, 82 °C and 55 °C, respectively. The dyes were dissolved separately in Milli-Q water and heated to remove the dissolved oxygen. The pre-heated aqueous solutions of the dyes were then added to the liquid lipid under constant stirring. The entire mixture was stirred vigorously for 15-20 minutes. The required temperature for the respective mesophases was maintained throughout the entire process. Since, both GML and GMO have a tendency for aerial oxidation, the LLC mesophases were prepared under inert conditions. The prepared samples were cooled to room temperature (25 °C) and then equilibrated for 48 h before carrying out any spectroscopic measurements. The LLC mesophases were obtained as clear gel-like materials. The LLC mesophases were characterised by polarised optical microscopy and small angle X-ray scattering measurements.

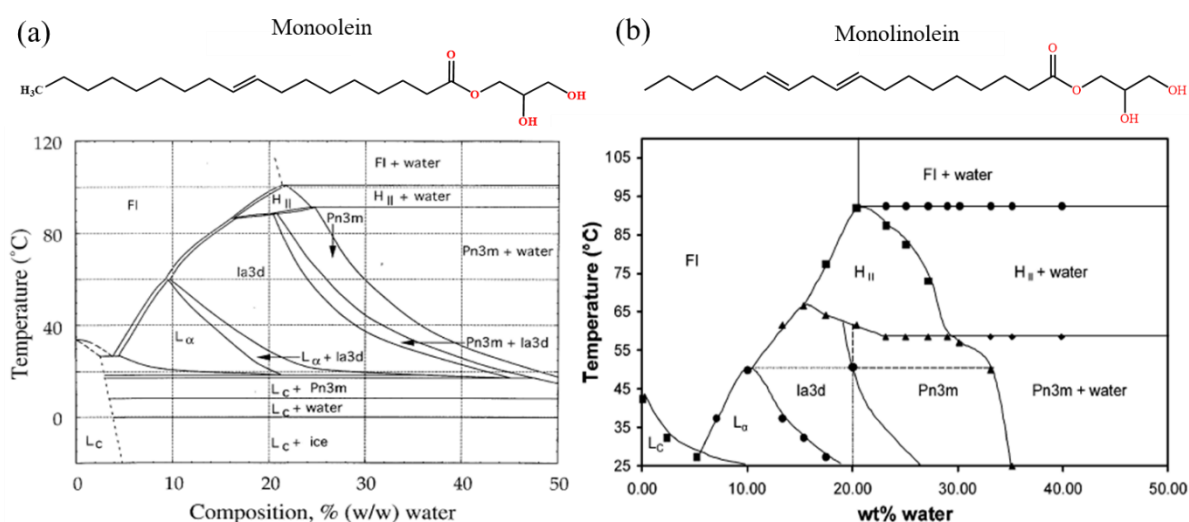


**Figure 2.1.** Binary phase diagram of (a) monoolein-water system (reproduced with permission from reference 3 (*Biomaterials*, 2000, **21**, 223-234)) and (b) monolinolein-water system (reproduced with permission from reference 4 (*Langmuir*, 2005, **21**, 3322-3333)).

## 2.3 Experimental Techniques

### 2.3.1 Polarised Optical Microscopy (POM)

Polarised optical microscopy is a contrast-enhancing imaging technique based on the principle of optical anisotropy in materials.<sup>5,6</sup> As the name suggests, the main components of a polarised optical microscope are a pair of polarisers, one set before the specimen and the other after the specimen (analyser). Unpolarised light from the source gets converted to plane polarised light at the first polariser before hitting the sample. The plane polarised light is directed onto an optically anisotropic sample (Figure 2.2). An optically anisotropic crystal

possesses direction-dependent refraction indices or in other words, the crystallographic axes are not equivalent in terms of optical properties. Thus, in an anisotropic crystal, the interaction of light with the crystallographic axes depends on the overall orientation of the crystal with respect to the incident beam. Typically, molecular order leads to two orthogonal optical axes in the anisotropic material, with each axes associated with a distinct refractive index.<sup>5</sup> As a result, when polarised light is directed onto an optically anisotropic crystal, the incident beam splits into two orthogonal rays that travel at different velocities. This optical phenomenon is termed double-refraction. The difference between the two refractive indices is coined as ‘birefringence’, and this is an intrinsic property of the material.

$$\text{Birefringence} = \Delta n = n_{\parallel} - n_{\perp} \quad (2.1)$$

Here,  $n_{\parallel}$  and  $n_{\perp}$  are the refractive indices for the light that is polarized parallel and perpendicular, respectively, to the two optical axis. One of the rays, which travels with a uniform velocity in all the directions of the crystal, is termed as the ordinary ray. The other ray has a velocity, which is dependent on the propagation direction within the crystal. This ray is called the extraordinary ray. The ordinary ray obeys the laws of refraction while the extraordinary beam does not. The ordinary and extraordinary rays exiting out of the sample are out of phase, owing to the different velocities of the two rays that cause retardation of one of the rays with respect to another. The two out of phase rays combine at the analyser after exiting the specimen. The phase lag gives rise to constructive and destructive interference of the two beams when they combine at the analyser. Notably, the analyser only combines those components of the ordinary and extraordinary rays travelling in the same direction and vibrating in the same plane. The interference of the two rays gives rise to bright and vivid polarisation colours in the images of even transparent samples. Simplistically, the polarisation colours can be thought of as white light minus the wavelengths that are interfered destructively.

POM provides structural information of optically anisotropic systems at a submicroscopic level.<sup>7</sup> The POM measurements of the prepared LLC samples were carried out at 298 K on a LEICA DM 2500 P (Germany) polarized light microscope equipped with Linkam TMS 94. The gel-like LLC samples were inserted between two microscope glass slides. The measurements were performed at 0° and 90° angles of the analyser. The H<sub>II</sub> mesophase gives rise to characteristic fan-shaped textures in POM images, representing the focal conic domains of the cylinders. On the other hand, the lattice structures of the bicontinuous cubic phases are highly symmetric. Thus, the bicontinuous cubic phases,  $Pn3m$  and  $Ia3d$ , are optically isotropic.

This implies that the cubic mesophases have a uniform refractive index in all the crystal directions; hence, these mesophases are not active to polarised optical microscopy. The cubic phases do not exhibit any optical textures in POM.

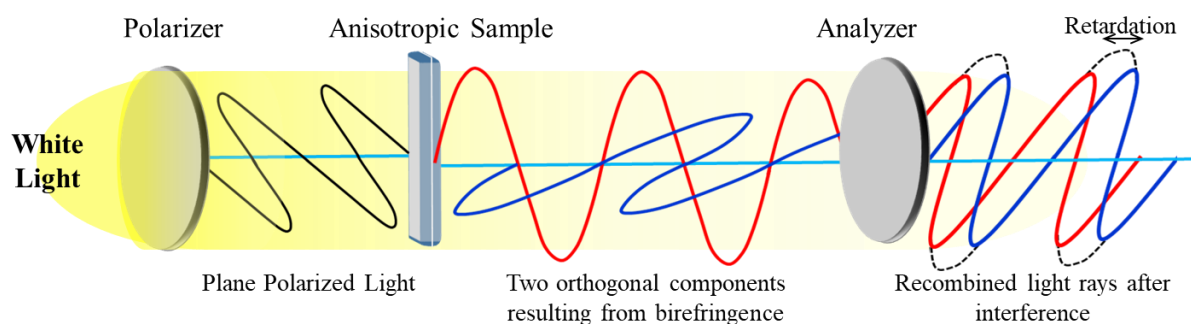


**Figure 2.2.** Schematic representation of the working principle of polarised light microscopy.

### 2.3.2 Small Angle X-ray Scattering (SAXS)

The X-ray scattering techniques like powder X-ray diffraction, single crystal X-ray diffraction, etc. belong to a class of non-destructive analytical methods that are employed to characterise the intrinsic structural information of materials.<sup>8</sup> The principle of these techniques is based on the measurement of X-ray scattering due to the interaction of an incident X-ray beam with matter. Small angle X-ray scattering also belongs to this category wherein the scattering angles are very small, almost close to zero. When a moderate energy X-ray beam hits a sample, it interacts with the electrons in the sample. The moderate energy of the X-ray beam is not sufficient to cause an electron release. Instead, the electron absorbs the energy and oscillates at the same frequency as the incident beam. The oscillating electrons produce coherent secondary X-ray waves, with the same wavelength as that of the incident beam but not in the same direction as the incident beam.<sup>8</sup> Thus, the X-ray waves exiting from the sample are scattered, and this is an instance of elastic scattering. These coherent secondary X-ray waves give rise to an interference pattern. Scattering processes are governed by the reciprocity law, which gives an inverse relationship between the scattering angle and the size of the scattering particles.<sup>8</sup> Small angle X-ray scattering is observed for those specimens which contain electron density inhomogeneities of colloidal size (tens to several thousand Å), which makes the scattering angle correspondingly small. The scattering angle contains the information about the structure at the nano and micro size regime, that is, the shape and size of the specimen as well as the nanoscopic arrangement of the domains. The degree of structural

ordering in the specimen influences the diffraction pattern and the possibilities of extracting structural information from it. Generally, the less ordered an object is, the less informative is the scattering pattern.<sup>9</sup>

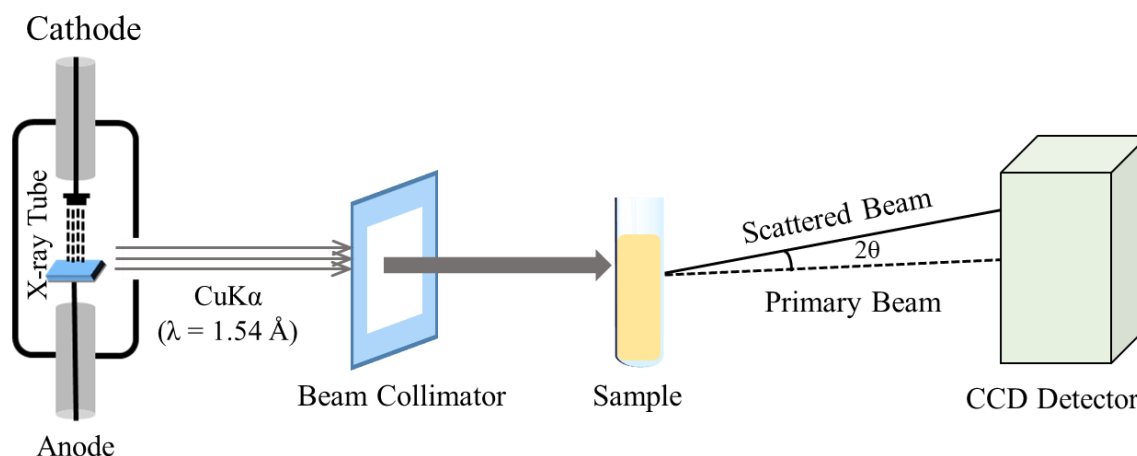


**Figure 2.3.** Schematic representation of the small angle X-ray spectrometer.

Instrumentally, SAXS is a relatively easy technique to perform (Figure 2.3). The sample is irradiated by X-rays, and the angle of the scattered X-ray beams as well as the intensities is probed by a detector. The incident X-ray beam was previously generated in X-ray tubes, with the metal anode being the source of the X-rays. The X-ray beams are generated as a result of the collision of high-velocity electrons on the anode. Nowadays, SAXS measurements are also being popularly carried out by high intensity X-rays of a synchrotron radiations. Usually, the  $\text{CuK}\alpha$  ( $1.54 \text{ \AA}$ ) radiation is used as the incident beam for SAXS measurements. The SAXS measurements in this thesis were carried out either on a line collimated Anton Paar SAXSpace system (Chapter 3) or a line collimated Anton Paar SAXSess mc2 system (Chapters 4 and 5). The line collimation ensures that the beam profile is long and narrow by confining the beam in one dimension. Both the instruments were equipped with a sealed tube copper X-ray source operating at 40 kV and 50 mA. Thus, the incident X-ray beam has a characteristic wavelength of  $1.54 \text{ \AA}$ . In the former system (Anton Paar SAXSpace), the sample was filled in the paste cell on a TCStage 150, and scattered data was collected by a 2-D CCD detector. The collected data was converted from 2-D to 1-D by azimuthal averaging using the Bruker software. In the latter system (Anton Paar SAXSess mc2), the sample was filled in the paste cell on a TCS 300-c stage, and the data was collected by a 2-D Princeton Instruments PI-SCX:4300 CCD detector. All the measurements were carried out at 298 K. The characteristic peak distance ratios for  $\text{H}_{\text{II}}$ ,

*Pn3m* and *Ia3d* are  $\sqrt{1}:\sqrt{3}$ ,  $\sqrt{2}:\sqrt{3}:\sqrt{4}:\sqrt{6}:\sqrt{8}$  and  $\sqrt{6}:\sqrt{8}:\sqrt{14}:\sqrt{16}:\sqrt{20}$ , respectively.<sup>10</sup> The radius of the aqueous nanochannels of each LLC mesophase were calculated from the diffraction peaks of each phase using reported methods.<sup>4, 11</sup>

For the two cubic phases *Ia3d* and *Pn3m*, the lipid chain length was first calculated, followed by the estimation of the aqueous channel dimensions. The lipid chain length ( $l$ ) can be obtained by the following equation.

$$\Phi_{lip} = 2A^* \frac{l}{a} + \frac{4\pi\chi}{3} \left(\frac{l}{a}\right)^3 \quad (2.2)$$

Here,  $\Phi_{lip}$  is the total volume fraction of the lipid (GMO or GML) used in the binary mixture of lipid and water for the preparation of the phases,  $A^*$  is the area of the surface in the unit cell with the lattice parameter equal to unity,  $\chi$  is the Euler-Poincare characteristic, and  $a$  is the lattice parameter. The value of the lattice parameter is calculated from the peak position of the highest intensity reflections (110 for *Pn3m* and 211 for *Ia3d* phases, respectively). Subsequently, the radius of the water nanochannels of the cubic phases is obtained by the given equation.

$$R_w = \left(\frac{A^*}{2\pi|\chi|}\right)^{1/2} a - l \quad (2.3)$$

The values of  $A^*$  and  $\chi$  are 3.091 and -8 for the *Ia3d* phase and 1.919 and -2 for the *Pn3m* phase.<sup>11</sup> The above equation can be simplified as follows for the two cubic phases,

$$\text{For } Ia3d \text{ phase,} \quad R_w = (0.2480)a - l \quad (2.4)$$

$$\text{For } Pn3m \text{ phase,} \quad R_w = (0.3908)a - l \quad (2.5)$$

For the  $H_{II}$  phase, the dimension of the water nanochannel was calculated by the following equation. The lattice parameter was obtained from the peak position of the highest intensity (100).

$$R_w = a \left(\frac{\sqrt{3}(1 - \Phi_{lip})}{2\pi}\right)^{1/2} \quad (2.6)$$

In all the studies, the radius of all the prepared mesophases was between 2-2.5 nm.

### 2.3.3 Steady State Absorption

All the steady state absorption measurements were recorded on a double beam, ultraviolet-visible (UV-Vis) spectrophotometer (Shimadzu-2450). The instrument is equipped with two lamps to span the entire wavelength range from ultraviolet (~ 200 nm) to near-infrared (~ 900 nm). A deuterium lamp covers the UV region, while a 50W halogen lamp covers the visible to near IR wavelength range. The path length of the quartz cuvette was 1 cm for all the measurements. All the steady state absorption experiments were carried out at room temperature.

### 2.3.4 Steady State Fluorescence Emission

The steady-state fluorescence spectra were recorded on a Jobin Yvon Fluoromax-4 spectrofluorometer (Horiba Scientific, USA). A high-pressure xenon arc lamp (150 W) covering an emission range of ~ 250-800 nm, is the light source in the instrument. The emitted light from the sample is detected using a photomultiplier tube (PMT), which works on the principle of the current generation by the photoelectric effect. A monochromator in the instrument ensures the selective control of the excitation wavelength. For the liquid samples of the dyes in solvents, the emission was collected at the right angle to the incident excitation to avoid the interference by stray light. For the gel-like LLC samples, a solid state sample holder was employed to carry out the measurements. The transparent LLC gels were placed on a quartz slide at an angle of 45° to the incident beam. Both emission and excitation spectra were measured using the steady state spectrofluorometer. The emission spectrum is the wavelength distribution of emission measured at a single excitation wavelength whereas an excitation spectrum represents the variations in the fluorescence intensity as a function of excitation wavelength for a fixed observation wavelength.<sup>12, 13</sup>

### 2.3.5 Fluorescence Lifetime Measurements

The lifetime of an excited state is the average time that a molecule exists in that state before returning to the ground state. Mathematically, the excited state lifetime is defined as the time required for 1/e<sup>th</sup> of the excited state molecules to relax down to the ground state.<sup>12</sup> The excited state fluorescence lifetimes of various systems in this thesis have been evaluated using two techniques – time correlated single photon count (TCSPC) and fluorescence upconversion. Typically, the excited state population decays down to the ground state exponentially, and the time dependent intensity for the deactivation via one channel or pathway can be expressed as,

$$I(t) = I_0 \exp^{-t/\tau} \quad (2.7)$$



where,  $I(t)$  is the time dependent fluorescence intensity,  $I_0$  is the intensity at the time  $(t) = 0$ . Fitting the exponential curve in the plot of  $I(t)$  vs  $t$  yields the fluorescence lifetime components ( $\tau$ ). For systems following multi-exponential decay functions as a result of multiple emitting species, the above equation is modified as,

$$I(t) = \sum_{i=1}^n \alpha_i \exp^{-t/\tau_i} \quad (2.8)$$

where,  $\tau_i$  represent the individual fluorescence lifetimes and  $\alpha_i$  gives the corresponding amplitudes.

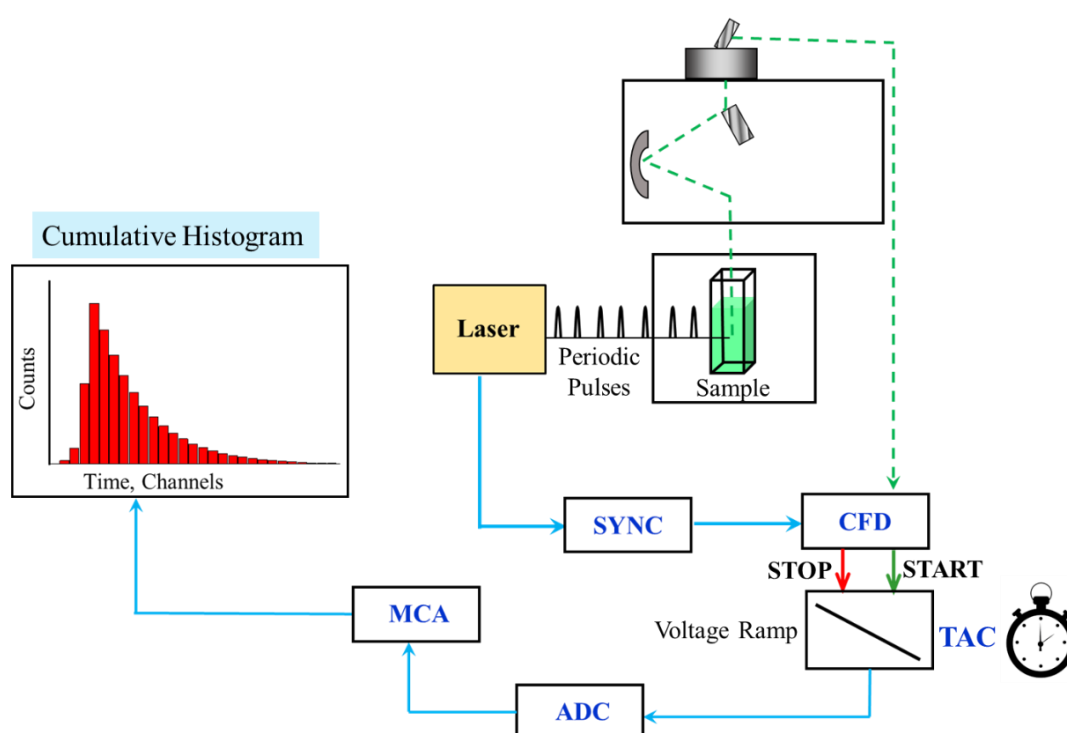


**Figure 2.4.** Schematic diagram of the setup for the time-correlated single photon counting instrument.

### 2.3.5.a Time-Correlated Single Photon Counting (TCSPC)

Analysis of multi-exponential decays is a significant issue as it requires a high signal-to-noise ratio. One technique that gives rise to extremely high temporal resolutions is TCSPC. TCSPC has been one of the most popular lifetime measuring methods to date. As the name might indicate, the principle of TCSPC is based on the accurate repetitive measurement of the arrival time of single photons from the emitting species.<sup>12, 14</sup> The conditions of TCSPC are such that the detector registers only a single photon over multiple excitation cycles. The arrival time

of each emitted photon is accurately measured by the TCSPC electronics and the photon arrival times are stored in a histogram. Under the condition of single photon detection, the histogram of photon arrivals per time bin represents the time decay that would have obtained from a “single shot” time-resolved analog recording.

In a TCSPC measurement, the sample is excited with a pulsed light source that could either be a laser or a flashlamp (Figure 2.4). The excitation pulse simultaneously generates a signal at the TCSPC electronics via the electric pulse associated with the optical pulse. The signal reaches the constant fraction discriminator (CFD) via the SYNC (which synchronizes the optical and electrical pulses). The CFD times the arrival of the photo-electron pulse with high precision. The electric signal is then passed to the time-to-amplitude converter (TAC), where it triggers the charging of the capacitor. Thus, a voltage ramp is generated in the TAC. Meanwhile, the arrival time of the emission photon is measured by the CFD, and a signal is sent to the TAC. This signal stops the charging of the capacitor. Thus, the voltage generated at the TAC is directly proportional to the time difference between the excitation and emission pulses. Consequently, the TAC acts like a stopwatch, and it is the heart of the TCSPC instrument. The voltage is converted to a numerical value by the analog-to-digital converter (ADC), and the values are stored in individual time bins in the form of a histogram. This process is repeated multiple times to achieve a decay curve with a high signal-to-noise ratio. The width of the time bins is determined by the time resolution of the TAC. Notably, all the electronics are associated with a ‘dead time’ after a photon event. Thus this necessitates a very low probability of registering more than one emission photon in every cycle. Typically, one emission photon is registered for every 100-200 excitation pulses. Most TCSPC instruments usually operate on the ‘reverse mode’. The working principle remains the same, only the emission pulse starts the capacitor charging in TAC, and the excitation pulse stops it. The reverse mode is employed because of the high repetition rate of the excitation lasers (1 MHz). The TAC must be reset and set to zero after each photon event prior to each excitation pulse. However, the ‘dead time’ of the TAC implies that the start pulse reaches the TAC before it can reset. To avoid this glitch, the TCSPC instruments are now run in the reverse mode.

All the TCSPC measurements were carried out on a Horiba Jobin Yvon IBH, UK spectrophotometer. The fluorescence signals were collected at the magic angle ( $54.7^\circ$ ), to eliminate the effects of rotational diffusion, and detected using an MCP-PMT (Hamamatsu, Japan) detector. In the experiments that have been included in this thesis, two LEDs have been

used for exciting the samples, 375 nm and 402 nm. The instrument response function obtained for the TCSPC system using these LEDs is  $\sim 100$  ps. All the decay profiles were deconvoluted to eliminate the distortion of the data arising from the finite decay time of the laser pulse and the response efficiency of the detector as well as the electronics. The lifetime profiles were fitted with a minimum number of exponentials using the lifetime analysis software (DAS 6.5) from IBH (UK). The quality of each fitting was judged by  $\chi^2$  values and the visual inspection of the residuals. A value of  $\chi^2 \approx 1$  was considered to be the best fit for the plots. The minimum lifetime component that could be detected after the deconvolution of the data was  $\sim 40$  ps.

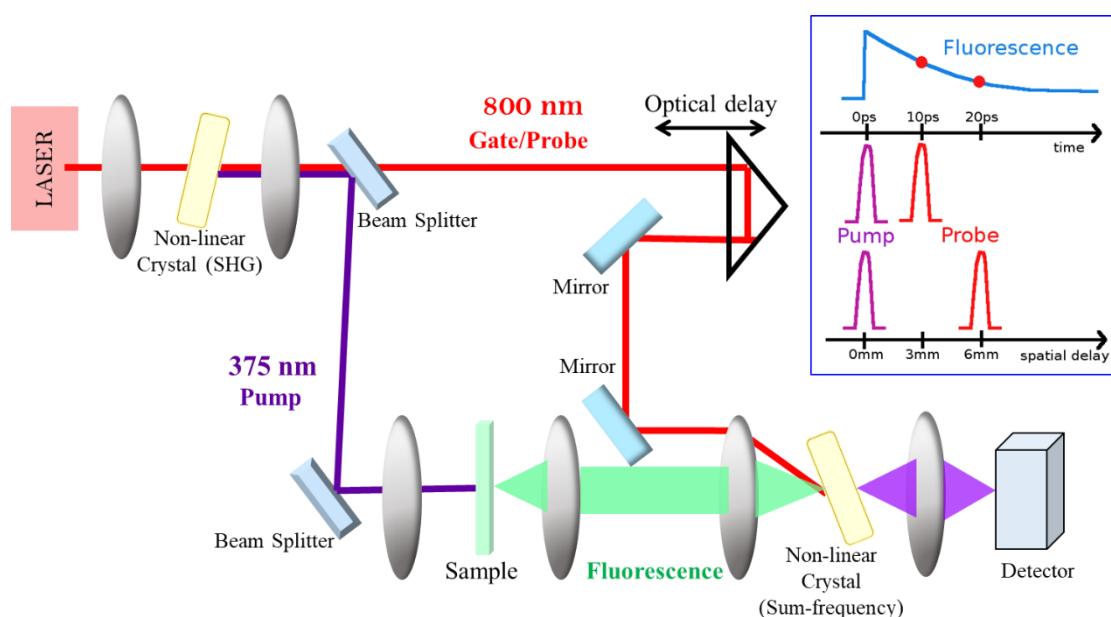


**Figure 2.5.** Schematic representation of the femtosecond time-resolved fluorescence upconversion setup.

### 2.3.5.b Femtosecond Time-Resolved Fluorescence Upconversion

Although TCSPC is an efficient technique to measure the fluorescence lifetimes of excited state species and the timescales of other excited state processes, the time resolution is limited to  $\sim 40$ -50 ps. It would not be possible to detect excited state processes in femtoseconds or less than tens of ps. The femtosecond fluorescence upconversion technique is utilised to measure the time domains of processes that occur in an ultrafast timescale ( $> 100$  fs). In the fluorescence upconversion technique, a tunable laser with ultra-short pulses is generally used to excite the sample.<sup>13</sup> The fundamental beam from the laser is directed onto a non-linear crystal for the generation of the second harmonic ray (Figure 2.5). The fundamental and generated second harmonic beams are separated using a beam splitter, and the latter beam is used to excite the

sample. Simultaneously, the fundamental beam passes through an optical delay line. The time-delayed fundamental beam and the emission light from the sample mix at another non-linear crystal, generating the upconverted signal. The greater the delay time between the fundamental beam and the fluorescence beam, the smaller is the fluorescence intensity. A fluorescence lifetime profile is thus obtained by measuring the intensities at each time delay.

The fluorescence upconversion setup used for the lifetime measurements in this thesis utilizes a tunable Mai Tai HP (Spectra Physics, USA), Ti:Sapphire laser as the excitation source. The Ti:Sapphire oscillator covers a wide range of wavelengths from 690 nm to 1040 nm. High quality, stable, horizontally polarized ( $>500:1$  horizontal), Gaussian pulses ( $TEM_{00}$ ,  $M^2 < 1.1$ ) with stable average power ( $>2.5$  W) and very high peak power ( $>300$  kW) ensures minimum fluctuation of the laser pulse. The Mai Tai laser is pumped by an  $Nd^{3+}$  ion doped Yttrium Vanadate crystalline matrix ( $Nd:YVO_4$ ) wherein the  $Nd^{3+}$  acts as the active lasing material. The most intense lasing beam for the  $Nd:YVO_4$  laser is at  $\sim 1064$  nm. The frequency doubled 532 nm light is used to pump the Mai Tai laser. Mai Tai uses an acousto-optic modulator (AOM) (constituted of a high quality optical material like quartz) to ensure the mode-locked output from Ti-Sapphire. The Mai Tai reliability is maintained using the ultra-stable regenerative mode-locking technique proven with the Spectra-Physics Tsunami® oscillator. The fluorescence upconversion setup uses a non-linear type-I  $\beta$ -barium borate (BBO) crystal to generate the second harmonic and a type-II BBO crystal for the generation of the sum frequency beam. The angle between the polarization of the second harmonic and fundamental pulses was maintained at the magic angle ( $54.7^\circ$ ) to eliminate effects from rotational diffusion. A fundamental beam wavelength of 750 nm was used for the measurements in this thesis. A cross-correlation function obtained using the Raman scattering from ethanol provided a full-width at half-maximum (FWHM) of  $\sim 350$  fs. The estimated uncertainties in the upconversion measurements are  $\sim 10$ -15%. The fluorescence decays were deconvoluted using a Gaussian-shaped excitation pulse by Igor Pro 6.0 analysis software.

### 2.3.6 Time-Resolved Fluorescence Anisotropy

Fluorescence anisotropy gives a direct measure of the change in spatial orientation of fluorophores in the time between the excitation and emission events. When a bulk of randomly oriented fluorophores is illuminated by polarised light, the fluorophores having transition moments in the direction of the electric vector of the incident light get preferentially excited.

This phenomenon is termed as ‘photoselection’.<sup>12, 13</sup> Since, a certain population of specifically oriented fluorophores are excited, it gives rise to anisotropic or polarised emission. However, any orientational change in the transition moments of the fluorophores during the excited state lifetime of the fluorophores leads to depolarisation of the fluorescence. The possible causes of fluorescence depolarization are the rotational diffusion and Brownian motion of the fluorophores and the non-parallel absorption and emission transition moments, torsional vibrations and the transfer of excitation energy to another molecule with a different orientation.<sup>13</sup> Of all these factors, the rotational diffusion plays a major role in causing the depolarisation and lowering the maximum values of anisotropy. Fluorescence anisotropy is defined as,

$$r = \frac{r_0}{1 + (\tau/\theta)} \quad (2.9)$$

Where,  $r_0$  is the intrinsic anisotropy of the fluorophores that would have been observed in the complete absence of rotational diffusion or depolarisation,  $\tau$  is the excited state lifetime of the fluorophores and  $\theta$  is the rotational correlation time for the diffusion process. Time-resolved fluorescence anisotropy measures the extent of depolarisation of the emission with respect to time following the photoselection phenomenon. Thus, the time-resolved fluorescence anisotropy measurements help to estimate the rotational dynamics of the fluorophores indirectly. Time-resolved fluorescence anisotropy ( $r(t)$ ) is mathematically defined as follows.

$$r(t) = \frac{I_{\parallel}(t) - I_{\perp}(t)}{I_{\parallel}(t) + 2I_{\perp}(t)} \quad (2.10)$$

Here,  $I_{\parallel}$  and  $I_{\perp}$  represent the time dependent fluorescence intensities polarised parallel and perpendicular to the polarisation of the incident light, respectively. Since the detector sensitivity and monochromator efficiency are biased towards a specific polarisation direction, generally the horizontal polarisation, an instrumental correction factor known as the G factor has to be applied to the above equation.

$$r(t) = \frac{I_{\parallel}(t) - GI_{\perp}(t)}{I_{\parallel}(t) + 2GI_{\perp}(t)} \quad (2.11)$$

The time-resolved anisotropy measurements were employed in Chapter 3 of this thesis to estimate the microviscosity inside the aqueous LLC nanochannels. The measurements were performed by the automated toggling method using TCSPC set-up. The samples were excited

using the 402 nm LED (IBH, UK, FWHM ~100 ps). In the toggling method, a movable emission polariser was used on the emission side while the excitation polariser was fixed vertically. The emission intensities at perpendicular and parallel polarizations were collected alternatively for 60 s until the peak difference between the parallel and perpendicular decays reached 7000 counts. The G factor was measured using horizontally polarized excitation light and collecting the horizontally ( $I_{HH}(t)$ ) and vertically ( $I_{HV}(t)$ ) polarized emission decay profiles for the same sample. The G factor was measured to be 0.60 for 402 nm excitation. For the LLC samples,  $r(t)$  takes the form of a sum of exponentials,

$$r(t) = r_0 \sum \beta_i \exp(-t/\tau_{r_i}) \quad (2.12)$$

where  $\beta_i$  and  $\tau_{r_i}$  are the fractional contribution of the total depolarization and rotational correlation times of the  $i^{\text{th}}$  component, respectively. Since fluorescence anisotropy gives a good estimation of the fluidity surrounding the fluorophore, the microviscosity inside the aqueous LLC channels (Chapter 3) was estimated by the Debye-Stokes-Einstein equation.<sup>12, 13</sup>

$$\eta = \frac{\tau_r k_B T}{V} \quad (2.13)$$

$\tau_r$  is the rotational diffusion time constant, obtained from the time-resolved fluorescence anisotropy exponential curves,  $T$  is the temperature,  $k_B$  is the Boltzmann constant and  $V$  is the hydrodynamic molecular volume of the fluorophore. Notably, the Debye-Stokes-Einstein equation is valid for fluorophores that are rigid and spherically symmetrical, moving in a homogenous Newtonian fluid and obeying the Stokes hydrodynamic law.<sup>13</sup>

## 2.4 Excited State Processes

One of the major advantages of fluorescence is the sensitive dependence of the excited state phenomenon on the properties of the surrounding medium. This sensitivity has been exploited to evaluate the fundamental physical properties of the water molecules in the aqueous LLC channels. Most fluorophores can undergo dynamic excited state processes before relaxing down to the ground state. These excited state processes are influenced by the surrounding media, which is reflected in the spectral data of the fluorophores. The excited state processes studied in this thesis are solvent relaxation, intramolecular proton transfer and proton coupled electron transfer. Each of the phenomena has been described in brief in the subsequent sections.

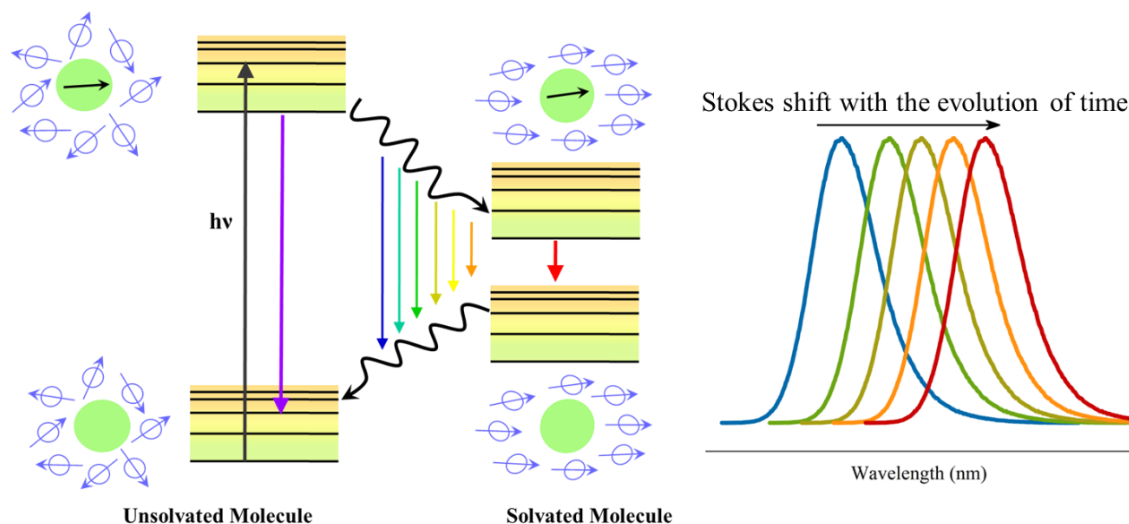


**Figure 2.6.** Schematic representation of the solvent reorganisation around excited state dipole and the resultant time dependent Stokes shift in the emission spectrum.

### 2.4.1 Excited State Solvent Relaxation

Certain molecules possess high dipole moments in the excited state compared to the almost negligible dipole moment in the ground state due to redistribution of electronic charge upon excitation. On photoexcitation of such molecules, an instantaneous dipolar state is created, and the solvent molecules surrounding the fluorophore find themselves in a high-energy random configuration at the time  $t = 0$ . Consequently, the solvent molecules start reorienting themselves around the excited state dipole to attain a stable equilibrium configuration (Figure 2.6). This reorientation of the solvent molecules around the excited state fluorophore is a time-dependent process. This rearrangement of the solvent molecules around the excited state dipole is termed as ‘solvation dynamics’, and if the solvent in question is water, the term is ‘hydration dynamics’.<sup>15, 16</sup> The motion of the water molecules mainly involves vibrational, rotational and translational motions. The rotational motion includes librational movements, which is a reciprocating motion wherein an object with an almost fixed orientation repeatedly moves back and forth. In addition, the intermolecular vibrations of the extended hydrogen-bonded network are also present.

The effect of hydration dynamics is manifested in the spectral characteristics of the fluorophores. The emission spectra of the fluorophore exhibit a continuous time-dependent Stokes’ shift (TDSS). At initial time scales, instantly after photoexcitation, the emission occurs from the unsolvated dipolar excited state as the solvent molecules do not have the required time to reorient themselves. However, with the evolution of time, as the solvent relaxation of the

dipolar state proceeds, the excited state gets more and more stabilised. The energy difference between the ground and excited states decreases with the evolution of time and consequently, the emission spectra get more and more red-shifted. TDSS is direct evidence of solvent relaxation of the excited state dipole, and this can be visualised by constructing a time-resolved emission spectra (TRES). TRES can be simplistically thought of as the emission spectra that would be observed if measured at regular intervals in time following the pulsed excitation.<sup>12</sup> To construct TRES, at first, a new set of intensity decays ( $I'(\lambda, t)$ ) have to be computed and normalized so that the time-integrated intensity at each wavelength is equal to the steady-state intensity at that wavelength.<sup>17</sup> This is done by multiplying a volume  $H(\lambda)$  to the instrument measured lifetime decays ( $I(\lambda, t)$ ), where

$$H(\lambda) = \frac{F(\lambda)}{\sum_i \alpha_i(\lambda) \tau_i(\lambda)} \quad (2.14)$$

here,  $F(\lambda)$  is the steady state emission spectrum,  $\tau_i$  is the lifetime of the  $i^{\text{th}}$  component and  $\alpha_i$  is the corresponding amplitude. Thus, the new set of normalised intensity decays are given by,

$$I'(\lambda, t) = I(\lambda, t) H(\lambda) = \sum_i \alpha'_i(\lambda) \exp[-t/\tau_i(\lambda)] \quad (2.15)$$

where,  $\alpha'_i = H(\lambda) \alpha_i(\lambda)$  (2.16)

The obtained time-resolved emission spectra are generally fit to a log-normal function,<sup>17</sup>

$$g(\nu) = g_0 \exp\left(-\ln(2) \times \left[\frac{\ln(1 + \alpha)}{b}\right]^2\right) \quad (2.17)$$

where,  $\alpha = \frac{2b(\nu - \nu_P)}{\Delta}$  and  $g_0$ ,  $b$ ,  $\nu_P$  and  $\Delta$  are the peak height, asymmetric parameter, peak frequency, and width parameter, respectively. The peak frequencies ( $\nu_P$ ) obtained from the log-normal fitting of TRES is then used to construct the decay of the solvent correlation function ( $C(t)$ ), which is defined as,

$$C(t) = \frac{\nu(t) - \nu(\infty)}{\nu(0) - \nu(\infty)} \quad (2.18)$$

where  $\nu(0)$  is the peak frequency at time  $t = 0$  immediately after the photoexcitation, and it is calculated by the extrapolation of the  $\nu(t)$  data to  $t \rightarrow 0$ .  $\nu(t)$  is the peak frequency at time  $t$ , and  $\nu(\infty)$  is the peak frequency at an infinite time when the solvent relaxation process is complete, and the solvent molecules are in equilibrium position around the excited state dipole. The value of  $\nu(\infty)$  is estimated as the peak frequency corresponding to the time at which the



peak maximum no longer exhibits spectral shift on varying the time. The decay of the solvent correlation function generally fits an exponential function,

$$C(t) = \sum \alpha_i \exp(-t/\tau_{si}) \quad (2.19)$$

where,  $\tau_i$  is the solvation time of  $i^{\text{th}}$  component with amplitudes of  $\alpha_i$ . The average solvation time is calculated as,

$$\langle \tau_{av} \rangle = \sum_{i=1}^n \alpha_i \tau_{si} \quad (2.20)$$

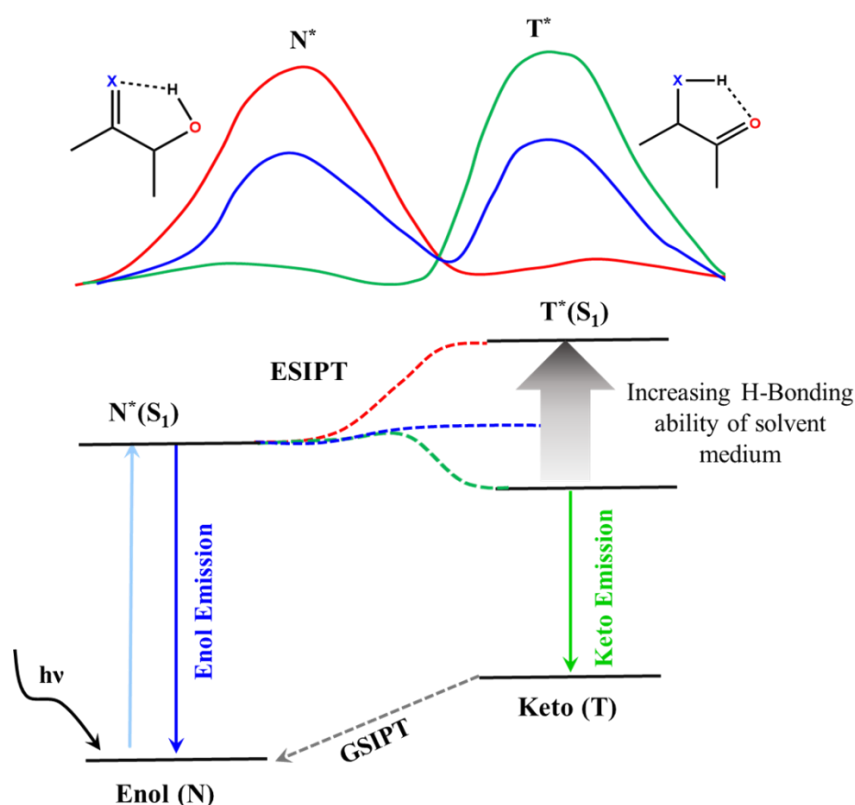


**Figure 2.7.** Schematic representation of the excited state intramolecular proton transfer (ESIPT) and the effect of the hydrogen bonding abilities of the surrounding medium on the ESIPT phenomenon.

#### 2.4.2 Excited State Intramolecular Proton Transfer (ESIPT)

Excited state intramolecular proton transfer (ESIPT) is one of the fundamental processes in both chemistry and biology.<sup>18, 19</sup> In addition to this, ESIPT has also gained significant attention owing to its potential applications as molecular probes, lasing materials, molecular logic gates, optical filters, etc.<sup>20, 21</sup> ESIPT was first observed in salicylic acid by Weller in the 1950s.<sup>22</sup> ESIPT generally comprises a four-level photocycle involving an excited state keto-enol tautomerisation (Figure 2.7). For ESIPT to occur, a hydrogen bond donating

and a hydrogen bond accepting moiety should be in close proximity within the molecule. Most ESIPT molecules exist in the enol/normal form in the ground state. On photoexcitation, the redistribution of electronic charge in the molecule causes an increase in the acidity of the hydrogen bond donating moiety and the basicity of the hydrogen bond accepting moiety.<sup>23</sup> This leads to an efficient and facile enol-keto tautomerisation in the excited state ( $N^* \rightarrow T^*$ ), followed by the radiative emission from the keto/tautomer species. After the relaxation of the excited state keto species to the ground state, it reverts to the original enol form via reverse proton transfer. ESIPT phenomenon is characterised by dual emission from the keto and enol species, large Stokes' shifted emission of the keto form with respect to the normal form and an ultrafast proton transfer dynamics ( $k_{\text{ESIPT}} > 10^{12} \text{ s}^{-1}$ ). However, the most attractive feature of ESIPT is its spectral sensitivity to the hydrogen bonding parameters of the surrounding medium. An efficient ESIPT requires a strong intramolecular hydrogen bond between the proton accepting and donating moieties within the molecule, but the intramolecular hydrogen bond gets influenced by the solvent medium (Figure 2.7). For instance, in non-polar aprotic solvents like benzene or n-heptane, the negligible hydrogen bond donating and accepting abilities of the solvent do not interfere with the intramolecular hydrogen bond in the ESIPT molecule. This leads to an efficient ESIPT process, and emission is observed almost exclusively from the tautomeric species. In addition, the ESIPT dynamics in such solvents are extremely fast. On the other hand, both polar protic and aprotic solvents, which have an appreciable hydrogen bond donating and accepting ability perturb the intramolecular hydrogen bond due to the formation of intermolecular solute-solvent hydrogen bonds. This competition from the intermolecular hydrogen bonds restricts the ESIPT efficiency. In such a case, dual emission is observed with the normal form's intensity increasing with the decrease in the ESIPT efficiency. In addition, the hydrogen-bonded solute-solvent complexes in such solvents also decrease the dynamics of the ESIPT process.

The transformation of one excited state species to another in the excited state is manifested clearly in the time-resolved area normalised spectrum (TRANES). TRANES is the extension of the time-resolved emission spectrum (TRES). TRANES is constructed by normalizing the area of each TRES profile such that the area of the spectrum at any time  $t$  is the same as the area of the spectrum at  $t=0$ .<sup>24</sup> A useful feature of TRANES is that an isoemissive point in the spectra supports the involvement of two emitting species in the sample. The occurrence of ESIPT leads to the decrease in the intensity of one of the species with a

concomitant increase in the intensity of the other species with the evolution of time. The ESIPT phenomenon has been employed to evaluate the intrinsic hydrogen bond donating and accepting abilities of the water molecules encased inside the LLC nanochannels (Chapter 4).

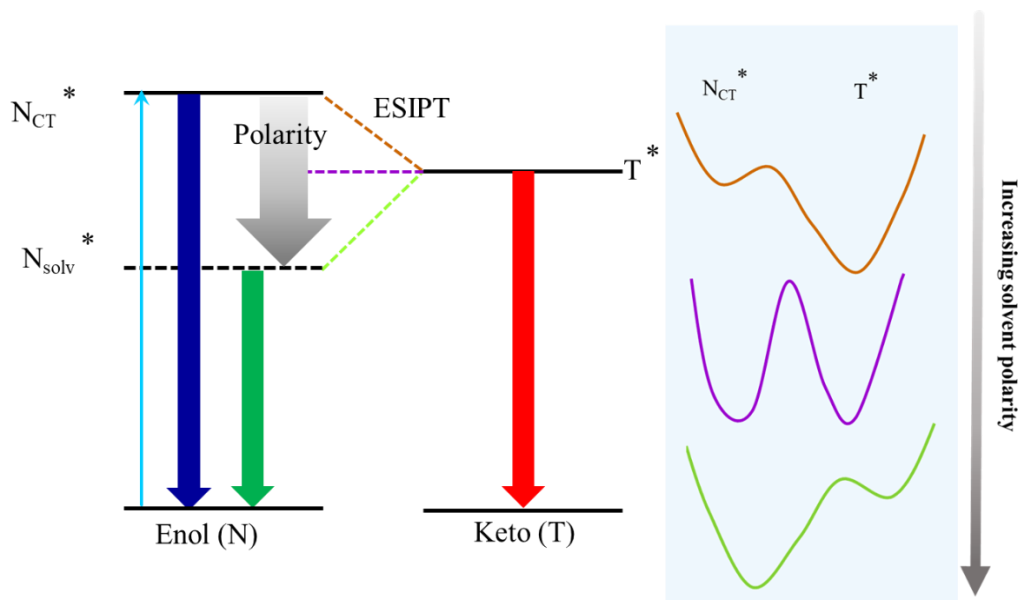


**Figure 2.8.** Schematic representation of the coupled ESIPT-ESICT phenomenon and the effect of the solvent polarity on the relative energies of the enol and keto species.

### 2.4.3 Excited State Proton Coupled Electron Transfer (PCET)

The phenomenon of excited state proton coupled electron transfer (PCET) combines the processes of excited state intramolecular proton transfer (ESIPT) and excited state intramolecular charge transfer (ESICT) both kinetically and energetically.<sup>25, 26</sup> Electronic redistributions of charge upon photoexcitation is one of the key requisites for ESIPT. However, for certain molecules, the electronic redistribution is enhanced, and a large dipole moment is generated in the excited state. This gives rise to a dielectrically stabilized charge-transfer (CT\*) excited state and the reaction leading to this state is referred to as excited state intramolecular charge transfer (ESICT). Molecules exhibiting PCET comprise of both proton accepting and donating moieties as well as electron-donating or accepting groups. The charge and proton transfer processes can occur either simultaneously or in a step-wise manner, and within the latter category, there are two additional possibilities. In the first pathway, ESIPT proceeds instantaneously upon photoexcitation leading to a highly charge-separated enol ( $N^*$ ) state. The subsequent ESIPT ( $N^* \rightarrow T^*$ ) is associated with a strong redistribution of the electronic density and may be subject to a drastic change of the dipole moment. In other words, the ESIPT

generated tautomeric species may have a negligible dipole moment. In the second pathway, ES IPT precedes ES ICT, that is ES ICT does not take place immediately after photoexcitation. Thus, the tautomeric species exists as the charge-transfer state and the enol form is the non charge-transfer state.

As a result of the proton transfer process, the spectral characteristics of PCET molecules are responsive to the hydrogen bond donating and accepting parameters of the surrounding media. However, what sets apart the PCET phenomenon is that in addition to the hydrogen bonding characteristics, the spectral features of the PCET molecules are also heavily dependent on the polarity and the dynamics of the solvent medium (Figure 2.8). The high dipole moment generated in the excited state due to the ES ICT process causes the charge-transfer species to be sensitive to the polarity of the surrounding solvent. While non-polar solvents are unable to stabilise the highly dipolar excited state, polar solvents tend to rearrange themselves around the excited state dipole in such a manner to achieve a stable equilibrium configuration. Thus, the relative energy between the charge-transfer and the non-charge transfer states are modulated by the polarity solvents. Additionally, the solvent polarity induced stabilisation of the charge-transfer state is dictated by the rate at which the solvent molecules reorient themselves, that is, the solvation dynamics. This multiparametric sensitivity of the PCET phenomenon has been exploited in Chapter 5 to characterise the various physical properties of the LLC water molecules as well as distinguish between the effects of solvent polarity and hydrogen bonding.

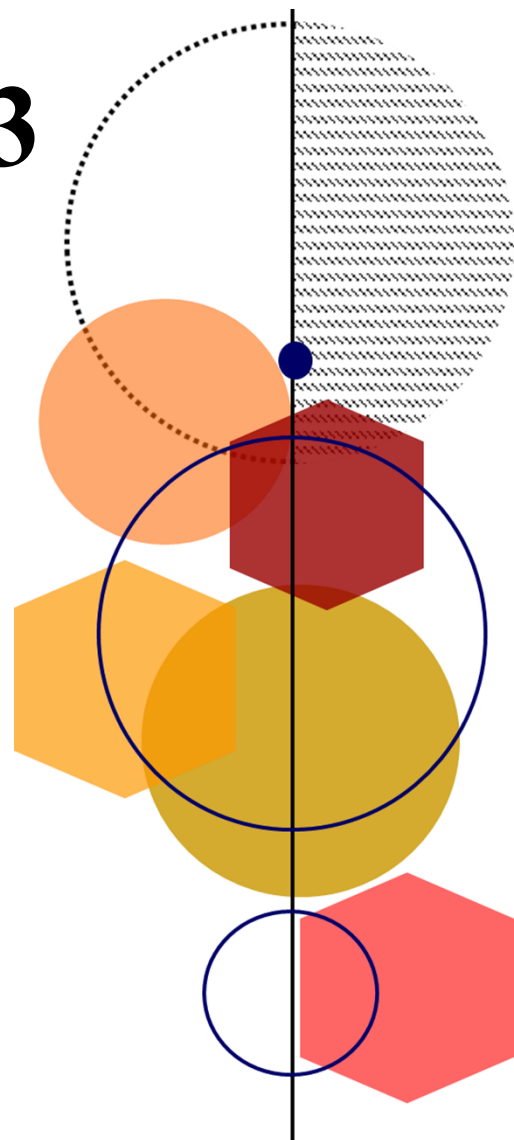
## 2.5 References

1. B. Liu, Y. Pang, R. Bouhenni, E. Duah, S. Paruchuri and L. McDonald, *Chem. Commun.*, 2015, **51**, 11060-11063.
2. I. P. Kerschgens, E. Claveau, M. J. Wanner, S. Ingemann, J. H. van Maarseveen and H. Hiemstra, *Chem. Commun.*, 2012, **48**, 12243-12245.
3. H. Qiu and M. Caffrey, *Biomaterials*, 2000, **21**, 223-234.
4. R. Mezzenga, C. Meyer, C. Servais, A. I. Romoscanu, L. Sagalowicz and R. C. Hayward, *Langmuir*, 2005, **21**, 3322-3333.
5. R. Oldenbourg, in *Biomedical Optical Phase Microscopy and Nanoscopy*, eds. N. T. Shaked, Z. Zalevsky and L. L. Satterwhite, Academic Press, Oxford, 2013, DOI: <https://doi.org/10.1016/B978-0-12-415871-9.00015-6>, pp. 311-338.

6. N. H. S. Hartshorne, A., *Crystals and the Polarising Microscope (A Handbook for Chemists and Others)*, Edward Arnold and Co., London, 1934.
7. R. Oldenbourg, *Cold Spring Harb. Protoc.*, 2013, **2013**, pdb.top078600.
8. O. G. Otto Kratky, *Small Angle X-ray Scattering*, Academic Press Inc., London, 1982.
9. D. I. S. L. A. Feigin, *Structure Analysis by Small-Angle X-Ray and Neutron Scattering*, Springer, United States, 1987.
10. C. V. Kulkarni, W. Wachter, G. Iglesias-Salto, S. Engelskirchen and S. Ahualli, *Phys. Chem. Chem. Phys.*, 2011, **13**, 3004-3021.
11. H. Qiu and M. Caffrey, *J. Phys. Chem. B*, 1998, **102**, 4819-4829.
12. J. R. Lakowicz, *Principles of Fluorescence Spectroscopy*, Springer, Boston, MA, United States, 3rd edn., 2006.
13. B. Valeur, *Molecular Fluorescence: Principles and Applications*, Wiley-VCH Verlag GmbH, 2001.
14. D. P. Desmond V. O'Connor, *Time-Correlated Single Photon Counting*, Academic Press, New York, 1984.
15. R. Jimenez, G. R. Fleming, P. V. Kumar and M. Maroncelli, *Nature*, 1994, **369**, 471-473.
16. N. Nandi and B. Bagchi, *J. Phys. Chem. B*, 1997, **101**, 10954-10961.
17. M. Maroncelli and G. R. Fleming, *J. Chem. Phys.*, 1987, **86**, 6221-6239.
18. C.-L. Chen, Y.-T. Chen, A. P. Demchenko and P.-T. Chou, *Nat. Rev. Chem.*, 2018, **2**, 131-143.
19. M. H. V. Huynh and T. J. Meyer, *Chem. Rev.*, 2007, **107**, 5004-5064.
20. J. Zhao, S. Ji, Y. Chen, H. Guo and P. Yang, *Phys. Chem. Chem. Phys.*, 2012, **14**, 8803-8817.
21. K.-C. Tang, M.-J. Chang, T.-Y. Lin, H.-A. Pan, T.-C. Fang, K.-Y. Chen, W.-Y. Hung, Y.-H. Hsu and P.-T. Chou, *J. Am. Chem. Soc.*, 2011, **133**, 17738-17745.
22. A. Weller, *Naturwissenschaften*, 1955, **42**, 175-176.
23. A. C. Sedgwick, L. Wu, H.-H. Han, S. D. Bull, X.-P. He, T. D. James, J. L. Sessler, B. Z. Tang, H. Tian and J. Yoon, *Chem. Soc. Rev.*, 2018, **47**, 8842-8880.
24. A. S. R. Koti, M. M. G. Krishna and N. Periasamy, *J. Phys. Chem. A*, 2001, **105**, 1767-1771.
25. A. P. Demchenko, K.-C. Tang and P.-T. Chou, *Chem. Soc. Rev.*, 2013, **42**, 1379-1408.

26. C.-C. Hsieh, C.-M. Jiang and P.-T. Chou, *Acc. Chem. Res.*, 2010, **43**, 1364-1374.

# Chapter 3

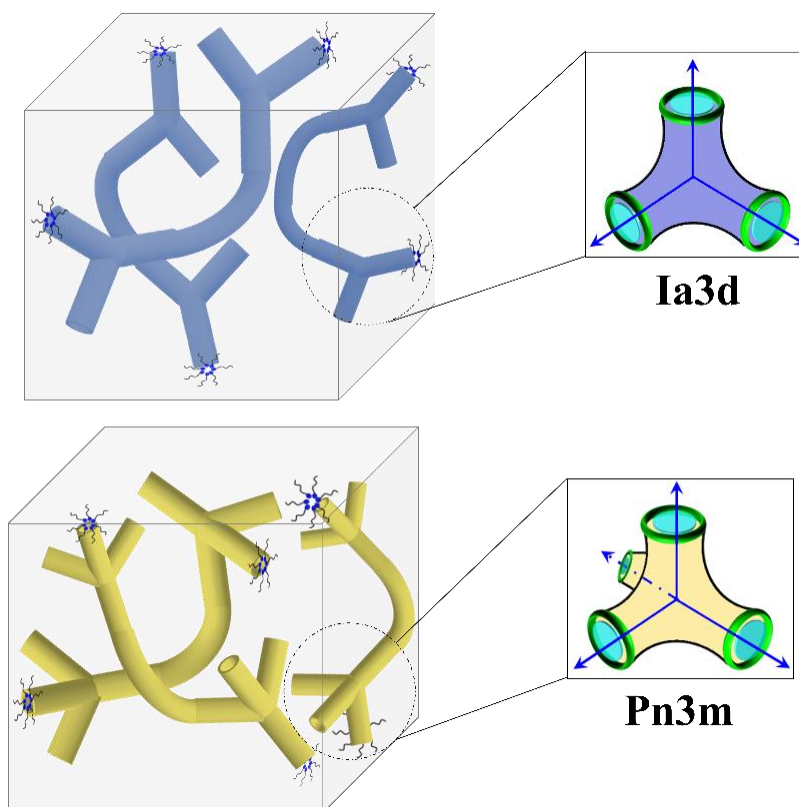


**Impact of Topology on the  
Characteristics of Water  
inside Cubic Lyotropic  
Liquid Crystalline Systems**

### 3.1 Introduction

Lyotropic liquid crystalline (LLC) ‘soft’ materials have emerged as a promising class of substance due to their utilization in a wide range of applications such as platforms for protein crystallization,<sup>1,2</sup> drug and nutrients delivery,<sup>3-5</sup> food technology<sup>6,7</sup> etc. Generally, unsaturated monoglyceride lipids, for instance, glyceryl monooleate (GMO) and monolinoleate (GML) are favoured for the synthesis of LLC mesophases owing to their biocompatibility and exceptional phase behaviour.<sup>8,9</sup> LLC materials of different characteristic topologies and symmetries, such as the tubular 1D inverse hexagonal phase ( $H_{II}$ ), the 2D planar lamellar phase ( $L_{\alpha}$ ) and the 3D bicontinuous cubic phases ( $V_2$ ) have been synthesised by controlling the content of amphiphile or water in the system and the temperature.<sup>10</sup> The fluid lamellar phase consists of amphiphilic bilayers separated by water domains and closely resembles the cellular membranes.<sup>6</sup> The  $H_{II}$  phase is a topologically inverted ‘water in oil’ system comprising of infinitely long and straight water-filled rods packed densely in a non-polar matrix of lipophilic chains.<sup>6,11</sup> The inverse bicontinuous cubic phases namely, gyroid ( $Ia3d$ ) and diamond ( $Pn3m$ ) are formed by the arrangement of a continuous lipid bilayer on mathematical minimal surfaces (Scheme 3.1).<sup>12</sup> <sup>13</sup> In the  $Ia3d$  mesophase, two interpenetrating but unconnected water networks join in a  $3\times 3$  junction at an angle of  $120^{\circ}$  and in  $Pn3m$  they join in a  $4\times 4$  manner at a tetrahedral angle of  $109.5^{\circ}$ .<sup>13</sup> Larsson was the first to suggest that the infinitely periodic continuous structure of the lipid membrane in the cubic phases closely resembles that of lipidic membranes in nature.<sup>14</sup> Consequently, the biological aspects of the cubic phases have garnered significant attention among researchers owing to their roles in membrane fusion, control of membrane protein functions and various intracellular structures of membranes.<sup>15,16</sup> The unique structural features of the cubic phases allow the transport of both hydrophilic and lipophilic targets, and the phases have been utilised extensively for the in vitro and in vivo delivery of drugs and oligopeptides.<sup>17</sup> <sup>18</sup> The cubic phases have also been used to facilitate the crystallization of membrane proteins inside its nanochannels, which do not tend to crystallize in the bulk<sup>1,19,20</sup> and for the detection of viruses and bacteria.<sup>21</sup> The nature of the nanochannels, dynamics of the water molecules and interfacial hydration are proposed to play an important role behind the various functionalities of the cubic LLC phases.<sup>22</sup> These parameters are in turn expected to be influenced by the specific geometrical characteristics of each mesophase. Thus, it is essential to establish a relationship between the structural features of the mesophase and the various fundamental properties of the aqueous LLC domains.

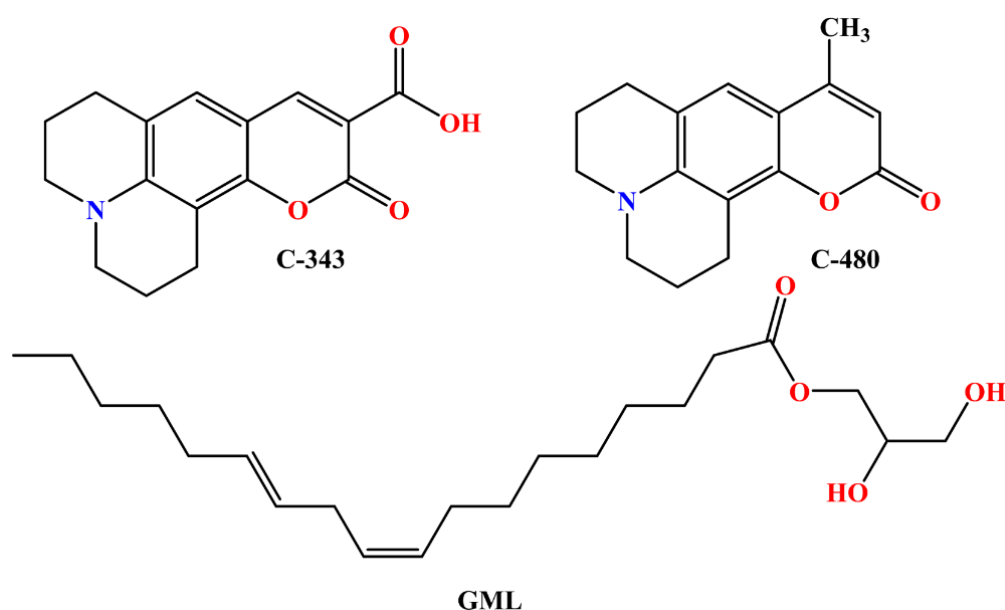




**Scheme 3.1.** Schematic representation of cubic LLC phases (*Ia3d* and *Pn3m*).

Water that is confined in a small volume of supramolecular assemblies is fundamentally different from bulk water.<sup>23, 24</sup> Unravelling the dynamics of water in biologically pertinent assemblies is crucial for understanding the ways in which the confined water influences the structure, reactivity, molecular recognition and dynamics in a biological interface. An important discovery is the two to four-fold slower dynamics of water in restricted assemblies as compared to bulk water.<sup>23, 24</sup> Considering the importance of the aqueous nanochannels of the LLC phases in dictating the macroscopic functionalities of the materials, our group has recently investigated the microenvironment inside the narrow channels of the  $H_{II}$  phase using coumarin-343 probe.<sup>25</sup> The study of solvation dynamics exhibited the existence of two types of water molecules inside the nanochannels. Dielectric relaxation spectroscopic studies of the reverse hexagonal phase corroborate this observation.<sup>26, 27</sup> It was shown that the dynamics of a large percentage of water molecules were slowed down due to interactions with the lipid interface and the remaining water located away from the interface adopts bulk water like behaviour. Importantly, Zhong *et al.* have mapped femtosecond scale hydration dynamics at different depths of the GMO based *Pn3m* cubic mesophase using a series of tryptophan alkyl esters.<sup>28</sup> They have reported three different dynamics denoting discrete water structures,

namely, 100-150 ps for the interfacial water at the lipid surface, 10-15 ps for the adjacent layer of hydrogen-bonded water molecules and < 1 ps for bulk-like water at the centre of the channel. Although tryptophan is an attractive solvation probe, it can only be used to detect ultrafast solvation components because of the existence of two rotamers having different lifetimes giving rise to an apparent dynamic spectral shift in a few hundred ps timescale.<sup>29</sup> Consequently, the major slow hydration components of the confined water remain undetected in the cubic LLC phases. In addition, the correlation of the structural disparities between the two cubic phases, *Ia3d* and *Pn3m*, to the behaviour of water molecules confined in the nanochannels has not been explored. It has been a general trend to group together the different bicontinuous cubic phases in terms of the properties of their nanoscopic domains and their macroscopic functionalities. However as the intrinsic nanoscopic structural aspects of the two cubic phases are quite different, it is of critical interest to determine whether the behaviour of the aqueous nanochannels in the two phases are similar or different from each other.



**Scheme 3.2.** Chemical structures of coumarin-343 (C-343), coumarin-480 (C-480) and 1-Linoleoyl-rac-Glycerol (GML).

Inspired by the relevance of the LLC water networks and the need for a detailed description regarding any differences between the behaviour of the aqueous nanochannels of the cubic mesophases, we have probed the dynamics of the confined water molecules by the time-dependent Stokes shift technique. In order to probe the dynamics of the water molecules localised at the different depths of the nanochannels, we have selected two polarity sensitive

coumarin probes (Scheme 3.2), namely, coumarin 343 (C-343) and coumarin 480 (C-480), with varying hydrophobicities. We have qualitatively assessed the micropolarity of the various water layers in the two phases by utilizing the sensitive solvatochromic behaviour of the coumarin molecules. We have also for the first time, quantitatively measured the microviscosity at different regions of the nanochannels by time-resolved fluorescence anisotropy. The experimental observations underline the substantial differences in the microviscosity for the two similar cubic phases. Although previously the two cubic phases have been considered to be similar in nature, our observations highlight that the behaviour of water in the nanochannels are essentially different in the light of their hydration dynamics and viscosity. We believe these new insights will help to boost the wide-scale applications of these phases in different fields.

## 3.2 Results and Discussion

### 3.2.1 Steady State Emission Study

The prepared mesophases were first characterised by small angle X-ray spectroscopy (SAXS) measurements (Figure 3A.2), before carrying out any of the fluorescence spectroscopic experiments. Steady state emission spectroscopy has been utilised to probe the location and microenvironment of the coumarin dyes inside the water nanochannels of the cubic LLC phases. In general, it has been observed that the local micropolarity and dielectric constant vary considerably in different regions of self-assembled systems.<sup>30-32</sup> Consequently, in order to map the polarity and microenvironment at different depths of the water channels in the *Ia3d* and *Pn3m* cubic LLCs, we have selected two coumarin probes (C-343 and C-480) of varying hydrophobicity. Structurally, C-480 is more hydrophobic in nature than C-343, as a methyl group in the former molecule replaces the carboxyl moiety in C-343. C-343 exhibits an emission maximum at ~490 nm in aqueous solution, which gets blue-shifted by 12 nm in the *Pn3m* phase (Figure 3.1(a)) and by ~10 nm in the *Ia3d* mesophase (Figure 3A.3 (a)). This blue shift in the emission maximum denotes that the probe experiences a markedly less polar environment when confined inside the LLC phases as compared to bulk water.<sup>33</sup> On the other hand, C-480 exhibits an emission peak at ~465 nm in both *Pn3m* (Figure 3.1(b)) and *Ia3d* (Figure 3A.3 (b)) phases, which is almost 23 nm blue-shifted compared to its characteristic emission maximum ( $\lambda_{em} = 488$  nm) in bulk water. The larger extent of blue shift in the emission peak of C-480 compared to C-343 suggests that the C-480 molecules reside at more hydrophobic depths of the aqueous nanochannels. Here it is pertinent to mention that, the

coumarin probes are well-known for their sensitive solvatochromic behaviour.<sup>34, 35</sup> Thus, they have been employed to qualitatively assess the micropolarity inside the different layers of the LLC nanochannels based on their emission properties in bulk solvents with known polarity. The emission maximum of C-343 in the cubic phases is similar to that in ethylene glycol<sup>36</sup> and that of C-480 in the LLCs is close to the emission maximum in ethanol.<sup>37</sup> Thus, the lower micropolarity probed by C-480 compared to C-343 reflects that C-480 molecules have a higher affinity to localise deeper inside the LLC nanochannels, at the lipid-water interface, than C-343. Importantly, the close proximities of the emission maxima in both the *Ia3d* and *Pn3m* mesophases for the two probes infer that the dyes are residing in comparable regions in the two phases and the local polarities of both the cubic phases are not significantly different.

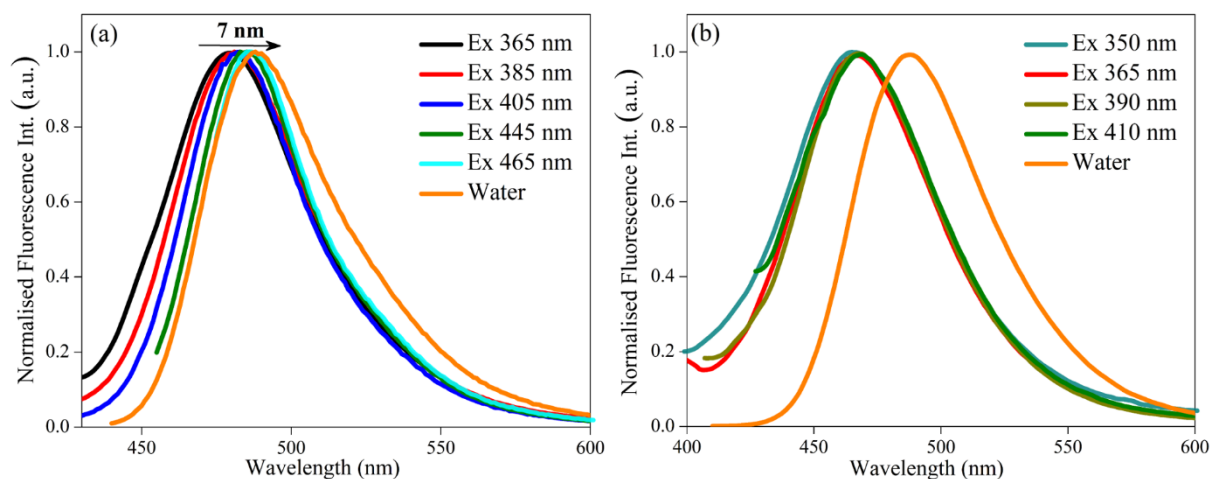


**Figure 3.1.** Excitation dependent emission spectra of (a) C-343 and (b) C-480 in the *Pn3m* phase. The arrow in (a) depicts the redshift in emission with excitation wavelength. The intensities have been normalised to 1.0 by dividing with the highest intensity of each spectrum.

The phenomenon of red edge excitation shift (REES) is an excellent tool to estimate the surrounding microheterogeneous environment perceived by the probes in the excited state inside the aqueous LLC nanochannels. A shift in the emission maxima towards lower energy on changing the excitation wavelength to the red side of the absorption band is termed as the red edge excitation shift (REES).<sup>38, 39</sup> A REES value of 7 and 5 nm were observed for C-343 in *Pn3m* (Figure 3.1(a)) and *Ia3d* (Figure 3A.3 (a)) phases, respectively, stipulating that the probe molecules are distributed over regions of varying polarity inside the nanochannels. Wavelengths near the ‘blue edge’ of the absorption spectra selectively excite the C-343 molecules that are residing in the relatively less polar regions near the lipid headgroup-water interface, whereas excitations at the ‘red end’ of the absorption spectra are responsible for the emission from the probe molecules in the polar central region of the nanochannel. Interestingly,

the emission wavelength in the case of C-480 remained unchanged regardless of the excitation wavelength in both the cubic phases (Figure 3.1(b) and Figure 3A.3 (b)). The absence of such excitation wavelength dependence on emission is a sign of homogeneous dielectric environment around the probe molecule. From the REES studies and polarity estimation it can thus be concluded that the C-480 molecules are mainly localised within the interfacial layer of the nanochannels, while the C-343 molecules are inhomogeneously distributed from the central aqueous core towards the interfacial region of the LLC nanochannels. The observed preferential localisation of the two coumarin probes at different regions of the nanochannels will be useful to elucidate the dynamics of the water networks at various layers of the LLC channels.

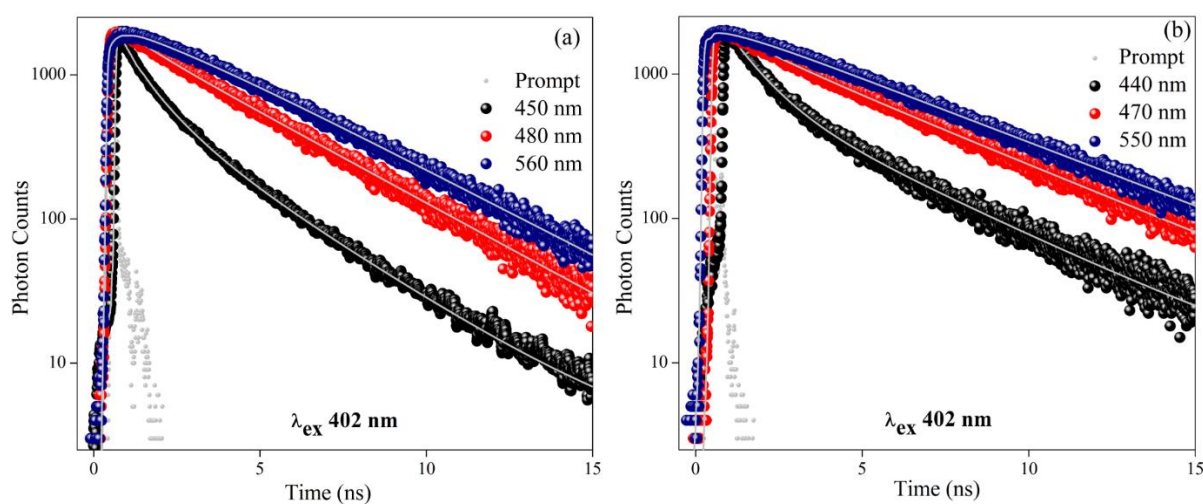


**Figure 3.2.** Lifetime decay profiles of (a) C-343 and (b) C-480 in the  $Pn3m$  phase at different emission wavelengths ( $\lambda_{ex}=402$  nm).

### 3.2.2 Hydration Dynamics of the Cubic LLC Phases

To study the dynamics of water inside the nanochannels of LLC, fluorescence lifetime decays were collected for C-343 and C-480 in both cubic phases over a series of collection wavelengths by exciting at 402 nm (Figure 3.2 and Figure 3A.4). Both the coumarin probes display an emission wavelength-dependent fluorescence decay characteristics inside the LLC mesophases. Lifetime transients collected at the blue end of the emission spectrum exhibit a fast decay and at longer wavelengths the transients comprise of a distinct growth followed by a slow decay. The fast decay at the shorter wavelengths generally represents the fluorescence from unsolvated dipoles created on the photoexcitation of the probe molecules. The appearance of the negative pre-exponential at longer wavelengths corresponds to the relaxation process of the excited state coumarin dipole by the surrounding solvent molecules. Notably, in both the

cubic phases, the decay transients of C-343 fit to a triexponential function, exhibiting two rise components at longer wavelengths, but transients of C-480 exhibit biexponential nature with only one rise component at longer wavelengths. This implies that C-343 molecules possibly probe two classes of water dynamics inside these mesophases contrary to C-480, which senses only one kind of water dynamics inside the nanochannels. This gives further support regarding the hypothesised location of the probe molecules in the nanochannels.

The time-resolved emission spectra (TRES) have been constructed by following the method given by Flemming and Maroncelli (Figure 3.3 and Figure 3A.5).<sup>40</sup> The hydration dynamics of C-343 and C-480 in the *Pn3m* and *Ia3d* phases have been evaluated by calculating the solvent correlation function from the peak frequencies obtained by the log-normal fitting of TRES. The solvent correlation function is defined as,

$$C(t) = \frac{\nu(t) - \nu(\infty)}{\nu(0) - \nu(\infty)} \quad (3.1)$$

where  $\nu(0)$  is the peak frequency at time,  $t=0$  when the electronic excitation of the probe occurs,  $\nu(t)$  is the peak frequency at any other time  $t$  and  $\nu(\infty)$  is the peak frequency at infinite time when the solvent relaxation process has been completed. The decay of  $C(t)$  with time ( $t$ ) for C-343 in both the cubic phases is fit to a triexponential function,

$$C(t) = \alpha_1 e^{-t/\tau_1} + \alpha_2 e^{-t/\tau_2} + \alpha_3 e^{-t/\tau_3} \quad (3.2)$$

here,  $\tau_1$ ,  $\tau_2$  and  $\tau_3$  are the hydration components with amplitudes  $\alpha_1$ ,  $\alpha_2$  and  $\alpha_3$  respectively. The decay features and fitting parameters of  $C(t)$  are provided in Figure 3.4 and Table 3.1, respectively. The average hydration time of C-343 in the *Pn3m* phase is 4.3 ns with the individual components being 140 ps (22%), 990 ps (40%) and 10.30 ns (38%). Importantly, the overall average hydration time ( $\sim 5$  ns) of C-343 in the *Ia3d* phase is slower than that in the *Pn3m* phase and consists of individual hydration components with time scales 164 ps (27%), 1.24 ns (40%) and 13 ns (33%). In contrast to the triexponential nature of the  $C(t)$  decay for C-343, the C-480 probe exhibits a biexponential behaviour. The average hydration time of C-480 in *Pn3m* is 3.3 ns with individual components  $\sim 880$  ps (70%) and 9 ns (30%). The dynamics of C-480 in the *Ia3d* phase slows down appreciably, the average hydration dynamics being  $\sim 5.5$  ns with individual components of 1 ns (71%) and 16 ns (29%). It is noteworthy to mention here that using our TCSPC setup we are missing the initial inertial hydration components ( $<50$

ps) such as the librational and intermolecular vibrational relaxations.<sup>41</sup> The missing components have been calculated by using the method proposed by Fee and Maroncelli (detailed discussion and related parameters have been provided in the [Appendix](#)).<sup>42, 43</sup> The percentage of the missing components using C-343 are found to be 22% and 23%, respectively, for the *Ia3d* and *Pn3m* phases. Because the absorption spectra of C-480 in nonpolar solvents are not structureless, the reliability of the missing component obtained from C-480 is questionable according to Fee and Maroncelli,<sup>42</sup> hence, the missing components have been calculated using only C-343.

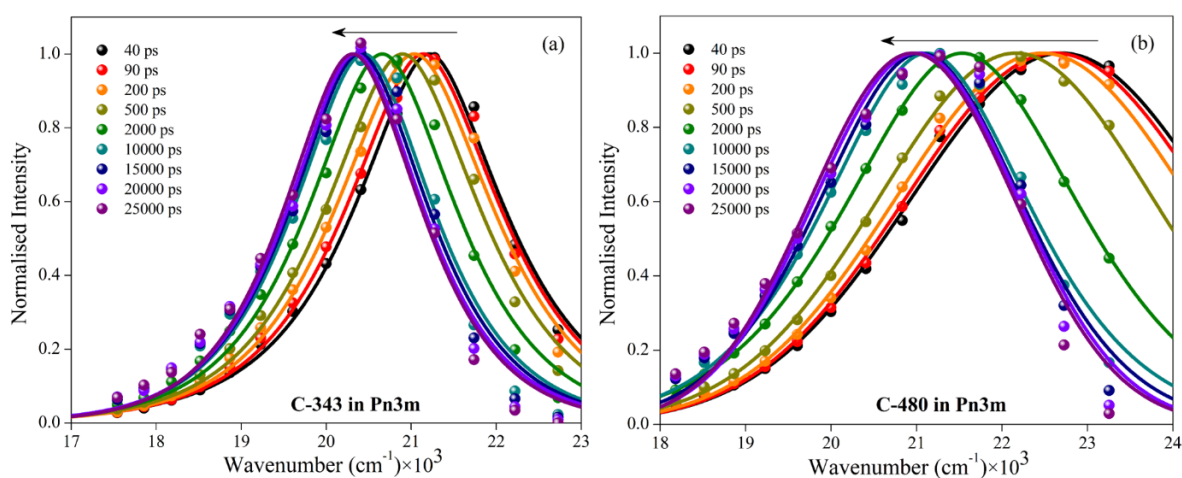


**Figure 3.3.** Time-resolved emission spectra (TRES) of (a) C-343 and (b) C-480 in the *Pn3m* phase. The arrow indicates the time-dependent Stokes shift. The fluorescence intensities have been normalised to 1.0 by dividing with the highest intensity of each spectrum.

The three distinct hydration dynamics observed for C-343 in *Pn3m* and *Ia3d*, clearly point out the discretely different water networks in the nanochannels of the cubic phases. It is important to note here that, even the fastest component ( $\sim 150$  ps) in both the phases is much slower compared to the dynamics of bulk water which is around 1 ps,<sup>40, 41</sup> connoting that the aqueous networks inside the restricted environment of LLC phases are significantly different than bulk water. Previous solvation studies inside other confined assemblies by MD simulations,<sup>44</sup> small angle neutron scattering (SANS),<sup>45</sup> dielectric relaxation spectroscopy<sup>46</sup> and nuclear magnetic resonance<sup>47</sup> studies establish that the translational diffusion coefficients of confined water are 2-6 times slower than those observed in bulk water. The appreciable retardation in the dynamics of water molecules in the LLC phases is anticipated to arise due to hydrogen bonding with the polar headgroups of the lipid molecules at the lipid-water interface. Notably, it has been seen that, the  $\gamma$ -hydroxy groups of the lipid are projected inwards to the nanochannels and are involved in hydrogen bonding with the interfacial water molecules, thus

restricting their mobility.<sup>27</sup> It has been reported that the hydrogen bonds between water molecules and the polar headgroup of the lipid are stronger by 4 kJ mol<sup>-1</sup> than the hydrogen bonds between two water molecules in bulk water.<sup>48</sup> Additionally, the water molecules at the immediate periphery of the lipid-water interface in turn also bind with the water molecules of the adjacent hydration shell and this domino effect is responsible for the slow hydration dynamics of each water layer, with the effect gradually decreasing towards the central core of the nanochannel. Thus, the water molecules at the central core of the nanochannels are perturbed to a minimum extent and they are expected to exhibit bulk water like dynamics (~1 ps). It is important to note here that several layers of bound water can exist where the water molecules at the immediate vicinity of the lipid layer have the maximum rigidity. On the basis of the above reasoning, the fast (~ 150 ps) component observed in both the phases is assigned to the dynamics of ‘pseudo-bound’ water. The observed intermediate (~ 1 ns) dynamics in *Ia3d* and *Pn3m* phases is ascribed to ‘trapped/bound’ water molecules buried in the lipid headgroup region due to lipid fluctuation. Another plausible cause for the slow hydration component is the slow self-diffusion of the probe from the less polar regions (near the lipid-water interface) to the more polar regions (at the central core) of the nanochannels.<sup>23, 49</sup> The origin of the ultraslow hydration component observed for C-343 in the two phases poses a unique question as the time scale of the component is too slow to correspond solely to water dynamics inside the aqueous channel. In fact, this kind of ultraslow dynamics (> 5 ns) has also been observed in other organised assemblies such as microemulsions,<sup>50</sup> micelles<sup>51</sup> and proteins.<sup>24</sup> Although the bimodal dynamic exchange model<sup>52, 53</sup> satisfactorily explains the slow component contribution ( $\geq 1$  ns), it is inadequate to explain this ultraslow component (~ 10 ns). The plausible reason for the origin of the ultraslow solvation component that has been put forward by Bagchi *et al.* is the role of the macromolecular chain dynamics.<sup>49</sup> They conceptualize that following the creation of the probe dipole, which is buried in the lipid bilayer, the neighbouring water molecules need to reorient to minimize the energy. This involves not only the rotation of the water molecules but also the ‘breathing’ motion of the associated surfactants. Thus, a possible cause for the ultraslow component in the LLC phases is the small amplitude ‘breathing’ motion of the lipid headgroup. Notably, the contribution of large amplitude motion of the lipid headgroups can be eliminated as they occur in a longer time scale (~ 100 ns).<sup>54</sup>



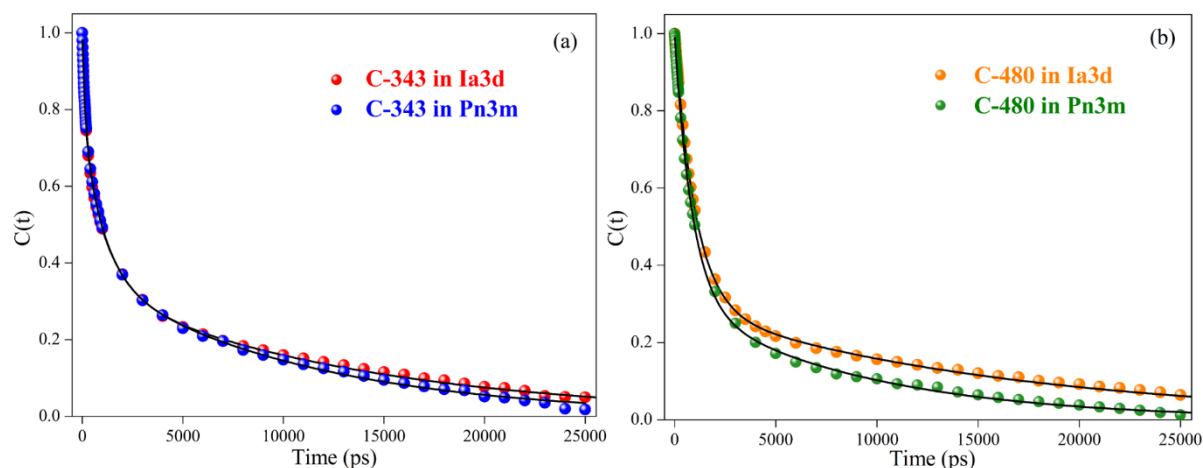


**Figure 3.4.** Solvent response function ( $C(t)$ ) of (a) C-343 and (b) C-480 in *Pn3m* and *Ia3d* LLC phases.

**Table 3.1.** Decay parameters of  $C(t)$  of C-343 and C-480 in *Pn3m* and *Ia3d* phases.

Sample	$\alpha_1$	$\tau_1$ (ns)	$\alpha_2$	$\tau_2$ (ns)	$\alpha_3$	$\tau_3$ (ns)	$\langle\tau_s\rangle^{a,b}$ (ns)
C-343 in <i>Pn3m</i>	0.22	0.14	0.40	0.99	0.38	10.3	4.31
C-343 in <i>Ia3d</i>	0.27	0.16	0.40	1.24	0.33	13.3	4.93
C-480 in <i>Pn3m</i>	-	-	0.70	0.88	0.30	9.13	3.35
C-480 in <i>Ia3d</i>	-	-	0.71	1.03	0.29	16.5	5.54

$$^a \langle\tau_s\rangle = \alpha_1\tau_1 + \alpha_2\tau_2 + \alpha_3\tau_3$$

$$^b \pm 10\%$$

C-480 exhibits biexponential hydration dynamics in contrast to C-343, with individual components  $\sim 880$  ps (70%) and 9 ns (30%) in *Pn3m* and  $\sim 1$  ns (71%) and 16 ns (29%) in the *Ia3d* phase (Table 3.1). It is evident from the hydration dynamics components of C-480 that the probe is unable to map the dynamics of ‘pseudo-bound’ water in the central part of LLC nanochannels of both the phases, which was probed by the more hydrophilic C-343 molecule ( $\sim 150$  ps). Thus, the observed dynamics suggest that the dynamics ( $\sim 1$  ns) of the ‘bound water’ molecules buried in the lipid headgroup region and the cooperative motions of the lipid headgroups ( $> 10$  ns) are probed by the C-480 molecules. This observation concurs with the steady state results, where the more hydrophobic C-480 probe is deemed to reside at the deeper layers of the nanochannels, and hence, the contribution of the ‘pseudo-bound’ water layers are absent in the components of hydration dynamics of this probe. Notably, the self-diffusion of

C-480 has a significant contribution towards the slower hydration dynamics in both *Ia3d* and *Pn3m* phases, which is reflected from the appreciable decrease in the FWHM of the TRES profiles at longer times. Additionally, the hydration dynamics slows down significantly in the *Ia3d* phase in comparison with the *Pn3m* phase. Although this has also been observed for C-343, the effect is more highlighted for the C-480 probe. An important point to note here is that the dynamics of the bulk-like water is very similar in both *Ia3d* and *Pn3m* phases and the difference in the hydration dynamics between the two phases arises mainly at the longer time scales.

While it is crucial to understand and assign the different categories of water molecules in the nanochannels, the principal motivation of this work is to interpret the differences in the microenvironment and hydration dynamics of the two cubic phases, *Ia3d* and *Pn3m*. We anticipate that the curvature of the lipid bilayers as well as the geometry of the phases is the key to rationalise the observed differences of the water dynamics between the *Ia3d* and *Pn3m* nanochannels. According to the bimodal theory of the dynamic exchange between the ‘bound’ and ‘free’ water molecules,<sup>52, 53</sup> inter-conversion between these molecules is the rate-determining step in solvation dynamics, which is governed by the diffusion of the water molecules. Here, it is assumed that the ‘free water molecules’ are free to rotate and the ‘bound water molecules’ can rotate only in restricted cooperation with the binding system. In the *Ia3d* phase, the two water channels have trifold connectivity ( $120^\circ$ ) whereas the *Pn3m* phase has tetrafold connectivity ( $109.5^\circ$ ).<sup>55</sup> From these geometrical characteristics of the two phases it can be reasoned that the tetrahedral connection angle of the water channels in the *Pn3m* phase would provide a faster pathway for the diffusion of ‘free/pseudo-bound’ water molecules compared to the trifold connected channels of the *Ia3d* phase, leading to a slower water dynamics in the latter phase. Apart from the diffusion-controlled exchange of bound and free water molecules, the slow hydration component has also been determined to arise from the self-diffusion of the probes, particularly for C-480. It is expected that the diffusion of the probe is also more facile in the water channels of *Pn3m* phase from the topologic features of the phases. This behaviour has also been mirrored in the literature-report of diffusion-controlled enzyme kinetics in the LLC matrices.<sup>56</sup> It is seen that at the same channel size, the tetrafold geometry of *Pn3m* provides the fastest diffusion of substrates to the entrapped enzymes active sites, and subsequent products also diffuse away fastest, due to the tetra-fold connectivity.<sup>56</sup> On the other hand, some recent reports suggest that the diffusion of point-like molecules will be faster in the *Ia3d* phase compared to *Pn3m* owing to the lesser presence of bottlenecks in

the former structure.<sup>57, 58</sup> Notably, from the results, it is evident that the dynamics of pseudo-bound water molecules are very similar in both *Ia3d* (0.16 ns) and *Pn3m* (0.14 ns) indicating that the diffusion behaviour for these water molecules in both the phases is similar. Consequently, for the prepared *Pn3m* and *Ia3d* phases at the same water content (22%), the effect of water nanochannel connectivity leading to a difference in the hydration dynamics between the two phases is minimum. We have also calculated the radius of the water nanochannels of both these phases (from the diffraction peaks of SAXS depicted in the [Appendix](#)), which lies in the range 2 nm - 2.3 nm. The larger radius of the water nanochannels compared to the size of the water molecules also concurs with the observed minimum differences in the dynamics of the pseudo-bound water molecules in the two phases. Thereby, it can be concluded the overall slower hydration dynamics in the *Ia3d* phases compared to *Pn3m* arises from some other structural factors rather than the water channel connectivity or radius of the two phases. The differences in the hydration dynamics of the two cubic phases are majorly observed in the third component (small amplitude motion of lipid head groups) and to a lesser extent in the second component (water molecules trapped in the lipid bilayer region). This implies that the differences in *Pn3m* and *Ia3d* mainly arises from the geometrical aspects of the lipid-water interface region.

In this regard, a salient feature is that the two cubic phases have subtle differences in their structural aspects with respect to the curvature elastic energy and the hydrophobic packing stress. The inverse bicontinuous cubic phases (*Ia3d* and *Pn3m*) having negative interfacial curvature (wherein the hydrophilic/hydrophobic interface curves towards the hydrophilic domain) are composed of a single continuous lipid bilayer draped on a minimal surface.<sup>59</sup> The lipid bilayers have been simplistically considered as an infinitely thin elastic surface where the curvature elastic energy is the energy cost associated with deformations of the surface by changing the mean or Gaussian curvature.<sup>59</sup> The hydrophobic packing stress is defined as the energy penalty required for deforming the lipid chain away from its preferred average shape.<sup>60</sup> The packing stress, the curvature elastic energy and negative curvature follow the order, *Ia3d* > *Pn3m*.<sup>15,61</sup> From the nanochannel radius calculations as well, it is evident that the *Pn3m* phase will have a higher negative value of Gaussian curvature as the two quantities are inversely related.<sup>57, 58</sup> Consequently, compared to *Ia3d*, in *Pn3m* the spontaneous curvature of the lipid bilayer towards water region decreases. This connotes that the hydrophilic headgroups of the lipid molecules that are facing towards the channels are more closely packed in the *Ia3d* phase than those in the *Pn3m* phase. This leads to a higher restriction in the rotational mobility

of the hydrophilic headgroups of the lipid molecules in the *Ia3d* phase compared to the *Pn3m* phase. This is evident in the increased value of the ultraslow component ( $>10$  ns), which is due to the slow amplitude motion of lipid headgroups, in the *Ia3d* phase in comparison with the *Pn3m* phase for both C-343 and C-480. Notably, the effect was more apparent for the C-480 probe, which is preferentially localised near the lipid regions than the C-343 probe due to its higher hydrophobicity. As a result, the motion of the lipid polar groups probed by C-480 in the *Pn3m* phase, which was  $\sim 9$  ns, slowed down significantly to  $\sim 16$  ns in *Ia3d* phase. Importantly, the curvature of the polar headgroups in turn also hinders the mobility of the water molecules bound to them (intermediate hydration component). It has been previously observed that, in systems with higher curvature, a water molecule in the periphery cannot have simultaneous favourable interactions with all of the polar headgroups near it, which increases the energy barrier leading to slower dynamics of the bound/trapped water molecules. This kind of topological effect termed as ‘curvature-induced frustration’,<sup>62</sup> is more pronounced in the *Ia3d* phase than the *Pn3m* phase, leading to the overall slower hydration dynamics in the *Ia3d* phase.

To sum up the results of hydration dynamics, we have used two coumarin molecules of ranging hydrophobicities to probe the dynamics of water at different layers in the aqueous nanochannels of cubic LLC phases. C-343 exhibits fast, slow and ultraslow hydration components whereas C-480 only shows the latter two components. It is noteworthy to mention here that we have previously reported the solvation dynamics of C-343 in the  $H_{II}$  LLC phase at the same water content and solvation components of similar time scales were obtained. We have anticipated the existence of two classes of water molecules in the nanochannels, where one hydration shell comprises water molecules bound to the hydroxyl groups of the lipid. The cooperative motions of the lipid molecules slow down the translational and rotational motions of these bound water molecules and are accountable for the slow hydration dynamics. Another hydration shell comprises of the ‘pseudo-bound’ water and is responsible for the fast dynamics. These water molecules are hydrogen-bonded to the bound water molecules, which causes a restriction in their motion and hence, they exhibit slower dynamics compared to bulk water. The ultraslow component is attributed to the small amplitude motion of the lipid headgroups. The dynamics of the ‘pseudo-bound’ ( $\sim 150$  ps) water detected in our case is similar to the slowest component observed by Zhong *et al.* in the *Pn3m* phase which they had attributed to one of the layers of bound water.<sup>28</sup> However, since tryptophan is unsuitable for detecting nanosecond dynamics, the contributions of the slow and ultraslow components have been missed in their study. Although the various aspects such as basicity of water confined in the

nanochannels,<sup>22</sup> structure-temperature relationship<sup>25, 27</sup> surfactant dependent packing stress *etc.*<sup>16</sup> of the different LLC phases have been documented, there is a stark lack in the comparison between the two cubic LLC phases, *Ia3d* and *Pn3m* in terms of the properties of the water molecules confined in the nanochannels. Considering the crucial applications of the two different cubic phases based on their nanochannels<sup>1, 17, 18, 20, 21</sup> we have explored hydration dynamics in the *Ia3d* and *Pn3m* phases and elucidated in details the influence of curvature topology and geometry on the differences in the observed water dynamics between the two phases.

### 3.2.3 Time-Resolved Fluorescence Anisotropy Study

The observed evidence of diverse water networks inside the LLC phases suggests that the local viscosities in the various regions of the nanochannels may also differ. In this regard, time-resolved fluorescence anisotropy measurement is considered to be an efficient technique to estimate the mobility of the probe molecule and hence predict its surrounding microviscosity (Figure 3.5, Table 3.2). Both from the steady state and the hydration dynamics studies, it is apparent that C-480 is largely localized near the hydrophobic interfacial regions of the channels whereas, C-343 is more evenly distributed in the nanochannels of the LLCs. Thus, the rotational diffusion time constants of C-343 is expected to provide more thorough information regarding the microviscosity at various depths in the aqueous channels of the LLC phases. Subsequently, we have carried out the time-resolved anisotropy measurements of C-343 in both the cubic phases, *Ia3d* and *Pn3m*, in order to understand the differences in the microviscosities experienced by the coumarin probe as a result of the geometrical architecture of the mesophases. The anisotropy transients of C-343 in both *Pn3m* and *Ia3d* phases exhibit triexponential decay with fast (~120 ps), intermediate (~ 1 ns) and slow nanosecond (~ 3 ns) components. Here, it is necessary to mention that the rotational relaxation of C-343 in bulk water occurs at ~ 130 ps time scale. Thus, the observed fast ~125 ps time constant in the LLC phases suggests the rotational motion of the probe in the central part of the water channels, where the water exhibits a bulk-like behaviour. The ~ 1 ns component in both the phases is believed to be originated from the rotational relaxation of the C-343 molecules that are partitioned in the region between the central ‘water pool’ and the ‘lipid-water interface’. The observed slowest rotational relaxation component is credited to the coumarin probe partitioned near the lipid-water interface regions of the nanochannels. The C-343 molecules in this region can take part in hydrogen bonding with the polar headgroups of the lipid and also with the

‘bound water’ molecules, which effectively hinders the mobility of the probe molecule. The slower rotational relaxation times of C-343 in the *Ia3d* phase compared to the *Pn3m* phase highlights the retarded mobility of the C-343 molecules due to the geometrical restrictions of the former phase, such as, higher negative curvature of the lipid bilayer towards the water domains, higher curvature elastic energy as well as the hydrophobic packing stress, which have been discussed in details in the previous section. The retarded relaxation dynamics in the *Ia3d* phase points towards a higher microviscosity faced by the C-343 molecules in the *Ia3d* nanochannels owing to the stiffness rendered to the water layers as a result of their restricted mobility. The microviscosity in the different regions of the aqueous nanochannels of the two cubic phases has been estimated by the Debye-Stokes-Einstein equation,<sup>63</sup>

$$\eta = \frac{\tau_r k_B T}{V} \quad (3.3)$$

where  $\tau_r$  is the rotational relaxation time obtained experimentally,  $k_B$  is the Boltzmann constant,  $T$  is the temperature in Kelvin scale and  $V$  is the volume of the probe molecule (considering a radius of 5.20 Å for C-343, refer to [Scheme 3A.1](#) in [Appendix](#)).

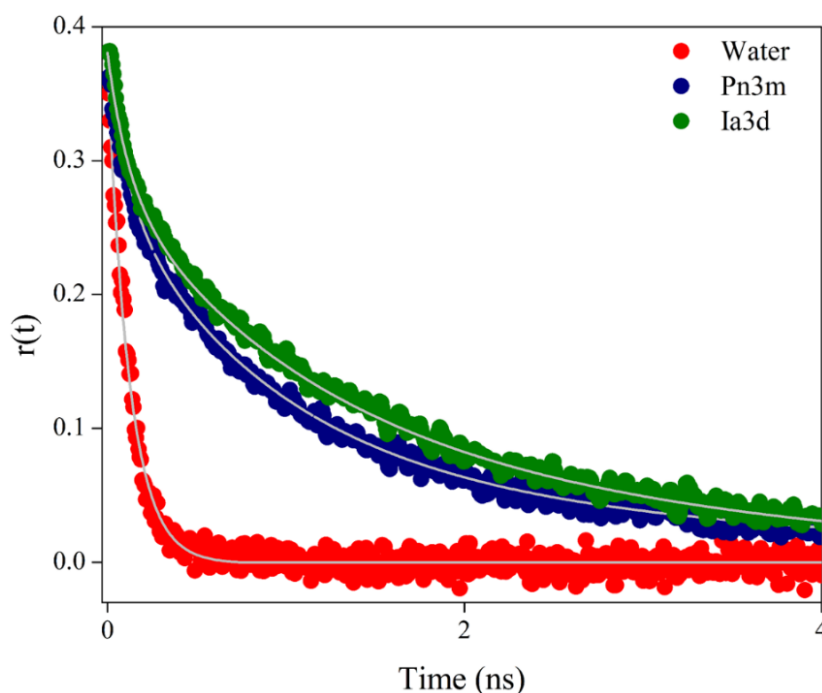


**Figure 3.5.** Time-resolved anisotropy measurements C-343 in both *Pn3m* and *Ia3d* phase. ( $\lambda_{\text{ex}} = 402$  nm and  $\lambda_{\text{em}} = 490$  nm)

**Table 3.2. Rotational relaxation dynamics parameters of C-343 in *Pn3m* and *Ia3d* phases.**

Medium	$r_0$	$\alpha_1$	$\tau_1$ (ns)	$\eta_1$ (cP)	$\alpha_2$	$\tau_2$ (ns)	$\eta_2$ (cP)	$\alpha_3$	$\tau_3$ (ns)	$\eta_3$ (cP)
Water	0.37	1.0	0.130	0.91	-	-	-	-	-	-
<i>Pn3m</i>	0.38	0.26	0.125	0.87	0.54	0.900	6.30	0.20	2.86	20.00
<i>Ia3d</i>	0.38	0.25	0.130	0.91	0.45	1.10	7.70	0.30	3.30	23.10

Using the fast-rotational relaxation time ( $\sim 130$  ps) of C-343, the calculated microviscosity for *Pn3m* and *Ia3d* phases turns out to be 0.87 and 0.91 respectively, which is close to the micro-viscosity sensed by C-343 in bulk water, implying the existence of ‘bulk water’ like region inside the central core of the nanochannels. The microviscosity calculated using the  $\sim 1$  ns rotational time constant is found to be 6.30 cP for *Pn3m* and 7.70 cP for *Ia3d*. This depicts the microviscosity sensed by C-343 molecules in the regions intermediate between the central ‘water pool’ and the lipid-water interface of the cubic nanochannels. The microviscosity in the interfacial regions of the nanochannels have been calculated from the slowest component, with the interfacial regions of *Ia3d* exhibiting a higher microviscosity (23.10 cP) than *Pn3m* (20.0 cP). Two plausible factors can be put forth to explain the high microviscosity of the water confined in the LLC nanochannels, one being the different hydrogen-bonded structure of the water in a confined geometry as compared to that of bulk. The other contributing factor is the hydrogen bonding between the water molecules and the  $\gamma$ -hydroxy groups of the lipid which is mainly responsible for the drastic  $> 20$ -fold increase in the microviscosity of the interfacial water compared to bulk water. This kind of bonding causes a certain ‘stiffness’ to the water molecules, which has also been previously reported for other gel-like materials.<sup>64</sup> In a nutshell, time-resolved fluorescence anisotropy studies provide insight into the existence of a microviscosity gradient inside the LLC phases, which is attributed to the variation of hydrogen-bonded networks inside the nanochannels.

### 3.3 Conclusion

The rationale behind this work was to elucidate the influence of the topology of the two cubic phases, *Ia3d* and *Pn3m*, on the distinct natures of their respective nanochannels with regards to micropolarity, microviscosity and the hydration dynamics. From the steady state fluorescence and REES studies of two coumarin probes (C-343 and C-480), it is clear that

hydrophobicity of the probes controls their distributions inside the nanochannels. The hydrophobic C-480 is lodged homogeneously near the less polar lipid headgroups, whereas C-343 is inhomogeneously distributed across the entire depth of the nanochannels. This gives an estimate of the micropolarity of the lipid-water interface as similar to ethanol and that of the more polar central core as like ethylene glycol. Utilising the preferential locations of the molecules, we have probed the hydration dynamics of the mesophases where the ultraslow component has been ascribed to the small amplitude motion of the lipid headgroups. The slow component is assigned to the restricted motion of the water molecules bound to the hydrophilic headgroups and the fastest component to the ‘pseudobound’ water molecules that are hydrogen-bonded to the bound water molecules. Previously reported hydration dynamics for the *Pn3m* phase did not include any slow components ( $> 150$  ps), and more importantly any comparison with the other cubic phases was completely absent. The principal importance of this work lies in the observation that the hydration dynamics of the bound water and the motion of the lipid headgroups is significantly slower in the nanochannels of the *Ia3d* phase than the *Pn3m* phase and this is credited to the subtle differences in topology and other geometrical aspects of the aqueous channels. The greater negative curvature of the lipid layer, higher curvature elastic energy and more hydrophobic packing stress in the *Ia3d* phases is expected to restrict the flexibility of the lipid headgroups and consequently also the rotational mobility of the water molecules bound to them as compared to the *Pn3m* phase. The different microviscosities in the two phases have been evaluated by time-resolved fluorescence anisotropy of C-343 and it is apparent that the microviscosity in the *Ia3d* phase is higher than the *Pn3m* phase.

### 3.4 References

1. E. Pebay-Peyroula, G. Rummel, J. P. Rosenbusch and E. M. Landau, *Science*, 1997, **277**, 1676.
2. A. Zabara, I. Amar-Yuli and R. Mezzenga, *Langmuir*, 2011, **27**, 6418-6425.
3. A. Angelova, B. Angelov, R. Mutafchieva, S. Lesieur and P. Couvreur, *Acc. Chem. Res.*, 2011, **44**, 147-156.
4. J. Lendermann and R. Winter, *Phys. Chem. Chem. Phys.*, 2003, **5**, 1440-1450.
5. R. Negrini and R. Mezzenga, *Langmuir*, 2011, **27**, 5296-5303.
6. N. Garti, D. Libster and A. Aserin, *Food Funct.*, 2012, **3**, 700-713.



7. R. Mezzenga, P. Schurtenberger, A. Burbidge and M. Michel, *Nat. Mater.*, 2005, **4**, 729.
8. C. V. Kulkarni, W. Wachter, G. Iglesias-Salto, S. Engelskirchen and S. Ahualli, *Phys. Chem. Chem. Phys.*, 2011, **13**, 3004-3021.
9. H. Qiu and M. Caffrey, *Biomaterials*, 2000, **21**, 223-234.
10. C. V. Kulkarni, *Nanoscale*, 2012, **4**, 5779-5791.
11. T. Mishraki-Berkowitz, P. Ben Ishai, A. Aserin, Y. Feldman and N. Garti, *Phys. Chem. Chem. Phys.*, 2015, **17**, 9499-9508.
12. J. M. Seddon, J. Robins, T. Gulik-Krzywicki and H. Delacroix, *Phys. Chem. Chem. Phys.*, 2000, **2**, 4485-4493.
13. I. Amar-Yuli, D. Libster, A. Aserin and N. Garti, *Curr. Opin. Colloid Interface Sci.*, 2009, **14**, 21-32.
14. K. Larsson, *J. Phys. Chem.*, 1989, **93**, 7304-7314.
15. C. Fong, T. Le and C. J. Drummond, *Chem. Soc. Rev.*, 2012, **41**, 1297-1322.
16. L. van 't Hag, S. L. Gras, C. E. Conn and C. J. Drummond, *Chem. Soc. Rev.*, 2017, **46**, 2705-2731.
17. J. C. Shah, Y. Sadhale and D. M. Chilukuri, *Adv. Drug Delivery Rev.*, 2001, **47**, 229-250.
18. C. J. Drummond and C. Fong, *Curr. Opin. Colloid Interface Sci.*, 1999, **4**, 449-456.
19. V. Borshchevskiy, E. Moiseeva, A. Kuklin, G. Büldt, M. Hato and V. Gordeliy, *J. Cryst. Growth*, 2010, **312**, 3326-3330.
20. A. Zabara, J. T. Y. Chong, I. Martiel, L. Stark, B. A. Cromer, C. Speziale, C. J. Drummond and R. Mezzenga, *Nat. Commun.*, 2018, **9**, 544.
21. J. J. Vallooran, S. Handschin, S. M. Pillai, B. N. Vetter, S. Rusch, H.-P. Beck and R. Mezzenga, *Adv. Funct. Mater.*, 2015, **26**, 181-190.
22. N. I. Zahid, O. K. Abou-Zied and R. Hashim, *J. Phys. Chem. C*, 2013, **117**, 26636-26643.
23. K. Bhattacharyya, *Acc. Chem. Res.*, 2003, **36**, 95-101.
24. S. K. Pal and A. H. Zewail, *Chem. Rev.*, 2004, **104**, 2099-2124.
25. B. Roy, S. Satpathi, K. Gavvala, R. K. Koninti and P. Hazra, *J. Phys. Chem. B*, 2015, **119**, 11721-11731.
26. W. Wachter, G. Trimmel, R. Buchner and O. Glatter, *Soft Matter*, 2011, **7**, 1409-1417.

27. P. B. Ishai, D. Libster, A. Aserin, N. Garti and Y. Feldman, *J. Phys. Chem. B*, 2009, **113**, 12639-12647.
28. J. Kim, W. Lu, W. Qiu, L. Wang, M. Caffrey and D. Zhong, *J. Phys. Chem. B*, 2006, **110**, 21994-22000.
29. K. Bhattacharyya, *Reviews in Fluorescence*, Springer US, 2004.
30. Y. Shiraishi, T. Inoue and T. Hirai, *Langmuir*, 2010, **26**, 17505-17512.
31. M. Vincent and J. Gallay, *J. Phys. Chem. B*, 2012, **116**, 1687-1699.
32. S.-Y. Park, O.-H. Kwon, T. G. Kim and D.-J. Jang, *J. Phys. Chem. C*, 2009, **113**, 16110-16115.
33. J. R. Lakowicz, *Principles of Fluorescence Spectroscopy*, Springer, Boston, MA, 3rd edition edn.
34. X. Liu, J. M. Cole and K. S. Low, *J. Phys. Chem. C*, 2013, **117**, 14731-14741.
35. X. Liu, J. M. Cole and K. S. Low, *J. Phys. Chem. C*, 2013, **117**, 14723-14730.
36. N. M. Correa and N. E. Levinger, *J. Phys. Chem. B*, 2006, **110**, 13050-13061.
37. N. S. Eremina, T. N. Kopylova, L. G. Samsonova and V. A. Svetlichnyi, *J. Appl. Spectrosc.*, 2005, **72**, 499-502.
38. J. R. Lakowicz and S. Keating-Nakamoto, *Biochemistry*, 1984, **23**, 3013-3021.
39. A. Chattopadhyay and S. Halder, *Acc. Chem. Res.*, 2014, **47**, 12-19.
40. M. Maroncelli and G. R. Fleming, *J. Chem. Phys.*, 1987, **86**, 6221-6239.
41. R. Jimenez, G. R. Fleming, P. V. Kumar and M. Maroncelli, *Nature*, 1994, **369**, 471.
42. R. S. Fee and M. Maroncelli, *Chem. Phys.*, 1994, **183**, 235-247.
43. H. Shirota, Y. Tamoto and H. Segawa, *J. Phys. Chem. A*, 2004, **108**, 3244-3252.
44. S. Biswas, S. Santra, S. Yesylevskyy, J. Maiti, M. Jana and R. Das, *J. Phys. Chem. B*, 2018, **122**, 3996-4005.
45. M. C. Bellissent-Funel and J. Teixeira, *J. Mol. Struct.*, 1991, **250**, 213-230.
46. D. K. George, A. Charkhesht, O. A. Hull, A. Mishra, D. G. S. Capelluto, K. R. Mitchell-Koch and N. Q. Vinh, *J. Phys. Chem. B*, 2016, **120**, 10757-10767.
47. M. C. Bellissent-Funel, S. H. Chen and J. M. Zanotti, *Phys. Rev. E*, 1995, **51**, 4558-4569.
48. A. Srivastava and A. Debnath, *J. Chem. Phys.*, 2018, **148**, 094901.
49. K. Bhattacharyya and B. Bagchi, *J. Chem. Sci.*, 2007, **119**, 113-121.
50. D. Chakrabarty, D. Seth, A. Chakraborty and N. Sarkar, *J. Phys. Chem. B*, 2005, **109**, 5753-5758.

51. K. Hara, H. Kuwabara and O. Kajimoto, *J. Phys. Chem. A*, 2001, **105**, 7174-7179.
52. N. Nandi and B. Bagchi, *J. Phys. Chem. B*, 1997, **101**, 10954-10961.
53. N. Nandi and B. Bagchi, *J. Phys. Chem. A*, 1998, **102**, 8217-8221.
54. R. Cassol, M.-T. Ge, A. Ferrarini and J. H. Freed, *J. Phys. Chem. B*, 1997, **101**, 8782-8789.
55. A. L. Mackay, *Nature*, 1985, **314**, 604.
56. W. Sun, J. J. Vallooran and R. Mezzenga, *Langmuir*, 2015, **31**, 4558-4565.
57. S. Assenza and R. Mezzenga, *J. Chem. Phys.*, 2018, **148**, 054902.
58. R. Ghanbari, S. Assenza and R. Mezzenga, *J. Chem. Phys.*, 2019, **150**, 094901.
59. G. C. Shearman, O. Ces, R. H. Templer and J. M. Seddon, *J. Phys.: Condens. Matter*, 2006, **18**, S1105.
60. G. C. Shearman, B. J. Khoo, M.-L. Motherwell, K. A. Brakke, O. Ces, C. E. Conn, J. M. Seddon and R. H. Templer, *Langmuir*, 2007, **23**, 7276-7285.
61. C. V. Kulkarni, T.-Y. Tang, A. M. Seddon, J. M. Seddon, O. Ces and R. H. Templer, *Soft Matter*, 2010, **6**, 3191-3194.
62. S. Roy, D. Skoff, D. V. Perroni, J. Mondal, A. Yethiraj, M. K. Mahanthappa, M. T. Zanni and J. L. Skinner, *J. Am. Chem. Soc.*, 2016, **138**, 2472-2475.
63. G. R. Fleming, *Chemical Applications of Ultrafast Spectroscopy*, Oxford University Press, New York, 1986.
64. N. Tamai, M. Ishikawa, N. Kitamura and H. Masuhara, *Chem. Phys. Lett.*, 1991, **184**, 398-403.

## 3.5 Appendix

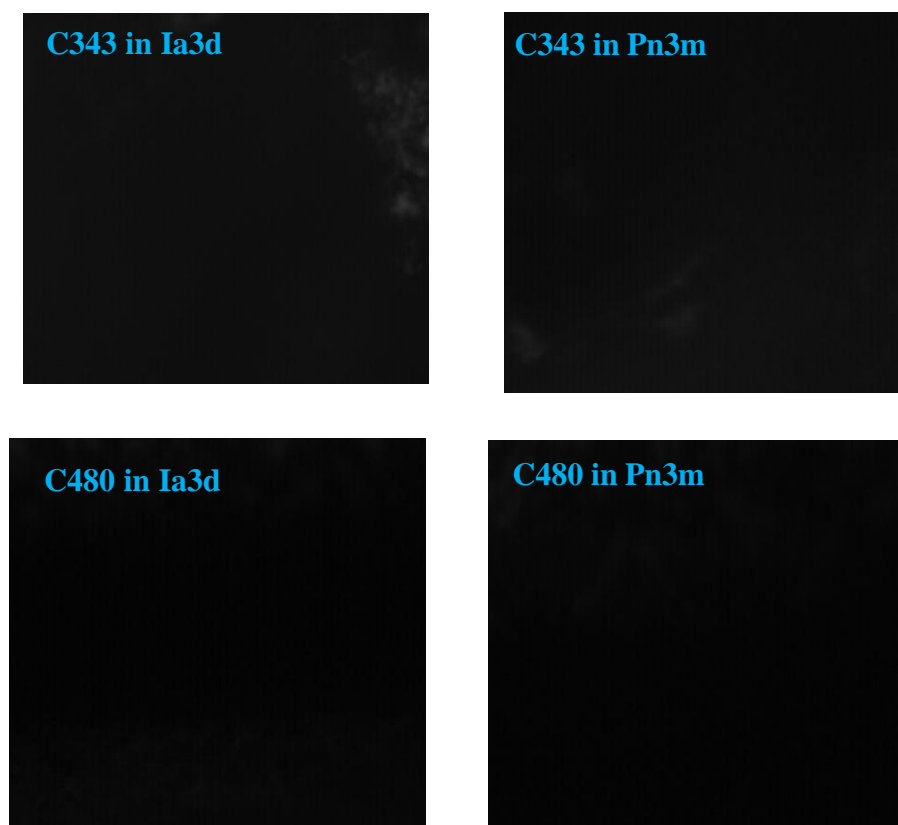


**Figure 3A.1.** Polarised optical microscopy images of dye loaded *Ia3d* and *Pn3m* phases. The blank images indicate the inactivity of the highly symmetric cubic phases towards polarised light.

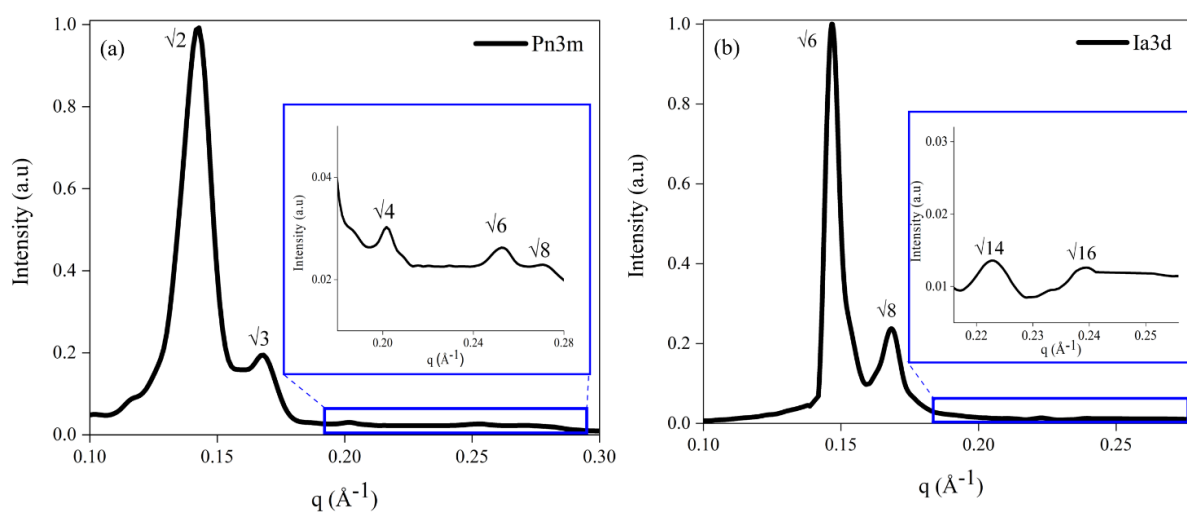


**Figure 3A.2.** Small-angle X-ray scattering pattern of (a) *Pn3m* and (b) *Ia3d* phases at 298 K.

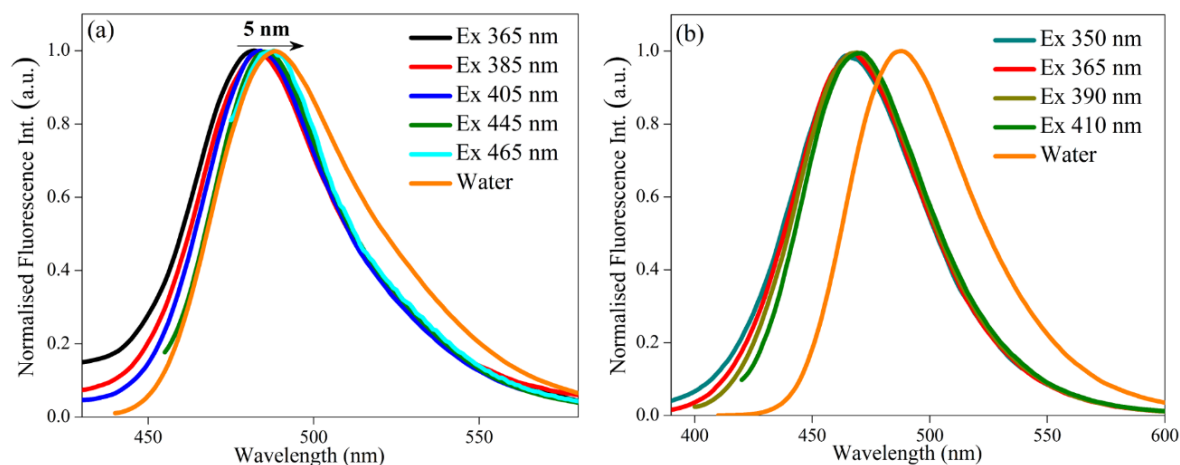


**Figure 3A.3.** Excitation dependent emission spectra of (a) C-343 and (b) C-480 in *Ia3d* phase. The arrow in (a) depicts the redshift in emission with excitation wavelength. The intensities are normalised to 1.0 by dividing with the highest intensity of each spectrum.

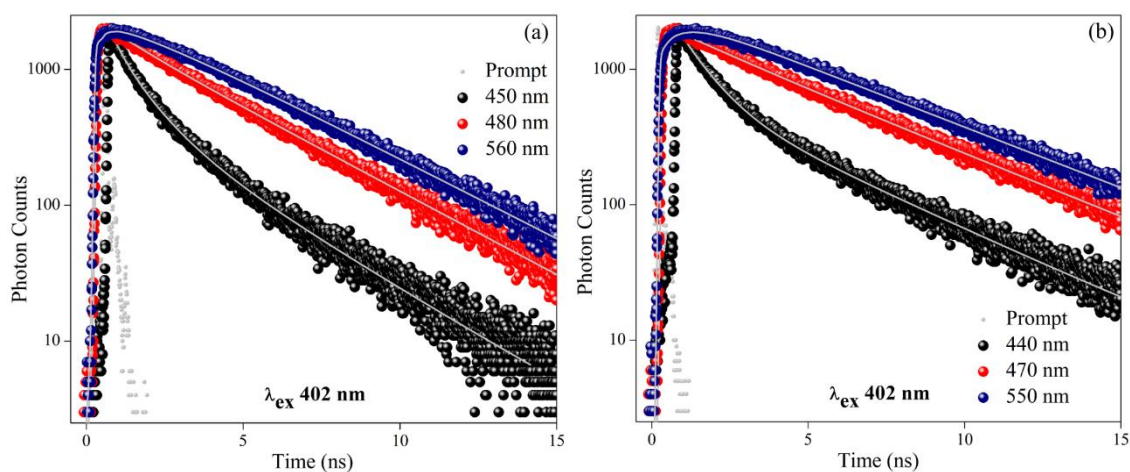


**Figure 3A.4.** Lifetime decay profiles of (a) C-343 and (b) C-480 in *Ia3d* phase at different emission wavelengths ( $\lambda_{\text{ex}}=402$  nm).

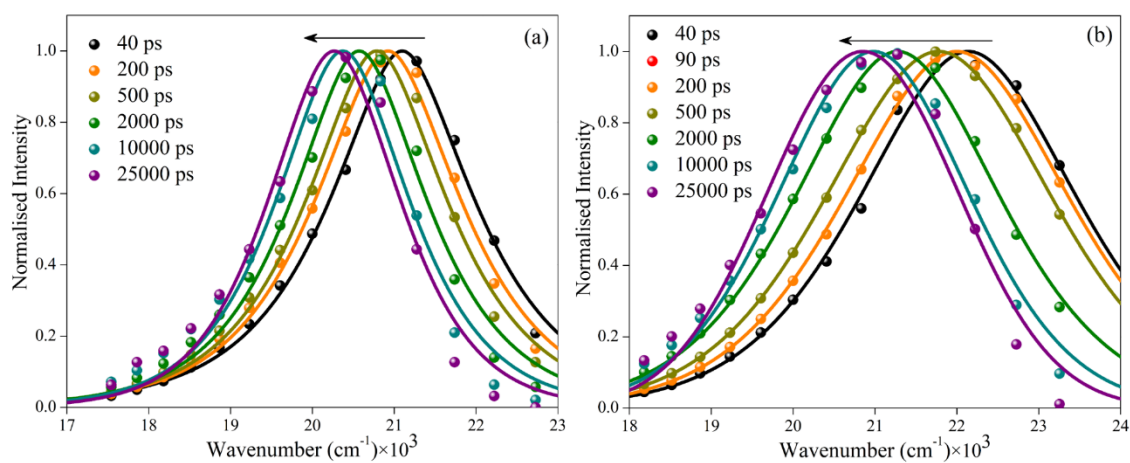


**Figure 3A.5.** Time-resolved emission spectra (TRES) of (a) C-343 and (b) C-480 in *Ia3d* phase. The arrow indicates the time-dependent Stokes shift.

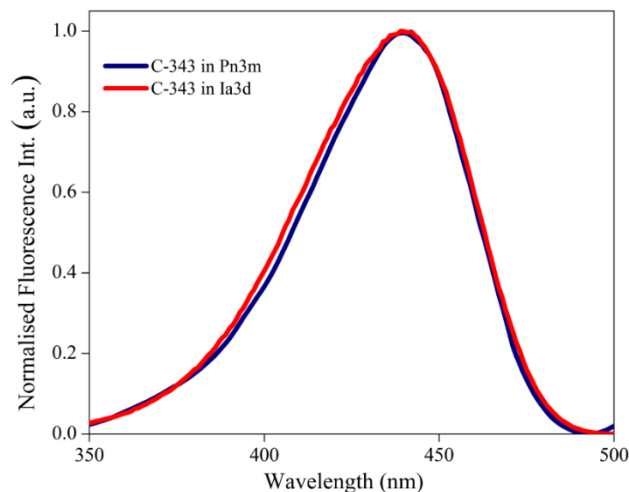


**Figure 3A.6.** Excitation spectra of C-343 in *Ia3d* and *Pn3m* LLC phases.

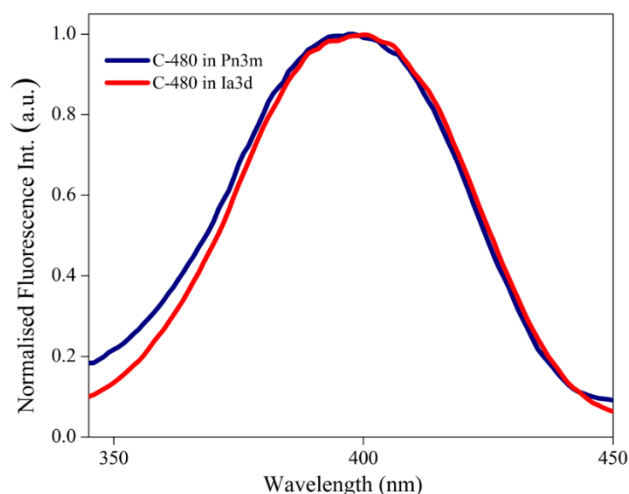
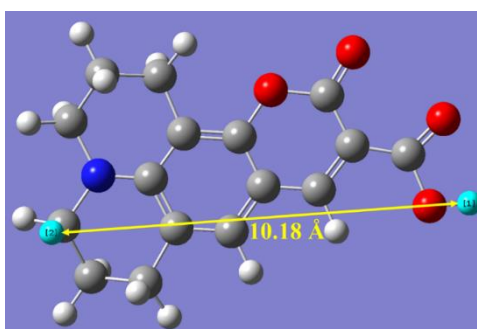


**Figure 3A.7.** Excitation spectra of C-480 in *Ia3d* and *Pn3m* LLC phases.



**Scheme 3A.1.** The longest diameter in the C-343 molecule taken for the microviscosity calculations based on the time-resolved fluorescence anisotropy has been marked.

### 3.5.1 Calculation of missing solvation components

The percentage of missing solvation component has been calculated by the method proposed by Fee and Maroncelli using C-343 loaded *Pn3m* and *Ia3d* phases.<sup>A1</sup> The time-zero

has been estimated from the steady state absorption and fluorescence data using the following equation,

$$\nu_{cal}(t = 0) \approx \nu_{p,md}(abs) - [\nu_{np,md}(abs) - \nu_{np,md}(fl)] \quad (3A.1)$$

where, the subscripts ‘p’ and ‘np’ denote polar and non-polar spectra, respectively. The frequencies in the above equation are mid-point frequencies and have been calculated by,

$$\nu_{md} = \frac{\nu_- + \nu_+}{2} \quad (3A.2)$$

where,  $\nu_-$  and  $\nu_+$  are the low and high frequencies on the half-height points of the spectrum. Hexane has been used as the non-polar solvent for this calculation. Here, we have considered the excitation spectra of C-343 in case of dye loaded LLC cubic phases, as the absorption peaks in the absorption spectra are masked by the intense scattering from the solid gel-like samples. The calculated time-zero frequency ( $\nu_{cal}(t=0)$ ), observed time-zero frequency ( $\nu_0$ ), the frequency at infinite time ( $\nu_\infty$ ) and the percentage of missing component is listed in [Table 3A.1](#). The proportion of missing component is defined as,

$$\frac{\nu_{cal}(0) - \nu(0)}{\nu_{cal}(0) - \nu(\infty)} \quad (3A.3)$$

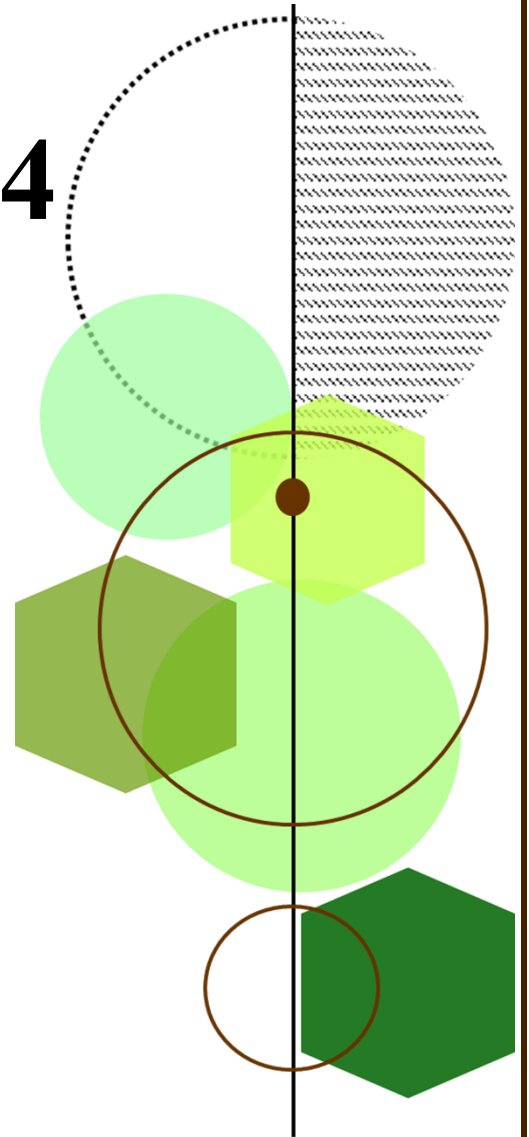
**Table 3A.1. Parameters for missing solvation component.**

Sample	$\nu_{cal}(0)/\text{cm}^{-1}$	$\nu(0)/\text{cm}^{-1}$	$\nu(\infty)/\text{cm}^{-1}$	Percentage of missing component
C-343 in <i>Pn3m</i>	21574	21282	20294	23%
C-343 in <i>Ia3d</i>	21441	21164	20220	22%

### 3.5.2 Appendix Reference

A1. R. S. Fee, M. Maroncelli, *J. Chem. Phys.*, 1994, **183**, 235-247.

# Chapter 4



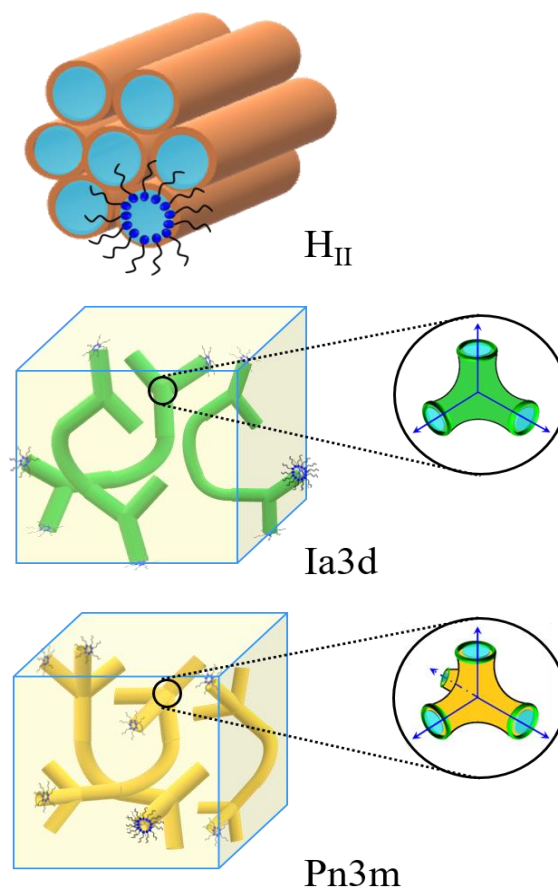
**Peculiar Hydrogen Bonding  
Behaviour of Water  
Molecules inside the  
Aqueous Nanochannels of  
Lyotropic Liquid Crystals**



## 4.1 Introduction

Water is the most prevalent and crucial liquid in nature but its properties are puzzling and far from well understood even today. In addition to the colossal presence of water in its bulk form, the water molecules are also salient in both biological systems and synthetic materials.<sup>1</sup> Investigations have led researchers to elucidate that the water molecules confined in these systems are essentially very different from bulk water in terms of their hydrogen-bonded structure and properties.<sup>1, 2</sup> For instance, confined water molecules often exhibit anomalous phase behaviour, like, low dimension ice formation.<sup>3, 4</sup> Additionally, the self-diffusion behaviour and mobility of entrapped water molecules or water in proximity to interfaces vary substantially from bulk water. Under confinement, the self-diffusion of water molecules is extensively influenced by the surface that is in contact with the water molecules, due to the hydrogen bonding and Coulombic interactions at the interface.<sup>5, 6</sup> These kinds of differential behaviours of water molecules confined in various self-assembled arrangements have far reaching implications in diverse fields such as nanotechnology,<sup>7</sup> electrochemistry and energy storage devices,<sup>8</sup> catalysis,<sup>9</sup> biology,<sup>10</sup> drug delivery,<sup>11</sup> *etc.* Consequently, it is essential to obtain a fundamental understanding of the physical properties of water molecules confined in nanopores as well as determine the factors that lead to the deviations in the behaviour of the confined water as compared to bulk. In this context, a class ‘soft’ lyotropic liquid crystalline (LLC) materials, comprising self-assembled structures of water and lipids have gained widespread popularity in recent years, on account of the intrinsic nature of the aqueous domains in them. The self-assembly of monoglyceride lipids gives rise to a number of inverse LLC phases, such as the 1D hexagonal phase ( $H_{II}$ ), the 2D planar lamellar phase ( $L\alpha$ ), and the 3D bicontinuous cubic phases ( $V_2$ ), as a function of water concentration and temperature (Scheme 4.1).<sup>12-14</sup> The inverse mesophases comprise of water domains that hydrate the lipid headgroups and are encased in a continuous lipid matrix. Owing to the unique behaviour of water molecules trapped in them, these materials have been extensively used in food technology,<sup>12, 15</sup> pharmaceuticals,<sup>16, 17</sup> as nanoreactors,<sup>18</sup> in biomedical sensing,<sup>19</sup> *etc.* The characteristic topology of the mesophases renders each nanostructure with certain properties that are useful in specific applications. For instance among these mesophases, the inverse hexagonal phase has been found to be promising as a drug and nutrients carrier and template for the synthesis of nanomaterials.<sup>18, 20, 21</sup> On the other hand, the inverted bicontinuous cubic phases have been used as protein-hosting reservoirs for the crystallization of membrane proteins which do not

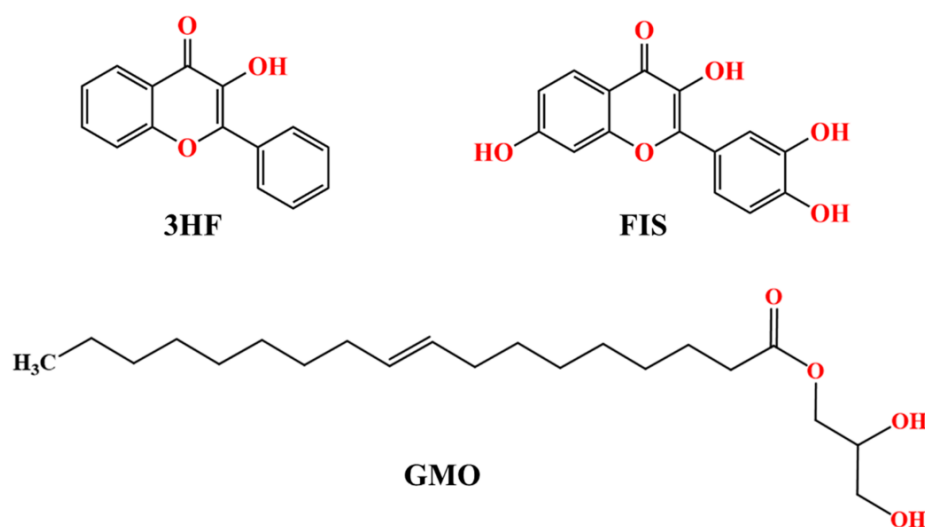
crystallize in bulk and as matrices for the detection of viruses and bacteria, including HIV and *Ebola*.<sup>22, 23</sup>



**Scheme 4.1.** Schematic representation of the inverse hexagonal ( $H_{II}$ ) and bicontinuous cubic ( $Ia3d$  and  $Pn3m$ ) LLC phases.

The macroscopic functions and applications of the LLC phases are expected to be dictated by the precise nature of the water nanochannels, dynamics of the trapped water molecules and the local heterogeneity of the phases.<sup>24</sup> Consequently, researchers have invested efforts in understanding the ways in which the trapped water molecules inside the nanochannels of LLC differ from bulk water in order to augment the applications of these materials in various fields. Following this, a number of studies have explored the existence of various classes of water molecules at different regions inside the LLC nanochannels, which are distinguished by their distinctly sluggish dynamics compared to bulk water.<sup>25-27</sup> In continuation of these efforts, we have recently studied how the differences in the structural topology of the water nanochannels of cubic LLC phases impact the hydration dynamics, micropolarity and

microviscosity of the contained water molecules.<sup>28</sup> However, there is still a lacuna in the understanding of the hydrogen bonding behaviour of the confined LLC water molecules in terms of their hydrogen bond donating and accepting abilities. As these parameters are fundamentally very important for a comprehensive knowledge of a solvent, it is pivotal to elucidate the hydrogen bonding nature of the water molecules contained inside the LLC materials. In addition, the implications of the slower hydration dynamics of the aqueous networks inside the LLC nanochannels are not completely comprehended, especially on intramolecular H-bonds. Notably, intramolecular hydrogen bonds are of special importance as they render conformational stability to most biomolecules like DNA and proteins by providing the directional organization for distinct folds.<sup>29</sup> The intramolecular hydrogen bonds can also induce conformational switching in synthetic molecules and impact the solubility, permeability and potency of drugs and other synthetic molecules.<sup>30, 31</sup> Keeping this in mind, it becomes crucial to understand the effects of the confined water molecules inside the nanochannels of LLC on the intramolecular hydrogen-bonds of encapsulated drugs or biomolecules.



**Scheme 4.2.** Chemical Structures of 3-Hydroxyflavone (3HF), Fisetin (FIS) and 1-Oleoyl-rac-glycerol (GMO).

One of the most efficient ways to probe the hydrogen bonding characteristics of the LLC water molecules and their effects on the intramolecular hydrogen bonds of target probes is by the phenomenon of ‘excited state intramolecular proton transfer’ (ESIPT) of model molecules. The ESIPT is generally a four-level photocycle ( $E \rightarrow E^* \rightarrow T^* \rightarrow T$ ) involving the keto (T) - enol (E) phototautomerisation.<sup>32, 33</sup> The important features of the ESIPT phenomenon

are, a large Stokes shifted emission of the phototautomer, dual emission, ultrafast ( $< 20$  ps) proton transfer and most importantly a spectral sensitivity to the dynamics of the surrounding solvent and its Kamlet-Taft parameters, which are the polarity, hydrogen bond donating and accepting abilities.<sup>34, 35</sup> Among all the ESIPT molecules, 3-Hydroxyflavone (3HF) is widely considered as a prototype for observing excited state intramolecular proton transfer and is an ideal model for our purpose (Scheme 4.2). We have also probed the fate of the excited state intramolecular proton transfer for fisetin (FIS) (Scheme 4.2), a derivative of 3HF, inside the aqueous nanochannels of LLC to substantiate that the effects of the LLC water molecules is not exclusive to only one particular molecule. The 3HF moiety behaves like a weak acid in the ground state ( $pK_a(S_0) = 8.35$ ), but the acidity drastically increases in the first excited state ( $pK_a(S_1) = -1.50$ ).<sup>36</sup> In addition to the effect of the trapped water molecules on ESIPT, we also determine the influence of structural topology of the aqueous LLC nanochannels on the ESIPT process. Interestingly we have observed that both the ESIPT probes point towards a heterogeneity in the hydrogen bond donating and accepting behaviour of the water molecules inside the nanochannels. Quite surprisingly, despite the general protic solvent (alcohol) like polarity of the water molecules throughout the nanochannels, the spectral features of the probes imply that in some regions of the nanochannels the hydrogen bonding behaviour is distinctly different from either alcohols or bulk water. It has been found that the ultrafast ESIPT dynamics gets retarded by almost 15 times inside the LLC nanochannels and the ESIPT rate is influenced by the structural topology of the LLC phases, with the process being the slowest in  $H_{II}$  and fastest in the  $Pn3m$  phase. In general, the rate of ESIPT is quite fast even in confined systems and such a dramatic extent of retardation is extremely rare. We believe that the insights in this work will add significantly to the existing knowledge about the properties of the aqueous LLC nanochannels, hence promoting and modulating the future applications of the LLC-based systems.

## 4.2 Results and Discussion

### 4.2.1 Characterization of LLC Phases

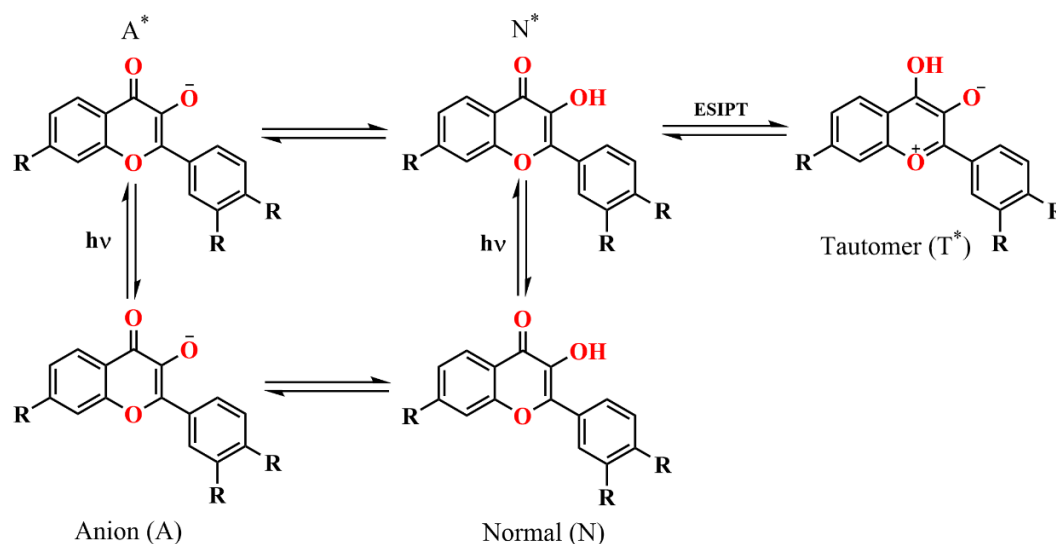
The LLC systems have been characterised by their observed signature textures in the cross polarizer, using polarised optical microscopy (POM). The reverse hexagonal ( $H_{II}$ ) phase shows birefringent “fan” like textures (Figure 4A.1) which is characteristic of the phase. However,  $Ia3d$  (G) and  $Pn3m$  (D) phases do not exhibit any optical textures in the POM images due to

their optically isotropic and highly ordered cubic symmetry. Thus, the mesophases,  $H_{II}$ ,  $Ia3d$  and  $Pn3m$  have been characterised by the SAXS measurements (Figure 4A.2), wherein the mesophases exhibit the characteristic ratios of their peak positions -  $H_{II}$  ( $\sqrt{1}:\sqrt{3}$ ),  $Pn3m$  ( $\sqrt{2}:\sqrt{3}:\sqrt{4}:\sqrt{6}:\sqrt{8}$ ) and  $Ia3d$  ( $\sqrt{6}:\sqrt{8}:\sqrt{14}:\sqrt{16}:\sqrt{20}$ ). The dimensions of the nanochannels have been calculated from the first intense peak in the diffraction pattern and it has been observed that the diameter of the nanochannels (4-5 nm for all the mesophases) is much larger than the size of either 3HF or FIS.

### 4.2.2 Steady State Emission Study

FIS typically absorbs at  $\sim 369$  nm and a significant absorption extends up to 420 nm in water and other polar protic solvents (Figure 4A.3). The peak at 369 nm corresponds to the normal (FN) form of FIS and the lower energy absorption at  $>400$  nm is attributed to the ground state anion (FA).<sup>37, 38</sup> Emission spectra of FIS are recorded at two different excitation wavelengths, one ( $\lambda_{ex} = 360$  nm) for the normal (FN) (Figure 4.1 (a)) and the other ( $\lambda_{ex} = 430$  nm) for the anionic (FA) (Figure 4.1 (b)) species, respectively. Excitation of FIS at both 360 nm and 430 nm in water leads to an extremely broad emission band centered  $\sim 495$  nm, indicating the contribution from multiple emitting species. The broad emission band encompasses the contributions majorly from the anionic form ( $\sim 490$  nm) and the phototautomeric form ( $FT^*$ ) which generally emits around 530 nm (Scheme 4.3). The phototautomer of FIS is generated by the intramolecular proton transfer process (ESIPT) from the excited state normal form of FIS (Scheme 4.3). In stark contrast to the emission behaviour of FIS in water ( $\lambda_{ex} = 360$  nm), the broad emission peak completely vanishes in all the FIS-loaded LLC phases and two distinctly well separated peaks appear at  $\sim 425$  nm and  $\sim 535$  nm (Figure 4.1 (a)). The emission peak at the lower wavelength ( $\sim 425$  nm) is attributed to the excited state normal form ( $FN^*$ ), whereas the other Stokes shifted peak ( $\sim 535$  nm) is ascribed to the  $FT^*$  species.<sup>37, 38</sup> Although on excitation at 360 nm the  $FA^*$  emission ( $\lambda_{em} = 490$  nm) is absent in the FIS-loaded LLC phases, on excitation at 430 nm (Figure 4.1 (b)) the LLC phases exhibit the  $FA^*$  peak in the range 485 - 490 nm with a small shoulder at  $\sim 535$  nm. In order to interpret the observations of FIS inside the nanochannels of the LLC phases, it is necessary to look into the spectral patterns of FIS in bulk solvents. The excited state behaviour of FIS and the relative population of each species is highly sensitive to the polarity, hydrogen bond donating ability ( $\alpha$ ) and hydrogen bond accepting ability ( $\beta$ ) of the surrounding medium with

the last factor often being more dominant.<sup>39</sup> Generally, the anionic species exists exclusively in solvents that have a good proton accepting capability ( $\beta$ ), like water or alcohols. In contrast, the formation of the phototautomer relies on the efficiency of the ESIPT process, which depends on the hydrogen bonding ability between the hydroxyl group and the adjacent carbonyl moiety of FIS. A good indication of the ESIPT efficiency is given by the relative fluorescence intensities of the normal and phototautomer forms ( $I_{N^*}/I_{T^*}$ ), which generally has an increasing trend with an increase in the  $\beta$  and  $\alpha$  values of solvents (Table 4A.1). To illustrate, solvents such as benzene that have low  $\beta$  and  $\alpha$  values, perturb the intramolecular hydrogen bond to a lesser extent leading to an efficient ESIPT process. In contrast, solvents having both high  $\beta$  and  $\alpha$  values can compete to form intermolecular hydrogen bonds with the carbonyl and hydroxyl moieties of the molecule, thereby, hindering the ESIPT process (Figure 4A.4, Table 4A.1). In aprotic solvents like acetonitrile and tetrahydrofuran, which have moderate  $\beta$  and  $\alpha$  values, FIS exhibits two well separated peaks for the  $N^*$  ( $\sim 420$  nm) and  $T^*$  ( $\sim 535$  nm) species, with the intensity of the latter peak being much higher than the former peak. In most polar protic solvents, because of their high hydrogen bond accepting abilities ( $\beta$ ), the solvents also give rise to anionic emission resulting in a broad emission feature.



Fisetin: R=OH

3-Hydroxyflavone: R=H

**Scheme 4.3.** Ground and excited state proton transfer pathways of fisetin and 3-Hydroxyflavone and the different possible excited state species.

FIS in the aqueous nanochannels of LLC phases exhibit two contrasting kinds of emission features conditional on the excitation wavelength - one similar to water/alcoholic solvents ( $\lambda_{\text{ex}} = 430 \text{ nm}$ :  $\text{FA}^*$  with shoulder at  $\text{FT}^*$ ) and the other comparable to medium polar aprotic solvents ( $\lambda_{\text{ex}} = 360 \text{ nm}$ :  $\text{FT}^*$  with a smaller peak at  $\text{FN}^*$  (Figure 4A.4). This leads us to believe that the FIS molecules sense a different solvent like environment depending upon their localisation in the nanochannels of LLC phases. Previously, we have reported that the micropolarity near the lipid-water interface is similar to ethanol and that near the intermediate and central region of the nanochannels is similar to ethylene glycol.<sup>25, 28</sup> Hence, it can be generalised that the LLC nanochannels have an overall ‘alcohol like’ polarity. Although one of the emission patterns of FIS-loaded LLC phases ( $\lambda_{\text{ex}} = 430 \text{ nm}$ ) matches quite well with the reported alcohol like environment in the nanochannels, the other emission spectra ( $\lambda_{\text{ex}} = 360 \text{ nm}$ ) are completely disparate from the emission features of FIS in alcohols or water (Figure 4A.4). These contrary emission patterns of FIS in the aqueous nanochannels of LLC phases and the simultaneous presence of the three forms of the molecule connotes that the hydrogen bond donating and accepting abilities of LLC water molecules is not homogenous throughout the nanochannels. Moreover, the emission spectra at 360 nm excitation of FIS inside the LLC phases also clearly signify that, despite the general alcohol like polarity throughout the aqueous nanochannels, the hydrogen bond donating and accepting abilities of the water molecules seem to be similar to less polar aprotic solvents in some regions of the nanochannels.

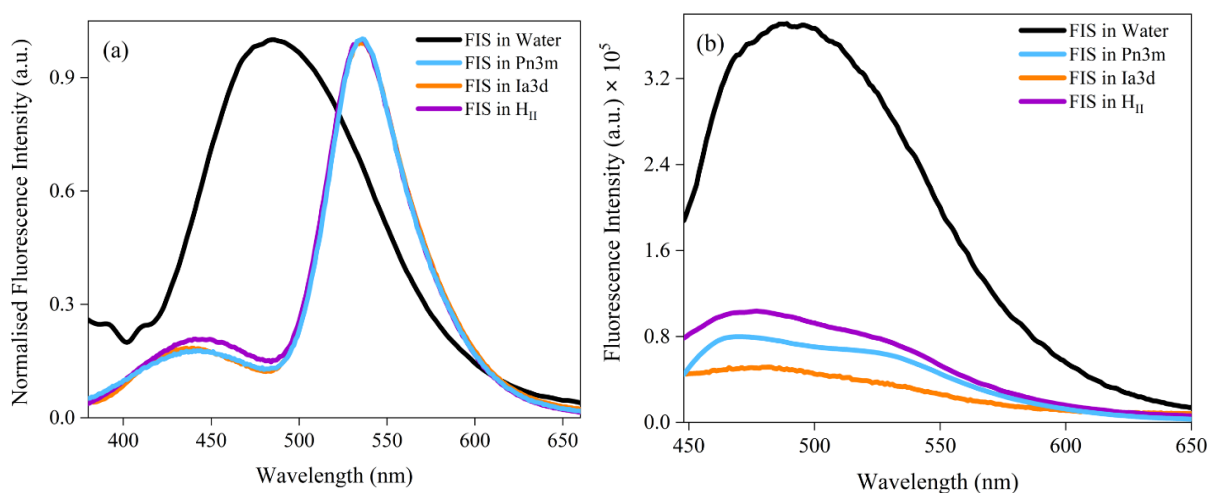


**Figure 4.1.** Steady state emission spectra of FIS in water and different LLC phases on excitation at (a) 360 nm and (b) 430 nm.

The observations so far underline the peculiar properties of the confined LLC water molecules in terms of their hydrogen bond donating and accepting abilities. To substantiate this claim, it is pertinent to establish that this unusual property of the confined LLC water molecules is sensed by other similar ESIPT probe molecules and is not exclusive to FIS. Consequently, we have probed the effects of the LLC water molecules on the excited state behaviour of the parent flavonoid molecule of FIS, namely, 3HF. Aqueous solution of 3HF exhibits a dominant absorption peak  $\sim 340$  nm with a hump at 300 nm and both these peaks correspond to the normal form (HN) of the molecule (Figure 4A.6).<sup>40</sup> 3HF in water shows two distinct emission peaks on excitation of the normal form, one being a significantly more intense peak at  $\sim 515$  nm and the other at  $\sim 420$  nm (Figure 4.2 (a)).<sup>40</sup> The peak at 515 nm corresponds to the tautomeric emission (HT\*) generated by the ESIPT process, while the other peak at 420 nm is attributed to the emission from the normal form (HN\*).<sup>40</sup> On confinement of 3HF in the aqueous nanochannels of the LLC phases, both the emissions for the HN\* and the HT\* species are observed. However, the HT\* emission gets red-shifted from 515 nm to  $\sim 530$  nm and the HN\* peak gets blue-shifted from 420 nm to  $\sim 407$  nm. It has been reported in literature that with a decrease in the polarity of the surrounding medium, the HN\* emission gets blue-shifted but the HT\* emission gets red-shifted for the 3HF molecule.<sup>40, 41</sup> The emission maximum positions for both HN\* and HT\* species in the nanochannels of LLC phases closely resemble with those of lesser polar solvents than water like methanol and acetonitrile (Figure 4A.7). It is pertinent to mention here that, one of the emitting forms of 3HF which is absolutely unique to alcohols and is completely absent in either water or even acetonitrile is the anionic form. The anionic form of 3HF absorbs  $\sim 410$  nm and gives rise to a broad structureless emission  $\sim 480$  nm.<sup>42</sup> Interestingly, on excitation of the 3HF-loaded LLC phases at 410 nm (Figure 4.2 (b)), an emission  $\sim 480$  nm is observed signifying the presence of anionic species. The evidence of anionic species in the LLC phases is also clear in the excitation spectra collected at the anionic emission ( $\lambda_{em} = 480$  nm). A peak  $\sim 410$  nm is manifested in the excitation spectra (Figure 4A.8 (a)), corresponding to the anionic species, which is also present in the excitation spectra of alcohols but absent in water. The aforementioned spectral observations resonate with the reported alcohol like polarity of the LLC nanochannels.<sup>25, 28</sup> In a nutshell, 3HF in the LLC phase exhibits emission from all the three species namely, normal (HN\*), phototautomer (HT\*) and anion (HA\*). Similar to FIS, the spectral behaviour of 3HF is dependent on the polarity as well as the  $\alpha$  and  $\beta$  values of the surrounding solvent medium with the ESIPT process being



the most favoured in non-polar aprotic solvents. The influence of solvents with different hydrogen bond donating and accepting abilities is manifested on the ratio of fluorescence intensities of the tautomeric species and the normal species, which dictates the ESIPT efficiency (Table 4A.1).<sup>43</sup> Interestingly, although the presence of anionic emission in the LLC nanochannels reflects an alcohol-like environment, the ratio of  $I_{\text{HN}^*}/I_{\text{HT}^*}$  in the LLC phases is quite different from the values for alcohols. In fact, the observed ratio of  $I_{\text{HN}^*}/I_{\text{HT}^*}$  is in between the values reported for aprotic solvents like acetonitrile and protic alcohols.<sup>43</sup> Thus, on one hand, although the anionic emission and positions of the  $\text{HN}^*$  and  $\text{HT}^*$  emission bands signal that the hydrogen bond donating and accepting abilities of LLC water molecules are similar to alcohols but on the other hand, the ratio of  $I_{\text{HN}^*}/I_{\text{HT}^*}$  signifies hydrogen bond donating and accepting abilities are very different from bulk alcohols. These contrasting observations concur with the previously drawn conclusions from the ESIPT behaviour of FIS in the LLC phases regarding the heterogeneity in the hydrogen bond donating and accepting abilities of water molecules inside the LLC nanochannels.

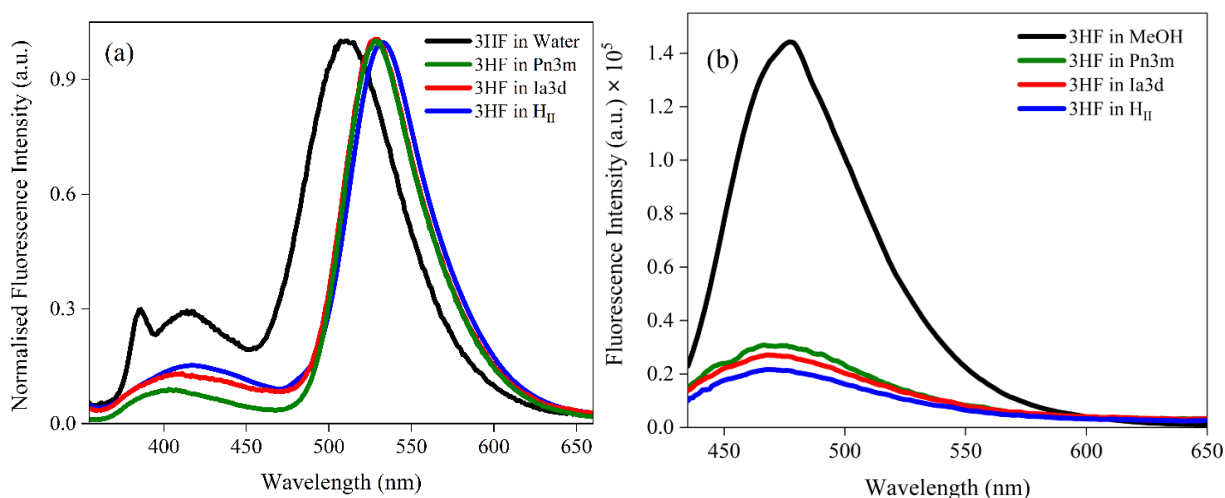


**Figure 4.2.** Steady state emission spectra of 3HF in bulk solvents and different LLC phases on excitation at (a) 340 nm and (b) 410 nm.

It has been observed for the lipid/surfactant based self-assembled systems that the water molecules buried near an amphiphile-water interface are generally basic in nature owing to their high  $\beta$  value and this basicity gradually decreases from the bound water to the intermediate water layers having bulk-like behaviour.<sup>44, 45</sup> Recent reports suggest that the pH of water near the hydrophilic headgroups of LLC phases mimics that of a pH > 8 bulk aqueous solution and act as a better nucleophile compared to bulk water.<sup>24, 46</sup> From these prior literature reports, we

believe that the FIS or 3HF molecules buried near the polar headgroups at the lipid-water interface may be responsible for the anionic ( $A^*$ ) emission. On the other hand, the FIS or 3HF molecules residing away from the polar headgroups, near the intermediate water layers, are accountable for the dual emission from the tautomeric ( $T^*$ ) and normal ( $N^*$ ) forms ( $\lambda_{\text{ex}} = 360/340$  nm). Interestingly, we observe that the fluorescence intensity of  $N^*$  is higher in  $H_{II}$  compared to the cubic LLC phases by  $\sim 1.75$  and  $\sim 1.16$  times for 3HF and FIS, respectively. Since all the phases are composed of the same two components (water and GMO) and are also prepared using equal amounts of water, even the observed small differences in the efficiency of ESIPT highlight that the variations in the structural topologies between the LLC phases influence the properties of the confined water thereby affecting the ESIPT process.

### 4.2.3 Time-Resolved Fluorescence Study

The steady state results depict the vast deviations in the spectral features encountered by the ESIPT probes in the aqueous LLC nanochannels as compared to that in bulk water. To further understand the consequences of the LLC water molecules on the ESIPT phenomenon, we have carried out time-resolved fluorescence studies to probe the dynamics of the ESIPT process. The lifetime measurements for FIS and 3HF in the LLC phases and bulk water have been carried out using an excitation source of 375 nm diode laser in TCSPC setup. The lifetime transients have been collected at 550 nm for the tautomeric forms of both FIS and 3HF and at 450 nm and 440 nm for the normal form in the case of FIS and 3HF, respectively. We have also carried out femtosecond fluorescence upconversion experiments of the tautomeric form of both FIS and 3HF in neat protic and aprotic solvents to comprehend the typical ultrafast timescale of the ESIPT dynamics. Although substantial efforts have been invested towards the study of the ESIPT dynamics of 3HF in neat solvents,<sup>47, 48</sup> there are no reports exploring the proton transfer dynamics of FIS in the ultrafast regime. The fluorescence upconversion decay transients (Figure 4.3) were collected at 550 nm for the excited state tautomeric form on excitation at 375 nm using the second harmonic of a mode-locked Ti-sapphire laser. Methanol, a polar protic solvent and acetonitrile, an aprotic solvent were chosen to corroborate with the steady state results, in which we have observed that the excited state behaviour of FIS in the LLC channels is similar to that in methanol and acetonitrile. The femtosecond upconversion profiles of FIS fit to a biexponential function with a growth and a decay component. Growth components of  $\sim 13$  ps in methanol and  $\sim 8$  ps in acetonitrile (Figure 4.3 (a), Table 4A.2). The

upconversion profiles of 3HF also fit to a biexponential function, exhibiting a growth component of  $\sim 15$  ps in the polar protic solvent, methanol whereas in the aprotic solvent, acetonitrile the observed growth component is  $\sim 10$  ps (Figure 4.3 (b), Table 4A.2). These growth components observed for both 3HF and FIS, signify the occurrence of an excited state interconversion process. The observed time scales of the rise/growth components match well with the time scale reported for 3HF in other neat polar protic and aprotic solvents.<sup>47-49</sup> Additionally, another rise time has been reported in the femtosecond timescale ( $< 200$  fs) for 3HF in neat hydrogen bonding solvents, which cannot be detected in our setup due to instrument response function (IRF) restrictions.<sup>47-49</sup> These two distinct rise time scales have been assigned to ESIPT process of the molecules which are intramolecularly hydrogen-bonded (fs time scale) and intermolecularly hydrogen-bonded with the solvent molecules (ps time scale) at the time of photoexcitation. It would have been ideal to carry out the upconversion experiments of FIS and 3HF in water as well, but the poor solubility of the molecules in water hampers the experiment, and hence the time-resolved experiments for both the ESIPT molecules in water have been studied using a TCSPC setup. Importantly, the rotatory restriction of the gel-like solid LLC mesophases and their heat-sensitive nature limits laser-based ultrafast time-resolved fluorescence upconversion measurements.

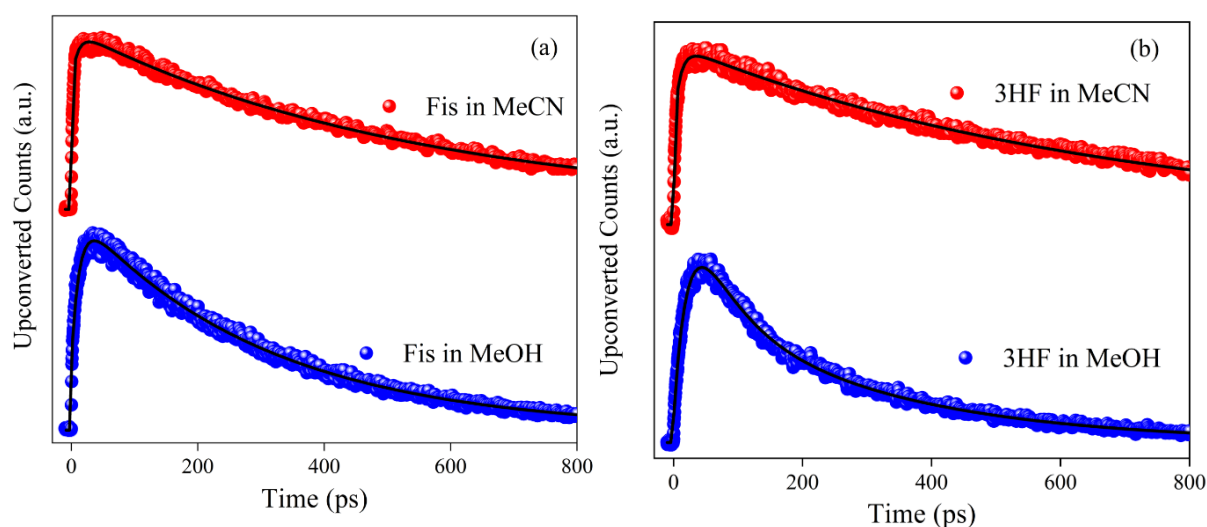


**Figure 4.3.** Fluorescence up-converted decay profiles of (a) FIS and (b) 3HF in methanol and acetonitrile collected at  $\lambda_{em} = 550$  nm on excitation at 375 nm. The solid lines denote the fits of the decay profiles.

FIS in water (for the  $FT^*$  species) exhibits a triexponential decay with lifetime components of  $\sim 1$  ns (9%),  $\sim 325$  ps (17%) and  $\sim 50$  ps (74%) (Table 4A.3) when collected at 550 nm ( $\lambda_{ex} = 375$  nm) (Table 4A.3). Notably, a rise component representative of the ESIPT process, is absent in the lifetime decay profiles of  $FT^*$  indicating that the ESIPT dynamics in water is too fast to be detected by our instrument ( $< 20$  ps). For the FIS-loaded LLC phases, the time-resolved profiles fit to a triexponential function with two nanosecond decay components of  $\sim 1$  ns and  $\sim 2.5$  ns (Figure 4.4 (a), Table 4.1). A third lifetime component of  $\sim 200$  ps exhibiting a negative pre-exponential factor is observed in the decay profile. This growth component matches well with one of the decay components ( $\sim 180$  ps) in the lifetime profile of  $FN^*$ , implying that the two forms are connected to each other. Hence, we assign this growth component to the ESIPT process, which facilitates the conversion of  $FN^* \rightarrow FT^*$ . To determine whether the ESIPT process for other molecules also occurs in a slower time scale in the aqueous nanochannels, we have also carried out lifetime measurements of 3HF in the LLC phases. 3HF in water (collected at 550 nm) exhibits a biexponential behaviour with a major contribution from a short lifetime component of  $\sim 200$  ps (99%) and a slight contribution from a long lifetime component of  $\sim 4.0$  ns (1%) (Table 4A.3). Similar to most ESIPT molecules, the ESIPT process of 3HF is not detected in bulk water as it occurs in an ultrafast time scale ( $< 20$  ps). Markedly, for the 3HF-loaded LLC phases as well, a lifetime component  $\sim 150$  ps at 550 nm with a negative pre-exponential factor is observed in the TCSPC experiments (Figure 4.4 (b), Table 4.2). This growth component matches one of the decay components in the lifetime profile of  $HN^*$  ( $\lambda_{em} = 440$  nm) and is attributed to the ESIPT process from  $HN^*$  to  $HT^*$ .

**Table 4.1. Lifetime fitting parameters of FIS in the LLC phases.**

Sample	$\lambda_{em}$	$\alpha_1$	$\tau_1$ (ns)	$\alpha_2$	$\tau_2$ (ns)	$\alpha_3$	$\tau_3$ (ns)
H <sub>II</sub>	550	0.31	0.897	-0.19	0.301	0.50	2.428
<i>Ia3d</i>	550	0.22	0.914	-0.19	0.220	0.59	2.570
<i>Pn3m</i>	550	0.24	1.087	-0.22	0.160	0.54	2.693
H <sub>II</sub>	450	0.38	0.646	0.46	0.181	0.16	2.851
<i>Ia3d</i>	450	0.42	0.603	0.48	0.172	0.10	2.563
<i>Pn3m</i>	450	0.50	0.469	0.35	0.120	0.15	2.248

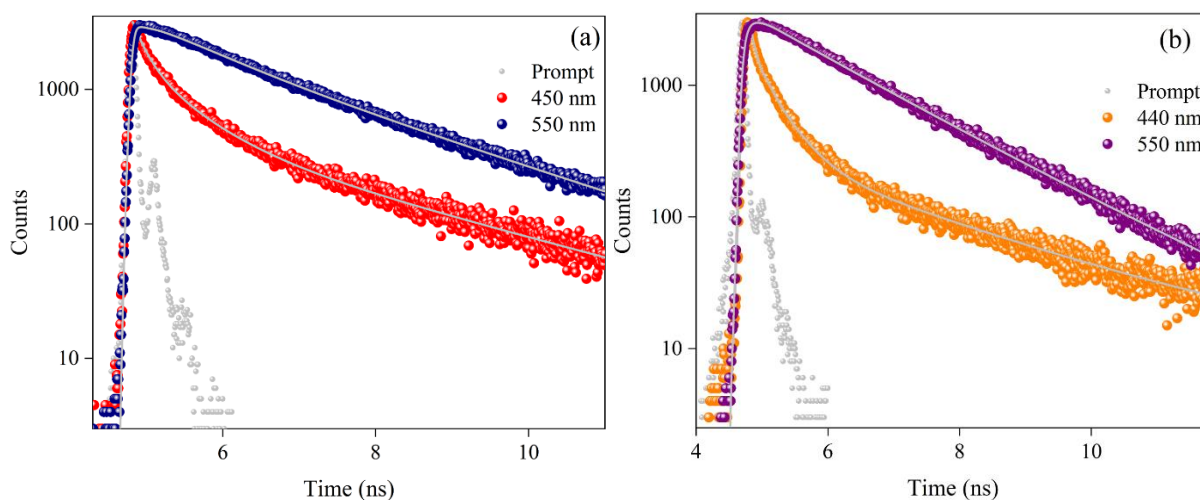


**Figure 4.4.** Fluorescence lifetime (TCSPC) profiles of (a) FIS and (b) 3HF in H<sub>II</sub> phase at different emission wavelengths on excitation at 375 nm. The solid lines denote the fits of the decay profiles.

**Table 4.2.** Lifetime fitting parameters of 3HF in the LLC phases.

Sample	$\lambda_{em}$	$\alpha_1$	$\tau_1$ (ns)	$\alpha_2$	$\tau_2$ (ns)	$\alpha_3$	$\tau_3$ (ns)
H <sub>II</sub>	550	0.23	0.989	-0.28	0.180	0.49	1.822
<i>Ia3d</i>	550	0.30	1.091	-0.41	0.104	0.29	1.906
<i>Pn3m</i>	550	0.21	0.998	-0.51	0.060	0.28	1.907
H <sub>II</sub>	440	0.47	0.380	0.46	0.125	0.07	2.124
<i>Ia3d</i>	440	0.25	0.391	0.65	0.086	0.10	2.485
<i>Pn3m</i>	440	0.25	0.340	0.70	0.060	0.05	2.489

Although, the growth components observed for both FIS and 3HF molecules clearly point toward the ESIPT process, occurring from the normal form to generate the tautomeric form, the existence of multiple emissive species in the excited state can be further reaffirmed by a recently developed technique called time-resolved area normalised emission spectrum (TRANES). TRANES is an extension of the more commonly used time-resolved emission spectrum (TRES), which helps to understand the transitions between different excited state species.<sup>50</sup> The constructed TRANES profiles for 3HF and FIS in the H<sub>II</sub>, *Pn3m* and *Ia3d* phases are given in [Figure 4.5](#), [Figure 4A.11](#) and [Figure 4A.12](#). It is evident from the TRANES profiles that with the increase in time, the intensity of the normal form decreases and the tautomeric form concomitantly increases inside the LLC phases. In addition, a clear iso-emissive point at ~500 nm is apparent for both 3HF and FIS in all the three phases. These observations elucidate

the presence of two distinct emissive species, that is, the normal form and the tautomeric form of the molecules. In addition, the two species are connected in the excited state, with the tautomeric species getting generated at the cost of the normal species. Notably, for 3HF, HT\* starts to form appreciably at  $\sim 150$  ps,  $\sim 100$  ps and  $\sim 70$  ps for the H<sub>II</sub>, *Ia3d* and *Pn3m* phases respectively, while for FIS, FT\* starts appearing at  $\sim 250$  ps,  $\sim 180$  ps and  $\sim 100$  ps respectively, for the H<sub>II</sub>, *Ia3d* and *Pn3m* phases. All the time scales are in good agreement with the timescale of the growth component observed in the decay profile for each molecule in the LLC phases.

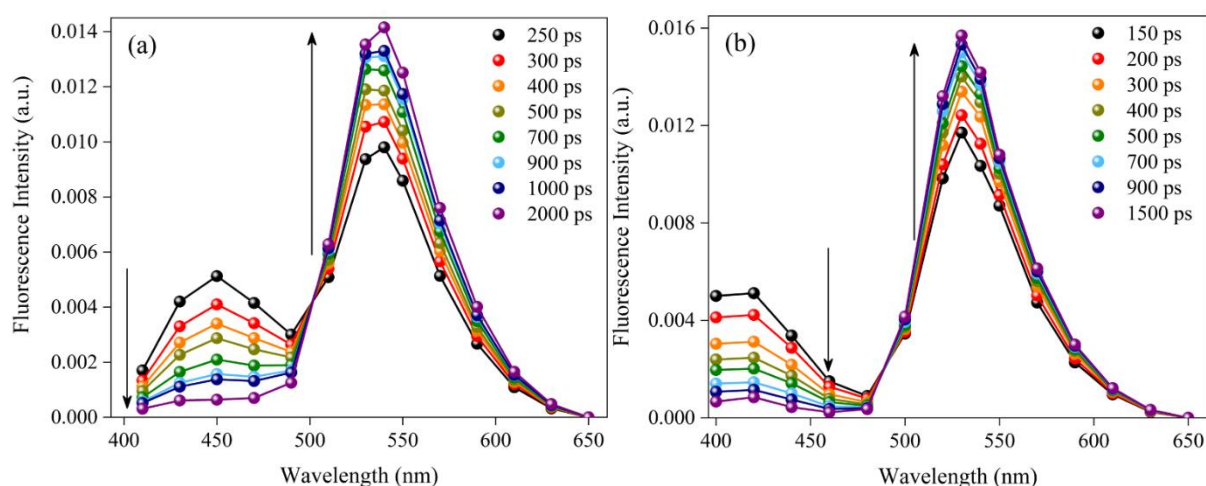


**Figure 4.5.** Time-resolved area normalised spectra of (a) FIS and (b) 3HF in H<sub>II</sub> LLC phase on excitation at 375 nm.

This kind of pronounced retardation by almost  $>15$  times observed in the ESIPT timescale of FIS and 3HF in the LLC phases as compared to bulk solvents is uncommon in literature. The excited state properties and proton transfer of FIS and 3HF have been studied in a number of self-assembled systems like cyclodextrin,<sup>51</sup> reverse micelles,<sup>39</sup> liposomes,<sup>52</sup> micelles,<sup>53</sup> proteins,<sup>54</sup> *etc.*, but in most of the molecular assemblies it is rare for the ESIPT dynamics to be sufficiently slow enough to be detected by TCSPC setup. As a matter of fact, for FIS, there are no reports for the slowing down of ESIPT in any media. In the case of 3HF, Mandal *et al.* for the first time observed  $>100$  ps ESIPT time constant in AOT reverse micelles.<sup>55</sup> They have attributed the retarded ESIPT dynamics to the formation of intermolecularly hydrogen-bonded 3HF:AOT complexes which hinders the intramolecular hydrogen bond within 3HF. However, in our case, we believe that the contribution of the 3HF/FIS:GMO complexes towards the prolonged ESIPT process in the LLC phases is not significant as it is evident from the steady state spectra, that the ESIPT molecules are distributed

heterogeneously throughout the nanochannels and not just limited near the headgroups of the GMO lipid. This implies that the dramatic retardation in the ESIPT dynamics is a reflection of the properties unique to the LLC nanochannels. In non-hydrogen bonding solvents like alkanes, it is reported for 3HF that the ESIPT reaction takes place in  $< 200$  fs, however, in both aprotic and protic (hydrogen bond acceptor and donor) solvents, the conditions become extremely complicated.<sup>47,49</sup> In the cases of both hydrogen bond donating and accepting solvents, a number of different solute-solvent complexes may arise as a result of the strong intermolecular hydrogen bonds of the ESIPT probe with the solvent. These intermolecular hydrogen bonds with the solvent disrupts the intramolecular hydrogen bond within the ESIPT molecule, which is necessary for the proton transfer reaction. Consequently, on photoexcitation, the solvent-bound ESIPT solute molecules have to initially break from the intermolecular hydrogen bonds in order to participate in the ESIPT process. This process slows down the ESIPT reaction and the corresponding growth component in the picosecond regime is observed in these solvents. Within this criterion, protic solvents perturb the ESIPT rate much more than the non-protic ones, which is evident from our femtosecond upconversion experiment as well. We have observed that the ESIPT timescale for both FIS and 3HF is slower in methanol than in acetonitrile (Figure 4.3, Table 4A.2). Subsequently, it can be reasonably assumed that the FIS and 3HF molecules are localised predominantly in the aqueous layers and at the lipid-water interface of the LLC systems wherein the molecules can exist in a complex bound state with the water molecules, which slows down the ESIPT rate to the picosecond regime. It can be concluded that the fraction of molecules residing in the lipid layer of the LLC phases is minor, since the surrounding alkane-like polarity of the lipid environment is not capable of slowing down the ESIPT dynamics.

To validate the formation of possible complexed structures with the water molecules inside the LLC nanochannels, we have constructed a FIS:Water complex and tested the stability or strength of the complex using theoretical calculations (computational details have been summarised in the Appendix). As the core moiety of FIS is 3HF, we believe that the calculations of FIS will serve to understand the properties of 3HF inside LLCs as well. The spectral transitions for FIS in the gas phase and the constructed FIS:Water complex have been explored to mimic the scenario of FIS in non-hydrogen bonding solvents and protic LLC environments, respectively (Figure 4.6 and Figure 4.7). It is important to note here that although the LLC nanochannels have multiple layers of water networks, we have only

considered FIS complex with one water molecule. In order to represent a complete hydration shell around the FIS molecules, we have used the IEFPCM solvent model for the calculations of the FIS:Water complex which imitates the solvent (hydration shell) environment. The potential energy curves for the proton transfer coordinates (PTC) in the case of FIS in the gas phase have been obtained by placing the hydrogen atom at different positions from the hydroxyl oxygen to the carbonyl oxygen along the O-H bond and calculating the single-point electronic energies at each position. Following this, the maxima of the potential energy surface (PES) is confirmed as the transition state. The PTC, 1D potential energy profile is obtained systematically by elongating the O-H bond with a step size of 0.02 Å from the normal to tautomer form of FIS. This is a simple approach to get the 1D profile and attain the transition state (TS), which determines the barrier of the profile. In the case of the FIS:Water complex, we have followed a similar procedure to obtain the 1D PES profile by elongating the O-H bond with a step size of 0.02 Å from the hydroxyl moiety of the molecule to the hydrogen-bonded water molecule. Subsequently, another hydrogen of the water molecule moves toward the carbonyl oxygen of FIS, resulting in the tautomeric form. We have also calculated the intrinsic reaction coordinate (IRC) for both FIS in the gas phase and FIS:Water complex in the ground state (Figure 4A.17). Intrinsic reaction coordinate (IRC) is the mass-weighted steepest descent path on the potential energy surface (PES), starting from the transition state structure, which is a first-order saddle point. The IRC profiles match well with the 1D PES profile of the proton transfer coordinate, which confirms the consistency of our result/method.

The spectral transitions for FIS in gas phase indicate that the ground state proton transfer (from normal (N) to tautomer (T)) requires almost 4 times the activation energy than the excited state proton transfer. It can thus, be safely concluded that the tautomeric form does not exist in the ground state. In addition, the forward ESIPT reaction is almost three folds energetically favourable than the backward ESIPT reaction making the process essentially irreversible. From the energy levels of FIS in gas phase, we observe that the Frank-Condon excited state ( $S_1'$ ) for the normal form is placed at 0.186 eV above the  $S_1$  of the transition state which ensures that the ESIPT process follows a lower activation barrier pathway. Noticeably, the calculated spectral transitions of FIS:Water complex yields some very intriguing observations. The ground state proton transfer has an activation barrier of ~ 0.55 eV, which is very similar to the activation barrier of FIS in the gas phase. However, unlike in the gas phase, the  $S_1$  for the transition state of FIS:Water complex has a higher energy by ~ 0.1 eV than the



Frank-Condon ( $S_1'$ ) excited state for the normal form. This implies that for the FIS:Water complex, the ESIPT process has a finite barrier. This activation barrier can be attributed to the disruption of the FIS:Water complex required for the process of ESIPT.

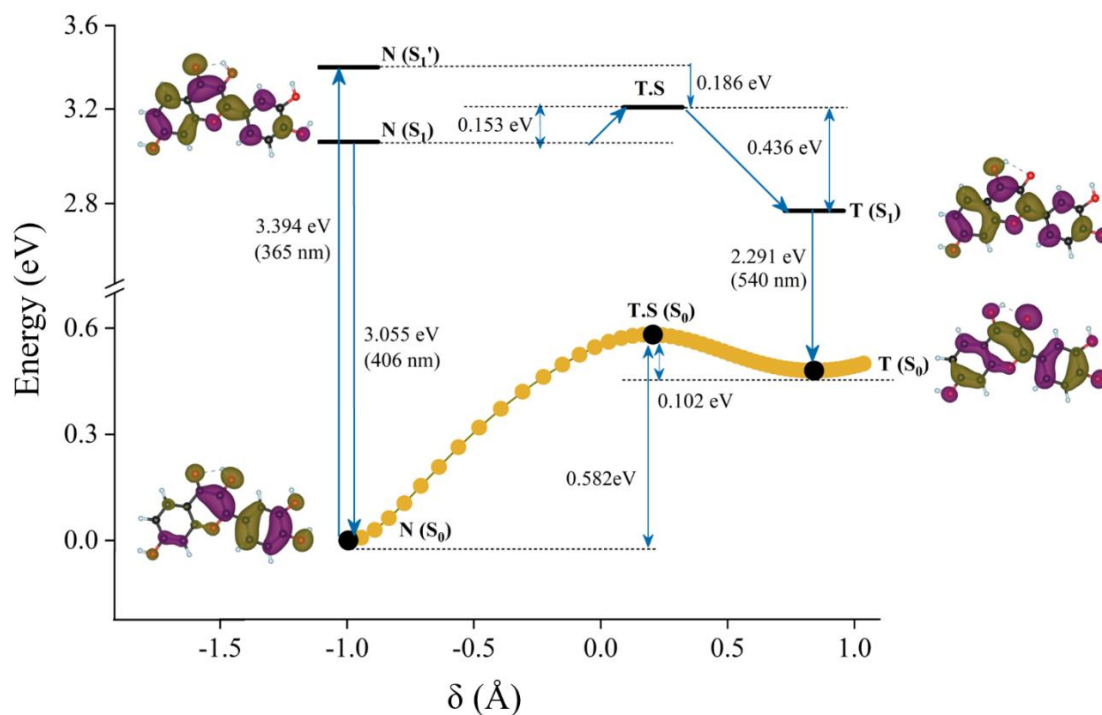


**Figure 4.6.** One-dimensional potential energy profile of the proton transfer coordinate of FIS in gas phase in the ground state and the scaled energies with respect to the ground state normal (N) species of FIS.  $\delta$  is the difference between the noncovalent (hydrogen) bond and the covalent bond of the reaction coordinate. Molecular orbitals of N and T of FIS are depicted in the figure.

The quantum mechanical calculations point towards the possibility of FIS/3HF existing in complex bound structures with the LLC water molecules in the excited state. This connotes that on photoexcitation of the normal form, it has to overcome an activation barrier to disrupt the intermolecular solvent hydrogen bonds in order to undergo the ESIPT process. The rate of the rupture of the solute-solvent complex is driven by the rate at which the intermolecular hydrogen bonds with the solvents break and reorient around the solute molecules.<sup>56, 57</sup> This is in turn dictated by the overall dynamics of the solvent molecules surrounding the fluorophore. In our previous papers and other reports in the literature, it has been established that the LLC nanochannels comprise of multiple aqueous networks, with the hydration dynamics of each water layer being different from the adjacent one.<sup>25, 27, 28</sup> The water molecules buried near the lipid headgroup region have dynamics as slow as 1 ns as a result of the hydrogen bonds with the lipid headgroups. This peripheral layer of water molecules is also hydrogen-bonded to the

adjacent water layer and in turn, slows down its dynamics. This kind of a domino effect results in a gradual retardation of the dynamics of each water layer in the LLC nanochannels, with the effect decreasing towards the central core of the channel. The ‘free’ water networks near the centre of the nanochannels is the fastest with a time scale  $\sim 10$ - $15$  ps and the intermediate ‘pseudo-bound’ water layer have a dynamics of  $\sim 150$  ps.<sup>25,27,28</sup> The drastic  $> 15$  times slower dynamics of the water even at the centre of the nanochannel compared to bulk water ( $\sim 1$  ps) results in the overall slower dynamics of the ESIPT process for the FIS and 3HF molecules inside LLCs. In addition to the retardation in the ESIPT rate of 3HF and FIS inside the LLC nanochannels, the time-resolved experiments also suggest that the topology of the LLC phases influences the extent of retardation. For both 3HF and FIS, we observe that the ESIPT time scale follows the order of  $Pn3m < Ia3d < H_{II}$ . The topological differences between the three LLC phases set them apart from each other in terms of the hydration dynamics of the contained water molecules. The  $H_{II}$  phase consists of densely packed cylinders arranged in a hexagonal lattice.<sup>13,15</sup> The two cubic phases are composed of a single continuous lipid bilayer draped on a minimal surface, which separates two interpenetrating but unconnected networks of water channels. The two water channels meet in a  $3 \times 3$  junction at an angle of  $120^\circ$  in  $Ia3d$  and a  $4 \times 4$  manner at an angle of  $109.5^\circ$  in  $Pn3m$ .<sup>13,15</sup> From these structural aspects, it can be rationalized that the diffusion of the water molecules would be slowest in the densely packed  $H_{II}$  phase and the fastest in the tetrafold  $Pn3m$  phase, leading to the slowest dynamics of the free/pseudo-bound water in the  $H_{II}$  and the fastest dynamics in the  $Pn3m$  phase. This has been elucidated in literature where for the LLC phases with the same channel radius and different topology, the diffusion of substrates and hence enzyme kinetics was found to be the highest in the  $Pn3m$  phase followed by  $Ia3d$  and lastly the  $H_{II}$  phase.<sup>58</sup> Moreover, the curvature of the lipid bilayer towards the water domains follows the order of  $Pn3m < Ia3d < H_{II}$ ,<sup>59</sup> which connotes that the lipid headgroups will be most closely packed in the  $H_{II}$  phase, leading to the highest restriction in the rotational mobility of the water molecules bound to the lipid headgroups in this phase. This kind of a topological effect known as the ‘curvature induced’ frustration<sup>60</sup> leads to the restricted dynamics of the water molecules bound to the lipid layer, with the extent of restriction following the order  $Pn3m < Ia3d < H_{II}$ . Thus, the observed trend in the ESIPT dynamics clearly mirrors the differences in the dynamics of the water networks inside the various structures of the LLC phases.

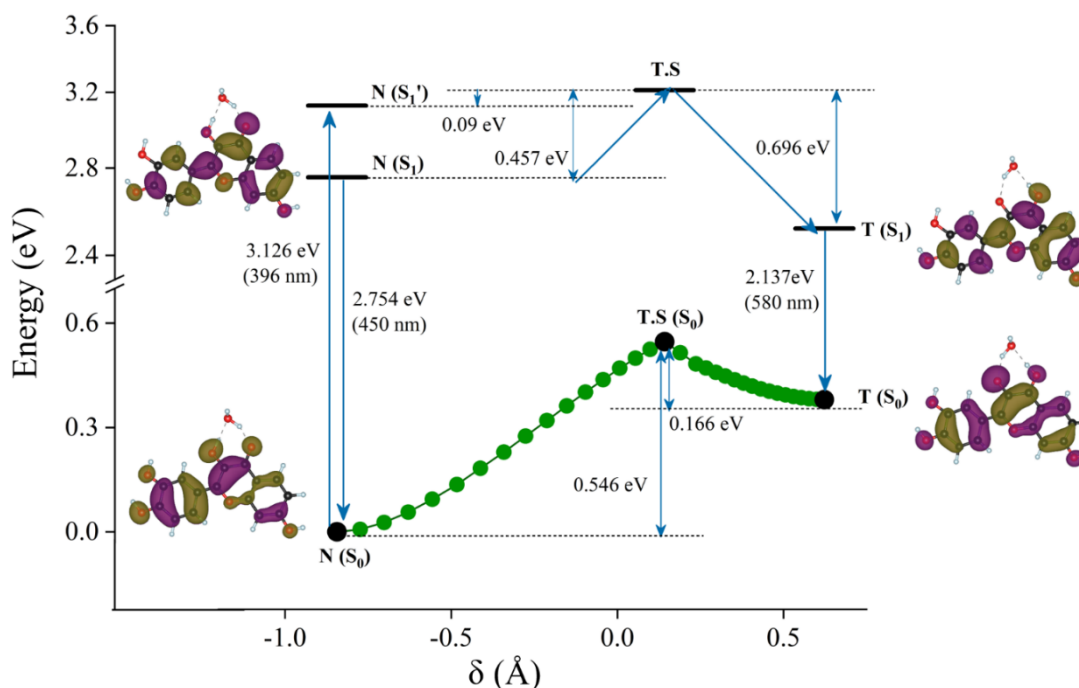


**Figure 4.7.** One-dimensional potential energy profile of the proton transfer coordinate of the constructed FIS:Water complex in the ground state and the scaled energies with respect to ground state normal (N) of FIS.  $\delta$  is the difference between the noncovalent (hydrogen) bond and the covalent bond of the reaction coordinate. Molecular orbitals of N and T of FIS have been depicted in the figure.

### 4.3 Conclusion

The focus of this work was to elucidate the hydrogen bond donating and accepting behaviour of the water molecules inside the aqueous nanochannels of lyotropic liquid crystal mesophases by employing the sensitivity of ESIPT phenomenon on the hydrogen bonding parameters of the surrounding solvents. From the steady state experiments of both FIS and 3HF, we have observed a heterogeneity in the hydrogen bond donating and accepting behaviour inside the LLC nanochannels. Despite the general alcohol like polarity of the aqueous nanochannels, on excitation of the normal form for both the ESIPT probes, the spectral pattern and ESIPT efficiency resembled closely with those of moderately polar aprotic solvents like tetrahydrofuran and acetonitrile. However, the anionic emission is also observed for both FIS and 3HF inside the LLC nanochannels, which signals the behaviour of polar protic solvents like alcohols. These contrasting observations connote that the hydrogen bond accepting and donating properties of the LLC water molecules does not match with either pure alcohols or water and are much more complex. The ESIPT process for FIS and 3HF in both polar protic and aprotic solvents occurs at an extremely fast time scale ( $<20$  ps). Interestingly, inside the

LLC phases, the ESIPT process gets slowed down by almost  $\sim 15$  times. This kind of dramatic slowing down in the rate of ESIPT is rare in the literature and it has been attributed to the exceptionally slow hydration dynamics of the LLC water molecules. The sluggish hydration dynamics inside the LLC phases slows down the rate of disruption of intermolecular solute-water complex, which is a necessary precondition for ESIPT to occur. The effect of hydration dynamics on the rate of ESIPT is also reflected from the trend in the ESIPT time scale observed in LLC phases of different topologies. The time scale of the ESIPT process for both FIS and 3HF has an order of  $H_{II} > Ia3d > Pn3m$ , which exactly follows the order of hydration dynamics inside these LLC phases.

#### 4.4 References

1. N. E. Levinger, *Science*, 2002, **298**, 1722-1723.
2. A. W. Knight, N. G. Kalugin, E. Coker and A. G. Ilgen, *Sci. Rep.*, 2019, **9**, 8246.
3. G. Algara-Siller, O. Lehtinen, F. C. Wang, R. R. Nair, U. Kaiser, H. A. Wu, A. K. Geim and I. V. Grigorieva, *Nature*, 2015, **519**, 443.
4. L. Ruiz Pestana, L. E. Felberg and T. Head-Gordon, *ACS Nano*, 2018, **12**, 448-454.
5. E. Chiavazzo, M. Fasano, P. Asinari and P. Decuzzi, *Nat. Commun.*, 2014, **5**, 3565.
6. N. Pérez-Hernández, T. Q. Luong, M. Febles, C. Marco, H.-H. Limbach, M. Havenith, C. Pérez, M. V. Roux, R. Pérez and J. D. Martín, *J. Phys. Chem. C*, 2012, **116**, 9616-9630.
7. K. Gethard, O. Sae-Khow and S. Mitra, *ACS Appl. Mater. Interfaces*, 2011, **3**, 110-114.
8. J. B. Mitchell, W. C. Lo, A. Genc, J. LeBeau and V. Augustyn, *Chem. Mater.*, 2017, **29**, 3928-3937.
9. Y. Yao, Y. Chen, Y. Liu, Y. Zhu, Y. Liu and S. Zhang, *Langmuir*, 2019, **35**, 5871-5877.
10. J. L. Skinner, P. A. Pieniazek and S. M. Gruenbaum, *Acc. Chem. Res.*, 2012, **45**, 93-100.
11. V. V. Chaban and O. V. Prezhdo, *ACS Nano*, 2011, **5**, 5647-5655.
12. R. Mezzenga, P. Schurtenberger, A. Burbidge and M. Michel, *Nat. Mater.*, 2005, **4**, 729-740.
13. C. V. Kulkarni, *Nanoscale*, 2012, **4**, 5779-5791.

14. C. V. Kulkarni, W. Wachter, G. Iglesias-Salto, S. Engelskirchen and S. Ahualli, *Phys. Chem. Chem. Phys.*, 2011, **13**, 3004-3021.
15. N. Garti, D. Libster and A. Aserin, *Food Funct.*, 2012, **3**, 700-713.
16. J. C. Shah, Y. Sadhale and D. M. Chilukuri, *Adv. Drug Delivery Rev.*, 2001, **47**, 229-250.
17. R. Negrini and R. Mezzenga, *Langmuir*, 2011, **27**, 5296-5303.
18. S. Ghosh, L. Ramos and H. Remita, *Nanoscale*, 2018, **10**, 5793-5819.
19. E. Otón, J. M. Otón, M. Caño-García, J. M. Escolano, X. Quintana and M. A. Geday, *Opt. Express*, 2019, **27**, 10098-10107.
20. T. Mishraki-Berkowitz, P. Ben Ishai, A. Aserin, Y. Feldman and N. Garti, *Phys. Chem. Chem. Phys.*, 2015, **17**, 9499-9508.
21. L. Bitan-Cherbakovsky, D. Libster, D. Appelhans, B. Voit, A. Aserin and N. Garti, *J. Phys. Chem. B*, 2014, **118**, 4016-4024.
22. A. Zabara, J. T. Y. Chong, I. Martiel, L. Stark, B. A. Cromer, C. Speziale, C. J. Drummond and R. Mezzenga, *Nat. Commun.*, 2018, **9**, 544.
23. J. J. Vallooran, S. Handschin, S. M. Pillai, B. N. Vetter, S. Rusch, H.-P. Beck and R. Mezzenga, *Adv. Funct. Mater.*, 2016, **26**, 181-190.
24. N. I. Zahid, O. K. Abou-Zied and R. Hashim, *J. Phys. Chem. C*, 2013, **117**, 26636-26643.
25. B. Roy, S. Satpathi, K. Gavvala, R. K. Koninti and P. Hazra, *J. Phys. Chem. B*, 2015, **119**, 11721-11731.
26. W. Wachter, G. Trimmel, R. Buchner and O. Glatter, *Soft Matter*, 2011, **7**, 1409-1417.
27. J. Kim, W. Lu, W. Qiu, L. Wang, M. Caffrey and D. Zhong, *J. Phys. Chem. B*, 2006, **110**, 21994-22000.
28. K. Das, B. Roy, S. Satpathi and P. Hazra, *J. Phys. Chem. B*, 2019, **123**, 4118-4128.
29. R. E. Hubbard and M. K. Haider, *Hydrogen bonds in proteins: role and strength. In: Encyclopedia of Life Sciences (ELS)*, John Wiley & Sons, Ltd: Chichester., 2010.
30. G. Caron, J. Kihlberg and G. Ermondi, *Med. Res. Rev.*, 2019, **39**, 1707-1729.
31. K. R. Castellano, *Molecules*, 2014, **19**.
32. V. S. Padalkar and S. Seki, *Chem. Soc. Rev.*, 2016, **45**, 169-202.
33. A. P. Demchenko, K.-C. Tang and P.-T. Chou, *Chem. Soc. Rev.*, 2013, **42**, 1379-1408.
34. P. Zhou and K. Han, *Acc. Chem. Res.*, 2018, **51**, 1681-1690.

35. A. C. Sedgwick, L. Wu, H.-H. Han, S. D. Bull, X.-P. He, T. D. James, J. L. Sessler, B. Z. Tang, H. Tian and J. Yoon, *Chem. Soc. Rev.*, 2018, **47**, 8842-8880.
36. G. A. Brucker and D. F. Kelley, *J. Phys. Chem.*, 1989, **93**, 5179-5183.
37. J. Mishra, J. Swain and A. K. Mishra, *J. Phys. Chem. B*, 2018, **122**, 181-193.
38. S. Selvam and A. K. Mishra, *Photochem. Photobiol. Sci.*, 2011, **10**, 66-75.
39. M. Funes, N. M. Correa, J. J. Silber and M. A. Biasutti, *Photochem. Photobiol.*, 2007, **83**, 486-493.
40. B. Jana, S. Senapati, D. Ghosh, D. Bose and N. Chattopadhyay, *J. Phys. Chem. B*, 2012, **116**, 639-645.
41. A. J. G. Strandjord and P. F. Barbara, *J. Phys. Chem.*, 1985, **89**, 2355-2361.
42. P. K. Mandal and A. Samanta, *J. Phys. Chem. A*, 2003, **107**, 6334-6339.
43. S. Lazzaroni, D. Dondi, A. Mezzetti and S. Protti, *Photochem. Photobiol. Sci.*, 2018, **17**, 923-933.
44. D. Roy, R. Karmakar, S. K. Mondal, K. Sahu and K. Bhattacharyya, *Chem. Phys. Lett.*, 2004, **399**, 147-151.
45. J. E. Hansen, E. Pines and G. R. Fleming, *J. Phys. Chem.*, 1992, **96**, 6904-6910.
46. B. Roy and P. Hazra, *Journal of Molecular Liquids*, 2019, **285**, 178-184.
47. S. Ameer-Beg, S. M. Ormson, R. G. Brown, P. Matousek, M. Towrie, E. T. J. Nibbering, P. Foggi and F. V. R. Neuwahl, *J. Phys. Chem. A*, 2001, **105**, 3709-3718.
48. A. Douhal, M. Sanz, L. Tormo and J. A. Organero, *ChemPhysChem*, 2005, **6**, 419-423.
49. B. J. Schwartz, L. A. Peteanu and C. B. Harris, *J. Phys. Chem.*, 1992, **96**, 3591-3598.
50. A. S. R. Koti, M. M. G. Krishna and N. Periasamy, *J. Phys. Chem. A*, 2001, **105**, 1767-1771.
51. A. Banerjee and P. K. Sengupta, *Chem. Phys. Lett.*, 2006, **424**, 379-386.
52. M. Mohapatra and A. K. Mishra, *J. Phys. Chem. B*, 2011, **115**, 9962-9970.
53. S. Mondal, S. Basu and D. Mandal, *Chem. Phys. Lett.*, 2009, **479**, 218-223.
54. S. Das, M. A. Rohman and A. Singha Roy, *J. Photochem. Photobiol., B*, 2018, **180**, 25-38.
55. S. Basu, S. Mondal and D. Mandal, *J. Chem. Phys.*, 2010, **132**, 034701.
56. D. Ghosh, A. K. Pradhan, S. Mondal, N. A. Begum and D. Mandal, *Phys. Chem. Chem. Phys.*, 2014, **16**, 8594-8607.

57. D. Ghosh, S. Batuta, S. Das, N. A. Begum and D. Mandal, *J. Phys. Chem. B*, 2015, **119**, 5650-5661.
58. W. Sun, J. J. Vallooran and R. Mezzenga, *Langmuir*, 2015, **31**, 4558-4565.
59. C. V. Kulkarni, T.-Y. Tang, A. M. Seddon, J. M. Seddon, O. Ces and R. H. Templer, *Soft Matter*, 2010, **6**, 3191-3194.
60. S. Roy, D. Skoff, D. V. Perroni, J. Mondal, A. Yethiraj, M. K. Mahanthappa, M. T. Zanni and J. L. Skinner, *J. Am. Chem. Soc.*, 2016, **138**, 2472-2475.

## 4.5 Appendix

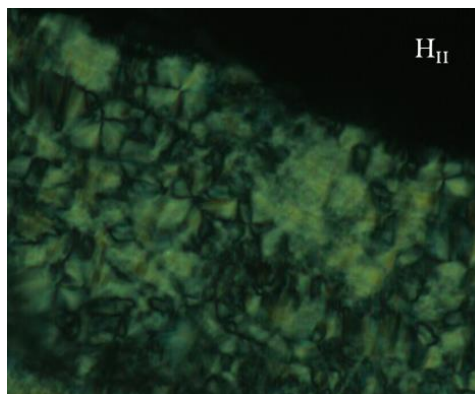


**Figure 4A.1.** Small-angle X-ray scattering pattern of the  $H_{II}$  phase at 298 K.

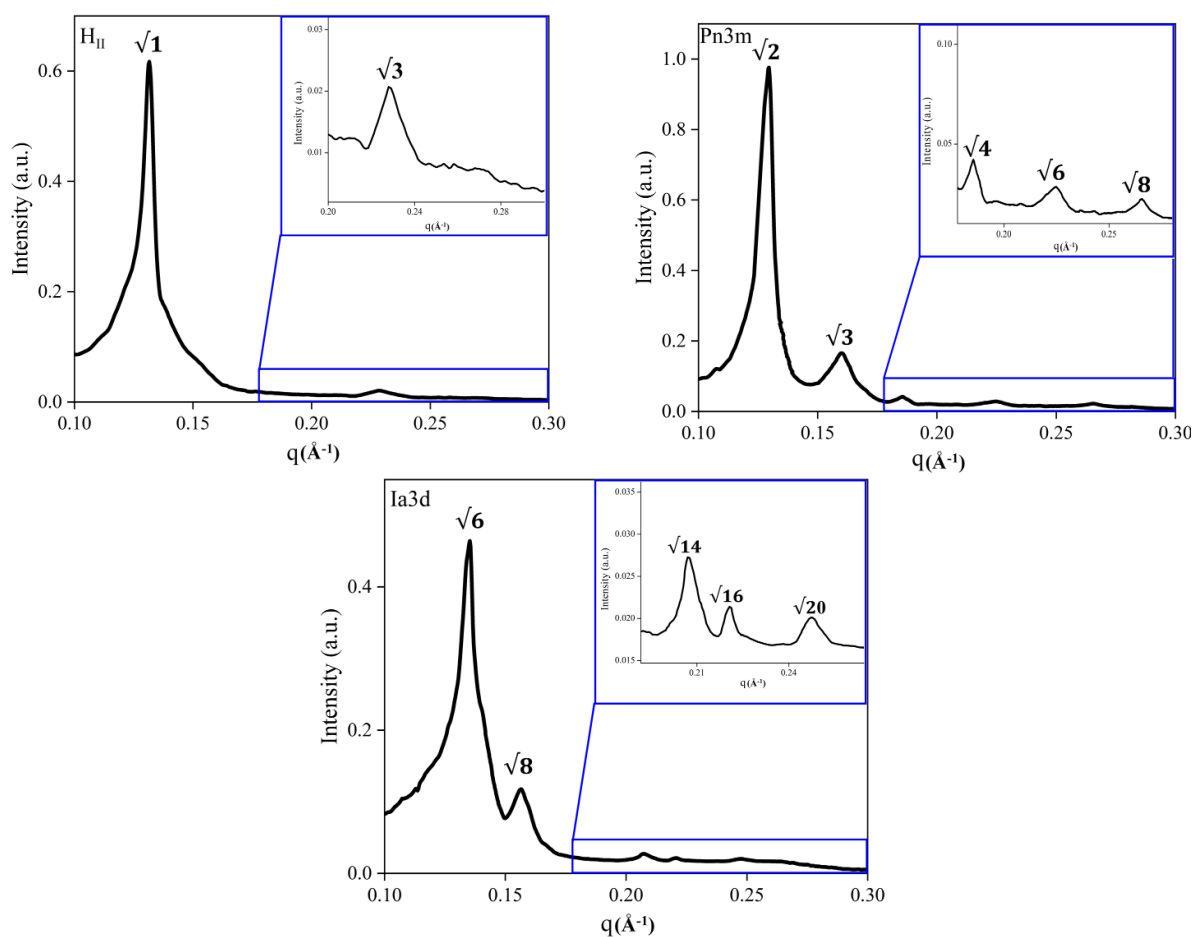


**Figure 4A.2.** Small-angle X-ray scattering pattern of  $H_{II}$ ,  $Pn3m$  and  $Ia3d$  phases at 298 K.



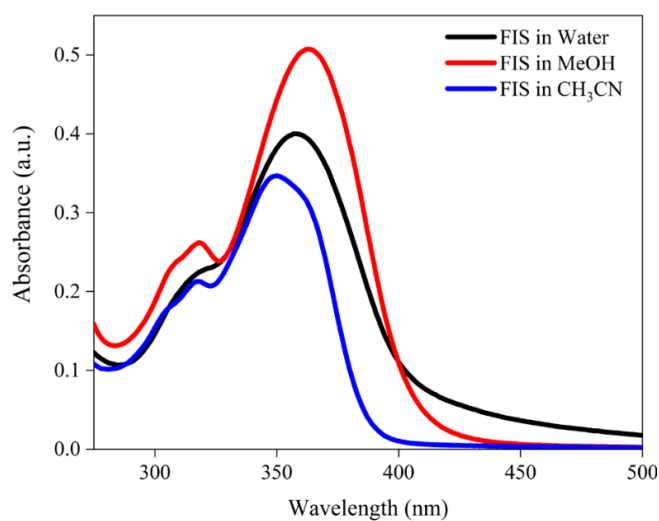


**Figure 4A.3.** Absorption spectra of FIS in aprotic and protic solvents.

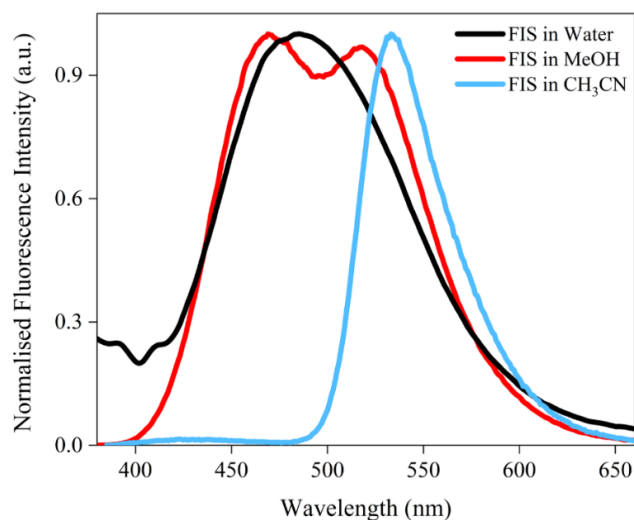


**Figure 4A.4.** Emission spectra of FIS in different protic and aprotic solvents at  $\lambda_{\text{ex}} = 360$  nm.

**Table 4A.1.** Kamlet-Taft solvent parameters for some solvents.

Solvent	$\alpha$	$\beta$	$I_{\text{N}^*} / I_{\text{T}^*}$ (FIS)	$I_{\text{N}^*} / I_{\text{T}^*}$ (3HF)
Methanol	0.98	0.66	0.9345	0.442
Ethanol	0.86	0.75	0.387	0.30
Acetonitrile	0.19	0.40	0.018 <sup>a</sup>	0.021 <sup>a</sup>
Tetrahydrofuran	0.0	0.55	0.014 <sup>a</sup>	0.070 <sup>a</sup>
Benzene	0.0	0.10	0.011	-

<sup>a</sup>Experimental value. The Kamlet-Taft parameters and values of  $I_{\text{N}^*} / I_{\text{T}^*}$  for 3HF have been taken from *Photochem. Photobiol. Sci.*, **2018**, *17*, 923. The values of  $I_{\text{N}^*} / I_{\text{T}^*}$  for FIS have been taken from *Photochem. Photobiol.* **2007**, *83*, 486.

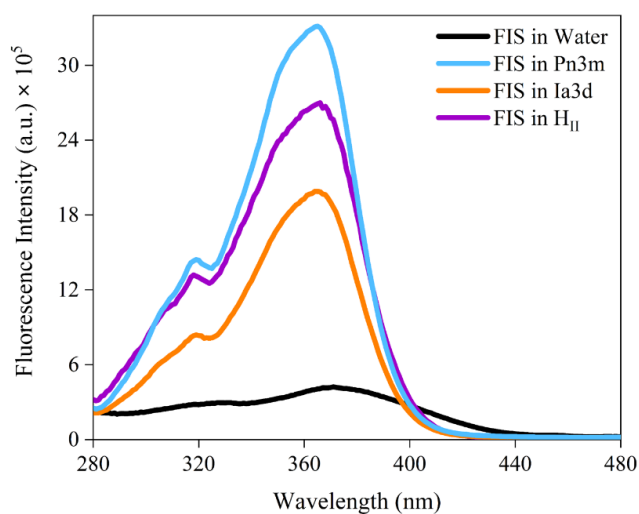


**Figure 4A.5.** Excitation spectra of FIS in water and LLC phases at  $\lambda_{em} = 540$  nm.

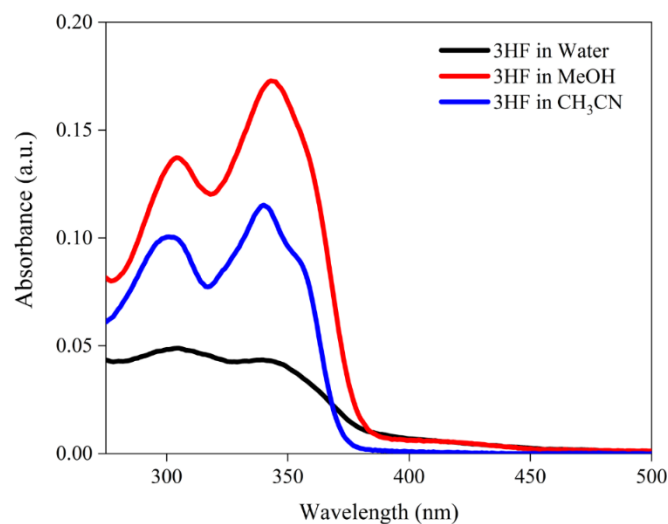


**Figure 4A.6.** Absorption spectra of 3HF in aprotic and protic solvents.

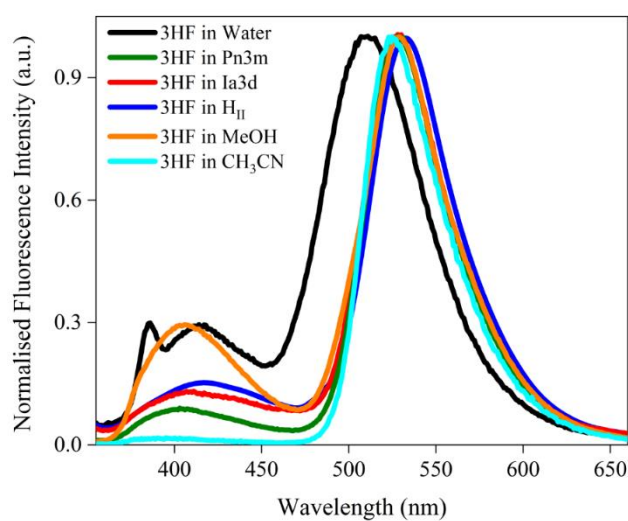


**Figure 4A.7.** Emission spectra of 3HF in different solvents and LLC phases ( $\lambda_{ex} = 340$  nm).

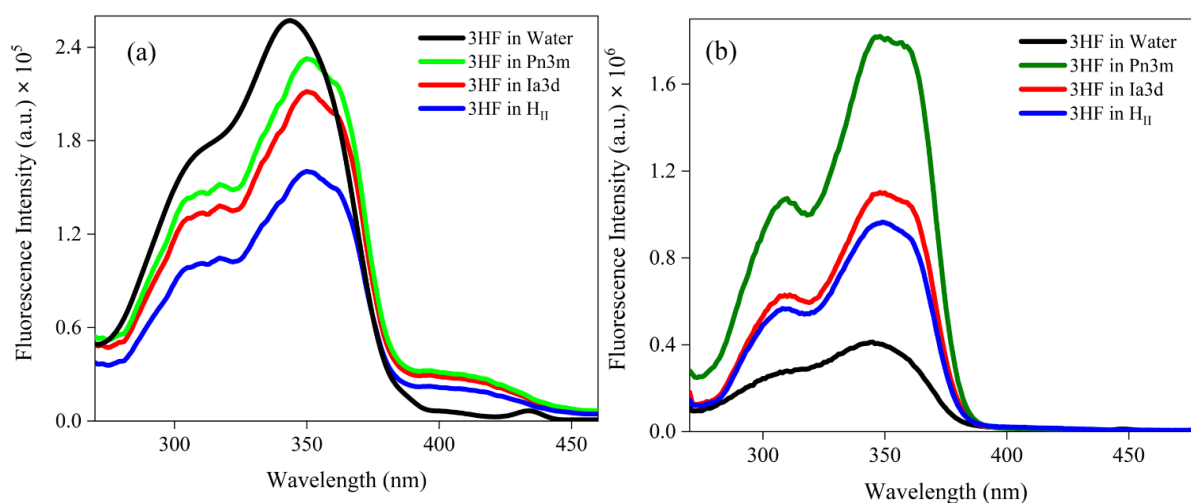


**Figure 4A.8.** Excitation spectra of 3HF in water and LLC phases at (a)  $\lambda_{em} = 480$  nm (b)  $\lambda_{em} = 530$  nm.

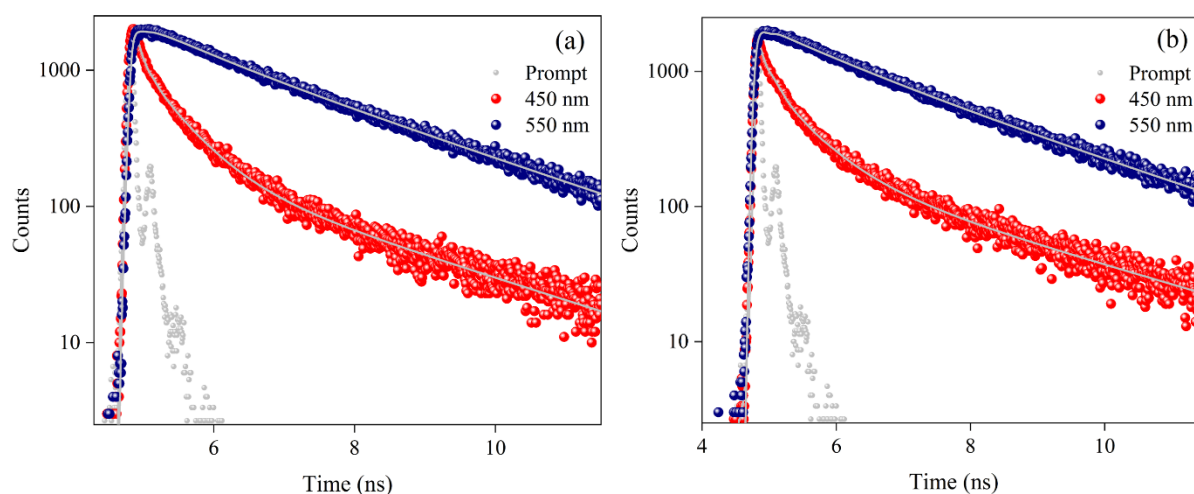


**Figure 4A.9.** Lifetime profiles of FIS in (a) *Ia3d* and (b) *Pn3m* LLC phases collected at different emission wavelengths. The solid lines denote the fits of the decay profiles. ( $\lambda_{ex} = 375$  nm).

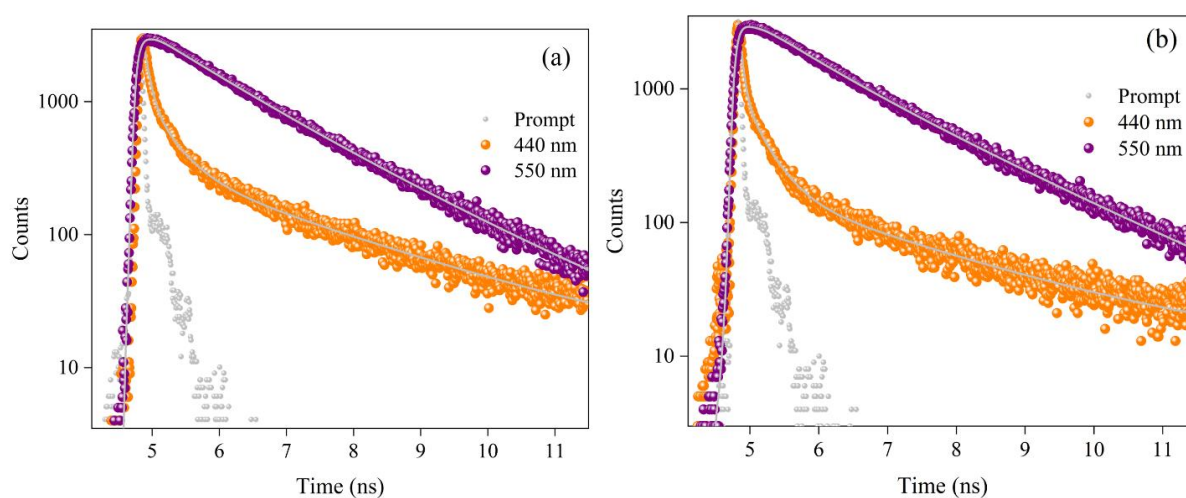


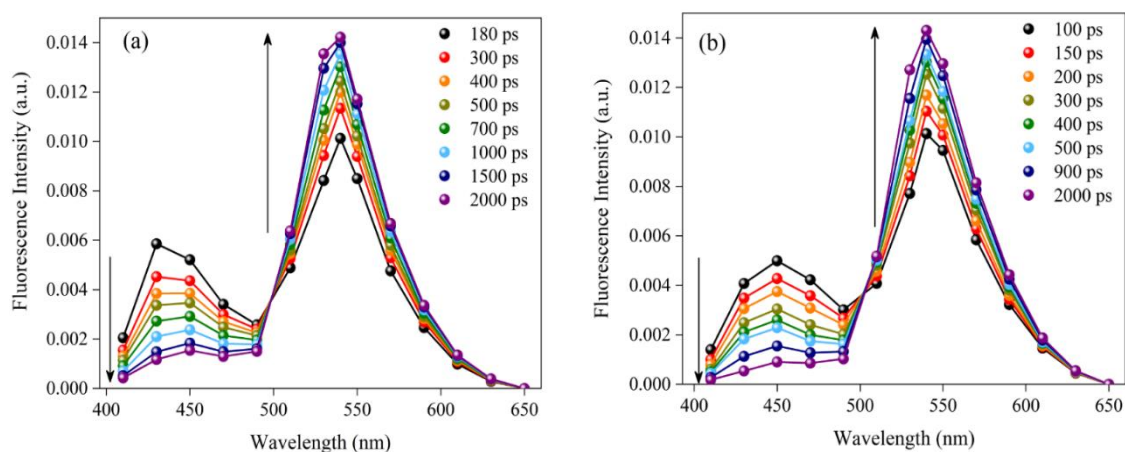
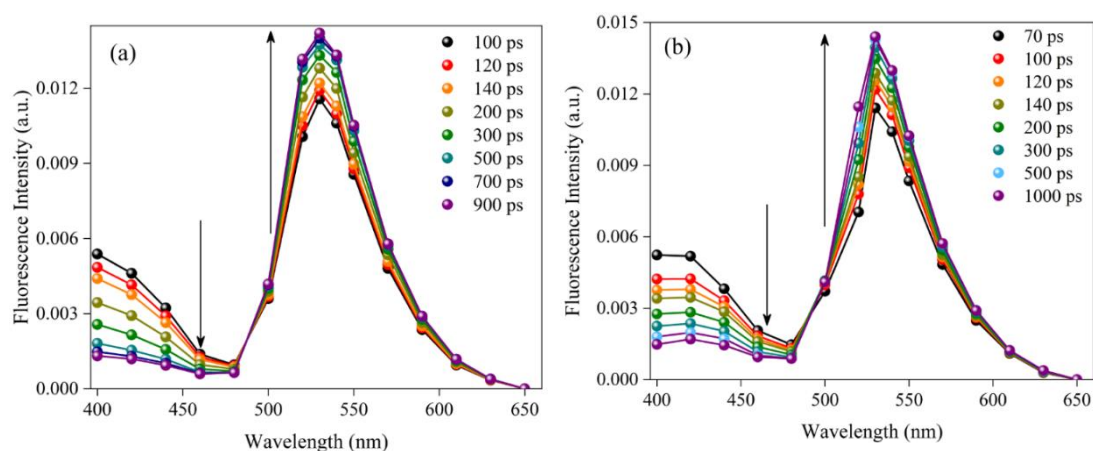
**Figure 4A.10.** Lifetime profiles of 3HF in (a) *Ia3d* and (b) *Pn3m* LLC phases collected at different emission wavelengths. The solid lines denote the fits of the decay profiles. ( $\lambda_{ex} = 375$  nm).

**Table 4A.2.** Lifetime fitting parameters of 3HF and FIS in neat solvents from femtosecond upconversion experiments.

Sample	$\alpha_1$	$\tau_1$ (ps)	$\alpha_2$	$\tau_2$ (ps)
3HF in MeOH	- 0.48	15	0.52	200
3HF in CH <sub>3</sub> CN	- 0.35	10	0.65	660
FIS in MeOH	- 0.40	13	0.60	300
FIS in CH <sub>3</sub> CN	- 0.31	8	0.69	530

**Table 4A.3.** Lifetime fitting parameters of FIS and 3HF in water from TCSPC experiments.

Sample	$\lambda_{em}$	$\alpha_1$	$\tau_1$ (ns)	$\alpha_2$	$\tau_2$ (ns)	$\alpha_3$	$\tau_3$ (ns)
3HF in water	550	0.99	0.170	0.01	3.781	-	-
FIS in water	550	0.09	1.045	0.74	0.050	0.17	0.325

**Figure 4A.11.** Time-resolved area normalised spectra of FIS in (a) *Ia3d* and (b) *Pn3m* ( $\lambda_{ex} = 375$  nm).**Figure 4A.12.** Time-resolved area normalised spectra of 3HF in (a) *Ia3d* and (b) *Pn3m* ( $\lambda_{ex} = 375$  nm).

### 4.5.1 Details of Quantum Chemical Calculations

In order to determine the ground state of the FIS (in FIS:Water) molecule in the gas (solvent) phase, the DFT based calculations were performed using the Gaussian Software (G09-rev-D).<sup>A1</sup> The B3LYP exchange-correlation functional<sup>A2</sup> and double zeta (6-311++G(d,p)) basis set<sup>A3</sup> were used for the calculations. The solvent (water) effects were taken into account using the Polarizable Continuum Model (PCM) using the integral equation formalism variant (IEFPCM) solvation model.<sup>A4</sup> The vertical excitations energies, oscillator strengths, and optimisation of excited state ( $S_1$ ) were computed at TD-DFT at the same level of theory. For the transition state (TS), the Synchronous Transit-Guided Quasi-Newton (STQN) Method was used. It results in the actual transition structure using an empirical estimate of the Hessian and suitable starting structures of FIS. The lowest energy structures of the FIS molecule were found to be planar (Figure 4A.13 a)). However FIS:Water lowest energy structures lost planarity and water molecule formed hydrogen-bonded with hydroxyl group (Figure 4A.13 b)). The proton transfer coordinate ( $\delta$ ) was defined as the difference between non-covalent bond ( $d_1$ ) and O-H covalent bond ( $d_2$ ) of FIS molecule. Similarly, another proton transfer coordinate ( $\delta'$ ) was defined as the difference between non-covalent bond ( $D_1$ ) with hydrogen bonded water molecule in FIS:Water complex and O-H covalent bond ( $D_2$ ) of the molecule. The one-dimensional (1D) potential energy profiles of both the proton transfer coordinates ( $\delta$  and  $\delta'$ ) were performed. The negative values of the proton transfer coordinate (PTC) result in tautomers of the FIS molecule. The important optimised hydrogen bonding parameters have been depicted in Figure 4A.14 and Figure 4A.15. Then further the PTC was compared with intrinsic coordinates (IRC) (Figure 4A.17). Furthermore, excited state study was performed by TDDFT and computed electron density difference map (EDDM) (Figure 4A.16) of the first excited transition by Gauss-Sum package.<sup>A5</sup> The EDDM profile displays the charge transfer of FIS molecule.

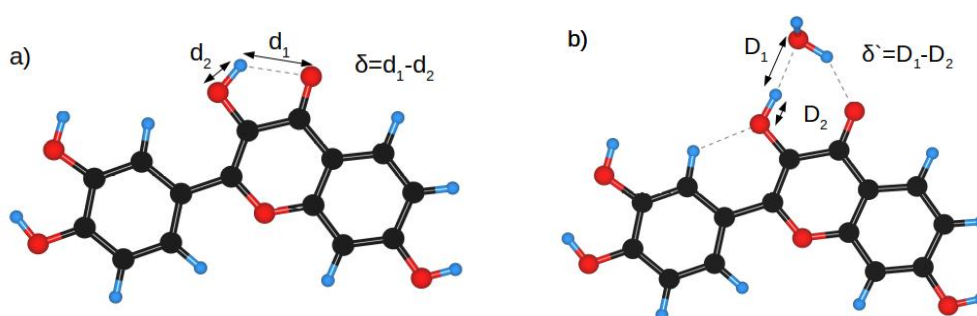


**Figure 4A.13.** Optimized geometries of a) FIS molecule and b) FIS:Water complex.

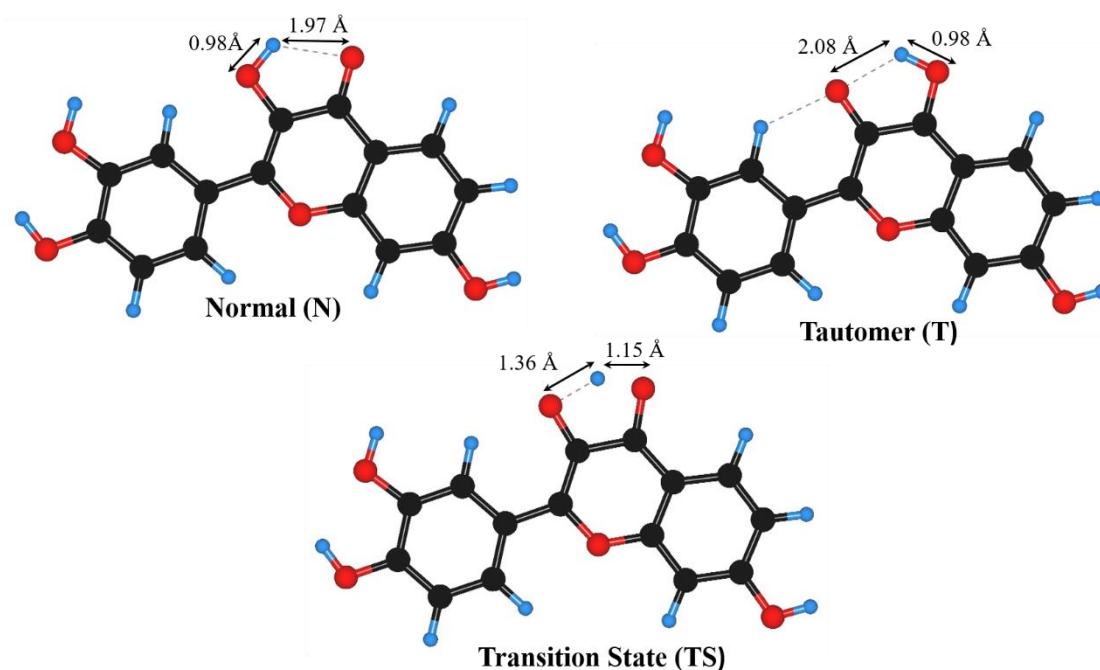


**Figure 4A.14.** Optimized ground state molecular structures of the normal, tautomer and proton transfer transition state structures of FIS in the gas phase. Bond distances are indicated with arrows.

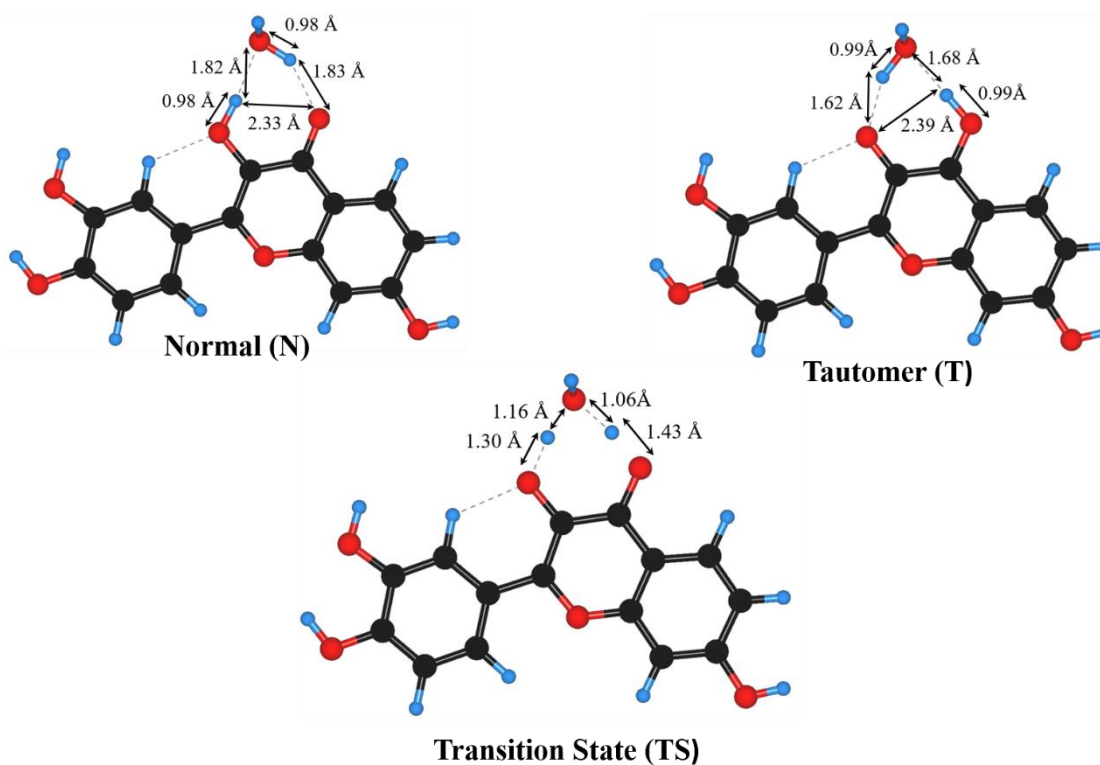


**Figure 4A.15.** Optimized ground state molecular structures of the normal, tautomer and proton transfer transition state structures of FIS:Water complex. Bond distances are indicated with arrows.

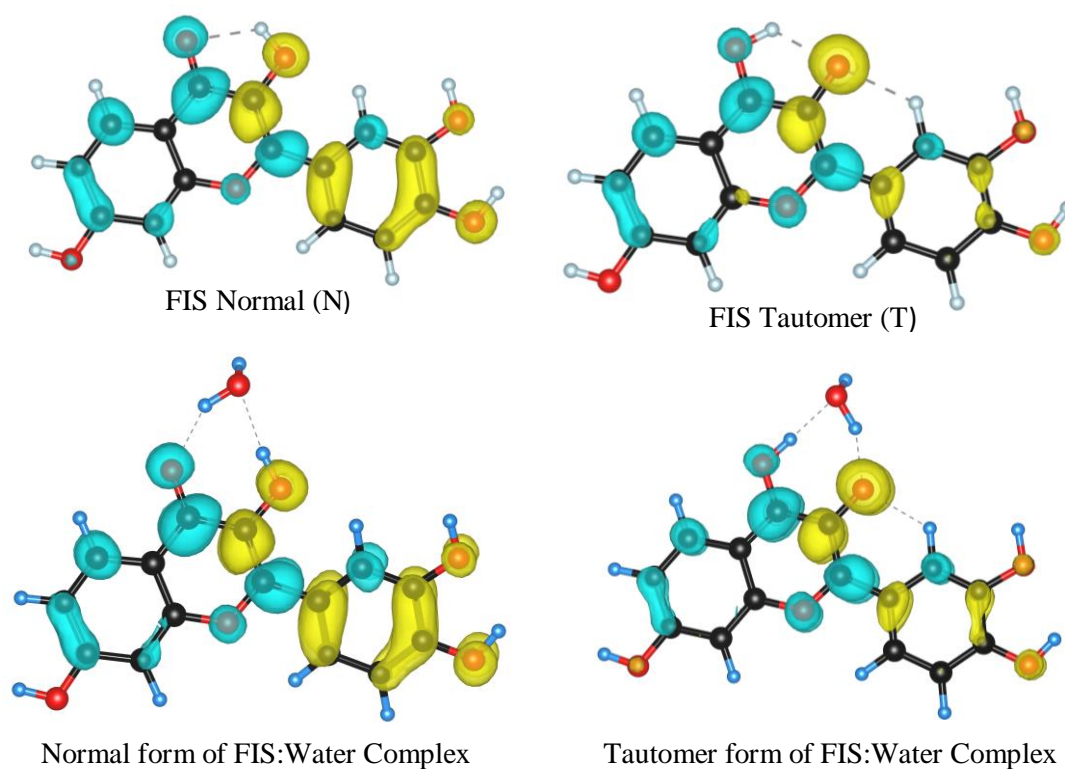


**Figure 4A.16.** Electron density difference maps (EDDM) of the normal and tautomer forms of FIS and the normal and tautomer forms of FIS:Water complexes. Hydrogen bonding is denoted by grey dashed lines.

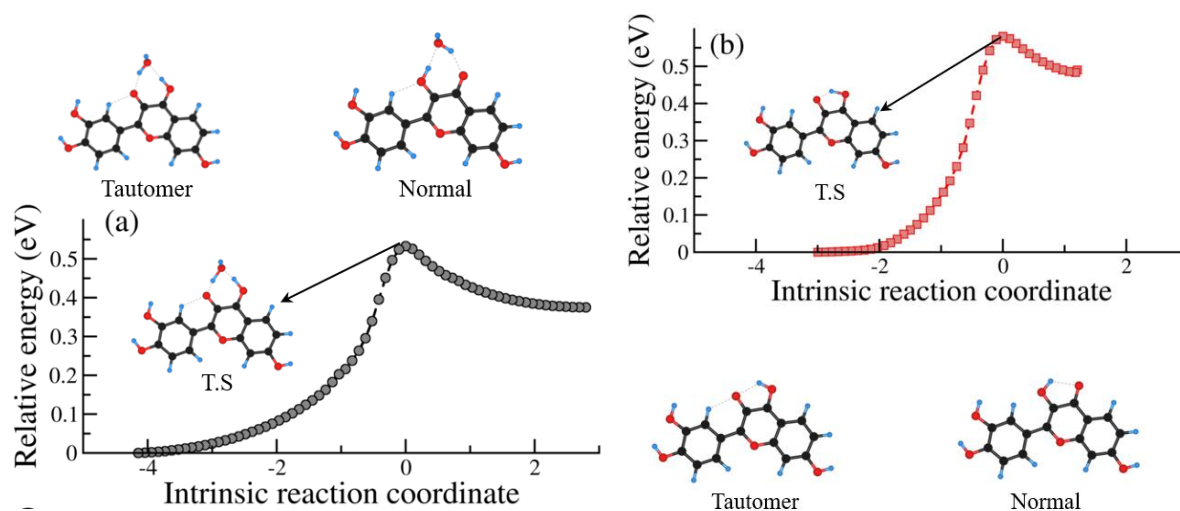


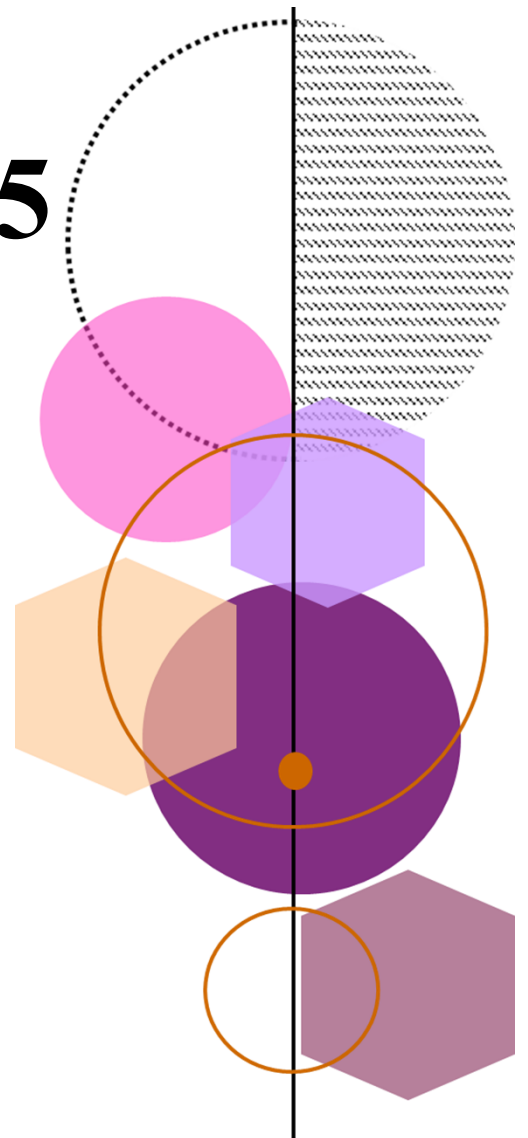
**Figure 4A.17.** The intramolecular reaction coordinate (IRC) profile of (a) FIS:Water complex and (b) FIS along proton transfer coordinate.

### 4.5.2 Appendix References

- A1. M. J. Frisch, G. W. Trucks, H. B. Schlegel, G. E. Scuseria, M. A. Robb, J. R. Cheeseman, G. Scalmani, V. Barone, B. Mennucci, G. A. Petersson, *et al.* *Gaussian 16 Rev. C.01*, Wallingford, CT, 2016.
- A2. J. Tirado-Rives, W. L. Jorgensen, *J. Chem. Theory Comput.*, 2008, **4**, 297-306.
- A3. R. Krishnan, J. S. Binkley, R. Seeger, J. A. Pople, *J. Chem. Phys.*, 1980, **72**, 650-654.
- A4. J. Tomasi, B. Mennucci, E. Cancès, *J. Mol. Struct.: THEOCHEM*, 1999, **464**, 211–226.
- A5. N. M. O'boyle, A. L. Tenderholt, K. M. Langner, *J. Comput. Chem.*, 2008, **29**, 839-845.



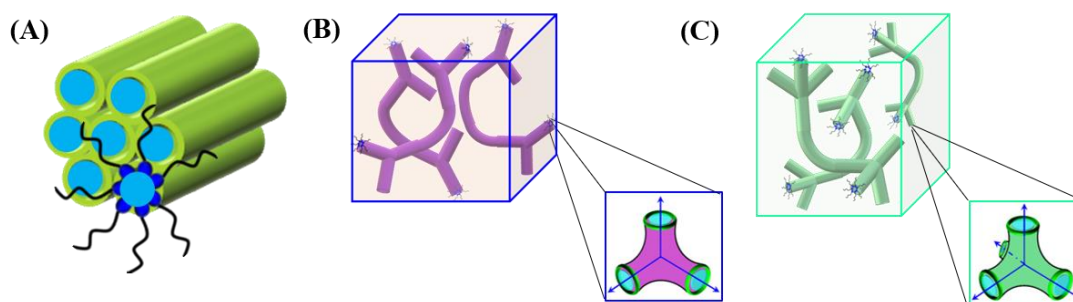
# Chapter 5



**Proton-Coupled Electron  
Transfer in the Aqueous  
Nanochannels of Lyotropic  
Liquid Crystals: Interplay of  
H-Bonding and Polarity  
Effects**

## 5.1 Introduction

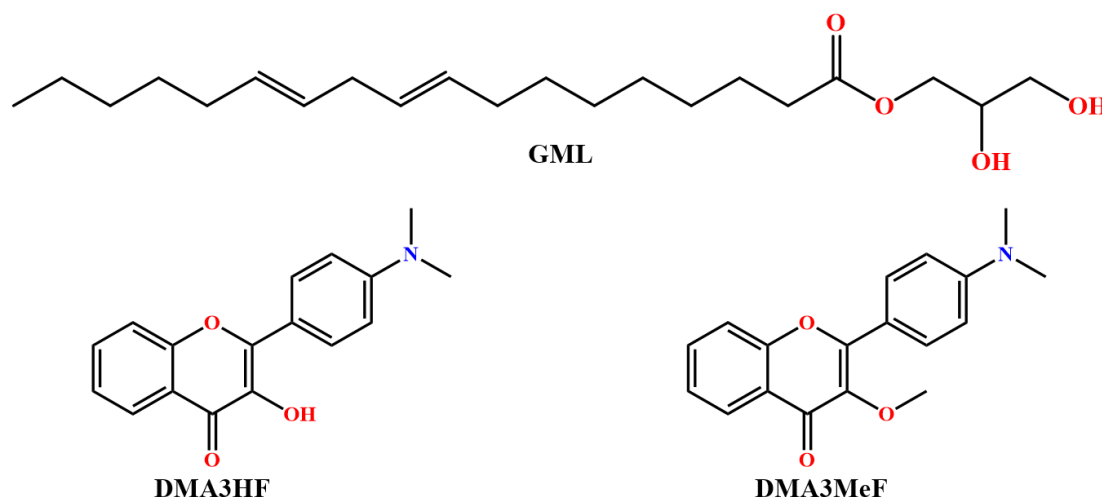
Water is the most anomalous solvent compared to solvents of similar molecular sizes and the reason behind this lies in the unique ability of the water molecules to form hydrogen bonds with four other water molecules in an approximately tetrahedral configuration.<sup>1, 2</sup> Additionally, the extended hydrogen-bonded network is not static in nature, instead the hydrogen bonds continually break and re-form at an ultrafast ps timescale.<sup>2, 3</sup> However, water that is confined in nanopores and at interfaces exhibits a peculiar hydrogen-bonded structural network and dynamics unlike that of bulk water.<sup>2-5</sup> The unique behaviour of nanoscopic and interfacial water influences a wide variety of functions and utilizations, such as biomolecule function,<sup>6</sup> protein folding,<sup>7</sup> catalysis,<sup>8</sup> conduction through nanotubes<sup>9</sup> *etc.*<sup>5</sup> The innumerable applications of nanoscopic water encompassing a broad range of fields have been inspiring researchers to decipher their unusual phenomena since the last couple of decades. In this regard, one of the systems that have garnered budding attention in the last few years is the ‘soft’ lyotropic liquid crystal (LLC). Lyotropic liquid crystals are self-assembled nanostructures of water and lipids, having either a concave or a convex lipid-water interface depending on the shape of the lipid molecule.<sup>10-12</sup> In particular, the concave lyotropic liquid crystal, wherein water domains are encased inside a continuous lipid matrix, has gained immense importance owing to its promising applications in a wide range of areas like food technology, pharmaceuticals and health, industry, material science and technology.<sup>10, 13</sup> One of the major attractions of LLC materials is the rich library of morphologies, such as the 1D inverse hexagonal phase ( $H_{II}$ ), the 2D lamellar phase ( $L_\alpha$ ), and the 3D bicontinuous cubic phases ( $V_2$ ), that can be obtained by simply varying the conditions of temperature and lipid-water composition (Scheme 5.1).<sup>12-14</sup>



**Scheme 5.1.** Schematic representation of the inverse (A)  $H_{II}$  (B)  $Ia3d$  and (C)  $Pn3m$  mesophases.

The intrinsically diverse nature of the morphologies renders each LLC structure with properties particular to it. For instance, the inverse hexagonal phase is a popular template for the synthesis of various nanomaterials.<sup>15</sup> The bicontinuous cubic phases have a strong resemblance to the lipidic membranes in nature.<sup>16</sup> These mesophases have been used as platforms for the crystallization of membrane proteins, which do not tend to crystallize in bulk medium, for the determination of their structure<sup>17</sup> and also for the detection of various pathogens, including the Ebola virus<sup>18</sup>. It has been popularly speculated that the specific macroscopic functions of the LLC materials are intimately interlinked with the arrangement and behaviour of the nanoscopic domains.<sup>12</sup> In particular, the behaviour of water molecules inside the nanochannels, such as, the precise nature of the water nanochannels, dynamics of the trapped water molecules and the local heterogeneity of the phases are perceived to dictate the macroscopic functions.<sup>12, 19</sup> Consequently, substantial efforts have been devoted to obtain an in-depth molecular picture of the various fundamental properties of both the lipidic and aqueous LLC domains. In this context, we have recently elucidated the hydrogen bond donating and accepting parameters at different regions of the LLC nanochannels as well as evaluated the effect of the water network on the proton transfer process.<sup>20</sup> A clear heterogeneity was observed in the hydrogen bonding parameters of the water molecules inside the LLC nanochannels. Besides this, the hydration dynamics of the LLC water channels have also been probed using dielectric relaxation spectroscopy and fluorescence spectroscopy by a number of researchers.<sup>21-24</sup> All the studies reveal the presence of multiple discrete aqueous layers in the LLC nanochannels, with the dynamics of each layer distinctly different from that of the adjacent one. In our previous reports, we have also explored the relationship between the structural morphology of the LLC phases and the properties of the aqueous nanochannels.<sup>20, 21</sup> Notably, in most of the fluorescence-based studies so far, the various properties of the LLC aqueous nanochannels have been probed by utilising molecules that are sensitive to a particular parameter such as either polarity or hydrogen bond accepting and donating parameters or hydration dynamics. This kind of approach faces a couple of major limitations. The first limitation is that since the LLC nanochannels are not dielectrically homogenous in nature, as evidenced by previous studies,<sup>21, 24</sup> the various probes are most likely to be distributed heterogeneously throughout the nanochannels as a result of their different structural hydrophobicities. Consequently, this gives rise to a location dependent sensing of the various

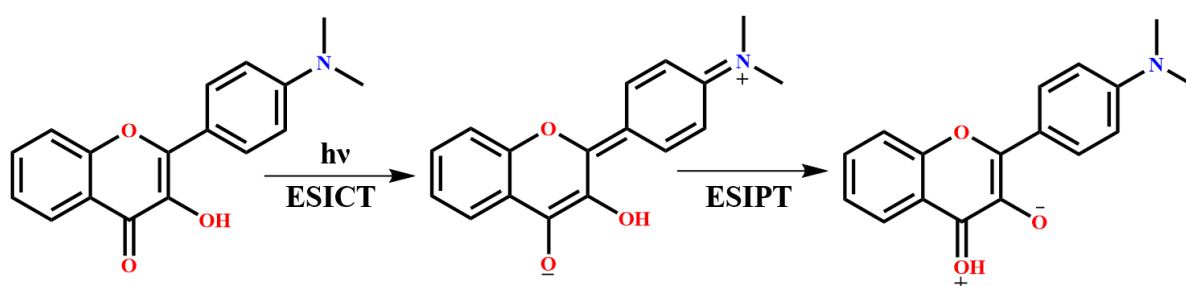
properties of the LLC water molecules. Secondly, as the probes are sensitive to a single parameter of the surrounding environment, none of them can simultaneously distinguish between the effects of hydrogen bonding abilities, micropolarity and hydration dynamics of the LLC nanochannels. These disadvantages necessitate the use of a single fluorescent probe where the number of independent environment-sensitive properties are large enough to characterize the interplay between the various aspects of the LLC nanochannels.



**Scheme 5.2.** Chemical structures of 1-Linoleoyl-rac-glycerol (GML), 4'-N,N-dimethylamino-3-hydroxyflavone (DMA3HF) and 4'-N,N-dimethylamino-3-methoxyflavone (DMA3MeF).

In this context, molecules that exhibit the phenomenon of proton-coupled electron transfer (PCET) are ideal multi-domain probes for the micro-heterogenous LLC nanochannels. Apart from being a fundamental process in both chemistry and biology, one of the most appealing facets of PCET is its multi-parametric environment sensitivity, which allows PCET molecules to act as reliable sensors.<sup>25-27</sup> In PCET, excited state intramolecular proton transfer (ESIPT) and excited state intramolecular charge transfer (ESICT) processes are coupled kinetically and energetically.<sup>25, 26</sup> Among the many PCET molecules known in the literature, the 4'-N,N-dialkylamino substituted 3-hydroxyflavone dye is one of the most well-explored molecules and is an ideal model system for PCET (Scheme 5.2). The PCET process in the 4'-N,N-dialkylamino substituted 3-hydroxyflavone involves an initial ESICT process on Frank-Condon photoexcitation. The normal/enol form of the molecule in the excited state ( $N^*$ ) undergoes a rapid and huge charge separation.<sup>27-30</sup> The charge-transfer characteristics of the  $N^*$  species render it extremely sensitive to the polarity of the surrounding medium. Polar solvents

tend to stabilise the energy of dipolar  $N^*$  species by reorienting themselves around the molecule to attain a stable configuration whereas, non-polar solvents are unable to do so. The ESICT process is followed by an ESIPT transformation of the excited state normal form to the keto/tautomeric form ( $T^*$ ) (Scheme 5.3). Stemming from the PCET phenomena, the 4'-N,N-dialkylamino substituted system displays significant differences in its fluorescence properties in comparison to the parent ESIPT 3-hydroxyflavone molecule. While the efficiency and the dynamics of ESIPT process in 3-hydroxyflavone are responsive to the hydrogen bonding parameters of the surrounding medium, the ESIPT phenomenon in 4'-N,N-dialkylamino substituted 3-hydroxyflavone is simultaneously sensitive to both the hydrogen bonding parameters as well as the solvent polarity. The influence of the solvent polarity on the energetics of the  $N^*$  species affects the relative energies between the  $N^*$  and the  $T^*$  species, which in turn affects the ESIPT efficiency.



**Scheme 5.3.** Schematic representation of the ESIPT and ESICT processes in DMA3HF. The scheme has been adapted from reference 26.

In this work, we have synthesised the multi-parametric environment sensitive molecule, 4'-N,N-dimethylamino-3-hydroxyflavone (DMA3HF), to probe the monolinolein (GML)-based LLC nanochannels of the  $H_{II}$ ,  $Pn3m$  and  $Ia3d$  phases (Scheme 5.2). To better understand the response of the PCET molecule in the heterogeneous LLC medium, we have also employed the 3-methoxy derivative of the molecule (DMA3MeF) as a control. As the hydroxyl moiety is replaced by a methoxy group, DMA3MeF acts exclusively as an ESICT molecule. The emission features of both the molecules suggest that they experience an acetonitrile-like environment inside the mesophases, based on which we hypothesize that the molecules are lodged deep into the lipid-water interface of the LLC nanochannels. However, a decreased ESIPT efficiency and significantly retarded dynamics (>20 times) of the process in the LLC phases as compared to those in bulk acetonitrile imply that the effect of polarity is not the

determinant factor for the process. The experimental results indicate that the hydrogen bonding effects of the LLC water molecules play a major role in influencing the nature of the proton transfer process inside the mesophases. The formation of strong intermolecularly hydrogen-bonded solute-solvent complexes, owing to the high hydrogen bond accepting tendencies of the water molecules at the interfacial regions, leads to an appreciable activation barrier for the ESIPT process in the LLC phases. The hydrogen bonding effects of the water molecules on the energetics of ESIPT have been modelled by using classical MD simulation of DMA3HF in explicit water medium. The observations on the simultaneous effect of the various physical parameters in the aqueous LLC nanochannels add a new facet to the existing molecular level description of these materials, which is crucial for the rapid and efficient application of these materials in diverse fields.

## 5.2 Results and Discussion

### 5.2.1 Characterization of LLC Phases

The prepared reverse hexagonal ( $H_{II}$ ) phase was characterised by the typical birefringent “fan” like textures in polarised optical microscopy (POM) images (Figure 5A.7). The  $Ia3d$  (G) and  $Pn3m$  (D) phases do not exhibit any optical textures in the POM images due to their optically isotropic and highly ordered cubic symmetry. The mesophases,  $H_{II}$ ,  $Ia3d$  and  $Pn3m$  have also been characterised by the SAXS measurements (Figure 5A.8). The LLC mesophases were observed to exhibit the characteristic ratios of their peak positions -  $H_{II}$  ( $\sqrt{1}:\sqrt{3}$ ),  $Pn3m$  ( $\sqrt{2}:\sqrt{3}:\sqrt{4}:\sqrt{6}:\sqrt{8}$ ) and  $Ia3d$  ( $\sqrt{6}:\sqrt{8}:\sqrt{14}:\sqrt{16}:\sqrt{20}$ ). The dimensions of the nanochannels have been calculated from the diffraction patterns. The diameters of the LLC nanochannels have been calculated as 4-5 nm.

### 5.2.2 Steady State Emission Studies

DMA3HF generally exhibits a single absorption peak  $\sim 400$  nm corresponding to the normal form of the molecule in most solvents.<sup>30-32</sup> The emission characteristics of DMA3HF ( $\lambda_{ex} = 400$  nm) are quite different from that of its parent compound 3HF. While 3HF exhibits almost a sole tautomeric emission in non-polar solvents and most borderline aprotic solvents,<sup>33-35</sup> DMA3HF displays dual emission peaks in most solvents, excepting highly non-polar solvents<sup>30, 31</sup>. The short wavelength emission band ( $\sim 420$  nm – 490 nm, depending on the polarity of the surrounding medium) is attributed to the normal form ( $N^*$ ) and the longer

wavelength band (~560 nm) is ascribed to the tautomeric emission ( $T^*$ ).<sup>30</sup> However, in polar protic solvents like low n-alcohols (methanol and ethanol), DMA3HF displays an apparent single emission peak ~ 530 nm. The reason for this lies in the highly solvatochromic behaviour of the charge transfer  $N^*$  peak, which gets red shifted in the polar alcohols.<sup>32, 36</sup> In addition, since the  $T^*$  species does not possess any appreciable charge-transfer characteristics its emission remains unaffected. This brings the  $N^*$  emission band close to that of  $T^*$ , resulting in an apparent single peak. A single emission peak of DMA3HF was expected in the aqueous LLC nanochannels, similar to that in polar protic alcohols. However, two distinct emission peaks were observed in all the three LLC phases, one centred ~ 495 nm and the other ~ 560 nm (Figure 5.1 (a)). The former emission band corresponds to the  $N^*$  species and the latter peak corresponds to the ES IPT generated tautomeric species. The origin of the excited state tautomeric species from the ground state normal form is confirmed by the excitation spectrum collected at the normal emission (Figure 5A.9). A single peak is manifested in the excitation spectrum coinciding with the absorption of the normal form.

The location of the DMA3HF molecules in the LLC nanochannels was estimated from the sensitive solvatochromic response of the charge-transfer  $N^*$  peak. The  $N^*$  peak of DMA3HF in the LLC mesophases matches closely with that in bulk acetonitrile, implying that the DMA3HF molecules experience an acetonitrile-like polarity inside the LLC phases. In our previous study (Chapter 3), by using the solvatochromic properties of coumarin molecules we have determined that the micropolarity at the central core of the LLC nanochannels resembles that of ethylene glycol, while the micropolarity near the interfacial layer is closer to ethanol. The acetonitrile-like polarity sensed by the DMA3HF molecules inside the nanochannels indicates that they are located deeper than interfacial regions of the LLC water nanochannels where the micropolarity is even less than that of ethanol. Notably, the polarity of the solvents have been compared following the Reichardt's solvent polarity  $E_T(30)$  or  $E_T^N$  scale.<sup>26</sup> It has been hypothesized that at least two layers of water molecules are bound at the lipid-water interface in the mesophases.<sup>21, 24</sup> One of the layers consists of rigid water molecules that are bound strongly to the lipid headgroups via hydrogen bonding interactions. The second layer comprises of water molecules that get trapped within the lipid headgroup region due to lipid fluctuations. It can be reasoned that the DMA3HF molecules are embedded deep within the lipid headgroups in the latter water layer. To confirm the location of DMA3HF inside the LLC channels, the spectral

features of DMA3MeF-loaded LLC mesophases were studied. Structurally, DMA3MeF exhibits a higher sensitivity to the polarity of the surrounding medium than DMA3HF. This is because the intramolecular H bond in DMA3HF compensates the negative charge on the carbonyl oxygen, which decreases the degree of charge transfer from the amino groups of the side aromatic ring and leads to a lower charge-transfer character in DMA3HF. DMA3MeF exhibits an emission maximum  $\sim 510$ -  $520$  nm corresponding to the normal form (N\*) in low n-alcohols (Figure 5.1 (b)). However, in all three LLC phases, the emission band gets blue-shifted to  $\sim 490$  nm (Figure 5.1 (b)). On comparison with the emission features of DMA3MeF in bulk solvents, it is evident that the emission maximum of DMA3MeF in the LLC phases is quite close to that in acetonitrile. Thus, it can be concluded that both the molecules are presumably trapped between the hydrophilic headgroups of the lipid molecules in the nanochannels.

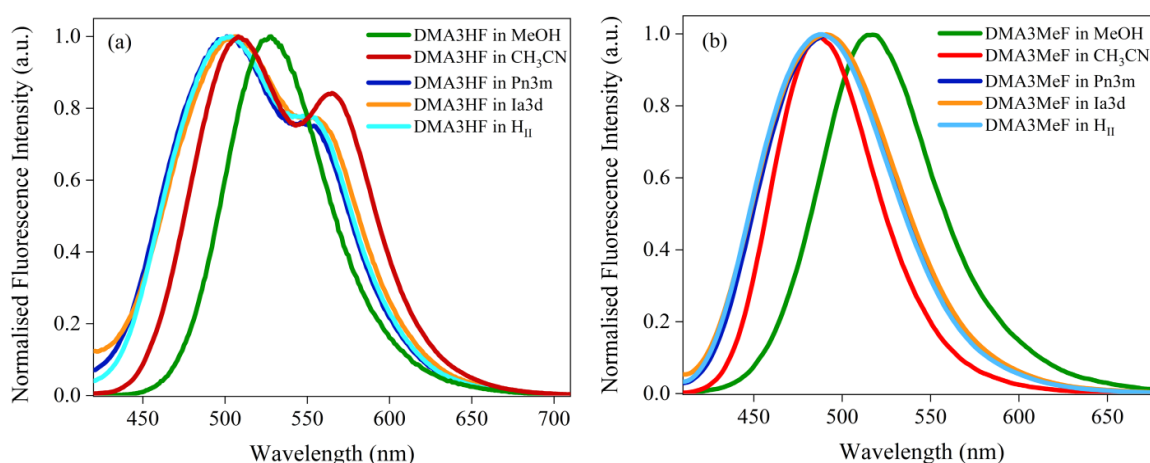


**Figure 5.1.** Steady state emission spectra of (a) DMA3HF and (b) DMA3MeF in the LLC phases and different bulk solvents ( $\lambda_{\text{ex}} = 400$  nm).

A distinctive feature in the emission profiles of both DMA3HF and DMA3MeF-loaded LLC phases is the red-shift in the N\* emission band on shifting the excitation wavelength to longer wavelengths (Figure 5.2, Figure 5A.10 and Figure 5A.11). The manifestation of red-edge excitation shift (REES) is evidence of a local heterogeneous dielectric environment around the probe molecules. The N\* band of DMA3HF displays a REES of  $\sim 10$  nm whereas the T\* emission position remains the same at all excitation wavelengths owing to its negligible dipole moment. In DMA3MeF, a REES of  $\sim 30$  nm is observed in the LLC phases. It is quite well established that the water molecules at the periphery of the lipid-water interface face an



extremely heterogeneous surface in terms of the local dielectric constant and this effect is more prominent for the water molecules that are lodged deep between the hydrophilic head group region of the lipids.<sup>37,38</sup> Consequently, excitations at the blue edge of the absorption maximum selectively excite the probe molecules residing in the relatively less polar regions in the deeper interfacial regions, while wavelengths at the red edge excite the molecules localised in the slightly more polar regions.

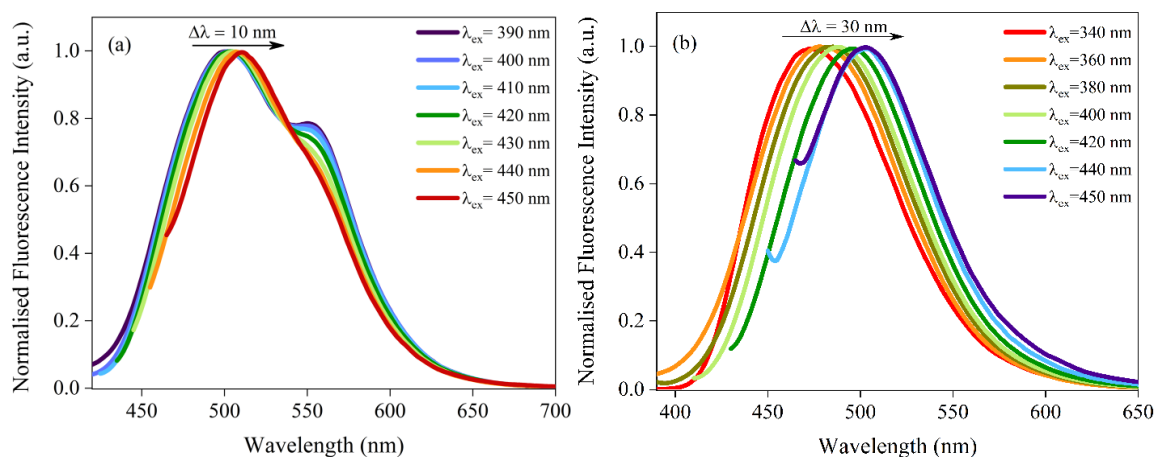


**Figure 5.2.** Excitation dependent emission spectra of (a) DMA3HF and (b) DMA3MeF in the  $H_{II}$  phase. The arrow depicts the red-shift in the emission maximum.

The emission properties that set DMA3HF apart from its parent 3-Hydroxyflavone (3HF) are mainly rooted in the charge-transfer quality of the  $N^*$  species.<sup>25,26</sup> Firstly, the large dipole moment of  $N^*$  in the excited state renders it with a very sensitive solvatochromic nature. Secondly, the ESIPT efficiency (given by the relative intensities of  $N^*$  and  $T^*$ ) is delicately dependent on both the polarity as well as the hydrogen bonding parameters of the surrounding media, which is very different from that of 3HF where the ESIPT efficiency is largely dominated by the hydrogen bonding parameters only. This point in particular enables DMA3HF to act as a multi-parametric probe. The relative energies of  $N^*$  and  $T^*$  dictate the overall equilibrium constant of the ESIPT reaction. A more polar surrounding media allows for a greater stabilisation of the  $N^*$  species relative to  $T^*$ . This results in a solvent-induced barrier for the ESIPT reaction, thus pushing the equilibrium towards  $N^*$  and giving rise to a significant  $N^*$  intensity. In contrast, in moderately polar and non-polar solvents an appreciable intensity of  $T^*$  is observed. In all three DMA3HF-loaded LLC phases, the ESIPT efficiency that is given by the relative intensities of the  $N^*$  and  $T^*$  species ( $I_{N^*}/I_{T^*}$ ) is  $\sim 1.35$ . This value is quite

different from that observed in bulk acetonitrile ( $I_{N^*}/I_{T^*}$  is  $\sim 1.18$ ), which is the polarity sensed by DMA3HF in the LLC phases. This observation suggests that the influence of polarity on the ESIPT reaction is undermined by a more dominant effect. Instead of polarity, the relative intensities of  $N^*$  and  $T^*$  of DMA3HF inside the LLC nanochannels are seemingly regulated by the hydrogen bonding parameters, in particular the hydrogen bond accepting ability ( $\beta$ ) of the water molecules in the lipid-water interface. It has been previously reported that the water molecules near the lipid-water interface of LLC phases possess a high hydrogen bond accepting ability.<sup>19, 20</sup> As a result, the water molecules trapped within the lipid headgroups can possibly form intermolecular hydrogen bonds with the DMA3HF molecules. This hinders the formation of the intramolecular hydrogen bond within DMA3HF and consequently restricts the ESIPT reaction.

### 5.2.3 Time-Resolved Fluorescence Study

The steady state results imply that both DMA3HF and DMA3MeF are localised deep inside the trapped water layer, in between the lipid headgroups of the LLC nanochannels. The ESIPT efficiency of DMA3HF inside the LLC phases is significantly curtailed by the appreciably high hydrogen bond donating ability of the water molecules trapped between the lipid headgroups. This connotes that the dynamics of the overall proton coupled charge transfer process of the DMA3HF molecule is disrupted inside the LLC mesophases. The dynamics of both the ESIPT and ESICT processes of DMA3HF are influenced by the properties of the surrounding medium and are typically ultrafast in bulk solvents. In non-polar aprotic solvents like cyclohexane, which are incapable of forming intermolecular hydrogen bonds with the molecule, the rate of the ESIPT process is  $\sim 2.1 \text{ ps}^{-1}$ .<sup>30</sup> However, the ESIPT rate slows down in solvents that have a moderate polarity as well as hydrogen bonding affinity. The ESIPT rate in solvents like acetonitrile and dichloromethane has been estimated to be  $\sim 1.33 \text{ ps}^{-1}$ .<sup>30</sup> On the other hand, in polar protic solvents like alcohols, a timescale of  $< 60 \text{ ps}$  has been reported for the ESIPT process.<sup>32</sup> The ICT process is ultrafast in most solvents ( $< 100 \text{ fs}$ )<sup>39</sup> and the charge transfer between the two excited state species cannot be easily detected even using fluorescence time-resolved techniques. Notably, the solvent relaxation of the charge-transfer  $N^*$  species can be detected using time-resolved fluorescence techniques. The lifetime measurements for both DMA3HF and DMA3MeF have been carried out using an excitation source of the 402 nm

diode laser in the TCSPC setup. The lifetime profiles of DMA3HF-loaded LLC phases have been collected over a series of wavelengths from 425 nm to 650 nm at regular intervals. The profiles of DMA3MeF have been collected at regular intervals in a range of 430 nm to 620 nm.

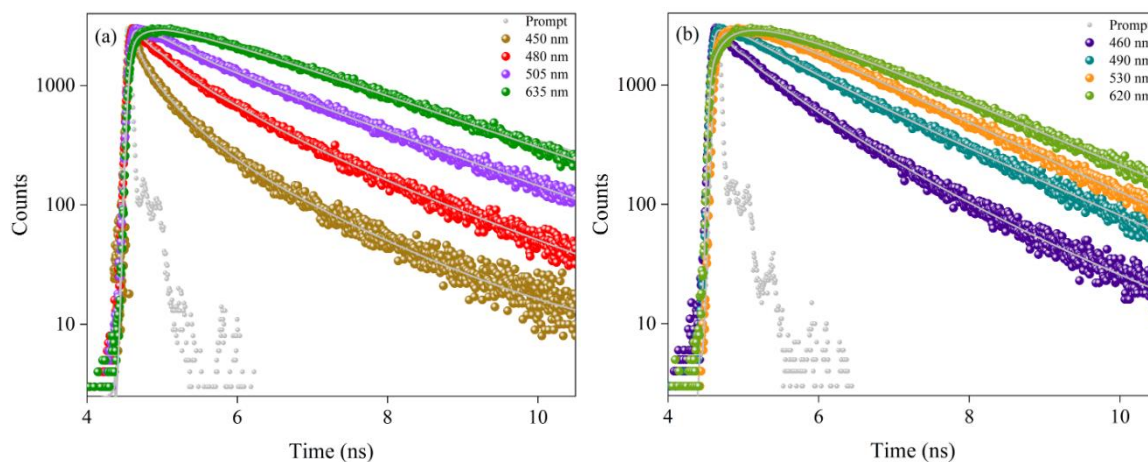


**Figure 5.3.** Fluorescence lifetime profiles of (a) DMA3HF and (b) DMA3MeF in the  $H_{II}$  phase collected at different emission wavelengths ( $\lambda_{ex} = 402$  nm). Solid lines depict the exponential fit.

The lifetime profiles of DMA3HF-loaded LLC phases exhibit a triexponential behaviour, with one long ns component ( $\sim 2$  ns) and two ps components ( $\sim 550$  ps and  $\sim 100$  ps) for all the collection wavelengths (Figure 5.3 (a), Figure 5A.12, Table 5A.1). These timescales present as decay components when the lifetime profiles are collected at the blue edge of the  $N^*$  emission band (425- 495 nm). However, for the profiles collected at the red edge of the steady state spectra, in the wavelength range of 535 - 650 nm, the two ps timescales ( $\sim 550$  ps and  $\sim 100$  ps) get converted into growth components. At the intermediate collection wavelengths, 520 and 535 nm, the lifetime profiles fit to two decay components ( $\sim 2$  ns and  $\sim 500$  ps) and one growth component ( $\sim 60$  ps). Notably, the lifetime profiles of the DMA3MeF-loaded LLC phases also exhibited similar characteristics (Figure 5.3 (b), Figure 5A.13, Table 5A.2). All the lifetime transients fit to a triexponential function with a ns component ( $\sim 1.6$  ns) and two ps components ( $\sim 500$  ps and  $\sim 100$  ps). The two picosecond lifetimes manifest as decay components in the profiles collected at the blue edge wavelengths of the emission spectrum and as growth components for the transients collected at the red edge wavelengths of the emission spectrum. The transformation of the decay components at the shorter collection wavelengths into growth components at longer wavelengths for both DMA3HF and DMA3MeF-loaded LLC phases clearly imply towards excited state interconversions. In the

case of DMA3MeF, which lacks the proton donor site, ICT and the subsequent solvent stabilisation of the charge-transfer state can occur in the excited state. However for the DMA3HF molecule, in addition to the mentioned excited state processes there is a possibility of ES IPT as well.

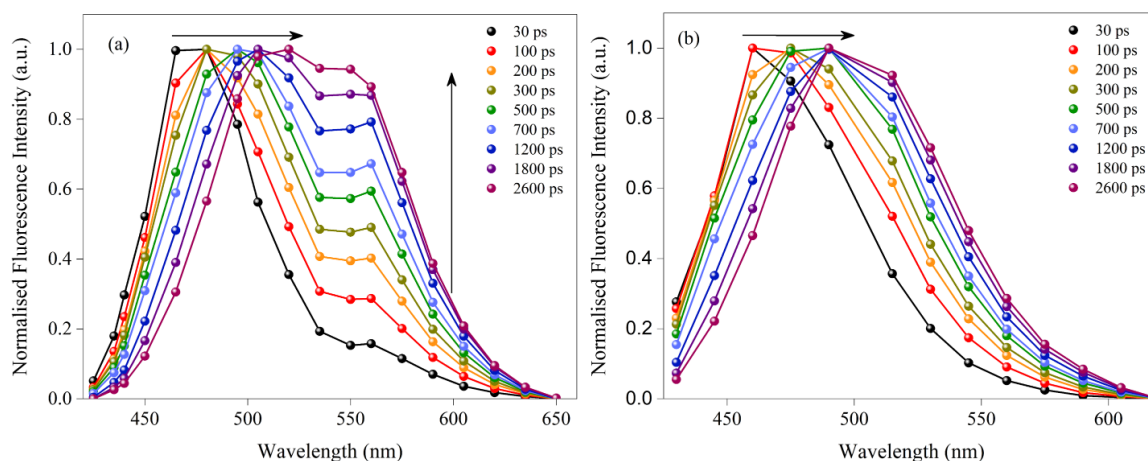


**Figure 5.4.** Normalised time-resolved emission spectra (TRES) of (a) DMA3HF and (b) DMA3MeF in the H<sub>II</sub> phase ( $\lambda_{\text{ex}} = 402$  nm).

In order to comprehend the origin of the growth components in the lifetime profiles and to gain a better understanding of the various possible excited state processes of the molecules in the LLC phases, time-resolved emission spectra (TRES) have been constructed. The spectra of DMA3HF loaded LLC phases exhibit dual emission at all the time delays, with the longer wavelength peak corresponding to the  $T^*$  species and the shorter wavelength band to the  $N^*$  species (Figure 5.4 (a), Figure 5A.14). The TRES profiles reveal a continuous dynamic Stokes shift in the  $N^*$  emission peak, while the peak position for  $T^*$  remains fixed. The observed time dependent Stokes shift (TDSS) points towards the solvent reorientation around the charge-transfer  $N^*$  species and its subsequent stabilisation, which is absent in the case of the less polar  $T^*$  species. It can be distinctly seen that the solvent relaxation persists till a nanosecond timescale ( $\sim 2.5$  ns), stipulating that the process in the LLC phases is significantly slow. As the proton transfer process is blocked in DMA3MeF by the 3-methoxy group, it acts exclusively as a solvation probe. Similar to DMA3HF, the TRES profile of DMA3MeF exhibits a continuous time dependent shift of the emission maximum towards longer wavelengths (Figure 5.4 (b), Figure 5A.15). The observed TDSS is the typical characteristic of solvation relaxation of a polar molecule and it is evident that the solvation dynamics in the LLC phases is extremely

slow, which corroborates with the observations of DMA3HF. Besides the TDSS of the  $N^*$  emission, the intensity of the  $T^*$  species of DMA3HF exhibits an increasing trend with the evolution of time. The observation reflects the generation of  $T^*$  species from  $N^*$  as a result of ESIPT. It has to be noted here that the increase in the  $T^*$  emission intensity and the TDSS of the  $N^*$  emission band both occur till a nanosecond timescale, implying that the solvent relaxation and the ESIPT processes occur simultaneously in the mesophases.

To understand the reasons behind the observed trends in the ESIPT and solvent relaxation processes of DMA3HF inside the LLC nanochannels, it is important to understand the nature of these phenomena in bulk solvents. The PCET mechanism of  $N,N'$ -dialkyl substituted 3-hydroxyflavone in conventional solvents has been well established.<sup>25, 30</sup> It has been elucidated that the energetics of the ESIPT process is closely linked with the solvent relaxation process in bulk solvents. The Frank-Condon photoexcitation of DMA3HF leads to the formation of an instantaneous dipolar excited state ( $N^*$ ) due to a rapid ESICT process. The creation of this highly polar excited state means that immediately after photoexcitation, the randomly oriented solvent molecules around DMA3HF find themselves in a high energy unfavourable configuration. Thus, the solvent molecules tend to reorganize around the dipolar  $N^*$  species to form a more energetically stabilized state ( $N^*_{\text{solv}}$ ). Notably, while the dipole moment of  $N^*$  is significantly larger than that of both  $N$  and  $T^*$ , the dipole moments of  $N$  and  $T^*$  are similar. This implies that immediately after photoexcitation the solvent configuration favours  $T^*$  rather than the highly polar  $N^*$  and hence, the solvent-polarization effect is decoupled from the ESIPT pathway. In other words, at initial time scales, the rates of ESIPT process ( $N^* \rightarrow T^*$ ) and the solvent relaxation process ( $N^* \rightarrow N^*_{\text{solv}}$ ) compete with each other. At longer time scales, after the completion of the solvent relaxation the energetics of the ESIPT process becomes complicated. Owing to the weak dipole moment of  $T^*$ , it undergoes negligible solvent relaxation, while a constant solvent relaxation of  $N^*$  stabilizes the energy of the state appreciably. Consequently, subsequent to the solvent equilibration of  $N^*$  ( $N^*_{\text{solv}}$ ), the relative energies between the  $N^*$  and  $T^*$  species changes as compared to the scenario immediately after the phototexcitation. The generated difference in the relative energies of  $N^*_{\text{solv}}$  and  $T^*$  causes the ESIPT pathway to be coupled with the solvent-polarity effect, thus creating an appreciable solvent induced barrier for the proton transfer process. Interestingly, while in bulk solvents the solvent relaxation proceeds in a relatively faster timescale and the ESIPT process continues till

longer times, both these processes seemingly occur simultaneously in the LLC phases. From the steady state results, it was evident that the DMA3HF molecules sense a polarity like acetonitrile inside the nanochannels. However, the surrounding polarity of the molecules is not sufficient to lower the energy of  $N^*$  to such an extent that it would give rise to  $> 20$  times retardation in the rate of ES IPT. This suggests that besides the solvent polarity induced activation barrier for the proton transfer process, the observed retardation in the ES IPT dynamics inside the LLC channels may be a result of hydrogen bonding effects. The DMA3HF molecules may be trapped in the form of solute-solvent complexes owing to the high hydrogen bond accepting ability of the water molecules at the vicinity of the lipid-water interface. The formation of these hydrogen-bonded complexes would hinder the formation of the intramolecular hydrogen bond requisite to the ES IPT process. Thus, the activation barrier for the ES IPT process in the nanochannels is also strongly coupled with the rate of disruption of the solute-solvent complex. This in turn is related to the rate at which the intermolecular hydrogen bonds between the solute and the solvent molecules break and reorient, that is, the solvation dynamics inside the nanochannels.<sup>32, 40</sup> The slow solvation dynamics, observed from the TDSS in the TRES, would ultimately slow down the rate of the ES IPT process. In addition, it is also possible that the DMA3HF and DMA3MeF molecules form hydrogen bonds with the hydrophilic headgroups of the lipid molecules.

To affirm the effects of intermolecular hydrogen bonding, we attempted to mimic the aqueous medium of the nanochannels by theoretical studies. Classical MD simulations were performed on DMA3HF in water and from the well-equilibrated simulation trajectories, 28 random configurations of the first solvation shell-truncated DMA3HF-(H<sub>2</sub>O)<sub>9</sub> cluster were collected (details of the computational calculations have been summarised in the [Appendix](#)). The ground state geometries of the selected DMA3HF-water clusters were optimised by DFT calculations. In addition to the 9 explicit water molecules surrounding DMA3HF, an implicit IEFPCM solvent model was used to mimic the aqueous layers in the LLC nanochannels as close to reality as possible. The orientation of the water molecules around DMA3HF in the various selected configurations of the DMA3HF-(H<sub>2</sub>O)<sub>9</sub> clusters were distinctly different from each other. Thus, from the probability distribution function plots, various discrete pathways of proton transfer could be deciphered. Among these, the most stable pathway was chosen based on the ground state energies. The geometry (CONFIG-2) involved the proton transfer via a

hydrogen-bonded water wire such that three explicit water molecules participated in the process (Figure 5.5 (b)). A second stable geometry (CONFIG-1) was chosen wherein the proton transfer occurred directly from the hydroxyl moiety of DMA3HF to the carbonyl group without the involvement of explicit water molecules (Figure 5.5 (a)). The energetics of the proton transfer process were compared for both the cases. At the ground state, CONFIG-2 was found to be more stable than CONFIG-1 by 0.12 eV. TDDFT calculations were performed to ascertain the nature of ESIPT in the two configurations. The prominent absorption observed from HOMO  $\rightarrow$  LUMO ( $S_0 \rightarrow S_1$ ), is ascribed to the  $\pi$ - $\pi^*$  transition of the DMA3HF molecule in the cluster. We also optimised the excited state structures, at the same level of theory, which reflected modulations in the hydrogen bond lengths as compared to those in the ground state. While the hydrogen bond lengthened in the hydrogen bond donating moiety, it shortened in the hydrogen bond accepting moiety. However, an overall strengthening in the hydrogen-bonded wire was observed as compared to that in the ground state (Table 5A.3). It is quite well established that the proton transfer of photoacids, involving solvent molecules, is dominated by the length of the hydrogen bonds in the solute-solvent complex.<sup>41, 42</sup> Consequently, the nature of hydrogen bonding in the excited state is key to understand the ESIPT process for CONFIG-2, involving the water wire. The ground and excited state 1D potential energy surface (PES) of the proton transfer coordinates were computed by increasing the O-H bond length of the hydroxyl moiety in DMA3HF for both configurations. An extremely high activation barrier of 0.512 eV (11.8 kcal/mol) in the ground state for the case of direct proton transfer (CONFIG-1) from the hydroxyl (H) to carbonyl oxygen (O) rules out the possibility of ground state proton transfer (Figure 5.6 (a)). However, the Franck-Condon state ( $S_1'$ ) is energetically lower than the transition state (TS) of the 1D proton transfer potential energy surface (PES) by 0.028 eV (0.64 kcal/mol). This clearly suggests that ESIPT is highly favourable and follows a relatively barrier-less pathway in the direct proton transfer case. Notably, the direct proton transfer pathway can be simplistically compared to the scenario of a non-hydrogen bonding solvent, like n-alkanes. The activation barrier for the backward ESIPT process is  $\sim$  0.31 eV.

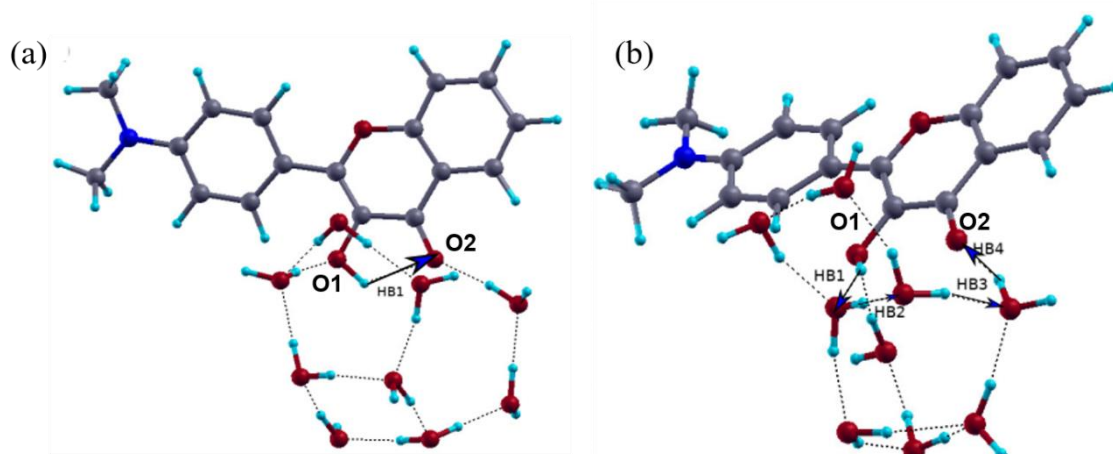


**Figure 5.5.** Electronic structures of the normal species of DMA3HF for (a) CONFIG-1: direct proton transfer without the involvement of explicit water molecules and (b) CONFIG-2: proton transfer via a water wire. The proton transfer pathways have been depicted by the arrows. The hydrogen bonds for the involved pathways have been labelled.

The activation barrier for the proton transfer is similarly high in the ground state of CONFIG-2 (1.254 eV), thus validating the absence of the tautomeric species in the ground state (Figure 5.6 (b)). However, the excited state scenario changes drastically for the proton transfer via the water wire. In this case, the Franck-Condon state is substantially higher than the TS of the 1D excited state proton transfer PES by 0.235 eV (5.53 kcal/mol). Thus, this proton transfer pathway faces an appreciable activation barrier in the excited state. Similarly, the barrier for the backward ES IPT is also higher as compared with the case of the direct proton transfer by  $\sim 0.22$  eV. The results were confirmed by varying the O-H bond distances of HB2, HB3 and HB4 in the water wire (Figure 5.5 (b)). Some of the other possible proton transfer pathways for the rest of the configurations mentioned before, involved proton transfer via one water molecule and abstraction of the O-H proton towards the bulk (or peripheral water molecules of the cluster) wherein the proton revolved within the water network (Figures 5A.18 and 5A.19). The theoretical calculations clearly reflect the dominant role of hydrogen-bonding in influencing the efficiency of the ES IPT pathways and provides ample support for the experimental observations. The energetics of the ES IPT process change entirely on the formation of the solute-solvent complexes and thus it connotes that in the LLC mesophases, the hydrogen bonding parameters play the driving force in dictating the nature of PCET rather than the effects of polarity.



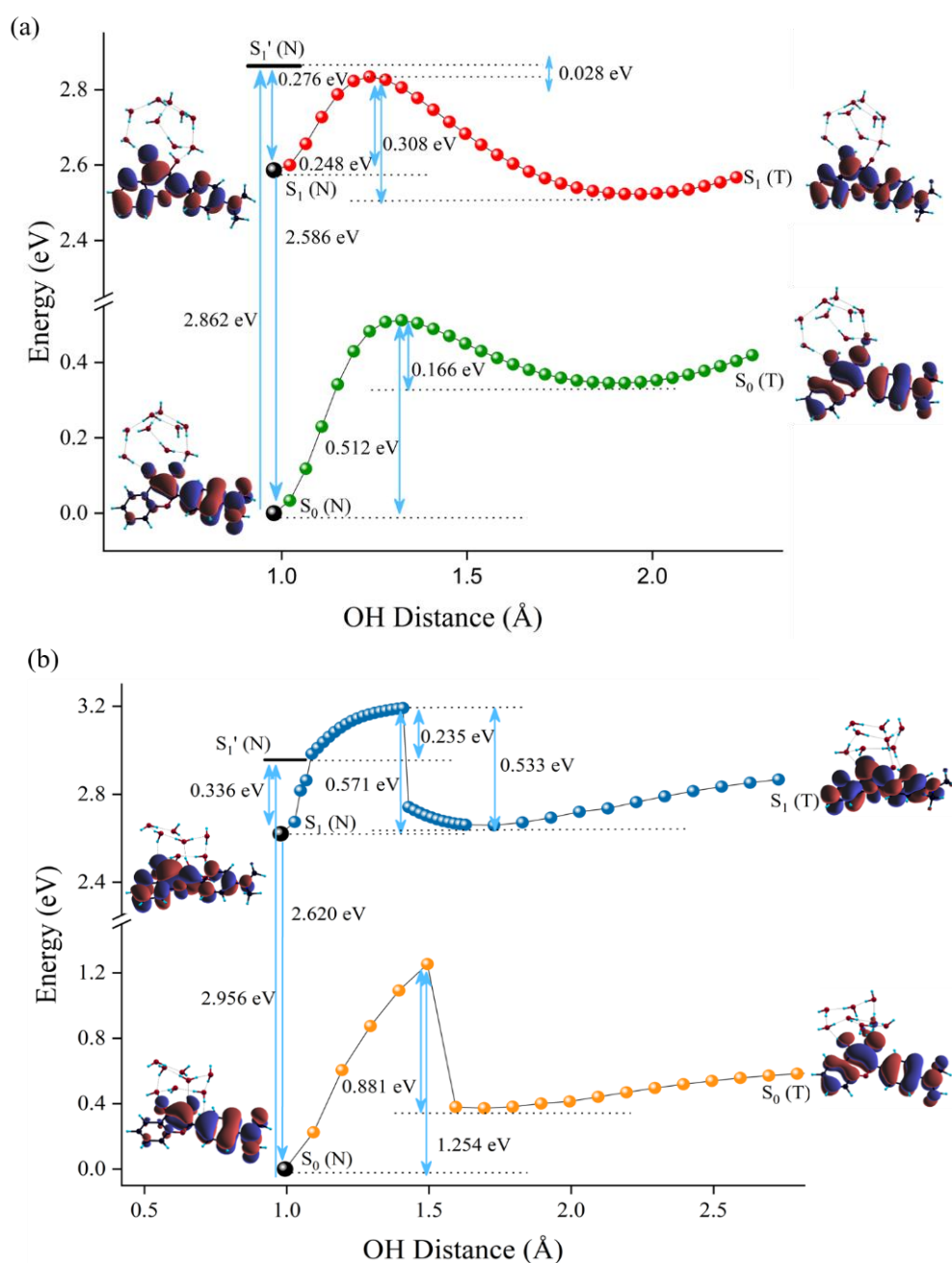


**Figure 5.6.** One-dimensional potential energy profiles of the proton transfer coordinate in the ground and excited state of DMA3HF for (a) CONFIG-1: direct proton transfer without the involvement of explicit water molecules and (b) CONFIG-2: proton transfer via a water wire.

### 5.3 Conclusion

The objective behind this study was to simultaneously distinguish between the effects of H-bonding abilities and the polarity of the water molecules in the LLC nanochannels as well as evaluate the interplay between both the effects. The multi-parametric sensitivity of the PCET

molecule, DMA3HF, was employed to probe the heterogeneous LLC nanochannels. The steady state results indicated that the DMA3HF molecules were localised within the headgroup region of the lipid molecules wherein they experience an acetonitrile-like polarity. This observation was corroborated from the steady state results of the solvatochromic ESICT molecule, DMA3MeF. However, both the ES IPT efficiency as well as the significant retardation (> 20 times) in the ES IPT dynamics of DMA3HF inside the mesophases deviates considerably from those in bulk acetonitrile, suggesting that the effect of polarity on ES IPT is dominated by a stronger effect. It has been hypothesized that the presence of solute-solvent complexes in the channels owing to the high hydrogen bond accepting ability of the water molecules near the lipid headgroup region, gives rise to a substantial activation barrier for ES IPT. The hypothesis was validated by the MD simulation-based theoretical calculations wherein the energetics of the ES IPT process was estimated for two distinct possible pathways. The activation barrier was found to be significantly high when the proton transfer occurred via a hydrogen-bonded water wire as opposed to the case of an almost barrier-less proton transfer pathway without the involvement of water molecules. The employed theoretical model involving the explicit water shell closely mimics the experimental conditions and thus can be extended to estimate the effects of extended hydrogen bonding in other systems as well. The experimental observations, supported by theoretical calculations, reveal that the hydrogen bonding capabilities of the LLC water molecules trump over the polarity effects in terms of their influence on the proton transfer process.

## 5.4 References

1. E. Brini, C. J. Fennell, M. Fernandez-Serra, B. Hribar-Lee, M. Lukšič and K. A. Dill, *Chem. Rev.*, 2017, **117**, 12385-12414.
2. L. G. M. Pettersson, R. H. Henchman and A. Nilsson, *Chem. Rev.*, 2016, **116**, 7459-7462.
3. M. D. Fayer and N. E. Levinger, *Annu. Rev. Anal. Chem.*, 2010, **3**, 89-107.
4. O. Björneholm, M. H. Hansen, A. Hodgson, L.-M. Liu, D. T. Limmer, A. Michaelides, P. Pedevilla, J. Rossmeisl, H. Shen, G. Tocci, E. Tyrode, M.-M. Walz, J. Werner and H. Bluhm, *Chem. Rev.*, 2016, **116**, 7698-7726.
5. A. W. Knight, N. G. Kalugin, E. Coker and A. G. Ilgen, *Sci. Rep.*, 2019, **9**, 8246.

6. L. Comez, L. Lupi, A. Morresi, M. Paolantoni, P. Sassi and D. Fioretto, *J. Phys. Chem. Lett.*, 2013, **4**, 1188-1192.
7. M.-C. Bellissent-Funel, A. Hassanali, M. Havenith, R. Henchman, P. Pohl, F. Sterpone, D. van der Spoel, Y. Xu and A. E. Garcia, *Chem. Rev.*, 2016, **116**, 7673-7697.
8. F. Goettmann and C. Sanchez, *J. Mater. Chem.*, 2007, **17**, 24-30.
9. G. Hummer, J. C. Rasaiah and J. P. Noworyta, *Nature*, 2001, **414**, 188-190.
10. C. Fong, T. Le and C. J. Drummond, *Chem. Soc. Rev.*, 2012, **41**, 1297-1322.
11. C. V. Kulkarni, *Nanoscale*, 2012, **4**, 5779-5791.
12. R. Mezzenga, J. M. Seddon, C. J. Drummond, B. J. Boyd, G. E. Schröder-Turk and L. Sagalowicz, *Adv. Mater.*, 2019, **31**, 1900818.
13. N. Garti, D. Libster and A. Aserin, *Food Funct.*, 2012, **3**, 700-713.
14. C. V. Kulkarni, W. Wachter, G. Iglesias-Salto, S. Engelskirchen and S. Ahualli, *Phys. Chem. Chem. Phys.*, 2011, **13**, 3004-3021.
15. S. Ghosh, L. Ramos and H. Remita, *Nanoscale*, 2018, **10**, 5793-5819.
16. K. Larsson, *J. Phys. Chem.*, 1989, **93**, 7304-7314.
17. A. Zabara, J. T. Y. Chong, I. Martiel, L. Stark, B. A. Cromer, C. Speziale, C. J. Drummond and R. Mezzenga, *Nat. Commun.*, 2018, **9**, 544.
18. J. J. Vallooran, S. Handschin, S. M. Pillai, B. N. Vetter, S. Rusch, H.-P. Beck and R. Mezzenga, *Adv. Funct. Mater.*, 2016, **26**, 181-190.
19. N. I. Zahid, O. K. Abou-Zied and R. Hashim, *J. Phys. Chem. C*, 2013, **117**, 26636-26643.
20. K. Das, S. Sappati and P. Hazra, *Phys. Chem. Chem. Phys.*, 2020, **22**, 6210-6221.
21. K. Das, B. Roy, S. Satpathi and P. Hazra, *J. Phys. Chem. B*, 2019, **123**, 4118-4128.
22. W. Wachter, G. Trimmel, R. Buchner and O. Glatter, *Soft Matter*, 2011, **7**, 1409-1417.
23. B. Roy, S. Satpathi, K. Gavvala, R. K. Koninti and P. Hazra, *J. Phys. Chem. B*, 2015, **119**, 11721-11731.
24. J. Kim, W. Lu, W. Qiu, L. Wang, M. Caffrey and D. Zhong, *J. Phys. Chem. B*, 2006, **110**, 21994-22000.
25. A. P. Demchenko, K.-C. Tang and P.-T. Chou, *Chem. Soc. Rev.*, 2013, **42**, 1379-1408.
26. C.-C. Hsieh, C.-M. Jiang and P.-T. Chou, *Acc. Chem. Res.*, 2010, **43**, 1364-1374.
27. C. A. Rumble, J. Breffke and M. Maroncelli, *J. Phys. Chem. B*, 2017, **121**, 630-637.

28. Z. Kuang, Q. Guo, X. Wang, H. Song, M. Maroncelli and A. Xia, *J. Phys. Chem. Lett.*, 2018, **9**, 4174-4181.
29. R. Das, A. S. Klymchenko, G. Duportail and Y. Mély, *J. Phys. Chem. B*, 2008, **112**, 11929-11935.
30. P.-T. Chou, S.-C. Pu, Y.-M. Cheng, W.-S. Yu, Y.-C. Yu, F.-T. Hung and W.-P. Hu, *J. Phys. Chem. A*, 2005, **109**, 3777-3787.
31. A. D. Roshal, J. A. Organero and A. Douhal, *Chem. Phys. Lett.*, 2003, **379**, 53-59.
32. D. Ghosh, S. Batuta, S. Das, N. A. Begum and D. Mandal, *J. Phys. Chem. B*, 2015, **119**, 5650-5661.
33. A. Douhal, M. Sanz, L. Tormo and J. A. Organero, *ChemPhysChem*, 2005, **6**, 419-423.
34. A. S. Klymchenko, C. Kenfack, G. Duportail and Y. Mély, *J. Chem. Sci.*, 2007, **119**, 83-89.
35. A. J. G. Strandjord and P. F. Barbara, *J. Phys. Chem.*, 1985, **89**, 2355-2361.
36. D. Ghosh, S. Batuta, N. A. Begum and D. Mandal, *Photochem. Photobiol. Sci.*, 2016, **15**, 266-277.
37. M. J. Higgins, M. Polcik, T. Fukuma, J. E. Sader, Y. Nakayama and S. P. Jarvis, *Biophys. J.*, 2006, **91**, 2532-2542.
38. H. Chakraborty, S. Haldar, P. L.-G. Chong, M. Kombrabail, G. Krishnamoorthy and A. Chattopadhyay, *Langmuir*, 2015, **31**, 11591-11597.
39. Y. Kimura, M. Fukuda, K. Suda and M. Terazima, *J. Phys. Chem. B*, 2010, **114**, 11847-11858.
40. C. A. Kenfack, A. S. Klymchenko, G. Duportail, A. Burger and Y. Mély, *Phys. Chem. Chem. Phys.*, 2012, **14**, 8910-8918.
41. Y. Liao, *Acc. Chem. Res.*, 2017, **50**, 1956-1964.
42. Z. Shi, P. Peng, D. Strohecker and Y. Liao, *J. Am. Chem. Soc.*, 2011, **133**, 14699-14703.

## 5.5 Appendix

DMA3HF and DMA3MeF were synthesised using reported protocols.<sup>A1, A2</sup> The details of the synthesis procedure have been given in Chapter 2. The synthesised compounds were characterised by  $^1\text{H}$  NMR,  $^{13}\text{C}$  NMR and HRMS. The spectra have been depicted below.

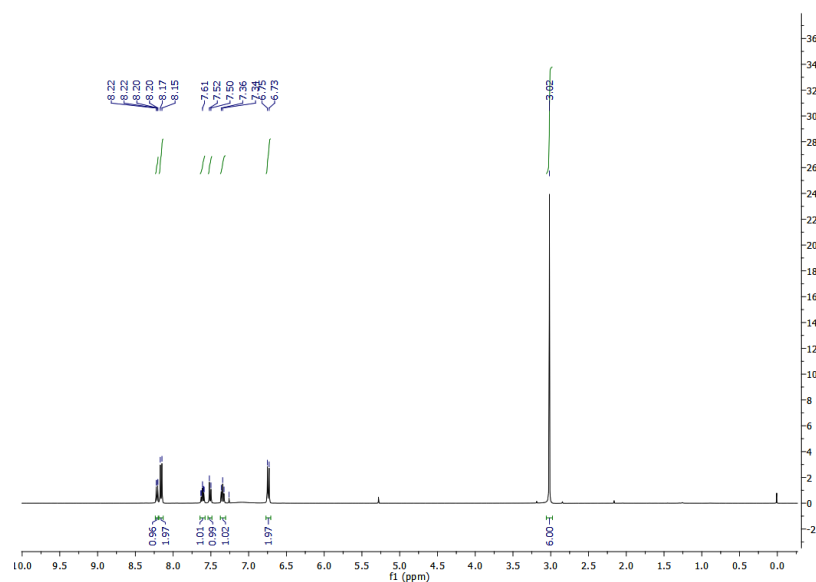


Figure 5A.1.  $^1\text{H}$  NMR of DMA3HF.

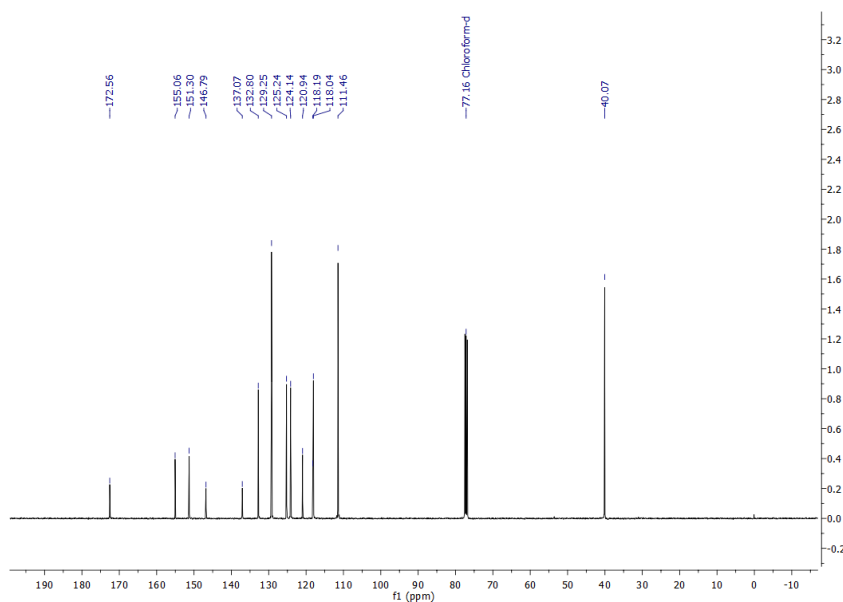


Figure 5A.2.  $^{13}\text{C}$  NMR of DMA3HF.

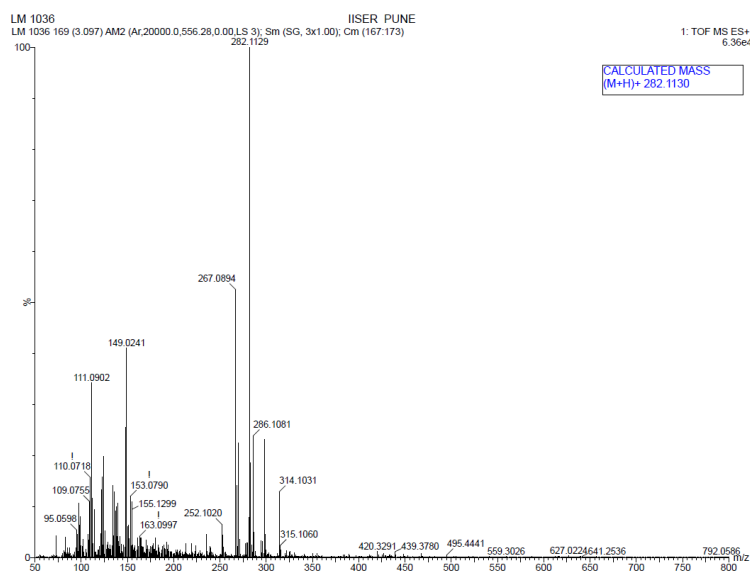
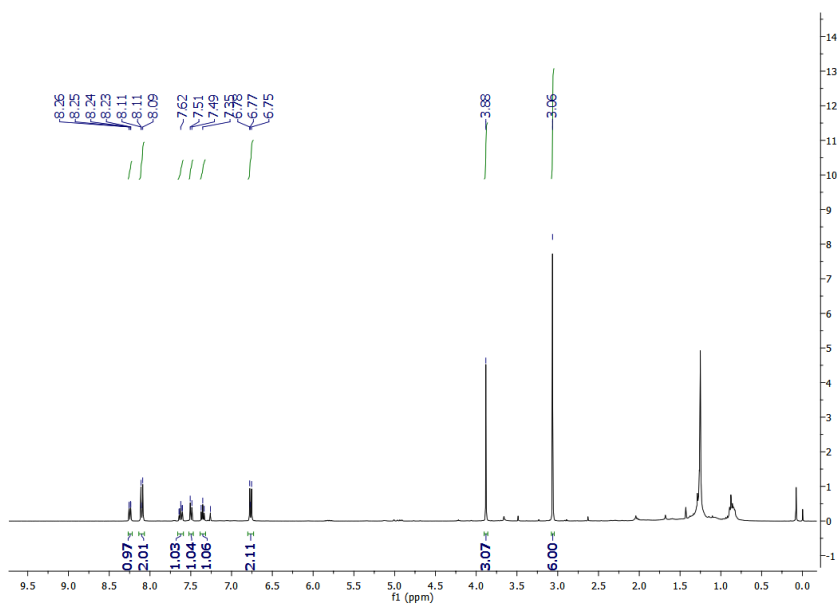


Figure 5A.3. HRMS of DMA3HF.

Figure 5A.4. <sup>1</sup>H NMR of DMA3MeF.

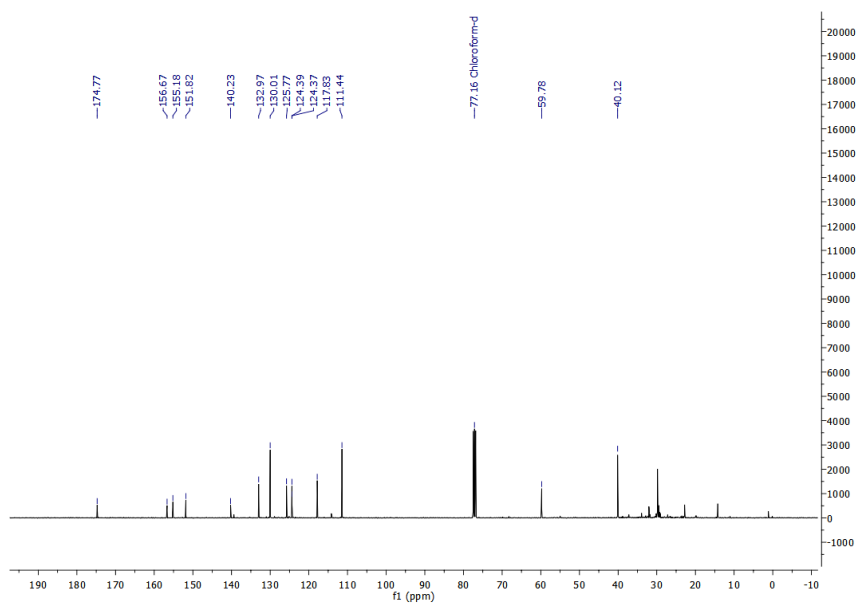


Figure 5A.5.  $^{13}\text{C}$  NMR of DMA3MeF.

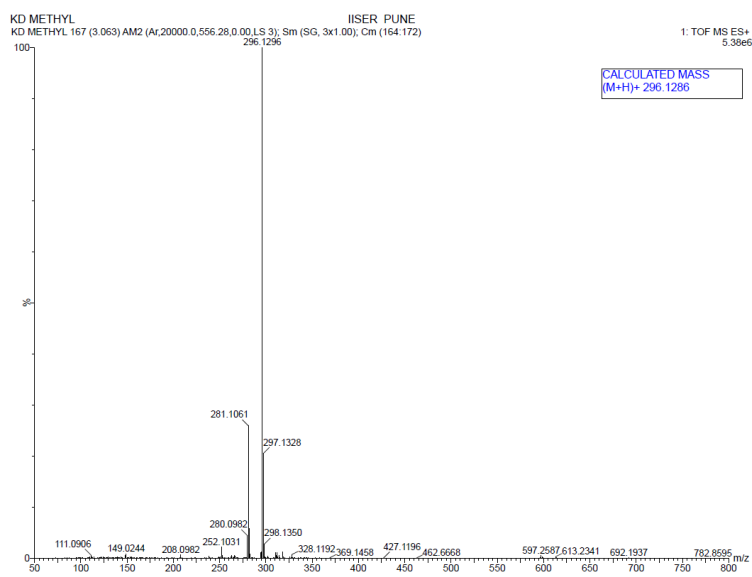
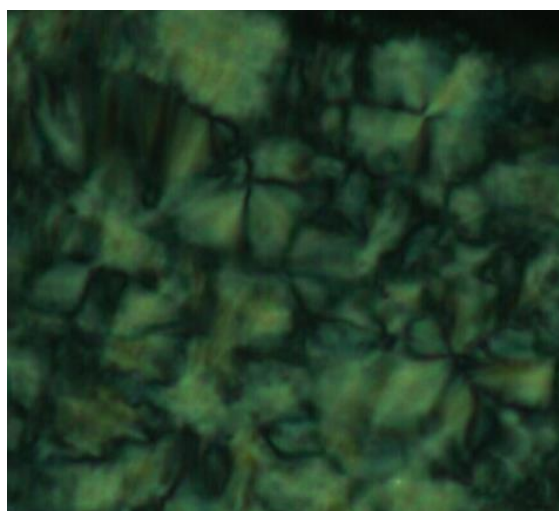
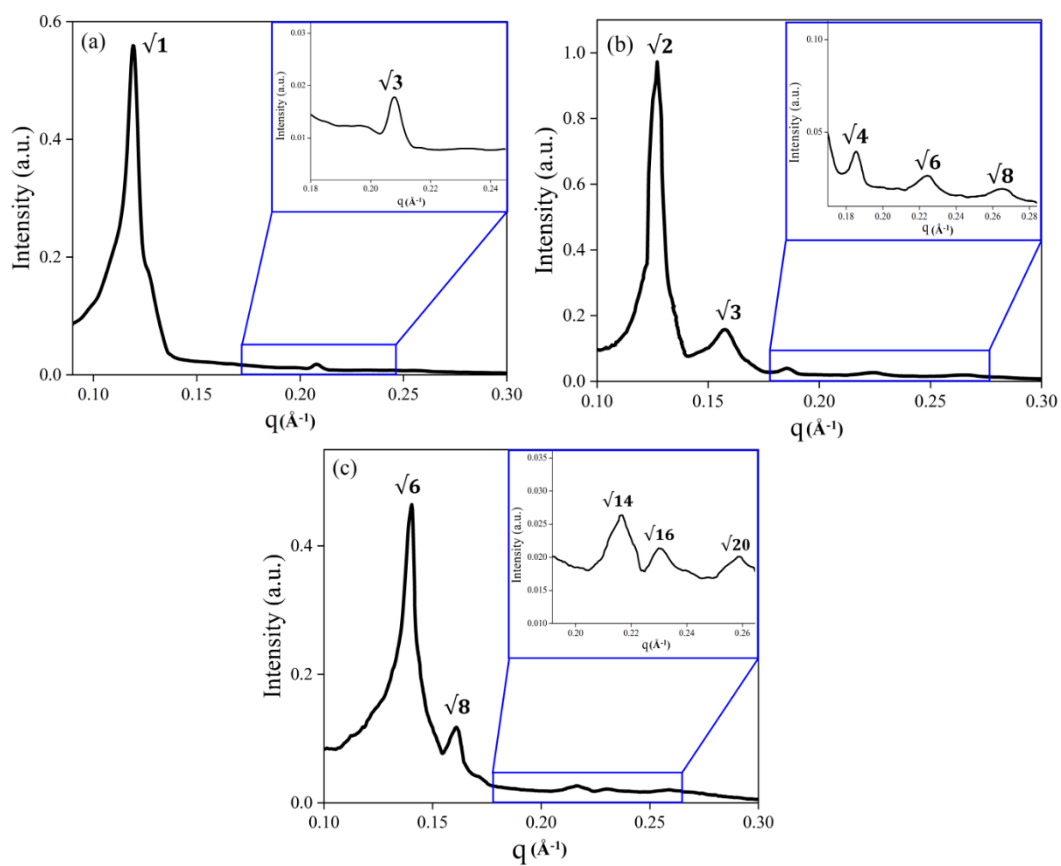


Figure 5A.6. HRMS of DMA3MeF



**Figure 5A.7.** Polarised optical microscopy image of the prepared H<sub>II</sub> phase.



**Figure 5A.8.** Small angle X-ray diffraction patterns of (a) H<sub>II</sub>, (b)  $Pn3m$  and (c)  $Ia3d$  phases.



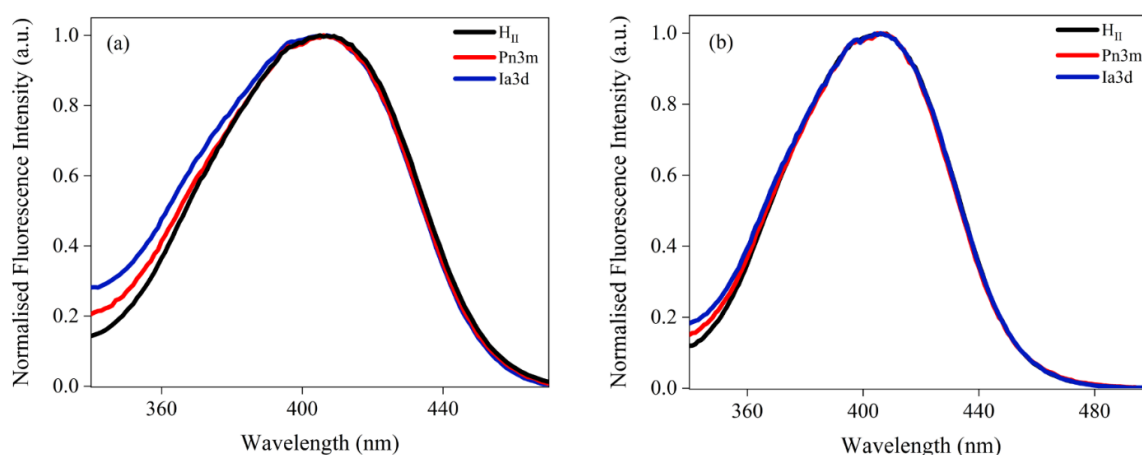


**Figure 5A.9.** Excitation spectra of DMA3HF loaded LLC phases, recorded at (a)  $\lambda_{em} = 500$  and (b)  $\lambda_{em} = 550$  nm.

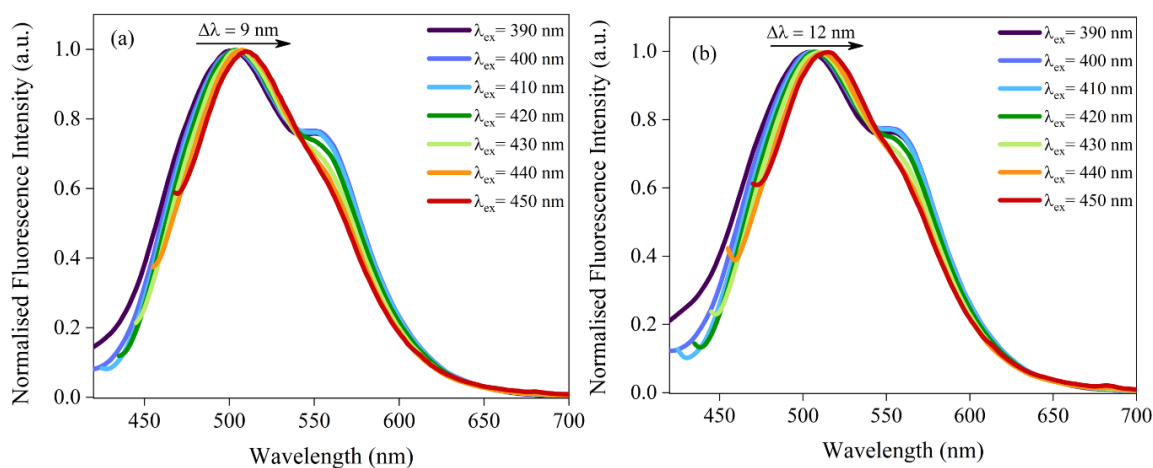


**Figure 5A.10.** Excitation dependent emission spectra of DMA3HF in (a) *Pn3m* and (b) *Ia3d* mesophases. The arrow depicts the red shift in the emission maximum.

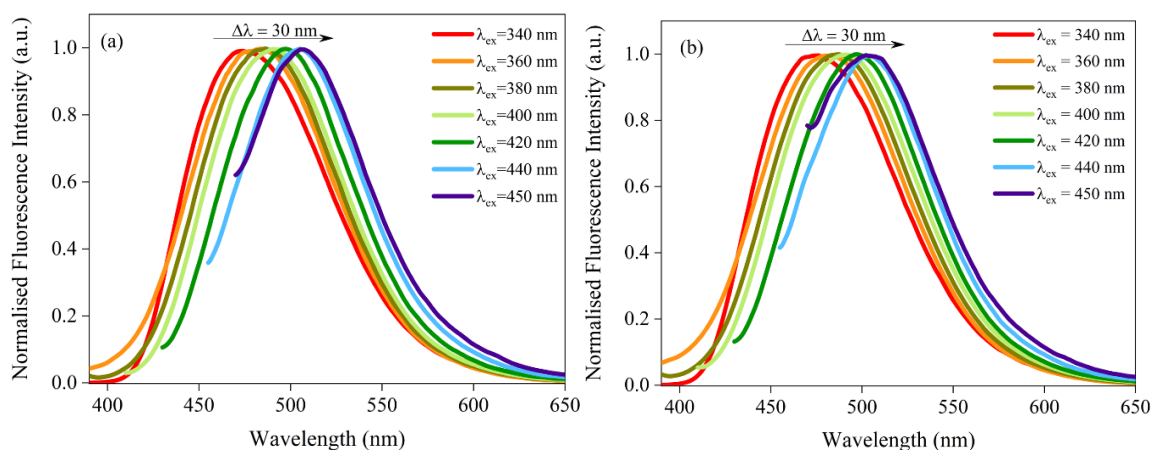


**Figure 5A.11.** Excitation dependent emission spectra of DMA3MeF in (a) *Pn3m* and (b) *Ia3d* mesophases. The arrow depicts the red shift in the emission maximum.

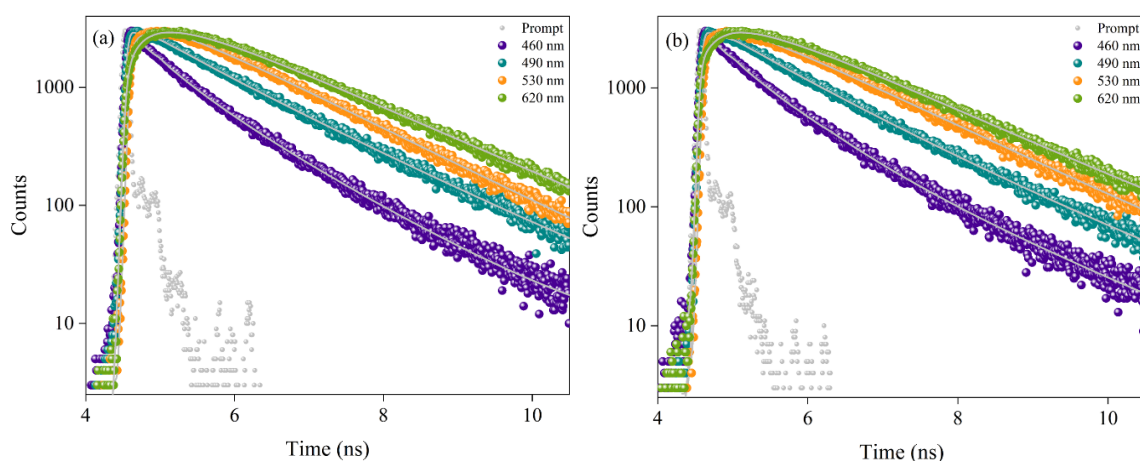


**Figure 5A.12.** Fluorescence lifetime profiles of DMA3HF collected at different emission wavelengths ( $\lambda_{\text{ex}} = 402$  nm) in (a) *Pn3m* and (b) *Ia3d* phases. The solid lines depict the exponential fit of the profiles.

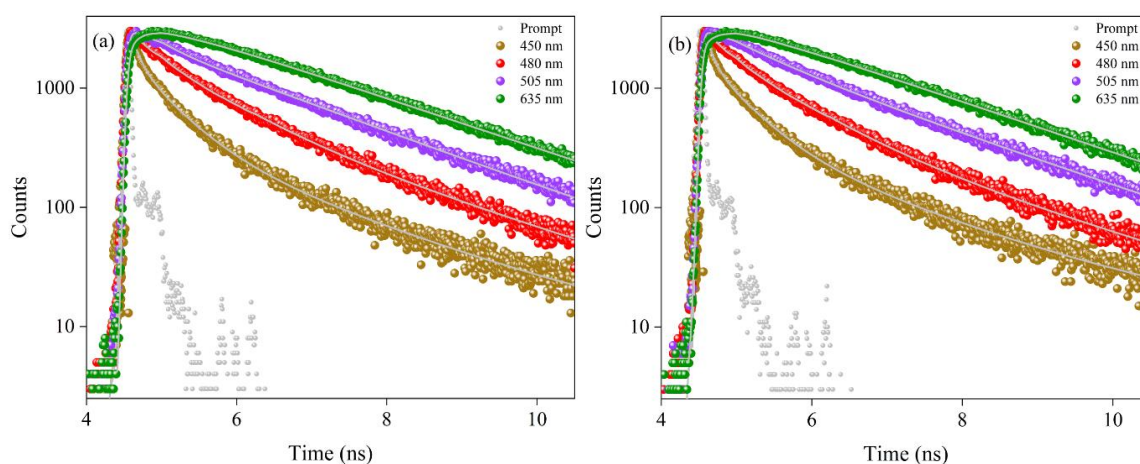


**Figure 5A.13.** Fluorescence lifetime profiles of DMA3MeF collected at different emission wavelengths ( $\lambda_{\text{ex}} = 402$  nm) in (a) *Pn3m* and (b) *Ia3d* phases. Solid lines depict the exponential fit.

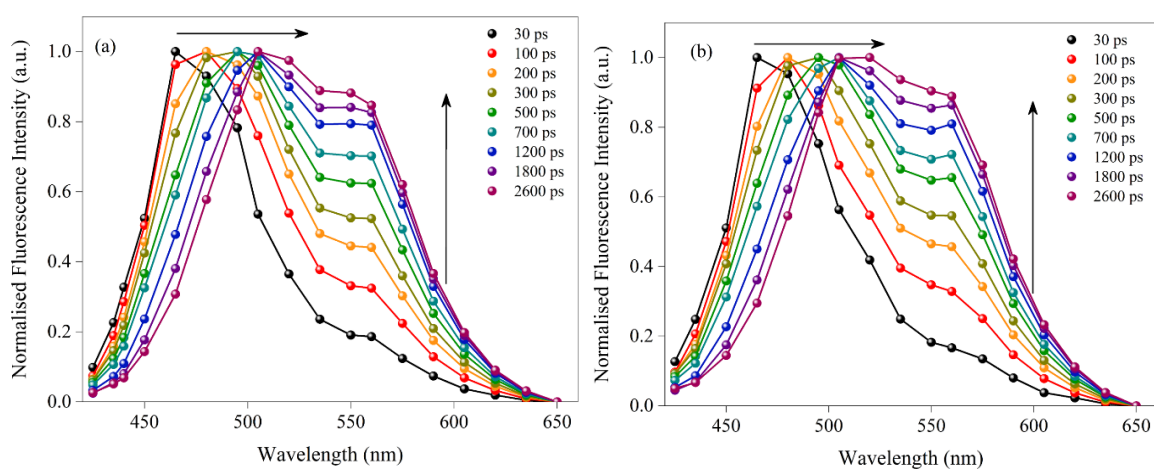


**Figure 5A.14.** Normalised time-resolved emission spectra (TRES) of DMA3HF in (a) *Pn3m* and (b) *Ia3d* phases ( $\lambda_{\text{ex}} = 402$  nm).

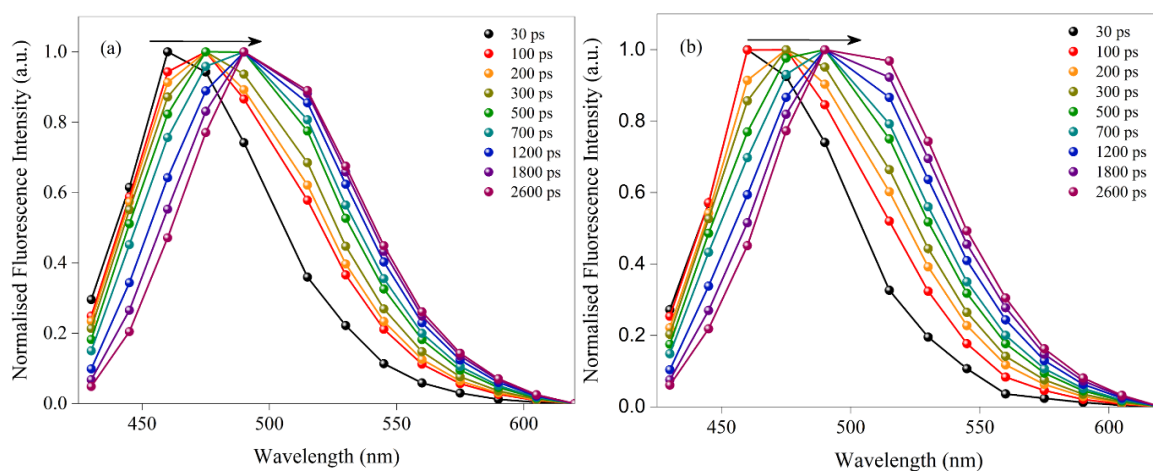


**Figure 5A.15.** Normalised time-resolved emission spectra (TRES) of DMA3MeF in (a) *Pn3m* and (b) *Ia3d* phases ( $\lambda_{\text{ex}} = 402$  nm).

**Table 5A.1.** Lifetime fitting parameters of DMA3HF in the LLC phases.

Sample	$\lambda_{\text{col}}$ (nm)	$\alpha_1$	$\tau_1$ (ns)	$\alpha_2$	$\tau_2$ (ns)	$\alpha_3$	$\tau_3$ (ns)
<i>H<sub>II</sub></i>	635	-0.15	0.640	0.62	2.070	-0.23	0.083
	505	0.27	0.530	0.48	1.958	-0.24	0.035
	450	0.45	0.424	0.18	1.406	0.37	0.088
<i>Pn3m</i>	635	-0.18	0.620	0.63	2.123	-0.19	0.100
	505	0.23	0.296	0.47	1.926	-0.29	0.044
	450	0.44	0.519	0.13	1.896	0.43	0.109
<i>Ia3d</i>	635	-0.15	0.663	0.66	2.077	-0.19	0.138
	505	0.30	0.748	0.65	2.048	-0.05	0.065
	450	0.43	0.516	0.13	1.901	0.44	0.092

**Table 5A.2.** Lifetime fitting parameters of DMA3MeF in the LLC phases.

Sample	$\lambda_{\text{col}}$ (nm)	$\alpha_1$	$\tau_1$ (ns)	$\alpha_2$	$\tau_2$ (ns)	$\alpha_3$	$\tau_3$ (ns)
HII	620	-0.32	0.573	0.55	1.671	-0.13	0.241
	530	-0.19	0.466	0.61	1.510	-0.20	0.056
	460	0.39	0.758	0.17	1.550	0.44	0.0163
<i>Pn3m</i>	620	-0.33	0.462	0.55	1.650	-0.12	0.116
	530	-0.21	0.408	0.62	1.448	-0.17	0.052
	460	0.32	0.524	0.37	1.236	0.31	0.124
<i>Ia3d</i>	620	-0.28	0.522	0.59	1.606	-0.13	0.177
	530	-0.18	0.414	0.57	1.524	-0.25	0.039
	460	0.43	0.740	0.14	1.681	0.43	0.171

## 5.5.1 Details of Computational Studies

### Classical Molecular Dynamics Simulation

Classical MD simulations were carried out using the GROMACS-5.0.6 software (with double precision). Water molecules have been explicitly represented and described by the SPC/E water model.<sup>A3</sup> The MD simulation studies were based on the general amber force field (GAFF)<sup>A4</sup> parameters. DMA3HF was optimized following the Merz-Kolmann charge calculation<sup>A5</sup> using Hartree-Fock theory with 6-311G(d) basis set using Gaussian 09.<sup>A6</sup> The antechamber module of AMBERTools<sup>A7</sup> was used for the restrained electrostatic potential charge (RESP) calculation<sup>A8</sup> and the generation of general amber force field (GAFF).<sup>A4</sup> Finally, the coordinates and topology were converted to the GROMACS format using the `amb2gmx.pl` program.<sup>A9</sup>

Briefly, DMA3HF was placed in a cubic box of length 33.29 Å and solvated with 1209 SPC/E water molecules. For the NVT simulations, a constant temperature of 300 K was maintained by coupling the system to a thermal bath with the Andersen algorithm and a time constant of 1 ps, whereas for the NPT simulations a constant pressure of 1 bar was maintained using the Berendsen barostat<sup>A10</sup> with isotropic scaling and a time constant of 2 ps. All Lennard-

Jones interactions were cut off at 10 Å and a particle mesh Ewald correction to the long-range electrostatic contribution was applied. The integration step was set to 2 fs and the X---H stretching modes were frozen with the LINCS algorithm.<sup>A11</sup>

After 2000 steps of energy minimization, simulated annealing (annealing time of 100 ps) was performed under NPT conditions to heat the system to 300 K. This was followed by equilibration at 300 K for 100 ps in the NPT ensemble. Starting from the equilibrated system, MD trajectories were recorded for 10 ns in the NVT ensemble.<sup>A12</sup> The data that was sampled at every 1 ps during the last 6 ns were used for the analysis. Random snapshots were selected from the remaining 4 ns trajectory for further analysis. The radial distribution function (RDF) of oxygen atoms (O<sub>1</sub> & O<sub>2</sub>) of the DMA3HF molecule and the oxygen atom of the explicit water molecule have been plotted (Figure 5A.17). The first solvation shell was truncated from DMA3HF at 4.1 Å.<sup>A13, A14</sup> Based on the above RDF criteria 9 explicit water molecules were found close to O1 and O2.

### Electronic Structure Calculations

To compute the ground and excited state profiles of proton transfer coordinates from the classical MD simulations, 28 snapshots<sup>A13</sup> were randomly selected from the Classical MD trajectory. All the geometries were optimized and the local minima were determined by frequency calculations. The ground state & excited state profiles were computed using a relaxed scan of PTC and the final profiles were categorised into multiple proton transfer pathways. In the ground state (S<sub>0</sub>), the structural isomers of DMA3HF were optimized at the DFT level using the hybrid B3LYP functional<sup>A15, A16</sup> and the wave functions were expanded in a 6-311++g(d,p) basis set<sup>A17</sup>. All the calculations were performed using the Gaussian application,<sup>A6</sup> and the solvent (water) effects were taken into account using the Polarizable Continuum Model (PCM) and the integral equation formalism variant (IEFPCM) solvation model.<sup>A18</sup>

The vertical excitation energies, oscillator strengths and optimisation of the excited state (S<sub>1</sub>) were computed at TD-DFT at the same level of theory. For the transition state (TS), the Synchronous Transit-Guided Quasi-Newton (STQN) method has been employed, which results in the actual transition structure using an empirical estimate of the Hessian and suitable starting structures of DMA3HF. Subsequently, a one-dimensional (1D) potential energy surface (PES)

scan with the proton transfer (PT) reaction coordinate was performed. The intrinsic reaction coordinate (IRC) was compared for both DMA3HF in the gas phase and the DMA3HF:9-water complex in the ground state. The IRC profiles were found to match well with the proton transfer coordinate. Previous literature studies<sup>A13, A14, A19, A20</sup> as well as our own calculations suggest that the spurious effects on the absorption spectra due to the “finite cluster” can be circumvented by using an IEFPCM model along with explicit water molecules. Hence, the explicit water molecules were then surrounded by a polarizable continuum model (IEFPCM) with a dielectric constant of 80. [Figure 5A.17](#) depicts the results of the  $g(r)$  between the center of mass of DMA3HF hydroxyl oxygen (O1) and carbonyl oxygen (O2) and  $O_w$  of water obtained from the classical molecular dynamics simulations. The first solvation shell was found at 4.1 Å. Multiple possible pathways for the proton transfer process were deciphered, out of which two of the most stable pathways were chosen for calculating the proton transfer energy surfaces in the ground and excited states (CONFIG-1 and CONFIG-2). All the pathways (CONFIG-S1 TO CONFIG-S6 and CONFIG-1, CONFIG-2) have been depicted in [Figures 5A.18 and 5A.19](#). The first four proton transfer pathways ([Figure 5A.18](#)) result in the transformation of normal to tautomer species, however the other four pathways ([Figure 5A.19](#)) do not result in tautomer.

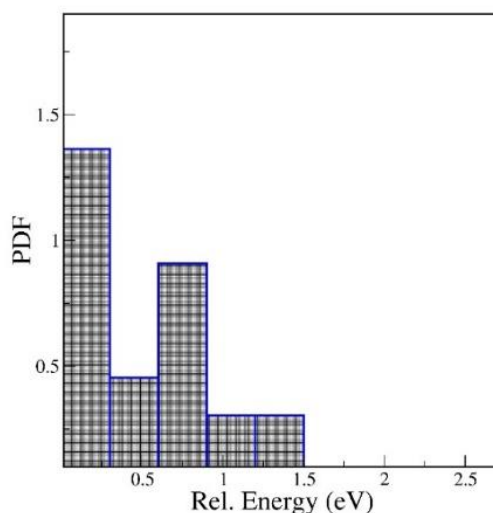


**Figure 5A.16.** Probability distribution of relative energy values of the different configurations.

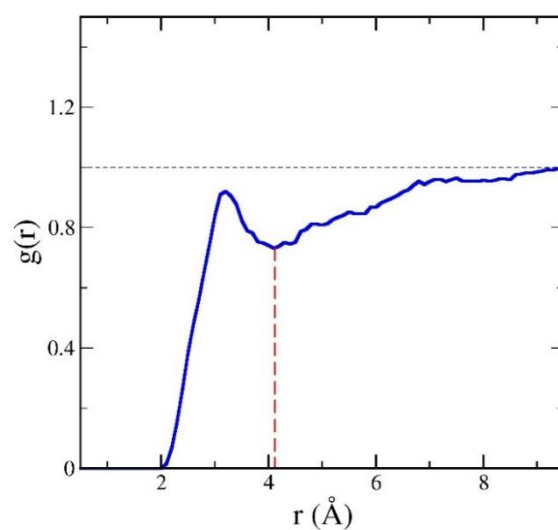


**Figure 5A.17.** The radial distribution function of the center of mass of hydroxy oxygen (O1) and carbonyl oxygen (O2) of DMA3HF and oxygen (Ow) of water molecule. The red dashed line indicates the first solvation shell. This RDF is obtained from classical molecular dynamic simulations.

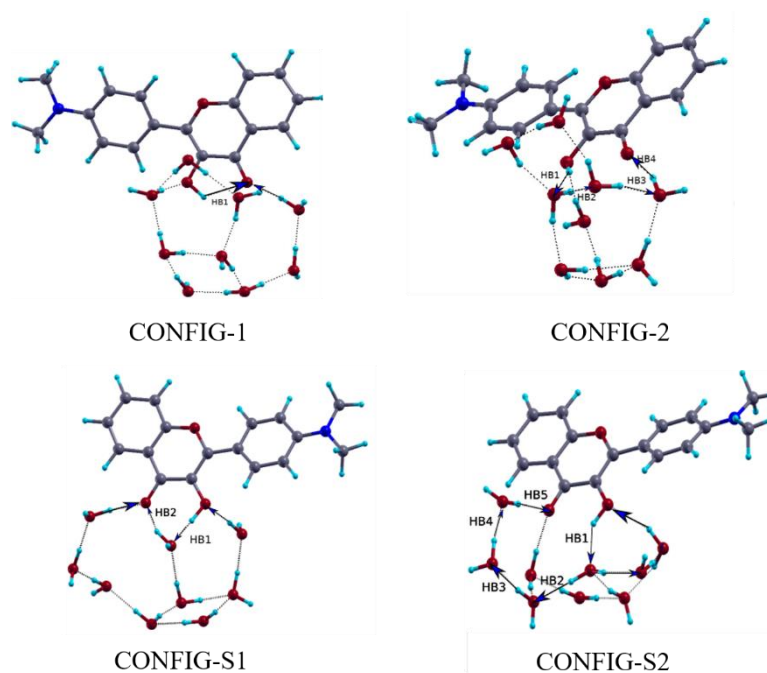


**Figure 5A.18.** Electronic structures of the normal form of DMA3HF for the various possible proton transfer pathways. The pathways have been depicted by arrows.

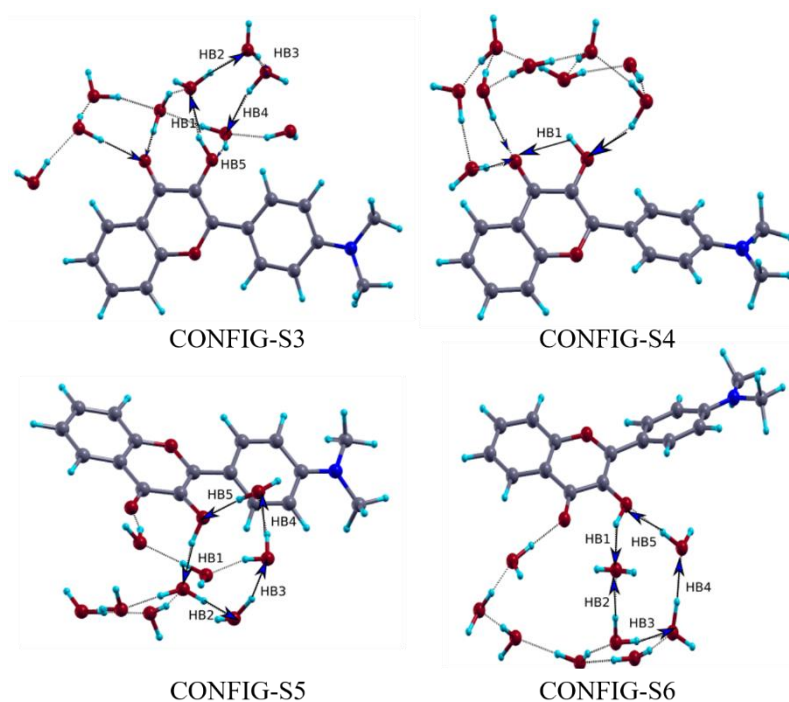


**Figure 5A.19.** Electronic structures of the normal form of DMA3HF for other alternate proton transfer pathways that do not result in the tautomeric species. The pathways have been depicted by arrows.

**Table 5A.3.** Hydrogen bond (HB) lengths from the hydroxyl oxygen (O1) to carbonyl oxygen (O2) in DMA3HF in the ground state. The covalent bond (O-H, in angstroms) and non-covalent bond (H-O, in angstroms) lengths have been depicted within the brackets.

Path	Relative Energy (eV)	HB1	HB2	HB3	HB4	HB5
CONFIG-1	0.124	(0.9796, 1.984)	--	--	--	--
CONFIG-2	0	(0.992, 1.798)	(0.987, 1.768)	(0.973, 1.91)	(0.984, 1.722)	--
CONFIG-S1	0.169	(0.983, 1.807)	(0.981, 1.799)	--	--	--
CONFIG-S2	0.064	(0.985, 1.942)	(0.979, 1.819)	(0.989, 1.730)	(0.985, 1.762)	(0.98, 1.81)



**Table 5A.4.** Hydrogen bond (HB) lengths from the hydroxyl oxygen (O1) to carbonyl oxygen (O2) in DMA3HF in the excited state. The covalent bond (O-H, in angstroms) and non-covalent bond (H-O, in angstroms) lengths have been depicted within the brackets.

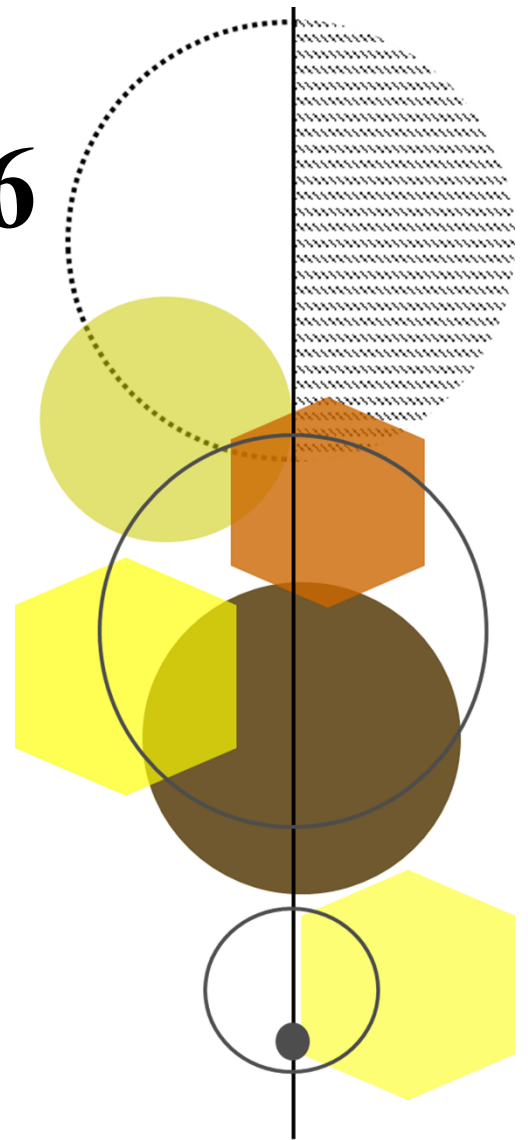
Configuration	HB1	HB2	HB3	HB4	HB5
CONFIG-2	(0.995, 1.848)	(0.985, 1.777)	(0.978, 1.872)	(0.996, 1.641)	--
CONFIG-1	(0.9792, 1.8872)	--	--	--	--
CONFIG-S1	(0.984, 1.785)	(0.993, 1.677)	--	--	--

### 5.5.2 Appendix References

- A1. B. Liu, Y. Pang, R. Bouhenni, E. Duah, S. Paruchuri, L. McDonald, *Chem. Commun.*, 2015, **51**, 11060-11063.
- A2. I. P. Kerschgens, E. Claveau, M. J. Wanner, S. Ingemann, J. H. van Maarseveen, H. Hiemstra, *Chem. Commun.*, 2012, **48**, 12243-12245.
- A3. H. J. C. Berendsen, J. R. Grigera, T. P. Straatsma, *J. Phys. Chem.*, 1987, **91**, 6269-6271.
- A4. J. Wang, R. M. Wolf, J. W. Caldwell, P. A. Kollman, *J. Comput. Chem.*, 2005, **25**, 1157-1174.
- A5. B. H. Besler, K. M. Merz, P. A. Kollmann, *J. Comput. Chem.*, 1990, **11**, 431-439.
- A6. M. J. Frisch, G. W. Trucks, H. B. Schlegel, G. E. Scuseria, M. A. Robb, J. R. Cheeseman, G. Scalmani, V. Barone, B. Mennucci, G. A. Petersson, *et al.*, Gaussian 09, Revision C.01; Gaussian Inc.: Wallingford, CT, 2009.
- A7. D. A. Case, T. E. Cheatham, T. Darden, H. Gohlke, R. Luo, K. M. Merz, A. Onufriev, C. Simmerling, B. Wang, R. J. Woods, *J. Comput. Chem.*, 2005, **26**, 1668-1688.
- A8. W. D. Cornell, P. Cieplak, C. I. Bayly, P. A. Kollman, *J. Am. Chem. Soc.* 1993, **115**, 9620-9631.
- A9. E. J. Sorin, V. S. Pande, *Biophys J.*, 2005, **88**, 2472-2493.
- A10. H. J. C. Berendsen, J. P. M. Postma, W. F. van Gunsteren, A. DiNola, J. R. Haak, *J. Chem. Phys.*, 1984, **81**, 3684-3690.

- A11. B. Hess, *J. Chem. Theory. Comput.*, 2008, **4**, 116-122.
- A12. G. Bussi, D. Donadio, M. Parrinello, *J. Chem. Phys.*, 2007, **126**, 014101.
- A13. S. Sappati, A. Hassanali, R. Gebauer, P. Ghosh, *J. Chem. Phys.*, 2016, **145**, 205102.
- A14. Y. K. Law, A. A. Hassanali, *J. Phys. Chem A*, 2015, **119**, 10816-10827.
- A15. C. Lee, W. Yang, R. G. Parr, *Phys. Rev. B: Condens. Matter Mater. Phys.*, 1988, **37**, 785-789.
- A16. A. D. Becke, *J. Chem. Phys.*, 1993, **98**, 5648-5652.
- A17. C. Filippi, F. Buda, L. Guidoni, A. Sinicropi, *J. Chem. Theory. Comput.*, 2012, **8**, 112-124.
- A18. J. Tomasi, B. Mennucci, E. Cancès, *J. Mol. Struct.: THEOCHEM*, 1999, **464**, 211–226.
- A19. L. Grisanti, D. Pinotsi, R. Gebauer, G. S. K. Schierleb, A. A. Hassanali, *Phys. Chem. Chem. Phys.*, 2017, **19**, 4030-4040.
- A20. K. Das, S. Sappati, P. Hazra, *Phys. Chem. Chem. Phys.*, 2020, **22**, 6210-6221.

# Chapter 6



## Future Prospects

The various studies presented in this thesis point towards the unique characteristics of the aqueous LLC nanochannels. The studies reflect the significant differences in the fundamental physical properties of the LLC water molecules as compared to bulk water. The main attraction is the vast heterogeneity in the LLC nanochannels compared to the homogenous behaviour of bulk solvents. The experimental observations presented in this thesis clearly suggest the presence of multiple water layers inside the nanochannels, with each layer possessing a distinct micropolarity, microviscosity, hydration dynamics and hydrogen-bonding ability. A gradient has been observed in these properties from the central core of the nanochannels to the lipid-water interface and this gradient in the physical properties of the microheterogeneous medium can be exploited in several applications.

One of the important applications of LLC materials is in the field of nanochemistry wherein the mesophases are employed as nanoreactors for the synthesis of a wide array of materials. LLCs consist of distinct hydrophobic, hydrophilic and amphiphilic domains that have already been employed to drive chain reactions, as mentioned in Chapter 1, by bringing close certain substrates while isolating other substrates. Thus, it can be similarly expected that the inherent microheterogeneity observed at the different regions of the aqueous nanochannels will enable certain specific reaction conditions (Figure 6.1). The LLC nanochannels can simplistically be considered as a collection of various sub-domains with the water molecules in each domain exhibiting particular behaviour. In other words, the reaction conditions at the centre of the nanochannels will be quite different compared to those in the lipid-water interface. Similarly, the reaction conditions at the interface will vary from those in the deeper aqueous layers, which are trapped between the lipid headgroups. The remarkable advantage of LLC materials as nanoreactors is that the peculiar physical properties inside the channels cannot be mimicked by any homogeneous medium. For instance, the condition of a high hydrogen bond accepting ability of the water molecules at the lipid-water interface despite a low micropolarity will not be possible to attain in a homogenous medium. Also, the variation of hydrogen bonding behaviour in the LLC channels from borderline aprotic solvent-like in the intermediate region to the high hydrogen bonding capabilities at the interface can be simultaneously used to drive multiple reactions. Additionally, the appreciably high microviscosity and hydration dynamics at the interfacial regions can also be employed to control the diffusion of various substrates.

Such custom reaction conditions enable the design of desired tailor-made materials depending on the properties of each sub-domain in the nanochannels.

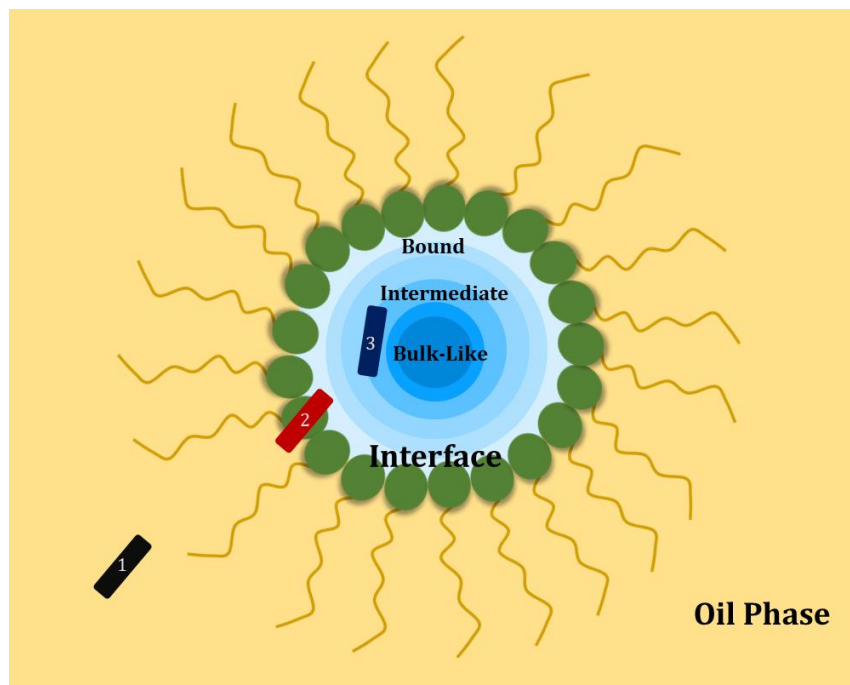


**Figure 6.1.** Schematic representation of the different nanoscopic domains in the cross-section of the inverse LLC mesophases and the multiple water layers in the aqueous domains. Specific reactions can be designed depending on the locations of targets (for example 1,2 and 3 depicted in the figure) at various locations in the mesophases based on the inherent properties of that particular domain.

Besides this, a molecular-level description of the fundamental properties at various regions of the nanochannels will help to determine the interactions between the mesophases and encapsulated drugs and biomolecules. This is particularly useful in the drug delivery and biomolecule-based applications of the mesophases. LLCs have been popularly utilized for the encapsulation and reconstitution of biomolecules.<sup>1</sup> A thorough understanding of the various properties of both the aqueous and lipidic domains can help to fabricate specific LLC mesophases for the selective interaction with different biomolecules. For example, Amar-Yuli et al. have designed  $H_{II}$  mesophases based on monoolein and cationic lipids to encapsulate the predominantly negatively charged DNA via the electrostatic interactions with cationic lipid.<sup>1,3</sup> They probed the controlled release of the DNA from the mesophase into the outside aqueous phase, in the presence of excess water. Besides, a comprehensive knowledge of the aqueous LLC nanochannels can be extended for designing other applications of the LLC mesophases.

For example, the insights on the effect of the LLC water molecules on the Maillard reaction inspired Mezzenga and co-workers to design precisely controlled in meso enzymatic reactions and new technologies for the detection of viruses, parasites, bacteria, and biomarkers.<sup>1, 2</sup> Understanding the precise nature of the aqueous nanochannels can thus help to devise new practical applications of the materials.

While we have attempted to characterise the aqueous networks inside the nanochannels, the observations indicate the necessity of probing the lipid-water interface of the LLC phases in a more targeted manner. This can be realised by anchoring specific fluorescent probes in the lipid-water interface by attaching the probes with long hydrophobic aliphatic chains. Depending on the aliphatic chain length, the probes can be lodged at different depths of the interface which will ensure the mapping of the entire interfacial region. It would also be advantageous to compare the properties of the aqueous domains in the inverse mesophases with that of the lamellar phase, having zero curvature. This might provide valuable insights regarding the effect of the lipid-water interfacial curvature on the properties of the water molecules.

The inherent microheterogeneity of the nanochannels implies a highly dynamic nature of the aqueous domains. Although, the studies reported in this thesis reflect new facets of the molecule-level properties in the LLC nanochannels, which adds significantly to the existing knowledge regarding these systems, further studies are required to augment the understanding, design, and application of these systems.

## References

1. R. Mezzenga, J. M. Seddon, C. J. Drummond, B. J. Boyd, G. E. Schröder-Turk and L. Sagalowicz, *Adv. Mater.*, 2019, **31**, 1900818.
2. J. J. Vallooran, S. Handschin, S. M. Pillai, B. N. Vetter, S. Rusch, H.-P. Beck and R. Mezzenga, *Adv. Funct. Mater.*, 2016, **26**, 181-190.
3. I. Amar-Yuli, J. Adamcik, S. Blau, A. Aserin, N. Garti and R. Mezzenga, *Soft Matter* 2011, **7**, 8162-8168.

**The End**

---